SCHOOL OF MATHEMATICS AND STATISTICS

ANALYSIS OF THE FLOW FIELD BETWEEN TWO ECCENTRIC ROTATING CYLINDERS IN THE PRESENCE OF A SLOTTED SLEEVE

by

Lee David Hird

This thesis is presented in fulfilment of the requirements

for the award of the Degree of

Doctor of Philosophy (Applied Mathematics)

of the

Curtin University of Technology

November 1997

Abstract

Overend et al [68] designed a viscometer to measure the viscosity of slurries that have a tendency to settle. This viscometer consists of a rotating ribbed rotor surrounded by a stationary slotted sleeve; this system is then placed eccentrically within an inclined rotating bowl. It is claimed that this viscometer overcomes most of the difficulties encountered when attempting to obtain accurate measurements for these types of mixtures. If the mixture being sheared within the annulus does not represent the true composition of the slurry being tested then the results are expected to be inaccurate. The presence of sediment at the bottom of the rotor or the formation of large masses of particles within the flow domain will affect the accuracy of the measurements obtained. This dissertation studies the amount of flow through the slotted sleeve and the region, or regions, of low shear rate within the flow domain. Assuming that end-effects are unimportant and that the slurries can be replaced by a single-phase fluid, three two-dimensional models are proposed. These models are designed to capture the large-slot construction of the sleeve and the, approximate, non-Newtonian behaviour of the slurries. The first two models solve analytically (using a regular perturbation scheme) and numerically (using a finite volume method) the moderate- and large-Reynolds-number flow, and the third model uses a finite volume method to study the flow patterns developed by pseudoplastic fluids. The results show that the mixing of the slurry is expected to be enhanced by moving the concentric system (i.e., the rotor and the slotted sleeve) close to the rotating bowl and using low to moderate speeds for the rotor and bowl. In addition, when the cylinders rotate in the same directions, two (counter-rotating) eddies are present within the flow domain; whereas, only one eddy (rotating counter-clockwise) is present when the cylinders rotate in opposite directions. The presence of eddies in the former situation inhibits the flow through the sleeve; while, for moderate rotor

speeds, the flow through the sleeve is enhanced in the latter. When the slurry is assumed pseudoplastic, we observe a region of low shear rate located near the dividing streamline present within the flow field. The distribution of shear rate within the flow field is shown to be affected by factors such as the rate of diffusion of the apparent viscosity and the value of the power law index. Therefore, this study suggests that for certain types of slurries, concentrations of particles exist within the domain and that the mixing of slurries can be impeded by the presence of eddies within the main flow field.

Certification

I certify that this thesis is my own work and that all references are duly acknowledged. This thesis has not been submitted, in whole or in part, in respect of any academic award at Curtin University of Technology or elsewhere.

Lee David Hird

November 1997

Acknowledgements

Reaching this point would not have been possible without the guidance of my reseach supervisor, Dr. Peg-Foo Siew. Our discussions have always left me looking at my work from a different perspective and wanting to learn more. I have also learnt much from his professionalism and attitude towards research. I would also like to thank my associate supervisors, Dr. Yong Hong Wu and Dr. Song Wang for their helpful suggestions.

To my parents, thank you for giving me the resilience to pursue my ambitions. Special thanks to my soulmate Amanda for her support and understanding, and for undertaking the arduous task of proof reading the many versions of this dissertation. I thank my close friends for their invaluable friendship and support.

I would like to thank my fellow postgraduate students for making the working environment one of mutual support and encouragement and for sharing their thoughts with me–their friendship will never be forgotten.

I wish to record my thanks to Curtin University of Technology for the receipt of a Postgraduate Research Scholarship and, therefore, making it possible for me to undertake postgraduate studies.

Contents

List of Figures

List of Tables

Chapter 1

Introduction

1.1 Background

In industry, an understanding of the rheological properties of slurries and how to alter these properties is important. For example, when the slurry is to be transported or used in a casting process, a dispersing agent (e.g., a surfactant) is often added to the slurry so that the particle concentration can be increased while leaving the fluidity of the slurry unaffected. The rheological properties of slurries can also give an indication of how to design equipment so that the slurry can be transported or mixed efficiently. The use of a viscometer is essential in estimating the properties of slurries. A viscometer commonly used to determine the dynamic viscosity of Newtonian and viscoinelastic fluids is the rotary viscometer. For this type of viscometer, the small annular gap between the two concentric cylinders is filled with the test fluid. If one cylinder rotates at a constant angular velocity, the fluid tends to rotate at the same angular velocity and exerts a torque on the stationary cylinder. The reaction torque on the stationary cylinder can be measured and the dynamic viscosity is then calculated once the dimensions of the viscometer, angular velocities of the cylinders and the temperature of the slurry are known. The greater the torque, the higher the viscosity. The prescribed speed of the rotating cylinder is chosen so that the shear-driven flow within the annulus remains

laminar. While a single experimental measurement is used to determine the dynamic viscosity of a Newtonian fluid, a series of one-point measurements must be made to determine the viscosity of a non-Newtonian fluid. These measurements are generated by continuously varying the shear rate whilst the shear stress is being measured.

Obtaining accurate and reliable results from a viscometer can be difficult since there are many factors that can influence the results. For example, the temperature of the liquid phase, the presence of slip along the walls of the viscometer, the size, shape, concentration and density of the particles and whether the particles remain suspended or begin to settle can affect the measurement of the viscosity. Wall slip can be reduced (or eliminated altogether) by profiling the walls of the viscometer (see Barnes [7]), and a constant temperature bath can be used to control the temperature of the slurry; however, maintaining the homogeneity of the slurry, while its rheological properties are being determined, is difficult to achieve.

The viscometer designed by Overend et al [68] used to measure the rheological properties of settling slurries consists of a modified rotary viscometer, of Searle type, lowered close to the wall of an inclined rotating bowl (see Fig. 1.1). The rotary viscometer consists of a rotating ribbed rotor surrounded by a fixed slotted sleeve. The slotted sleeve is designed to encourage the entrainment of the slurry onto the rotor, and the bowl rotates to ensure that the slurry is well-mixed. To measure the dynamic viscosity, the rotor rotates with a given azimuthal velocity; this exerts a torque on the slurry, forcing the fluid to shear, and the shear stress acting on the rotor is determined. The viscometer has the ability to continuously vary the shear rate whilst the shear stress is determined; hence, a rheogram can be produced and the dynamic viscosity of the test fluid can be determined as the shear rate varies. Throughout the measuring process, the temperature of the slurry is held constant by immersing

the apparatus into a constant temperature bath, and the rotational speeds of the rotor and the bowl can be varied independently of each other.

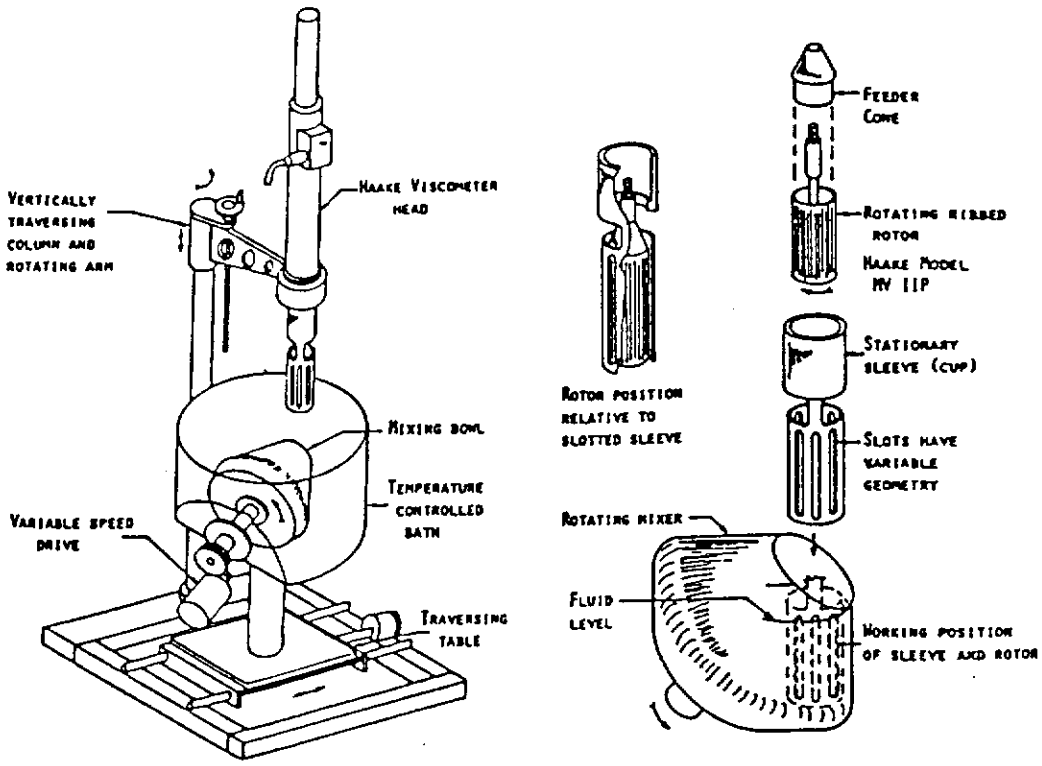

Figure 1.1: The viscometer (reproduced with the permission of Overend et al).

In a recent paper by Phan-Thien et al [71], the movement of particles suspended in a viscous Newtonian fluid between two eccentric cylinders is considered. The shear-induced movement produced when the inner cylinder rotates steadily and the outer cylinder is stationary is observed both experimentally and numerically. Their results show that particles migrate to regions of low shear rate. Although the work done by Phan-Thien et al [71] is only two dimensional and a slotted sleeve is not placed within the flow domain, their work does bring the effectiveness of the viscometer designed by Overend et al [68] into question. The existence of concentrations of particles within the flow field and the role of the slotted sleeve in dispersing this mass is uncertain. Clearly, if there do exist concentrations of particles within the flow field, the dynamic viscosity measured would represent the viscosity of a slurry with less particle

density than the slurry tested. Furthermore, the amount of mixing will also affect the homogeneity of the slurry; thus, there is a need to understand the flow around this modified viscometer.

The aim of this dissertation is to gain an understanding of the flow field developed within the modified viscometer designed by Overend et al [68]. This will be achieved by considering three two-dimensional models of the viscometer. These models are used to understand the laminar flow field developed when the two bounding cylinders rotate uniformly. The first two models determine, analytically and numerically, the flow fields developed by Newtonian fluids (of small kinematic viscosity), and the third model uses pseudoplastic (shear thinning) fluids, without a yield stress, to determine the fully developed flow field. By applying these models, those parameters that affect the flow through the slotted sleeve, such as, the existence and location of eddies and also those parameters that affect the existence of regions of large, or small, shear within the flow domain can be determined. Although, in each of the models considered here, the slurry is replaced by a single-phase fluid, the study will nevertheless throw light on the effectiveness of the viscometer.

This dissertation is composed of chapters, sections and subsections. Within each section, equations are labelled sequentially, for example, equation (2.3.1) denotes the first equation in Section 3 of Chapter 2. Also, in each chapter the figures and tables are labelled sequentially, for example, Fig. 2.1 represents the first figure in Chapter 2 and Table 4.1 denotes the first table in Chapter 4.

The remainder of this chapter reviews the current literature concerning the laminar flow of Newtonian and non-Newtonian fluids between rotating cylinders. Chapter 2 introduces each model and their corresponding dynamical equations used to study the flow within the viscometer. Chapters 3, 5 and 7 give a clear exposition of the techniques used to determine the flow fields using the proposed models. The results obtained for each model are discussed

in Chapters 4, 6 and 8. Thus, Section 2.2 and Chapters 3 and 4 introduce the first model, present the analytical techniques used to solve the governing equations and discuss the results obtained. Similarly, Section 2.3 and Chapters 5 and 6 present the second model, develop the numerical solution and discuss the flow fields developed. For the third model, the process of defining the constitutive equations and numerically solving the governing equations through to displaying the flow fields for various parameters are given in Section 2.4 and Chapters 7 and 8.

1.2 Overview

Initially, we limit our discussion to Newtonian fluids. Given the advancement in the properties of lubricants and their ability to perform at high speeds, much of the work done in studying the azimuthal annular motion between eccentric rotating cylinders has been aimed at extending the theory of hydrodynamic lubrication for the laminar flow within a journal bearing. Wannier [92] solved analytically Stokes flow between eccentric rotating cylinders without restricting the geometry. Here, he showed that Reynolds equation can be reproduced from the first-order correction to Stokes equation when expanded in powers of the film thickness. Subsequent studies have focussed on the curvature and inertial correction effects. Typically, these higher-order corrections are solved analytically and the results compared with controlled experiments. In the study of inertial correction, Kulinski and Ostrach [51] use the eccentricity to perturb the full momentum equations; Yamada and Nakabayashi [96] ignore completely the curvature of the problem, and Kamal [50] expand the momentum equations in inverse powers of kinematic viscosity. DiPrima and Stuart [31] use a regular perturbation scheme, based on a modified Reynolds number and clearance ratio, to generate both inertial and curvature corrections of any order; however, they neglected terms when calculating the Reynolds

approximation. This is pointed out by Myllerup and Hamrock [66] who fully implement the perturbation scheme to generate the correct higher-order terms.

When considering the flow between eccentric rotating cylinders, the eccentricity ratio influences the character of the developed flow. For example, if the eccentricity ratio is sufficiently large, eddies are known to occur within the flow domain. This phenomenon was first shown experimentally by Bentwich and Elata [11] who considered Stokes flow between two long eccentric rotating cylinders. The most comprehensive study to date on the generation of eddies is that undertaken by Ballal and Rivlin [5]. Without any restrictions placed on the geometry, a perturbation of the Navier-Stokes equation is made using inverse powers of kinematic viscosity. Both Stokes flow and the inertial correction are obtained. Conditions when stagnation points, separation points and eddies exist are given, and the effect of the inertial correction on the location of these phenomena is examined. Ballal and Rivlin [5] point out that the solutions to Stokes flow and the linearised inertial correction given by Kamal [50] are incorrect. These discrepencies are also pointed out by Ashino and Yoshida [3].

The high-Reynolds-number (small kinematic viscosity) flow between eccentric rotating cylinders has also been studied. Using a regular perturbation based on the eccentricity, Wood [95] showed that if the cylinders rotate in the same direction, the asymptotic expansions generated for the stream and vorticity functions are uniform within the entire flow field and the well-known property (see Batchelor [9]) of vorticity being concentrated within the boundary layer, but approximately uniform within the inviscid core, is reproduced. The asymptotic expansion for the stream function is used to generate higher-order corrections to Prandtl's boundary layer equation. Chipman and Duck [24] solved numerically the high-Reynolds-number flow between eccentric rotating cylinders; however, unlike Wood [95] the eccentricity here is of unitary

order. To determine the flow field, Prandtl's boundary layer approximation along the two cylinders is coupled with the kinematic (Poisson) equation describing the motion within the inviscid region. Central-differencing is used to discretise the coupled system and direct methods are used to solve the linear equations. The flux between the two cylinders and the inviscid core vorticity are calculated by minimising the sum of shear rates along the outer edge of the boundary layers located along the walls of the cylinders. This technique gives a means of estimating the instance when the flow within the boundary layers fails to be unidirectional.

Sood and Elrod [84] appear to be the earliest workers to solve numerically the full non-linear Navier-Stokes equations between eccentric cylinders. Without resticting the eccentricity, a finite difference method is used to solve Stokes flow when only the inner cylinder rotates. The movement of the separation and reattachment points resulting from the inertial correction is noted. When only the outer cylinder undergoes uniform rotation, the pressure distribution on the inner cylinder is given for various eccentricities, clearance ratios and Reynolds numbers (where Reynolds numbers up to 10^3 are used). Sood and Elrod [84] noted discrepancies in the pressure fields, when the clearance ratio is varied, between their results and those generated by Yamada and Nakabayashi [96].

San Andres and Szeri [78] use a Bubnov-Galerkin finite element method based on B-splines to solve the full Navier-Stokes equations. No restrictions are placed on the geometry and the accuracy of the numerical method is investigated by solving Stokes flow for various conditions and comparing the results with the analytical results of Ballal and Rivlin [5]. The inertial effects on the pressure field are discussed and comparisons with the perturbation solution of DiPrima and Stuart [31], the noninertial solution of Ballal and Rivlin [5] and the classical noninertial lubrication approximation are made. Changes in the

eddy centre location and the separation and reattachment points due to the inertial effects are shown. The orientation of the separation and reattachment points for various ranges of eccentricity observed by San Andres and Szeri [78] are compared with those presented by Ballal and Rivlin [5], there being some contradictory results between the two studies for small eccentricities.

Mineral slurries are often non-Newtonian in character and their rheological behaviour is estimated experimentally. If the concentration of the minerals is high, the slurry has a yield stress and the Bingham fluid is often used as a rheological model. The difficulty in modelling the flow of a viscoplastic fluid is in determining the yield surface. This is often achieved numerically, (see Bercovier and Engelman [12], Huilgol and Panizza [46], Szabo and Hassager [85] and Tanner and Milthorpe [87]) but has also been determined analytically for some rectilinear flows (Craster [27]) and for flows in a concentric annulus (see Bittleston and Hassager [14]). The viscometer designed by Overend et al [68] is used by the Curtin University Slurry Research Group to analyse mineral slurries. From the rheograms given to us, some mineral slurries can be Newtonian (e.g., silicon-based slurries) and others viscoplastic (e.g., Nickle ore slurries). However, if the concentration of particles is low enough, the slurry will not have a yield stress; thus, the need to determine the plug regions is removed and the slurry now behaves like a pseudoplastic (shear-thinning) fluid. Moreover, the rheological properties of some slurries can be controlled by varying the particle size and concentration (see Logos and Nguyen [54]) or by adding a dispersing agent (see Roh et al [75]) so that the slurry can be modelled by a pseudoplastic fluid. The Ostwald-de Waele power law model (see Bird et al [13]) is often used to define the constitutive equations; however, workers have used the Hershel-Bulkley model as it encompasses Newtonian, Bingham and power law fluids.

Various types of mixtures can be modelled by power law fluids. For exam-

ple, yellow clay in water, coal in water, alumina slurries, napalm in kerosene, paper pulp in water, cement rocks in water. Also liquids such as paints, oils and detergents can be modelled using power law fluids. In engineering practices, polymers are added to oils to enhance the performance of lubricants within journal bearings. Normal stresses are usually of secondary importance when compared with shear stresses; therefore, lubricants can be modelled using pseudoplastic fluids (see Dien and Elrod [30], Johnson and Mangkoesoebroto [49] and Safar [77]). Power law fluids have also been used to model the extruders for molten plastics, well bore fluid recirculation for the removal of drill cuttings and the polymer melt in a coating process (see for example Malik and Shenoy [56] and Yang and Chukwu[97]). These processes are characterised by the axial Couette flow within concentric and eccentric annuli and the performance of the non-Newtonian fluid can be measured by determining the velocity profile and volumetric flow rate. Whether the application of power law fluids is used to understand the performance of lubricants in a journal bearing (where Reynolds equation is often solved) or used to model Poiseuille or Couette flow, the transport equations are simplified either by aproximations used (as in the former example) or by the geometry of the problem (as in the latter example). The simple form of the resultant transport equations allow either analytical or numerical solutions to be obtained.

In a recent paper by Phan-Thien et al [71], the movement of particles suspended in a viscous Newtonian fluid between two eccentric cylinders is considered. Their results show that the particles migrate to regions of low shear rate. When the inner cylinder rotates steadily and the outer cylinder is fixed, the shear-induced movement is observed experimentally, using nuclear magnetic resonance imaging. Neglecting inertial terms, a numerical treatment is carried out by solving the coupled constitutive and diffusion equations using an explicit finite volume method based on the artificial viscosity method. The

Newtonian constitutive equation accounts for the viscosity being dependent on the local concentration of particles, while the diffusion equation models the shear-induced movement of the particles. Steady-state velocity and concentration contours are given and compared with the experimental results. When flow reversal is not present, good agreement is obtained between the numerical and experimental results. When an eddy is observed experimentally, the highest concentration of particles occurs along the dividing streamline; however, for the same flow parameters, no eddy is observed numerically and the region of highest particle concentration is located along the surface of the outer cylinder.

The work done by Phan-Thien et al [71] illustrates the need to examine the flow field within the viscometer designed by Overend et al [68]. A first attempt to understand the flow around the slotted sleeve is given by Hird and Siew [42] who consider the case of a Newtonian fluid in the small-Reynolds-number limit. The sleeve is assumed to have numerous small slots so that a good approximation is to replace the sleeve with a rigid permeable membrane on which a no-slip condition is imposed. The low-Reynolds-number limit allows the solution in the two regions bounded between a rotating cylinder and the membrane to be determined analytically, and assuming Darcy's law governs the radial flow through the membrane, the flow fields can be matched across the membrane. The results obtained using this crude model show that the entrainment of the fluid is inhibited by the presence of an eddy located within the main flow domain. In practice, the slots in the modified viscometer are large enough to encourage the entrainment of the slurry onto the rotor and the slurry is often non-Newtonian. We, therefore, propose three two-dimensional models designed to take into account the large-slot construction of the slotted sleeve and the non-Newtonian behaviour of the slurry. These models represent a significant improvement on the model used by Hird and Siew [42]. The

information gained using these models will give further understanding to the flow of the slurries induced by the viscometer.

Chapter 2

Introducing the Models

2.1 Defining the Two-Dimensional Problem

Overend et al [68] have developed a viscometer that is claimed to be capable of measuring effectively the dynamic viscosity of settling slurries. This new viscometer was developed by adding an outer rotating bowl to a rotary viscometer of Searle type. The rotary viscometer consists of a rotating ribbed rotor surrounded by a stationary slotted sleeve possessing open ends. The rotor and sleeve are then placed close to the wall of the bowl. To measure the dynamic viscosity of a slurry, the bowl is first filled until the annular region between the rotor and the sleeve is taken up by the slurry. As the tangential velocity of the rotor is varied from zero to a preset value, the shear stress needed to shear the slurry within the annulus, at a given shear rate, is measured by the torque-sensing transducer connected to the driving mechanism of the rotor. Plotting shear stress against shear rate generates a rheogram and the dynamic viscosity is measured. The bowl is inclined to ensure the slurry is well-mixed, the slotted sleeve is designed to encourage the entrainment of the slurry onto the rotor, and the rotor is ribbed to reduce slip effects. The rotational speeds of the rotor and bowl can be varied independently of each other, and to ensure that the temperature of the slurry is held fixed while the dynamic viscosity is being measured, the bowl is immersed into a constant temperature bath. The

numerous rotational speeds of the rotor, measurement intervals, et cetera, are programmed prior to the measurement, and rheograms are readily produced. Measurements of the dynamic viscosity of Newtonian fluids with known properties are used to calibrate the apparatus. To test the effectiveness of the bowl, Overend et al [68] performed an experiment where the rotation of the bowl is stopped for a period of time whilst the rotational rate of the rotor is programmed to continuously vary from zero to a chosen limit and back to zero again. The rheograms produced show numerous troughs where the shear stress decreases and then increases rapidly as the speed of the bowl is switched from zero to a fixed value. A rheogram produced when the rotational speed of the bowl is unaltered is superimposed onto this experiment. During the periods when the bowl is rotating, the shear stress shear rate relationship follows the rheogram produced when the rotation of the bowl is not impulsive but varied steadily. This viscometer is used by the Curtin University Slurry Research Group (CUSRG) to analyse mineral-based slurries. From consultation with the CUSRG, speeds of $0 - 300$ rpm and $0 - 120$ rpm are typically used for the rotor and bowl, respectively, during the measuring process.

To study the three-dimensional flow generated by the viscometer, a numerical approach must be undertaken. Due to the features of slurries and the apparatus, developing a three-dimensional model is expected to be difficult. For example, because the bowl has an irregular shape and the axes of the rotor and bowl are not parallel (see Fig. 1.1), the geometry is difficult to model. Also, to capture the effects generated by the size, density and concentration of the slurry, a multiphase fluid should be used to model the slurry; however, an attempt to describe the flow of silica suspensions using a power law model has been given by Chandler and Jones [20]. Here the viscosity function is modified to take into account the particle concentration, size and shape. In addition to the difficulties mentioned, attempting to take into account features such as

end-effects, corner singularities in the stress and velocity gradients, the presence of wall slip and the effect of viscous dissipation on the temperature of the slurry adds to the complexity of the model.

Our primary interest is in modelling the flow field in the presence of the slotted sleeve. Laboratory observations of the apparatus suggest that, at low to moderate rotational speeds, the flow appears to be laminar over much of the length of the viscometer. Also, Cole [25] has studied the flow of a Newtonian fluid between concentric and eccentric cylinders and concluded that the length of the cylinders has a negligible effect on estimating the onset of secondary flow (i.e., Taylor vortices). Therefore, we do not expect any significant information will be lost if we consider the flow without the complications introduced by end conditions. We, therefore, consider a two-dimensional model where the rotary viscometer is assumed long enough so that the entry conditions do not affect the flow field under consideration and the bowl is replaced with a cylinder of infinite length with axis parallel to the axis of the coaxial system placed within. The rotary viscometer is now replaced with an inner cylinder (rotor) surrounded by a stationary sleeve having radius a. The rotor has radius c and rotates uniformly with angular velocity ω_1. This assembly is placed within the outer cylinder, or bowl, with offset of the cylinder axes given by $a\epsilon$. The bowl having radius b rotates uniformly with angular velocity ω_2. Oxy axes are taken in the plane perpendicular to the axes of rotation with origin at the centre of the rotor. Let Ω represent the region of the xy-plane between the rotor and bowl denoted by $\partial\Omega_1$ and $\partial\Omega_2$, respectively (see Fig. 2.1). Also, we denote the s surface elements of the sleeve by $\partial\Omega_3^q$ $(q = 1, \ldots, s)$. The sleeve used in practice is designed to facilitate the entrainment of the slurry onto the rotor. Typically, only one-third of the sleeve is solid. For notational ease, $\partial\Omega_3$ is used when it is not necessary to identify $\partial\Omega_3^q$ individually. Instead of using a multiphase fluid to model the slurry, we replace the slurry with a

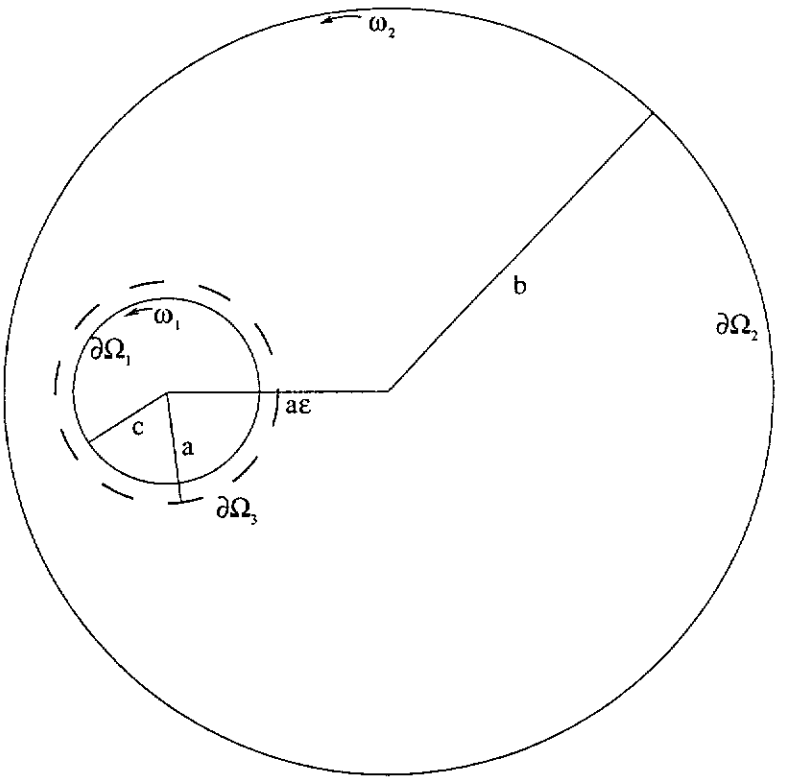

Figure 2.1: The two-dimensional flow domain.

generalised Newtonian fluid and since, in practice, the viscometer is immersed into a constant temperature bath, we only consider isothermal flows.

We now develop the equations governing the two-dimensional flow of generalised Newtonian fluids. From these equations, the governing equations used in each of the three models can be extracted. For incompressible fluids, the conservation of mass is given by

$$\frac{\partial u_i}{\partial x_i} = 0, \tag{2.1.1}$$

where u_i (in Cartesian coordinates) represents the velocity component along the x_i axis and where the Einstein summation convention is used. Futhermore, if σ_{ji} denotes the components of the Cauchy stress tensor, then it denotes the ith component of stress on a surface normal to the x_j axis. In the absence of

any body forces, the ith component of the linear momentum equation is

$$\rho\frac{\partial u_i}{\partial t}+\rho u_j\frac{\partial u_i}{\partial x_j}=\frac{\partial \sigma_{ji}}{\partial x_j}, \tag{2.1.2}$$

where ρ is the density of the fluid. By writing the Cauchy stress tensor in terms of the deviatoric stress tensor τ_{ji}, i.e.,

$$\sigma_{ji}=\tau_{ji}-p\delta_{ji} \tag{2.1.3}$$

where p represents the isotropic pressure, and δ_{ji} is the Kronecker delta, then equation(2.1.2) becomes

$$\rho\frac{\partial u_i}{\partial t}+\rho u_j\frac{\partial u_i}{\partial x_j}=-\frac{\partial p}{\partial x_i}+\frac{\partial \tau_{ji}}{\partial x_j}. \tag{2.1.4}$$

Taking the curl of (2.1.4) gives

$$\rho\frac{\partial \zeta_i}{\partial t}+\rho\left(\frac{\partial u_j}{\partial x_k}\frac{\partial u_m}{\partial x_j}\epsilon_{kmi}+u_j\frac{\partial \zeta_i}{\partial x_j}\right)=\frac{\partial^2\tau_{jm}}{\partial x_k\partial x_j}\epsilon_{kmi}, \tag{2.1.5}$$

where $\zeta_i=\dfrac{\partial u_m}{\partial x_k}\epsilon_{kmi}$ and ϵ_{kmi} are the components of the skew-symmetric permutation tensor. Further, noting the result,

$$\epsilon_{kmi}\frac{\partial u_j}{\partial x_k}\frac{\partial u_m}{\partial x_j}+\epsilon_{kmj}\frac{\partial u_m}{\partial x_k}\frac{\partial u_i}{\partial x_j}=0,$$

and using (2.1.1), equation (2.1.5) becomes

$$\rho\left(\frac{\partial \zeta_i}{\partial t}+u_j\frac{\partial \zeta_i}{\partial x_j}-\zeta_j\frac{\partial u_i}{\partial x_j}\right)=\frac{\partial^2\tau_{jm}}{\partial x_k\partial x_j}\epsilon_{kmi}. \tag{2.1.6}$$

In two-dimensions (2.1.6) simplifies to

$$\frac{\partial \zeta}{\partial t}+u_1\frac{\partial \zeta}{\partial x_1}+u_2\frac{\partial \zeta}{\partial x_2}=\frac{1}{\rho}\frac{\partial^2\tau_{jm}}{\partial x_k\partial x_j}\epsilon_{km3}, \tag{2.1.7}$$

where $\zeta_3=\zeta$ represents the magnitude of the vorticity function. We now define the constitutive equation for the fluid by

$$\tau_{jm}=2g(\dot{\gamma})\dot{\gamma}_{jm}. \tag{2.1.8}$$

In general, the viscosity function, $g(\dot{\gamma})$, is a function of the invariants of the rate-of-deformation tensor; however, since the fluid is incompressible and we anticipate that shear viscosity will dominate in the developed flow, $g(\dot{\gamma})$ is a scalar function of the second invariant of the rate-of-deformation tensor, $\dot{\gamma}_{jm}$, viz

$$\dot{\gamma} = \sqrt{2(\dot{\gamma}_{jm} : \dot{\gamma}_{jm})}$$

where $\dot{\gamma}_{jm} = \frac{1}{2}\left(\frac{\partial u_j}{\partial x_m} + \frac{\partial u_m}{\partial x_j}\right)$. After some manipulation, we find

$$\begin{aligned} \frac{1}{\rho}\frac{\partial^2 \tau_{jm}}{\partial x_k \partial x_j}\epsilon_{km3} &= \frac{g}{\rho}\nabla^2\zeta - \frac{\zeta}{\rho}\nabla^2 g + \frac{2}{\rho}(\nabla \times [\nabla g \cdot \nabla]\,\mathbf{v}) \cdot \mathbf{k}, \\ &= \nabla \cdot \left(\frac{g}{\rho}\nabla\zeta - \frac{\zeta}{\rho}\nabla g\right) + \frac{2}{\rho}(\nabla \times [\nabla g \cdot \nabla]\,\mathbf{v}) \cdot \mathbf{k}. \end{aligned} \tag{2.1.9}$$

where $\mathbf{v}$ denotes the velocity vector. Therefore, the unsteady, isothermal flows of incompressible, viscous, generalised Newtonian fluids in the domain, Ω, (see Fig. 2.1) are modelled by

$$\begin{aligned} \frac{\partial \zeta}{\partial t} - \nabla \cdot \left(\frac{g}{\rho}\nabla\zeta - \left[\mathbf{v} + \frac{1}{\rho}\nabla g\right]\zeta\right) &= \frac{2}{\rho}(\nabla \times [\nabla g \cdot \nabla]\,\mathbf{v}) \cdot \mathbf{k}, \\ \nabla^2\psi + \zeta &= 0, \\ \text{and} \qquad \tau_{ij} &= 2g(\dot{\gamma})\dot{\gamma}_{ij}. \end{aligned} \tag{2.1.10}$$

where the stream function, ψ, represents the vector potential of the solenoidal vector field. Using the Herschel-Bulkley model (see Craster [27]), we define

$$g(\dot{\gamma}) = \frac{\tau_o \eta(\dot{\gamma})}{\dot{\gamma}} \tag{2.1.11}$$

where

$$\eta(\dot{\gamma}) = \tau_c + k_1 \left(\frac{\dot{\gamma}}{\dot{\gamma}_o} \right)^{\alpha} \tag{2.1.12}$$

for a fully yielded fluid. Here τ_c, τ_o and $\dot{\gamma}_o$ represent the yield stress and reference values for the stress and shear rate. Also, k_1 is a dimensionless constant and α is the power law, or flow behaviour, index. The Herschel-Bulkley model is capable of modelling Newtonian ($\alpha = 1$, $\tau_c = 0$), Bingham ($\alpha = 1$) and power law fluids. Although slurries have been modelled using Bingham fluids, if the particle concentration is sufficiently small the slurries are pseudoplastic in behaviour. Thus, we will use the rheological equation for power law fluids characterised by the two parameters k_1 and α and take the power law index to be less than or equal to unity. The smaller the power law index becomes, the greater the degree of non-linearity in $\eta(\dot{\gamma})$ and, therefore, the greater the non-Newtonian behaviour of the fluid. k_1 is a measure of the consistency of the fluid, the higher the value of k_1, the more viscous the fluid becomes. The governing equations given in (2.1.10) are made dimensionless using a, $b\omega_2$ and $\dot{\gamma}_o$ as the scales for length, velocity and shear rate; hence,

$$\begin{aligned} p_o \frac{\partial \zeta}{\partial t} - \nabla \cdot (Sh \nabla \zeta - [\mathbf{v} + S \nabla h]\, \zeta) &= 2S \left(\nabla \times [\nabla h \cdot \nabla]\, \mathbf{v} \right) \cdot \mathbf{k}, \\ \nabla^2 \psi + \zeta &= 0, \end{aligned}$$

where

$$\begin{aligned} \tau_{ij} &= 2h(\dot{\gamma}) \dot{\gamma}_{ij}, \\ \text{and} \qquad h(\dot{\gamma}) &= \frac{\eta(\dot{\gamma})}{\dot{\gamma}} = k_1 \dot{\gamma}^{\alpha - 1}. \end{aligned} \tag{2.1.13}$$

Here, $S = \dfrac{\tau_o}{\rho a b \omega_2 \dot{\gamma}_o}$ is a dimensionless group, t denotes time and we have put $\tau_c = 0$. We note that S can be thought of as the ratio of shear forces to inertial forces. This interpretation will be used to understand some of the results

given in Chapter 8. When the fluid is Newtonian, $\alpha = 1$, $Sh = 1/Re$ (where Re denotes the Reynolds number) and equation (2.1.13) reduces to equation (2.2.1) for the stationary problem (i.e., $p_o = 0$) and reduces to equation (2.3.1) for the transient problem (i.e., $p_o = 1$).

The no-slip conditions on the solid surfaces $\partial\Omega_1$, $\partial\Omega_2$ and $\partial\Omega_3$ yield the boundary conditions

$$\left.\begin{aligned} \nabla\psi \cdot \mathbf{n} = \quad & \bar{U} \quad \forall\, \boldsymbol{x}\in\partial\Omega_1 \text{ and } t \in (0,\mathrm{T}], \\ \nabla\psi \cdot \mathbf{n} = \quad & -1 \quad \forall\, \boldsymbol{x}\in\partial\Omega_2 \text{ and } t \in (0,\mathrm{T}], \\ \text{and} \quad \nabla\psi \cdot \mathbf{n} = \quad & 0 \quad \forall\, \boldsymbol{x}\in\partial\Omega_3 \text{ and } t \in (0,\mathrm{T}], \end{aligned}\right\} \tag{2.1.14}$$

where $\mathbf{n}$ represents the unit outward normal vector and $\bar{U} = c\omega_1/b\omega_2$ denotes the dimensionless azimuthal velocity of the rotor. Along each of the boundaries, the stream function is represented by

$$\psi = 0 \quad \forall \boldsymbol{x}\in\partial\Omega_1,\ \psi = K_2 \quad \forall \boldsymbol{x}\in\partial\Omega_2 \quad \text{and } \psi = K_3^q \quad \forall \boldsymbol{x}\in\partial\Omega_3^q, q = 1,\ldots,s. \tag{2.1.15}$$

These correspond to no flow through the solid boundaries.

Apart from the experimental observations, little is known about the flow field around the slotted sleeve. This dissertation applies three models in an attempt to describe the flow of viscous fluids around the slotted sleeve. The first two models assume the fluid is Newtonian and determine the flow field first analytically and then numerically. The third model replaces the slurry with a power law fluid (i.e., shear-thinning). The governing equations for each model considered here can be written in the form given in (2.1.13). We are interested in solving stationary problems whose solutions are regarded as the long-term solution of the transient problem given in (2.1.13).

If the non-linearly coupled equations given in (2.1.13) are solved simultaneously then the above boundary conditions are sufficient to determine the stream and vorticity functions at a point $\boldsymbol{x}$ $(= (x_i, y_i))$ in Ω and at a given time

$t \in (0,T]$; however, in our numerical simulation we will estimate the vorticity along the no-slip surfaces and solve the system in (2.1.13) iteratively.

In the first model, we use the regular perturbation scheme employed by Wood [95] to study the high-Reynolds-number flow. As in the model used by Hird and Siew [42], the analytic model considered here replaces the slotted sleeve with a rigid permeable membrane; however, unlike their work, the dependence of the flow through the sleeve on the rotational speed of the rotor is captured in the first model by prescribing a slip velocity along the membrane. The flow field within each region is solved with this additional boundary condition and, using Darcy's law, the solutions are matched across the membrane by determining the unknown radial velocity along the membrane.

The second model assumes the slotted sleeve has infinitesimal thickness and uses the exponentially fitted finite volume method given by Miller and Wang [60] to solve the time dependent vorticity-transport equation and Poisson equation for a varied range of Reynolds number, eccentricities and rotational speeds. The first two models use Newtonian fluids to model the slurry and the values of Reynolds number considered cover the range 50-1000. This range is obtained from rheograms supplied to us by the CUSRG. Given the dimensions of the apparatus and the range of rotational speeds used in practice, the flow patterns obtained using this model approximate the flow fields developed within the viscometer by fluids with kinematic viscosities similar to silicon-based slurries, olive oil, linseed oil, light machine oil, aqueous solutions of glycerol (of no more than 50% by weight) and aqueous solutions of sucrose (of no more than 50% by weight).

Mineral slurries of high particle concentration behave like viscoplastic fluids. As the fluid stiffens if the stress placed on the fluid does not overcome the yield stress, these fluids can present computational difficulties. However, if the particle concentration is small enough, no yield stress is expected to exist and

the slurry behaves like a pseudoplastic fluid. Therefore, for the third model, we use the Herschel-Bulkley model (see Craster [27]) to define the constitutive equation for power law fluids; however, in this model the stress vanishes with shear rate. To ensure that the apparent viscosity remains bounded as the shear rate decreases, the bi-viscosity model employed by Tanner and Milthorpe [87] is used. As is common when using power law fluids (see Wilkinson [94]), the flow behaviour index is assumed constant over the range of shear rates considered and we assume that the heat generated through the viscous dissipation does not appreciably alter the temperature of the fluid; therefore, the flow can be regarded as isothermal. The latter assumption has been verified numerically by Pascal [69] for the flow of pseudoplastic fluids in a concentric annulus. The full momentum equations describing the laminar two-dimensional isothermal flow can be written as an inhomogeneous advection-diffusion equation. A finite volume method, based on the method given by Miller and Wang [60], is then used to determine the flow field. Only two parameters are used for the constitutive equation for the power law fluid (i.e., the fluid consistency coefficient and the flow behaviour index). In the analysis considered here, the fluid consistency coefficient is held fixed while the flow behaviour index takes on values between 0.8 and 0.2. This range for the power law index models clay-water mixtures, coal-water mixtures, napalm in kerosene and aqueous solutions of CMC (carboxymethylcellulose), to mention a few. The governing equations and boundary conditions used to define the flow field within each model will now be given.

2.2 Model One: Replacing the Slotted Sleeve with a Permeable Membrane

Hird and Siew [42] obtained an analytical solution for the small-Reynolds-number flow between eccentric rotating cylinders. Their model assumes that

the sleeve placed around the inner cylinder has numerous small slots; this assumption allows the sleeve to be replaced with a rigid permeable membrane. Along the membrane, a no-slip condition is imposed, while the radial velocity is driven by the pressure difference across it. However, the viscometer used in practice contains large slots; therefore, two non-zero velocity components must be defined along the membrane. Furthermore, if Newtonian fluids are used to model slurries then the Reynolds number will cover a reasonable range. For example, for some silicon-based slurries the Reynolds number can vary from 50 to 1000. The current work is designed to model the flow through a sleeve possessing large slots. This is achieved by replacing the slotted sleeve with a non-deformable permeable membrane. Consequently, the the radial velocity through the membrane becomes a function of the tangential velocity; therefore, by allowing the membrane to permit some slip, a non-zero tangential velocity component is introduced. The slip velocity along the membrane is prescribed before the flow field is solved and the radial velocity through the membrane is assumed to be governed by Darcy's law.

To determine the flow field, the momentum equations are written in terms of the stream and vorticity functions and use is made of the regular perturbation scheme employed by Wood [95]. Wood considered the large-Reynolds-number flow between two eccentric rotating cylinders using a perturbation scheme where the small parameter is dependent on the centre displacement between the two cylinders. Using a conformal transformation to map the eccentric cylinders to concentric cylinders, the first-order stream function in the image plane can be expanded asymptotically in powers of $1/\sqrt{Re}$ and this expansion is shown to hold in the entire flow field. The vorticity consists of a component that is uniform in the region where viscous forces are small and components that are significant in each boundary layer but decaying exponentially away from these boundaries. The phenomenon of vorticity being uniform

across closed streamlines lying entirely within a region where viscosity is considered small has also been shown by Batchelor [9]. A necessary condition for Wood's analysis to hold is that both bounding cylinders must rotate in the same sense. We use this perturbation scheme to obtain the flow field between the rotor and the membrane (referred to as the inner region) and the flow field between the membrane and the outer cylinder (referred to as the outer region). By construction, the asymptotic forms of the stream and vorticity functions in both region are the same; thus, once one region is solved, in terms of the currently unknown radial velocity, the behaviour of the flow field in the remaining region is known. The solutions in each region are matched across the membrane and the radial velocity along the membrane is determined using Darcy's law (see Hird and Siew [43]).

In using the perturbation scheme, the unperturbed flow reduces to simple shearing between two rotating cylinders with the membrane possessing slip placed between them. As two velocity profiles exist in the unperturbed flow yielding two vorticity distributions, this membrane is a source of discontinuity for the vorticity. This discontinuity also holds for higher-order solutions.

Batchelor [10, page 303] defines a boundary layer as "... a region in which viscous diffusion of vorticity is significant...". In large-Reynolds-number flows a vortex sheet is generated along no-slip surfaces as a consequence of the inviscid solution not satisfying the no-slip condition along the boundary. This vortex sheet allows the irrotationally flowing fluid to just slip over the fluid at (relative) rest in contact with the boundary. By introducing a membrane with some slip, the flow field considered here possesses three regions where the viscous diffusion of vorticity is significant. Although the presence of a boundary layer along the membrane can be justified, the behaviour of the stream function within the boundary layer located on the membrane cannot be approximated from Prandtl's boundary layer equation; however, by using

a permeable membrane, an analytic solution can be found and used to study, to some degree, the effects of a number of parameters on the flow through the membrane.

2.2.1 Governing Equations in the Physical Plane

If the slotted sleeve is replaced with a non-deformable permeable membrane and the region Ω contains a Newtonian fluid then, in view of equation (2.1.13), $\mathbf{f} \cdot \mathbf{k} = 0$ and $Sh = 1/Re$. The governing equations for a stationary problem ($p_o = 0$) are given by

$$\left.\begin{aligned} \nabla \cdot \left(\frac{1}{Re} \nabla \zeta - \zeta \mathbf{v} \right) &= 0, \\ \text{and} \qquad \nabla^2 \psi + \zeta &= 0. \end{aligned}\right\} \tag{2.2.1}$$

If polar coordinates are introduced, with the initial ray, $\theta = 0$, passing through the centres of the circles, (2.2.1) has the equivalent form

$$\left.\begin{aligned} \frac{1}{Re} \nabla^2 \zeta + \frac{1}{r} \frac{\partial(\psi, \zeta)}{\partial(r, \theta)} &= 0, \\ \text{and} \quad \nabla^2 \psi(r, \theta) + \zeta(r, \theta) &= 0, \end{aligned}\right\} \tag{2.2.2}$$

where

$$\nabla^2 = \frac{1}{r} \frac{\partial}{\partial r} \left(r \frac{\partial}{\partial r} \right) + \frac{1}{r^2} \frac{\partial^2}{\partial \theta^2}, \qquad \nabla = \left[\frac{\partial}{\partial r}, \frac{1}{r} \frac{\partial}{\partial \theta}, 0 \right],$$

and the Reynolds number is

$$Re = \frac{ab\omega_2}{\nu}. \tag{2.2.3}$$

The flow field is determined from the boundary conditions

$$\left.\begin{aligned} \frac{\partial \psi}{\partial r}(c/a, \theta) &= -\bar{U}, & \frac{\partial \psi}{\partial \theta}(c/a, \theta) &= 0, \\ \frac{\partial \psi}{\partial r}(1, \theta) &= -G(\theta), & \frac{\partial \psi}{\partial \theta}(1, \theta) &= F(\theta), \\ \frac{\partial \psi}{\partial \mathbf{n}}(\tilde{b}, \theta) &= -1, \qquad \text{and} & \frac{\partial \psi}{\partial \mathbf{t}}(\tilde{b}, \theta) &= 0. \end{aligned}\right\} \tag{2.2.4}$$

Here $\mathbf{n}$ and $\mathbf{t}$ represent the unit outward normal and tangential vectors to the outer boundary and $\tilde{b}$ represents the curve of the outer cylinder, viz

$$\tilde{b} = \epsilon\cos\theta + \sqrt{(b/a)^2 - (\epsilon\sin\theta)^2}.$$

The dimensionless functions $G(\theta)$ and $F(\theta)$ represent the azimuthal and radial velocity components on the membrane. The stream and vorticity functions defined in terms of the velocity field are given by

$$\mathbf{v} = \left[\frac{1}{r}\frac{\partial\psi}{\partial\theta}, -\frac{\partial\psi}{\partial r}\right] \quad \text{and} \quad \zeta = (\nabla \times \mathbf{v}) \cdot \mathbf{k} = \frac{1}{r}\left(\frac{\partial(rv_\theta)}{\partial r} - \frac{\partial v_r}{\partial\theta}\right), \tag{2.2.5}$$

where $\mathbf{v} = [v_r, v_\theta]$. As we will discuss later, the equations of motion and boundary conditions given above, together with the condition that the pressure field is single-valued, represents a well-posed mathematical problem. In Section 2.2.2 we apply a conformal transformation to map the physical plane to an image plane. This is used to simplify the solution process as the behaviour of the flow field in one region can be established from the flow field in the other region.

2.2.2 Mapping the Problem to an Image Plane

To map the geometry from the physical (z) plane to an image (w) plane, we introduce the following bilinear mapping (see Wood [95])

$$z = \frac{w+\gamma}{1+w\gamma}, \quad z = re^{i\theta}, \text{ and } \quad w = \rho\, e^{i\phi}, \tag{2.2.6}$$

where

$$\gamma = -\frac{\left(\frac{b}{a}\right)^2 - 1 - \epsilon^2 - \sqrt{\left(\left(\frac{b}{a}\right)^2 - 1 - \epsilon^2\right)^2 - 4\epsilon^2}}{2\epsilon}. \tag{2.2.7}$$

Under this transformation, the circles $|z| = 1$ and $|z - \epsilon| = b/a$ are mapped to concentric circles $\rho = |w| = 1$ and $\rho = |w| = \beta$ in the image plane (see Fig. 2.2), with β given by

$$\beta = \frac{(b/a)}{1 - \epsilon\gamma}. \tag{2.2.8}$$

The circle $|z| = c/a$ is mapped to the circle $|w - d| = \lambda$ where both d and λ depend on the parameter γ, viz

$$d = \frac{\left(1 - (c/a)^2\right)(-\gamma)}{1 - (c\gamma/a)^2}, \qquad \text{and} \qquad \lambda = \frac{c/a\,(1-\gamma^2)}{1 - (c\gamma/a)^2}. \tag{2.2.9}$$

The governing equations in the $\rho\phi$-plane are given by

$$\left.\begin{aligned} \frac{1}{Re}\nabla^2\zeta + \frac{1}{\rho}\frac{\partial(\psi,\zeta)}{\partial(\rho,\phi)} &= 0, \\ \text{and} \qquad J(\rho,\phi)\nabla^2\psi(\rho,\phi) + \zeta(\rho,\phi) &= 0, \end{aligned}\right\} \tag{2.2.10}$$

where

$$\nabla^2 = \frac{1}{\rho}\frac{\partial}{\partial\rho}\left(\rho\frac{\partial}{\partial\rho}\right) + \frac{1}{\rho^2}\frac{\partial^2}{\partial\phi^2}.$$

The stream function, $\psi(\rho,\phi)$, can be defined in terms of the dimensionless

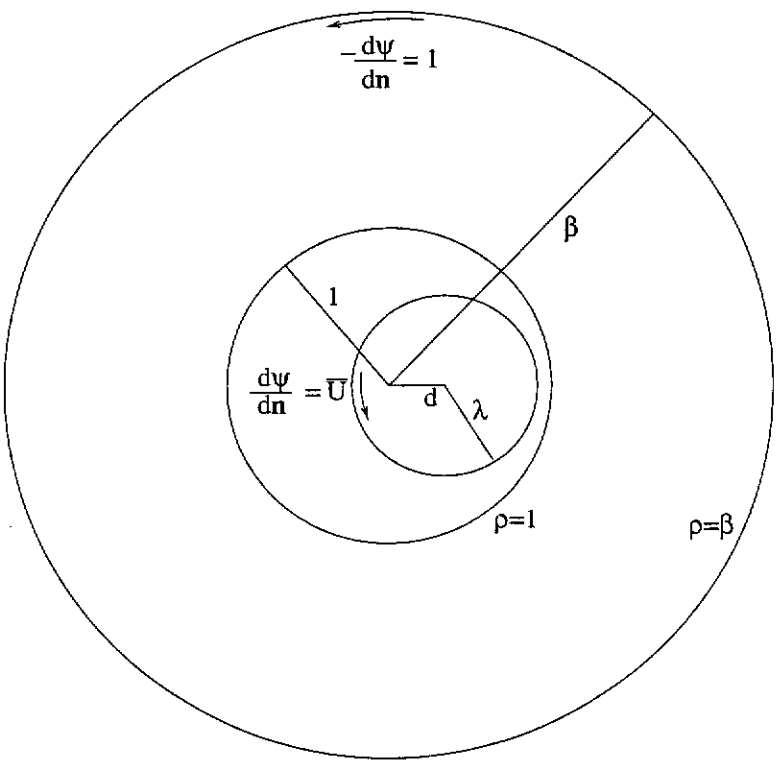

Figure 2.2: The image plane w.

velocity components in the increasing ρ and ϕ directions through

$$v_\rho(\rho,\phi) = \frac{\sqrt{J}}{\rho}\frac{\partial\psi}{\partial\phi}(\rho,\phi), \quad \text{and} \quad v_\phi(\rho,\phi) = -\sqrt{J}\frac{\partial\psi}{\partial\rho}(\rho,\phi), \tag{2.2.11}$$

and the dimensionless Jacobian of the transformation is given by

$$\left|\frac{dw}{dz}\right|^2 = J(\rho,\phi) = \left(\frac{1+2\gamma\rho\cos\phi+\gamma^2\rho^2}{1-\gamma^2}\right)^2. \tag{2.2.12}$$

See Hird [41] for the derivation. Equation (2.2.4) now becomes

$$\left.\begin{aligned} \frac{\partial\psi}{\partial\mathbf{n}}(\tilde{\rho},\phi) &= \bar{U}, & \frac{\partial\psi}{\partial\mathbf{t}}(\tilde{\rho},\phi) &= 0, \\ \frac{\partial\psi}{\partial\rho}(1,\phi) &= -\frac{g(\phi;\gamma)}{\sqrt{J(1,\phi)}}, & \frac{\partial\psi}{\partial\phi}(1,\phi) &= \frac{f(\phi;\gamma)}{\sqrt{J(1,\phi)}}, \\ \frac{\partial\psi}{\partial\rho}(\beta,\phi) &= -\frac{1}{\sqrt{J(\beta,\phi)}}, \quad \text{and} & \frac{\partial\psi}{\partial\phi}(\beta,\phi) &= 0, \end{aligned}\right\} \tag{2.2.13}$$

where $\mathbf{n}$ and $\mathbf{t}$ denote the outward normal and tangent vectors along the inner cylinder and $\tilde{\rho}$ represents the equation of the surface of the inner cylinder, given by

$$\tilde{\rho} = d\cos\phi + \sqrt{\lambda^2 - (d\sin\phi)^2}, \tag{2.2.14}$$

and $\bar{U}\left(=\dfrac{c\omega_1}{b\omega_2}\right)$ represents the dimensionless azimuthal velocity along the inner cylinder. The functions $f(\phi;\gamma)$ and $g(\phi;\gamma)$ given above represent the radial and azimuthal velocities along the membrane in the $\rho\phi$-plane and are obtained from $F(\theta)$ and $G(\theta)$ through use of the transformation given in equation (2.2.6). From equations (2.2.7) and (2.2.12) we observe that as $\epsilon \to 0$, $J(\rho,\phi) \to 1$ and the cylindrical polar coordinates are recovered.

The existence of the stream function is ensured by imposing no-net-flux conditions across the boundaries, viz

$$\int_{\rho=1}\sqrt{J(1,\phi)}\frac{\partial\psi}{\partial\phi}ds = 0, \quad \int_{\rho=\beta}\frac{\sqrt{J(\beta,\phi)}}{\beta}\frac{\partial\psi}{\partial\phi}ds = 0, \text{ and } \int_{\rho=\tilde{\rho}}\nabla\psi\cdot\mathbf{t}ds = 0. \tag{2.2.15}$$

In the w-plane, $ds^2 = d\rho^2/J + (\rho^2/J)d\phi^2$ (see Hird [41]). From equation (2.2.13), the last two integrals in (2.2.15) are readily satisfied, while the first integral establishes the following condition for $f(\phi;\gamma)$

$$\int_0^{2\pi}\frac{f(\phi;\gamma)}{\sqrt{J(1,\phi)}}d\phi = 0. \tag{2.2.16}$$

Furthermore, as the flow is rotational, Stokes' circulation theorem introduces a non-zero circulation condition along the membrane

$$-\int_{\rho=1} \nabla\psi \cdot \nu ds = \int_0^{2\pi} \frac{g(\phi;\gamma)}{\sqrt{J(1,\phi)}} d\phi \neq 0. \tag{2.2.17}$$

Here, ν represents the unit vector normal to the membrane and pointing in the increasing radial direction. From the no-penetration conditions along the bounding cylinders and the radial flow condition through the membrane, the stream function can be defined so that the streamlines along these surfaces are given by

$$\psi(\tilde{\rho},\phi) = 0, \quad \psi(1,\phi) = K_3 + h(\phi;\gamma), \quad \text{and} \quad \psi(\beta,\phi) = K_2, \tag{2.2.18}$$

and will replace the boundary conditions used to generate them. Here $h(\phi;\gamma)$ represents the anti-derivative of $f(\phi;\gamma)/\sqrt{J(1,\phi)}$. When imposing the Dirichlet condition along the membrane, all the constants of integration are absorbed into K_3 and the continuity of the stream function in the entire flow domain is ensured. As the domain is multiconnected, the Dirichlet conditions along the membrane and outer circle are known up to an additive constant. These arbitrary constants are determined by supplementing the boundary conditions with the condition that the pressure field be single-valued within the flow field. Mathematically, this requires

$$\int_C \frac{\partial p}{\partial \mathbf{t}} ds = 0, \tag{2.2.19}$$

where C represents any closed contour lying within the flow field and $\mathbf{t}$ is the unit vector tangent to contour C. Given the dimensionless Navier-Stokes equations for two-dimensions

$$(\mathbf{v}\cdot\nabla)\,\mathbf{v} = -\nabla p + \frac{1}{Re}\nabla^2\mathbf{v}, \tag{2.2.20}$$

and using the identity

$$(\mathbf{v}\cdot\nabla)\,\mathbf{v} = \frac{1}{2}\nabla\,(\mathbf{v}\cdot\mathbf{v}) - \mathbf{v}\times(\nabla\times\mathbf{v}),$$

the change in pressure along contour C is given by

$$\frac{\partial p}{\partial \mathbf{t}} = \nabla p \cdot \mathbf{t} = -\frac{1}{2}\frac{\partial (\mathbf{v}\cdot\mathbf{v})}{\partial \mathbf{t}} + (\mathbf{v}\times(\nabla\times\mathbf{v}))\cdot\mathbf{t} + \frac{1}{Re}\left(\nabla^2\mathbf{v}\right)\cdot\mathbf{t}.$$

Noting,

$$(\mathbf{v}\times(\nabla\times\mathbf{v}))\cdot\mathbf{t} = \zeta\mathbf{v}\cdot\nu, \quad \text{and} \quad \left(\nabla^2\mathbf{v}\right)\cdot\mathbf{t} = -\frac{\partial\zeta}{\partial\nu},$$

produces the equation

$$\frac{\partial p}{\partial \mathbf{t}} = -\frac{1}{2}\frac{\partial (\mathbf{v}\cdot\mathbf{v})}{\partial \mathbf{t}} + \zeta\mathbf{v}\cdot\nu - \frac{1}{Re}\frac{\partial\zeta}{\partial\nu}. \tag{2.2.21}$$

Integrating (2.2.21) around the membrane ($\rho = 1$), we have from equation (2.2.19)

$$\int_0^{2\pi} \frac{f(\phi;\gamma)}{\sqrt{J(1,\phi)}}\,\zeta|_{\rho=1} - \left(f(\phi;\gamma)\frac{\partial f}{\partial\phi}(\phi;\gamma) + g(\phi;\gamma)\frac{\partial g}{\partial\phi}(\phi;\gamma) + \frac{1}{Re}\left.\frac{\partial\zeta}{\partial\rho}\right|_{\rho=1}\right) d\phi = 0. \tag{2.2.22}$$

This condition must be satisfied for the pressure field to be single-valued. As we show later, this equation is automatically satisfied from the forms of $f(\phi;\gamma)$, $g(\phi;\gamma)$ and the vorticity function $\zeta(\rho,\phi)$ used to determine the flow field. Thus, K_2 will be determined from the net-flux between the membrane and the outer cylinder and K_3 will be determined from the solution to the inner region. Consequently, the differential equation given in (2.2.10), the boundary conditions in (2.2.13) and (2.2.18), together with the pressure condition (2.2.22), represent a well-posed mathematical problem.

We note that γ defined in equation (2.2.7) when multiplied by its conjugate surd can be expanded in powers of the small parameter ϵ to give

$$\gamma = -\frac{\epsilon}{(b/a)^2 - 1} - \frac{\epsilon^3 (b/a)^2}{\left((b/a)^2 - 1\right)^3} + O(\epsilon^5). \tag{2.2.23}$$

Further, if we define the eccentricity ratio, $\bar{\epsilon}$, by

$$\bar{\epsilon} = \frac{\epsilon}{(b/a) - 1} \tag{2.2.24}$$

then instead of using b/a and ϵ, the actual geometric parameters of the problem, we can use $\bar{\epsilon}$ and exploit the dependence of γ on ϵ and use a perturbation scheme in powers of γ to determine the flow field. The determination of an analytic solution for small eccentricities and the results produced are presented in Chapters 3 and 4 respectively.

2.3 Model Two: Choosing from a host of Numerical Techniques

The first model studies the high-Reynolds-number flow of an incompressible Newtonian fluid contained between two eccentric rotating cylinders of infinite length. The slotted sleeve is replaced with a rigid permeable membrane and for small eccentricities the governing equations will be solved analytically. Consequently, only a limited amount of information can be extracted from this study. The second model also uses Newtonian fluids but, unlike the first model, the slotted sleeve, together with the rotor, are placed arbitrarily within the flow domain (see Fig. 2.1). The second model is an improvement upon the first as a wider class of problems can be studied; however, as an analytical treatment is not possible, the flow field is approximated numerically (see Hird et al [44]). In the second and third models, the slotted sleeve is retained to study the developed flow fields; however, additional problems are introduced. Workers have shown (see Moffatt [63] and Henriksen and Hassager [40]) that both the stress and velocity gradients possess an algebraic singularity at re-entrant corners. Attempts to deal with corner singularities include developing finite difference equations based on the asymptotic behaviour of these functions or using local mesh refinement about the singular points to determine the functions' character (see Crochet et al [28] and Tanner and Huang [86]). While the stream function is continuous in the entire flow domain, the vorticity becomes unbounded at the corners of each of the surface elements of the slotted sleeve.

To deal with the corner singularities in our flow domain, we assume that the slotted sleeve is of infinitesimal thickness and use local mesh refinement to determine the behaviour of the vorticity from the neighbouring nodes at the end points of each surface element of the slotted sleeve.

The laminar flow within the flow domain, Ω, given in Fig. 2.1 is governed by the two-dimensional Navier-Stokes equations. Formulated in terms of the (dimensionless) stream (ψ) and vorticity (ζ) functions, the governing equations are given in equation (2.2.1). There exists a myriad of techniques designed to solve the governing non-linear equations. The well-established methods are the finite difference, finite element, finite volume, boundary element and spectral methods. The choice of technique is often based on personal experience and preference, the flow domain to be discretised (e.g., bounded, unbounded or irregular) and the range of Reynolds numbers considered. The numerical scheme used to determine the flow field in our case is based on the ease of use and implementation of the computer routines, the ability to deal with the geometry of the problem and the accuracy and stability of the method over the range of Reynolds numbers considered.

From a numerical point of view, the ψ-ζ formulation given in (2.2.1) is attractive because the mass conservation condition is automatically satisfied (a condition that introduces difficulties when the governing equations are written in terms of the primitive variables); however, before (2.2.1) can be solved the question of whether or not to approximate ζ along the no-slip boundaries arises. This seemingly innocent question still remains a contentious issue. If no boundary conditions for ζ (and $\partial\zeta/\partial n$ when applicable) are determined, then the coupled Poisson and vorticity-transport equation given in (2.2.1) must be solved simultaneously. Although, it was initially thought that this cannot be done (see Taylor and Hood [88]), this causes no theoretical difficulties as the Poisson equation usually possesses all the necessary boundary conditions to

make the problem well-posed (see Gresho [35]). Campion-Renson and Crochet [18] were the first to solve the coupled system, using a finite element method, without the need to introduce any boundary conditions for ζ, and Glowinski and Pironneau [34] analysed methods for solving the ψ-ζ equations and discussed the important relationship between the tangential velocity and the unknown vorticity along the no-slip boundaries. Boundary element methods use Green's functions to replace the governing differential equations with integral equations and have the advantage over finite element methods in that the method enables the solution field along the boundaries to be decoupled from the solution fields at interior points. Thus, the integral equations can be used to determine ζ (and $\partial\zeta/\partial n$) along the no-slip boundaries instead of attempting to define them a priori. The discretisation of these integral equations can produce dense, asymmetric matrices and are, therefore, computationally expensive to solve; however, recent workers have produced iterative solution schemes that are stable for high Reynolds numbers (see Hriberšek and Škerget [45], Liao and Zhu [52] and Rodriguez-Prada et al [74]).

To deal with the question of boundary conditions for the vorticity, an alternative approach regards the vorticity-transport equation as a partial differential equation and, therefore, boundary conditions must be imposed to render the problem well-posed. Specifying these conditions on no-slip boundaries is difficult as they cannot be determined directly from the no-slip conditions (i.e., $\partial\psi/\partial n$). The accuracy of the boundary conditions used for ζ is important as the no-slip boundaries are a source of generation of the vorticity and the subsequent convection, or diffusion, of this function defines the flow field. Consequently, poor evaluation of these boundary conditions can affect the convergence of the numerical scheme being used to solve the Poisson and vorticity-transport equations (see Gupta and Manohar [38]). To circumvent this inherent difficulty, temporal schemes have been used to stabilise the solu-

tion process. Thus, the stationary problem is replaced with a non-stationary problem and at any given time step the governing equations are solved in sequence using the boundary conditions. The values of the vorticity along the no-slip boundaries are estimated from a discretisation of the Poisson equation for the stream function using the current (or exact if known) distribution of Dirichlet and Neumann boundary conditions. In this approach the Poisson equation is not over determined as the no-slip conditions are used implicitly through determining boundary conditions for the vorticity. When applying finite difference and finite element methods, many different estimates for the vorticity have been used. In a recent paper by Mukhopadhyay and Basu [64], a Robins boundary condition is used instead of the conventional Dirichlet and Neumann boundary conditions to solve the Poisson equation. Both the Robins boundary condition and Poisson equation are discretised using second-order accurate forward differencing producing second-order accurate vorticity values on the no-slip boundaries. Using an ADI method to solve the vorticity-transport equation and SOR to solve the Poisson equation, the flow past a stationary cylinder with Reynolds number up to 10, 000 is solved. The method is shown to be more stable and produces more accurate results than those produced using the conventional boundary conditions when first-order discretisations are used to determine the unknown vorticity values on the no-slip boundaries. For a sample of the various discretisations used for the vorticity, see the work of Baker [4], Comini et al [26], Gesho [35], Gupta and Manohar [38] and Ikegawa [47] and references contained therein.

Not all workers have used time marching schemes to introduce the boundary conditions for vorticity, for example, Dhatt et al [29] employ a direct method. Using a finite element method, the boundary values for the vorticity are determined so that the no-slip condition $\partial\psi/\partial n$ is satisfied. This is achieved by inserting the discretised form of this condition directly into the system of

non-linear algebraic equations formed by discretising the vorticity-transport equation. Using the Newton-Raphson method to solve the coupled governing equations, this technique reportedly produces a faster rate for convergence of high-Reynolds-number flows than iterative schemes.

Determining the vorticity along the no-slip boundaries of a multiconnected domain introduces complications due to the homologous property of the stream function. The stream function is often completely specified on only one boundary and known up to an additive constant on the remaining boundaries. These constants can be determined by imposing the condition that the pressure field is single-valued within the domain (see Gunzburger and Peterson [37]). This condition introduces an additional equation involving the stream and vorticity functions (see equations (2.2.19) and (2.2.21)). As our flow domain, Ω, is multiconnected and possesses the added difficulty introduced by $\partial\Omega_3$ being segmented, Dirichlet boundary conditions must be determined along with the flow field. The details of how these boundary conditions are determined will be discussed later.

Given the lack of information for the stream function on the solid boundaries $\partial\Omega_2$ and $\partial\Omega_3$ (if the boundary conditions on $\partial\Omega_1$ are completely specified), we choose to estimate the vorticity values on the no-slip boundaries by replacing the stationary problem given in equation (2.2.1) with a non-stationary problem. A discretisation of the Poisson equation will be used to determine ζ along $\partial\Omega_1$, $\partial\Omega_2$ and $\partial\Omega_3$ and the ψ-ζ fields will be determined in sequence. As we are only interested in the long-term solution of the transient problem, a first-order accurate temporal scheme is used, namely the fully implicit backward-Euler method. Despite the increase in computational cost in using an implicit scheme, this scheme is known to be unconditionally stable when applied to Navier-Stokes equations (see Simo and Armero [82]) permitting larger time steps than would be possible with explicit schemes. We now consider the

spatial discretisation of Ω.

The range of Reynolds number used to develop the flow fields considered in the second model will be 50-1000, thus, covering moderate to high values of Reynolds number. For this range, the vorticity-transport (advection-diffusion) equation is parabolic; however, for the high-Reynolds-number flow the solution is expected to be hyperbolic in character. That is, for advection dominated flows, the velocity gradients normal to the no-slip boundaries become large and, therefore, the solution changes abruptly across these boundary layers. The numerical method used to solve this equation must be stable and produce accurate results. For advection-dominated flows, finite difference methods based on centred-difference schemes are known to be unstable and solutions often exhibit oscillatory behaviour close to the boundary layers. Consequently, upwind schemes have been used to approximate the convective derivatives with solution values upstream. The upwinded convective term can be constructed by adding an artificial diffusion term to the central difference treatment. The effect of upwinding is to increase the stability of the numerical scheme and to suppress the node-to-node oscillations near the boundary layers; however, the upwind technique has been criticised as it is only first-order accurate, whereas, centred-differences are second-order accurate. This loss of accuracy produces overly diffuse solutions even for simple flows (see Brandt and Yavneh [15]). Some finite difference analysts do not use upwinding but instead choose to refine the mesh to remove the oscillatory behaviour. This produces a significant increase in the amount of computational work required but the development of multigrid methods (see Ghia et al [33]) has enhanced the rate of convergence. The use of finite difference methods to solve advection dominated flows in complex geometries become cumbersome, especially if boundary fitted coordinates schemes are needed to determine the flow fields. For this reason, the use of finite element methods are a natural choice to simulate flows in irregular

domains.

Gresho and Lee [36] do not advocate the use of upwinding in finite element methods to suppress the oscillatory solutions; they argue that these fluctuations are giving a strong message regarding the accuracy of the simulation. Instead of upwinding, the use of finite element methods together with a well-designed mesh (i.e., locally refined) will give meaningful and accurate results. Furthermore, Gresho and Lee [36] point out that if upwinding is applied to a mesh that is too coarse the solutions generated for (relatively) small and large Reynolds numbers would differ little as the effective Reynolds number may be too far from the true Reynolds number. We note that computationally efficient, stable and accurate boundary element methods have also been developed to solve high-Reynolds-number flow, see for example, Hriberšek and Škerget [45] and Liao and Zhu [52].

The credibility of upwinding has been addressed by Brooks and Hughes [16] who assert that the optimal upwinding methods may be able to give more accurate results than the centred-difference method when the mesh is suitably defined. Furthermore, if only the global features of the flow field are desired then refining the mesh is only used to prevent oscillations. The problems introduced by classical upwinding have been removed in the new generation of upwinding techniques, the so-called streamline upwinding methods as they remove the oscillations and the spurious crosswind diffusion. For a review of a few of the common upwinding techniques and recent advances, see the work of Bank et al [6], Ratish Kumar and Naidu [73] and Perrochet [70]. The ideas behind the streamline upwinding methods have also led to the introduction of stable spectral methods for the two-dimensional Navier-Stokes equations (see Canuto and Van Kemenade [19]).

The search for fast, accurate and robust numerical schemes to solve the Navier-Stokes equations is still being undertaken. Workers are looking at dif-

ferent schemes to achieve this, for example, Achdou and Pironneau [2] use a mixed finite element-boundary element multistep method to solve the two-dimensional transient ψ-ζ formulation while Chang [21] and Perrochet [70] use a space-time element approach to solve the Navier-Stokes equations.

A robust method capable of modelling advection dominated flows and is easily implemented is the exponentially fitted finite volume method given by Miller and Wang [60]. For this method the flow domain, Ω, is easily decomposed using the Delaunay triangulation and Voronoi (Dirichlet) tessellations. These meshes are the dual of each other and have the important property that they are mutually orthogonal. This method reduces to the centred- and upwind- difference schemes, respectively for low and high Reynolds numbers and is shown to be an improvement over these methods for triangulations based on standard finite difference meshes. Since the finite volume method of Miller and Wang [60] is capable of modelling advection dominated flows and is easily implemented, we will employ this method to simulate the flow fields. Over a given cell-centred control volume (Voronoi tessellation), the governing equations are decomposed into a series of flux integrals along the sides (faces) of the Voronoi polygon. Summing these face contributions, a conservative system results for the control volume. The flux integrals along each face are approximated using the control region approximation used by McCartin [58]. The assembly of the face contributions from all the control volumes yields a system of algebraic equations. At each time step we use a Picard-type iterative scheme to decouple the system of equations, and to take advantage of the sparsity of the matrices formed, iterative methods (i.e., Congugate Gradients methods) are used to solve these equations. The dual Delaunay triangulation and Voronoi tessellations appears to be first used by MacNeal [55] and has been applied successfuly when seeking numerical solutions to semiconductor device equations (see McCartin [58], and Buturla et al [17]). We now formally

define the governing equations used to estimate the flow field within Ω.

2.3.1 Governing Equations

For the steady-state flow of a Newtonian fluid, equation (2.1.13) reduces to (2.2.1); however, to solve (2.2.1) numerically, we replace the stationary problem with a non-stationary problem. Hence at a point $\boldsymbol{x}$ $(= (x_i, y_i))$ in Ω and at a given time $t \in (0,T]$, the Navier-Stokes equations governing the laminar flow of an incompressible homogeneous Newtonian fluid (i.e., having constant kinematic viscosity) are given by

$$\left.\begin{aligned} \nabla^2\psi + \zeta &= 0, \\ \text{and} \quad \frac{\partial\zeta}{\partial t} - \nabla\cdot\left(\frac{1}{Re}\nabla\zeta - \zeta\mathbf{v}\right) &= 0. \end{aligned}\right\} \tag{2.3.1}$$

Equation (2.3.1) represents a non-linearly coupled system of equations; however, we introduce an iterative scheme to decouple this system where at each time step, the discretised governing equations are solved in sequence (starting with the discretised Poisson equation) using current, and exact, boundary conditions. The vorticity along the no-slip boundaries are determined by applying the no-slip condition $\partial\psi/\partial n$ to a discretisation of the Poisson equation. Furthermore, since the flow domain is multiconnected, the no-slip conditions prescribed along $\partial\Omega_1$, $\partial\Omega_2$ and $\partial\Omega_3$ (see equation (2.1.14)) do not uniquely determine the streamlines along these surfaces. However, if the streamline along $\partial\Omega_1$ is set to zero (see equation (2.1.15)) then the Dirichlet boundary conditions along $\partial\Omega_2$ and $\partial\Omega_3$ (i.e., K_2 and K_3^q) are determined as part of the solution process. The assembly of each of the governing equations generates a sparse system of equations and are solved using the Conjugate Gradients Squared method (CGS) given by Sonneveld [83]. To determine the effect of the slotted sleeve on the flow field, contour plots are generated for various eccentricities, rotational speeds and directions and Reynolds numbers. The application of the finite volume method to the above governing equations and

the method of solution are given in Chapter 5 and the contour plots generated are given in Chapter 6.

2.4 Model Three: Using Pseudoplastic Fluids to Model Slurries

The use of power law fluids to model flow problems is both extensive and diverse. Since polymers added to oils exhibit pseudoplastic (shear-thinning) behaviour, power law fluids have been used to model the laminar flow of lubricants in journal bearings (see Dien and Elrod [30], Johnson and Mangkoesoebroto [49] and Safar [77]). Power law fluids model the flow of liquid foods in ducts (generalised Couette flow) (see Ilicali and Engez [48]) and the study of power law fluids in concentric and eccentric annuli has been used to model the extruders for molten plastics, well bore fluid recirculation for the removal of drill cuttings and the polymer melt in a coating process (see for example Flumerfelt et al [32], Hanks and Larsen [39], Lin and Hsu [53], Malik and Shenoy [56], Tiu and Bhattacharyya [89] and Yang and Chukwu[97]). The application of power law fluids to understand the performance of lubricants in journal bearings is used in conjunction with Reynolds equation and therefore the transport equations are simplified. Also the equations describing Poiseuille or annular axial flow can be solved both analytically (see Malik and Shenoy [56] and Yang and Chukwu [97]) and numerically (see Miyazaki [62], Chen and Zhao [23]). Here, we solve the full non-linear momentum equations governing the laminar flow of pseudoplastic fluids.

Slurries have been modelled using viscoplastic fluids. The yield surface for these fluids has been determined numerically (see Bercovier and Engelman [12] and Tanner and Milthorpe [87]) and analytically (see Craster [27]) using the Herschel-Bulkley model. This model possesses the rheological equations of state for Newtonian, Bingham and power law fluids. To simplify our anal-

ysis, we assume the fluids used in our model have yielded everywhere so that the need to determine the plug regions is removed. We, therefore, concentrate on studying the flow field of slurries with a low concentration of particles and are pseudoplastic in behaviour. To determine the flow field, we use the Herschel-Bulkley model to define the constitutive equations for a power law fluid and apply the finite volume method used in the second model to solve the transient equations of motion. Further, as the viscometer is immersed in a constant temperature bath, we assume that the heat generated by viscous dissipation does not alter the temperature of the fluid, that is the flow is assumed isothermal. For the laminar flow of pseudoplastic fluids in concentric cylinders, this assumption has been validated numerically by Pascal [69]. Considering isothermal flows simplifies the analysis as only two equations of conservation now govern the flow field.

The work undertaken by Phan-Thien et al [71] has shown that the movement of particles suspended in a viscous Newtonian fluid between two eccentric cylinders is towards the regions of low shear rate. It is, therefore, worthwhile to study the regions of low and high shear rate in the current model as this may indicate where the particles in a slurry are likely to agglomerate: little cohesion between the particles is likely to occur in regions where shearing forces are large.

2.4.1 Governing Equations

Equation (2.1.13) represents the governing equations used to solve the transient (i.e., $p_o = 1$) problem for pseudoplastic fluids, that is, $\alpha - 1$ is negative and where $h(\dot{\gamma})$ can be viewed as the (dimensionless) apparent viscosity. The no-slip and no-penetration conditions for the two-dimensional flow within, Ω, are given in equations (2.1.14) and (2.1.15). To solve (2.1.13), we will employ the finite volume method used in the second model; however, since the apparent

viscosity is a function of the shear rate, additional complications can arise. The use of the Herschel-Bulkley model to characterise the rheological behaviour of pseudoplastic fluids has a servere limitation, namely, both $h(\dot{\gamma})$ and its derivatives become unbounded as the shear rate vanishes. The singularity in these functions is removed by adopting the following bi-viscosity model given by Tanner and Milthorpe [87], viz

$$\tau_{ij} = \begin{cases} 2h(\dot{\gamma})\dot{\gamma}_{ij} & \text{for} \quad 2(\dot{\gamma}_{ij} : \dot{\gamma}_{ij}) > (\dot{\gamma}_c)^2, \\ 2h(\dot{\gamma}_c)\dot{\gamma}_{ij} & \text{for} \quad 2(\dot{\gamma}_{ij} : \dot{\gamma}_{ij}) \leq (\dot{\gamma}_c)^2, \end{cases} \tag{2.4.1}$$

where the critical shear rate, $\dot{\gamma}_c$, is predefined. Thus, at very low shear rates, the material is assumed to behave as a highly viscous fluid. The steady-state solution obtained from (2.1.13) will give the scalar fields for ψ, ζ and $h(\dot{\gamma})$. To study the behaviour of the pseudoplastic fluid in Ω, we restrict our study to large eccentricity (i.e., $\bar{\epsilon} = 0.7$) with the bounding cylinders rotating in opposite senses. An understanding of the flow developed by this non-Newtonian fluid is gained by varying the dimensionless parameter S, the critical shear rate $\dot{\gamma}_c$, the relative rotational speed $\bar{U}$ and the power law index α. A means of determining steady-state solutions is presented in Chapter 7 and the contour plots generated for various sets of parameters are given in Chapter 8.

Chapter 3

An Analytic Solution for Small Eccentricity and Large Reynolds Number

Using the first model, we determine analytically the flow field generated within Ω. When the slotted sleeve is replaced with a rigid permeable membrane, the governing equations and boundary conditions defining the flow are given in Section 2.2.2. A regular perturbative scheme will now be outlined and used to linearise the non-linear differential equations.

3.1 Solving Model One: A Regular Perturbation Scheme

To determine the flow field for the first model, we note from equation (2.2.23), that the parameter γ is small when the eccentricity, ϵ, is small; thus, to linearise the non-linear vorticity transport equation given in (2.2.10), we introduce a regular perturbation about the concentric geometry in terms of the parameter γ. This follows the perturbation scheme used by Wood [95]. Therefore, in the

outer regime, the stream and vorticity functions are approximated through

$$\left.\begin{aligned} \psi(\rho,\phi;\gamma) &= \sum_{n=0}^{\infty}\psi_n(\rho,\phi)\gamma^n, \\ \text{and}\quad (1-\gamma^2)^2\zeta(\rho,\phi;\gamma) &= \sum_{n=0}^{\infty}\zeta_n(\rho,\phi)\gamma^n. \end{aligned}\right\} \tag{3.1.1}$$

Furthermore, the radial and azimuthal velocity components along the membrane, $f(\phi;\gamma)$ and $g(\phi;\gamma)$, are approximated using the perturbation schemes

$$f(\phi;\gamma)=\sum_{n=1}^{\infty}f_n(\phi)\gamma^n \quad \text{and} \quad g(\phi;\gamma)=\sum_{n=0}^{\infty}g_n(\phi)\gamma^n. \tag{3.1.2}$$

The geometry within the inner regime in the w-plane is governed by the eccentricity ratio, $\tilde{\epsilon}$

$$\tilde{\epsilon}=\frac{d}{1-\lambda}. \tag{3.1.3}$$

From equation(2.2.9) and noting that $c/a<1$ we observe

$$\tilde{\epsilon}<\frac{2|\gamma|}{1+\gamma^2}, \quad \text{and} \quad d<|\gamma|;$$

thus, both the eccentricity ratio and centre displacement are smaller than γ, and d may be used as the perturbation parameter for the inner regime. If this approach is used then the boundary conditions perturbed using the parameter γ must be written in terms of the inner parameter d. From equation (2.2.9), γ expanded in powers of d is given by

$$\gamma=-\frac{(a/c)^2}{(a/c)^2-1}d+\frac{(a/c)^4}{((a/c)^2-1)^3}d^3-\frac{2(a/c)^6}{((a/c)^2-1)^5}d^5+O(d^7),$$

where the number of terms used in perturbing the inner regime is dictated by the terms used in the outer regime. However, by considering γ as the perturbation parameter for both regimes, the form of the inner solution is known once the outer solution is generated. We note that for $\gamma \ll 1$, d and λ have the simple forms

$$d=-\alpha\gamma+O(\gamma^3), \quad \text{and} \quad \lambda=\frac{c}{a}+O(\gamma^2), \tag{3.1.4}$$

where $\alpha = (1 - (c/a)^2)$.

In the inner regime the vorticity and stream functions are defined by $\bar{\zeta}(\rho, \phi)$ and $\bar{\psi}(\rho, \phi)$ and are approximated using

$$\left.\begin{aligned} \bar{\psi}(\rho, \phi; \gamma) &= \sum_{n=0}^{\infty} \bar{\psi}_n(\rho, \phi)\gamma^n, \\ \text{and} \quad (1-\gamma^2)^2\bar{\zeta}(\rho, \phi; \gamma) &= \sum_{n=0}^{\infty} \bar{\zeta}_n(\rho, \phi)\gamma^n. \end{aligned}\right\} \tag{3.1.5}$$

The perturbation schemes given in (3.1.1) and (3.1.5) are applied to both the governing equations and the boundary conditions in each regime; however, the inner rotating circle must be expanded in γ. To ensure the stream function is continuous in the entire flow field we impose the continuity condition across the membrane

$$\psi_n(1, \phi) = \bar{\psi}_n(1, \phi), \quad \text{for } n = 0, 1, \ldots. \tag{3.1.6}$$

The slip velocity, $g(\phi; \gamma)$ is prescribed prior to determining the flow field and the flow field in each regime is solved in terms of the (as yet) unknown radial velocity. By determining the radial velocity $f(\phi; \gamma)$ from the pressure difference across the membrane, the flow field in each regime can be matched across their common boundary. If the pressure field in the outer and inner regimes are denoted by $\Pi(\rho, \phi; \gamma)$ and $P(\rho, \phi; \gamma)$ respectively and are approximated using the perturbation schemes

$$\Pi(\rho, \phi; \gamma) = \sum_{n=0}^{\infty} \Pi_n(\rho, \phi)\gamma^n, \quad \text{and} \quad P(\rho, \phi; \gamma) = \sum_{n=0}^{\infty} P_n(\rho, \phi)\gamma^n, \tag{3.1.7}$$

then, if Darcy's law is assumed to govern the flow through the membrane, $f_n(\phi)$ is obtained from the expression

$$f_n(\phi) = -\kappa \left(\Pi_n(\phi) - P_n(\phi)\right), \qquad n = 1, 2, \ldots, \tag{3.1.8}$$

where κ represents a constant dependent on the permeability of the membrane and the dynamic viscosity of the fluid (see Scheidegger [79]).

To simplify our analysis we assume the slip velocity can be described by the zeroth-order term g_0, which is taken to be constant, and hence, in the ensuing analysis we put

$$g_n = 0 \quad n = 1, 2, \ldots.$$

In linearising the equations in (2.2.10), the zeroth-order equations represent Couette flow between rotating cylinders with a cylindrical membrane located between them. The basic solution shows that the vorticity is discontinuous across the membrane. This discontinuity is also seen in higher-order solutions. To solve the first-order equations, $f_1(\phi)$ is represented by a Fourier series; this representation satisfies the flux condition given in (2.2.16). From the nature of the first-order governing equations and boundary conditions, the stream and vorticity functions can be written in such a way that their form depends on the solution to a coupled set of Euler and Bessel equations. The Reynolds number is found only in the Bessel equation where it forms part of the argument in the defined Bessel (i.e., Hankel) functions. Thus, for large-Reynolds-number flow, both the order and argument of these functions are large and complex; consequently, asymptotic techniques are used to represent these functions in this limit. In obtaining local expansions for the Hankel functions, no assumptions are placed on the relative magnitudes of the orders and argument, precluding the use of tabulated expansions. The value of the slip velocity, g_0, determines the form of these asymptotic expansions and, consequently, also the asymptotic representations for the first-order stream and vorticity functions.

The true flow field is mapped onto the w-plane using the conformal transformation given in (2.2.6) and the stream function in the image plane is determined through a perturbation scheme. If a linear approximation is used to describe this function, then according to Segel [80], the flow field determined in this plane will adequately describe the true flow field if the perturbation parameter, γ, is small enough to ensure the convergence of the perturbation

schemes (3.1.1), (3.1.5).

3.2 Linearising the Governing Equations

The equations of motion given in equation (2.2.10) together with the Neumann and Dirichlet boundary conditions defined in equations (2.2.13) and (2.2.18) govern the flow field in both the inner and outer regions. These equations will be linearised by applying the perturbation schemes given in equations (3.1.1) and (3.1.5). By construction, the form of the stream and vorticity functions at each order of γ are the same for both regions. Thus, we proceed to outline the form of the solutions in each region noting explicit differences in the forms of the functions concerned. Here, we only show perturbed problems up to $O(\gamma^2)$.

To facilitate the expansion of the boundary conditions in equation (2.2.13) we note the expansions for $J^{-1/2}(\rho,\phi)$ and $J^{1/2}(\rho,\phi)$, viz

$$J^{-1/2}(\rho,\phi) = 1 - 2\rho\cos\phi\gamma + \left[2\rho^2\cos 2\phi + \rho^2 - 1\right]\gamma^2 - \left[2\rho^3\cos 3\phi + 2\rho(\rho^2-1)\cos\phi\right]\gamma^3 + \ldots \tag{3.2.1}$$

and

$$J^{1/2}(\rho,\phi) = 1 + 2\rho\cos\phi\gamma + \left[1+\rho^2\right]\gamma^2 + 2\rho\cos\phi\gamma^3 + \ldots. \tag{3.2.2}$$

The equations of motion and boundary conditions along the membrane and outer boundary are readily expanded in powers of γ but the boundary conditions along the inner cylinder require special attention. The inner cylinder, when mapped onto the image plane, is centred a small distance away from the centre of the $\rho\phi$-plane. As the description of this boundary is dependent on the expansion parameter γ as seen in equation (2.2.9), the boundary conditions must be applied to the surface described by $\gamma = 0$ namely the circle $\rho = c/a$ that is different from the mapped boundary. This expansion is achieved by

expanding the boundary conditions in powers of distance from $\tilde{\rho}$ to λ (with λ defined in equation (3.1.4)). If we write the boundary condition

$$\frac{\partial \psi}{\partial \mathbf{n}}(\tilde{\rho}, \phi) = \bar{U}$$

as

$$\frac{\sqrt{J(\tilde{\rho}, \phi)}}{\lambda} \left[\left. \frac{\partial \psi}{\partial \rho} \right|_{\rho=\tilde{\rho}} (\tilde{\rho} - d\cos\phi) + \frac{d\sin\phi}{\tilde{\rho}} \left. \frac{\partial \psi}{\partial \phi} \right|_{\rho=\tilde{\rho}} \right] = -\bar{U} \tag{3.2.3}$$

and expand $\dfrac{\partial \psi}{\partial \rho}$ and $\dfrac{\partial \psi}{\partial \phi}$ in powers of $(\tilde{\rho} - \lambda)$ then upon using the expansion

$$\tilde{\rho} = \lambda + d\cos\phi - \frac{d^2}{2\lambda}\sin^2\phi + \ldots$$

obtained from (2.2.14) and the expansions given in equations (3.1.5) and (3.2.2), equation (3.2.3) yields the boundary conditions

$$O(1) : \left. \frac{\partial \bar{\psi}_0}{\partial \rho} \right|_{\rho=\lambda} = -\bar{U}$$

$$O(\gamma) : \left. \frac{\partial \bar{\psi}_1}{\partial \rho} \right|_{\rho=\lambda} - \alpha\cos\phi \left. \frac{\partial^2 \bar{\psi}_0}{\partial \rho^2} \right|_{\rho=\lambda} = 2\lambda\bar{U}\cos\phi$$

$$\begin{aligned} O(\gamma^2) : \left. \frac{\partial \bar{\psi}_2}{\partial \rho} \right|_{\rho=\lambda} - \alpha\cos\phi \left. \frac{\partial^2 \bar{\psi}_1}{\partial \rho^2} \right|_{\rho=\lambda} - \left(\frac{\alpha^2 \sin^2\phi}{2\lambda} + 2\alpha\lambda\cos^2\phi \right) \left. \frac{\partial^2 \bar{\psi}_0}{\partial \rho^2} \right|_{\rho=\lambda} \\ + 2\lambda\cos\phi \left. \frac{\partial \bar{\psi}_1}{\partial \rho} \right|_{\rho=\lambda} - \frac{\alpha}{\lambda^2}\sin\phi \left. \frac{\partial \bar{\psi}_1}{\partial \phi} \right|_{\rho=\lambda} = \\ -\bar{U}\left(-2\alpha\cos^2\phi + \frac{\alpha^2}{2\lambda^2}\sin^2\phi - \lambda^2 - 1 \right). \end{aligned} \tag{3.2.4}$$

We note that since in the unperturbed flow the stream function is a function of the radial position alone, simplifications are made in producing the above boundary conditions. Simplifications are also made in the remaining boundary conditions. The Dirichlet boundary condition along the inner cylinder can be expanded in a similar manner to the Neumann boundary condition there; thus,

to $O(\gamma^2)$ we have

$$O(1): \quad \bar{\psi}_0(\lambda) = 0,$$

$$O(\gamma): \quad \bar{\psi}_1(\lambda,\phi) - \alpha\cos\phi \left.\frac{\partial\bar{\psi}_0}{\partial\rho}\right|_{\rho=\lambda} = 0,$$

and

$$O(\gamma^2): \quad \bar{\psi}_2(\lambda,\phi) - \alpha\cos\phi \left.\frac{\partial\bar{\psi}_1}{\partial\rho}\right|_{\rho=\lambda} + \frac{\alpha^2\cos^2\phi}{2}\left.\frac{\partial^2\bar{\psi}_0}{\partial\rho^2}\right|_{\rho=\lambda} - \frac{\alpha^2\sin^2\phi}{2\lambda}\left.\frac{\partial\bar{\psi}_0}{\partial\rho}\right|_{\rho=\lambda} = 0. \tag{3.2.5}$$

The Dirichlet condition for $\psi(\rho,\phi)$ along the membrane (see equation (2.2.18)) can be written as

$$\psi(1,\phi) = \int^{\phi} \frac{f(\phi;\gamma)}{\sqrt{J(1,\phi)}} d\phi + K_3.$$

Applying (3.1.2) and (3.2.1) we find

$$\begin{aligned} \psi_0(1) &= K_3, \\ \psi_1(1,\phi) &= \int^{\phi} f_1(\phi)d\phi = h_1(\phi), \\ \text{and} \quad \psi_2(1,\phi) &= \int^{\phi} (f_2(\phi) - 2f_1(\phi)\cos\phi)\, d\phi = h_2(\phi), \end{aligned} \tag{3.2.6}$$

and so on. The azimuthal velocity imposed along the membrane is easily expanded to give

$$\begin{aligned} O(1): \frac{\partial\psi_0}{\partial\rho}(1) &= -g_0, \\ O(\gamma): \frac{\partial\psi_1}{\partial\rho}(1,\phi) &= 2g_0\cos\phi, \\ \text{and} \\ O(\gamma^2): \frac{\partial\psi_2}{\partial\rho}(1,\phi) &= -2g_0\cos 2\phi, \end{aligned} \tag{3.2.7}$$

while the Neumann condition along the outer boundary is expanded to give

$$\begin{aligned} O(1): \frac{\partial\psi_0}{\partial\rho}(\beta) &= -1, \\ O(\gamma): \frac{\partial\psi_1}{\partial\rho}(\beta,\phi) &= 2\beta\cos\phi, \\ \text{and} \\ O(\gamma^2): \frac{\partial\psi_2}{\partial\rho}(\beta,\phi) &= 1 - \beta^2 - 2\beta^2\cos 2\phi. \end{aligned} \tag{3.2.8}$$

The Dirichlet condition along the outer cylinder is easily expanded in powers of γ. The linearised equations of motion together with the perturbed boundary conditions to $O(\gamma^2)$ are given below. When $\gamma \to 0$ the flow in each region reduces to the Couette flow between concentric cylinders. In the outer region the flow is governed by

$$\frac{1}{Re}\nabla^2\zeta_0 = 0, \quad \text{and} \quad \zeta_0 = -\nabla^2\psi_0 \tag{3.2.9}$$

with imposed boundary conditions

$$\begin{aligned} \frac{\partial\psi_0}{\partial\rho}(\beta) &= -1, & \psi_0(\beta) &= K_2, \\ \frac{\partial\psi_0}{\partial\rho}(1) &= -g_0, \quad \text{and} & \psi_0(1) &= K_3. \end{aligned} \tag{3.2.10}$$

In the inner region we solve

$$\frac{1}{Re}\nabla^2\bar{\zeta}_0 = 0, \quad \text{and} \quad \bar{\zeta}_0 = -\nabla^2\bar{\psi}_0 \tag{3.2.11}$$

together with the boundary conditions

$$\begin{aligned} \frac{\partial\bar{\psi}_0}{\partial\rho}(1) &= -g_0, & \bar{\psi}_0(1) &= K_3, \\ \frac{\partial\bar{\psi}_0}{\partial\rho}(\lambda) &= -\bar{U}, \quad \text{and} & \bar{\psi}_0(\lambda) &= 0. \end{aligned} \tag{3.2.12}$$

The equations of $O(\gamma)$ in the outer region are given by

$$\frac{1}{Re}\nabla^2\zeta_1 + \frac{1}{\rho}\frac{\partial\psi_0}{\partial\rho}\frac{\partial\zeta_1}{\partial\phi} = 0, \quad \text{and} \quad \zeta_1(\rho,\phi) = -\nabla^2\psi_1 - 4\rho\cos\phi\nabla^2\psi_0 \tag{3.2.13}$$

and are solved subject to

$$\begin{aligned} \frac{\partial\psi_1}{\partial\rho}(\beta,\phi) &= 2\beta\cos\phi, & \psi_1(\beta,\phi) &= 0, \\ \frac{\partial\psi_1}{\partial\rho}(1,\phi) &= 2g_0\cos\phi, \quad \text{and} & \psi_1(1,\phi) &= h_1(\phi). \end{aligned} \tag{3.2.14}$$

In the inner region the first-order functions are determined from

$$\frac{1}{Re}\nabla^2\bar{\zeta}_1 + \frac{1}{\rho}\frac{\partial\bar{\psi}_0}{\partial\rho}\frac{\partial\bar{\zeta}_1}{\partial\phi} = 0, \quad \text{and} \quad \bar{\zeta}_1(\rho,\phi) = -\nabla^2\bar{\psi}_1 - 4\rho\cos\phi\nabla^2\bar{\psi}_0 \quad (3.2.15)$$

subject to

$$\begin{aligned} \frac{\partial\bar{\psi}_1}{\partial\rho}(1,\phi) &= 2g_0\cos\phi, & \bar{\psi}_1(1,\phi) &= h_1(\phi), \\ \frac{\partial\bar{\psi}_1}{\partial\rho}(\lambda,\phi) &= 2\lambda\bar{U}\cos\phi + \alpha\cos\phi\left.\frac{\partial^2\bar{\psi}_0}{\partial\rho^2}\right|_{\rho=\lambda}, \quad \text{and} & \bar{\psi}_1(\lambda,\phi) &= -\alpha\bar{U}\cos\phi. \end{aligned} \quad (3.2.16)$$

Similarly, the equations of $O(\gamma^2)$ are given by

$$\begin{aligned} \frac{1}{Re}\nabla^2\zeta_2 + \frac{1}{\rho}\left(\frac{\partial\psi_0}{\partial\rho}\frac{\partial\zeta_2}{\partial\phi} + \frac{\partial(\psi_1,\zeta_1)}{\partial(\rho,\phi)}\right) &= 0, \\ \text{and} \quad -\nabla^2\psi_2 - 4\rho\cos\phi\nabla^2\psi_1 - 2\rho^2(2+\cos2\phi)\nabla^2\psi_0 &= \zeta_2 \end{aligned} \quad (3.2.17)$$

together with the boundary conditions

$$\begin{aligned} \frac{\partial\psi_2}{\partial\rho}(\beta,\phi) &= 1 - \beta^2 - 2\beta^2\cos2\phi, \\ \frac{\partial\psi_2}{\partial\rho}(1,\phi) &= -2g_0\cos2\phi, \\ \psi_2(\beta,\phi) &= 0, \\ \text{and} \\ \psi_2(1,\phi) &= h_2(\phi), \end{aligned} \quad (3.2.18)$$

in the outer region. In the inner region, the corresponding equations are

$$\begin{aligned} \frac{1}{Re}\nabla^2\bar{\zeta}_2 + \frac{1}{\rho}\left(\frac{\partial\bar{\psi}_0}{\partial\rho}\frac{\partial\bar{\zeta}_2}{\partial\phi} + \frac{\partial(\bar{\psi}_1,\bar{\zeta}_1)}{\partial(\rho,\phi)}\right) &= 0, \\ \text{and} \quad -\nabla^2\bar{\psi}_2 - 4\rho\cos\phi\nabla^2\bar{\psi}_1 - 2\rho^2(2+\cos2\phi)\nabla^2\bar{\psi}_0 &= \bar{\zeta}_2, \end{aligned} \quad (3.2.19)$$

together with the conditions

$$\begin{aligned}
\frac{\partial\bar{\psi}_2}{\partial\rho}(1,\phi) &= -2g_0\cos 2\phi, \\
\frac{\partial\bar{\psi}_2}{\partial\rho}(\lambda,\phi) &= -\bar{U}\left(-2\alpha\cos^2\phi+\frac{\alpha^2}{2\lambda^2}\sin^2\phi-\lambda^2-1\right) \\
&\quad +\alpha\cos\phi\left.\frac{\partial^2\bar{\psi}_1}{\partial\rho^2}\right|_{\rho=\lambda}+\left(\frac{\alpha^2\sin^2\phi}{2\lambda}+2\alpha\lambda\cos^2\phi\right)\left.\frac{\partial^2\bar{\psi}_0}{\partial\rho^2}\right|_{\rho=\lambda} \\
&\quad -2\lambda\cos\phi\left.\frac{\partial\bar{\psi}_1}{\partial\rho}\right|_{\rho=\lambda}+\frac{\alpha}{\lambda^2}\sin\phi\left.\frac{\partial\bar{\psi}_1}{\partial\phi}\right|_{\rho=\lambda} \\
\bar{\psi}_2(1,\phi) &= h_2(\phi),
\end{aligned}$$

and

$$\bar{\psi}_2(\lambda,\phi) = \alpha\cos\phi\left.\frac{\partial\bar{\psi}_1}{\partial\rho}\right|_{\rho=\lambda}-\frac{\alpha^2\cos^2\phi}{2}\left.\frac{\partial^2\bar{\psi}_0}{\partial\rho^2}\right|_{\rho=\lambda}-\frac{\bar{U}\alpha^2\sin^2\phi}{2\lambda}. \tag{3.2.20}$$

Using equations (3.1.7) and (2.2.22), $\Pi_n(\rho,\phi)$ $(n=0,1,2,\ldots)$ is single-valued if

$$\begin{aligned}
&O(1): \frac{1}{Re}\int_0^{2\pi}\left.\frac{\partial\zeta_0}{\partial\rho}\right|_{\rho=1}d\phi=0, \\
&O(\gamma): \int_0^{2\pi}f_1(\phi)\zeta_0-\frac{1}{Re}\left.\frac{\partial\zeta_1}{\partial\rho}\right|_{\rho=1}d\phi=0, \\
&O(\gamma^2): \int_0^{2\pi}f_2(\phi)\zeta_0+f_1(\phi)\zeta_1|_{\rho=1} \\
&\qquad -\left(f_1(\phi)\frac{\partial f_1(\phi)}{\partial\phi}+2\cos\phi f_1(\phi)\zeta_0+\frac{1}{Re}\left.\frac{\partial\zeta_2}{\partial\rho}\right|_{\rho=1}\right)d\phi=0,
\end{aligned} \tag{3.2.21}$$

and so on. A similar set of equations can be generated for the pressure field within the inner region. We now determine the basic solution, namely, the Couette flow between concentric cylinders with the membrane located between them.

3.3 Couette Flow between Concentric Cylinders

When $\gamma \to 0$, axisymmetric flow between the inner and outer cylinders results where the motion is simple shearing and independent of Reynolds number. Within the annulus, the fluid in contact with the membrane slips over this surface with velocity g_0 and the presence of the membrane in the flow domain causes vorticity to be generated from both sides of the membrane. Further, a biharmonic equation in the stream function governs the flow field; however, due to the axisymmetric nature of the flow, this can be replaced with a fourth-order Euler equation. Thus, the stream function in each region is characterised by

$$\psi_0(\rho) = -\frac{A}{2}\rho^2 - B\ln\rho + C + D\rho^2\ln\rho. \tag{3.3.1}$$

From equation (3.2.21), we deduce that both $\Pi_0(\rho)$ and $P_0(\rho)$ are single-valued if, and only if, $D = 0$ and the remaining constants can be determined from the boundary conditions given in equation (3.2.12). Hence, if the above coefficients for the inner region, $\lambda \leq \rho \leq 1$ are denoted by the subscript i then from (3.2.12)

$$\begin{aligned} A_i &= \frac{g_0 - \lambda\bar{U}}{1-\lambda^2}, \\ B_i &= \frac{-\lambda(\lambda g_0 - \bar{U})}{1-\lambda^2}, \\ \text{and} \quad C_i &= \frac{\lambda\bar{U}(2\ln\lambda - \lambda^2) + g_0\lambda^2(1-2\ln\lambda)}{2(1-\lambda^2)}. \end{aligned} \tag{3.3.2}$$

The basic solution for the inner region is therefore

$$\bar{\psi}_0(\rho) = \frac{\lambda\bar{U}}{2(1-\lambda^2)}\left(\rho^2 + 2\ln(\lambda/\rho) - \lambda^2\right) - \frac{g_0}{2(1-\lambda^2)}\left(\rho^2 + 2\lambda^2\ln(\lambda/\rho) - \lambda^2\right). \tag{3.3.3}$$

Using the above solution, the streamline along the membrane, K_3, can be determined, viz

$$K_3 = \frac{\lambda\bar{U}\,(1 + 2\ln\lambda - \lambda^2) - g_0\,(1 + 2\lambda^2\ln\lambda - \lambda^2)}{2(1-\lambda^2)}. \tag{3.3.4}$$

In the outer region, $1 \leq \rho \leq \beta$, the coefficients for the dominant solution are given by

$$A_o = \frac{\beta - g_0}{\beta^2 - 1},$$

$$B_o = \frac{\beta(\beta g_0 - 1)}{\beta^2 - 1}, \tag{3.3.5}$$

$$\text{and} \quad C_o = \frac{A_o}{2} + K_3.$$

Thus the stream function in the outer region, $\psi_0(\rho)$, has the form

$$\psi_0(\rho) = \frac{g_0}{2(\beta^2 - 1)}\left(\rho^2 - 2\beta^2 \ln \rho - 1\right) + \frac{\beta}{2(\beta^2 - 1)}\left(-\rho^2 + 2\ln \rho + 1\right) + K_3. \tag{3.3.6}$$

Putting $\rho = \beta$ in (3.3.6) leads to

$$K_2 = \frac{A_o}{2}(1 - \beta^2) - B_o \ln \beta + K_3. \tag{3.3.7}$$

The basic solution matches that of Hird and Siew [42] for the no-slip case ($g_0 = 0$). From the zeroth-order equations of motion, the vorticity in each region is given by $\zeta_0 = 2A_o$ and $\bar{\zeta}_0 = 2A_i$. We note that g_0 is suitably prescribed so that the vorticity of the unperturbed motion is non-zero in both regions. The leading-order vorticity is clearly discontinuous across the membrane; this discontinuity can be removed if the slip velocity is allowed to take on a value such that $A_o = A_i$. The first-order equations of motion will now be solved.

3.4 The First-Order Solution

A necessary condition for the asymptotic analysis given by Wood [95] to hold is that the bounding cylinders must rotate in the same direction. In this dissertation, both the sense of rotation of the cylinders and the sign of the slip velocity are initially unrestricted but we too show that the tangential velocities of the membrane and bounding cylinders must be in the same direction for the ensuing asymptotic expansions to hold. In the following analysis, we assume

that the effect of the slip along the membrane is captured only in the zeroth-order solution; therefore, we impose no-slip conditions along the membrane when solving for higher-order terms. This assumption does not compromise the condition placed on $g(\phi;\gamma)$ given in equation (2.2.17). In addition, we observe that equation (2.2.16) is satisfied if we assume that the radial velocity $f(\phi;\gamma)$ has the Fourier decomposition

$$f_1(\phi) = \sum_{m=1}^{\infty} a_m \cos m\phi + b_m \sin m\phi. \tag{3.4.1}$$

These assumptions for $f(\phi;\gamma)$ and $g(\phi;\gamma)$ will make the analytical approach tractable. Using the zeroth-order solution for the inner and outer regions obtained in Section 3.3, the first-order equations of motion given in equations (3.2.13) and (3.2.15) simplify. Thus, in the outer region, we determine $\psi_1(\rho,\phi)$ and $\zeta_1(\rho,\phi)$ from

$$\begin{aligned} \left(A_o + \frac{B_o}{\rho^2}\right)\frac{\partial \zeta_1}{\partial \phi} &= \frac{1}{Re}\nabla^2\zeta_1, \\ \text{and} \qquad \zeta_1 &= -\nabla^2(\psi_1 - A_o\rho^3\cos\phi), \end{aligned} \tag{3.4.2}$$

together with the boundary conditions given in equation (3.2.14), while $\bar{\psi}_1(\rho,\phi)$ and $\bar{\zeta}_1(\rho,\phi)$ are determined from

$$\begin{aligned} \left(A_i + \frac{B_i}{\rho^2}\right)\frac{\partial \bar{\zeta}_1}{\partial \phi} &= \frac{1}{Re}\nabla^2\bar{\zeta}_1, \\ \text{and} \qquad \bar{\zeta}_1 &= -\nabla^2(\bar{\psi}_1 - A_i\rho^3\cos\phi), \end{aligned} \tag{3.4.3}$$

together with the boundary conditions given in equation (3.2.16).

We observe from the above governing equations and boundary conditions that the first-order stream function in both regions will have the same form. Thus, we will only show the method used to determine the flow in the outer region and use these results to give the corresponding expressions for the inner region. The asymptotic methods used to determine the first-order stream function in the outer region are given in Section 3.5. The corresponding expansions, valid within the inner region, are given in Section 3.6.

Since Reynolds number is large, equation (3.4.2) represents a singular perturbation problem; however, a composite solution, satisfying all boundary conditions, is looked for instead. To this end, the governing equations for the outer region given in equation (3.4.2) can be simplified through the substitutions

$$\psi_1(\rho,\phi;Re) = A_o\rho^3\cos\phi + \Re\left(\sum_{m=1}^{\infty}\chi_m(\rho;Re)e^{im\phi}\right) \tag{3.4.4}$$

and

$$\begin{aligned}\zeta_1(\rho,\phi;Re) &= -\Re\left(\nabla^2\left[\sum_{m=1}^{\infty}\chi_m(\rho;Re)e^{im\phi}\right]\right)\\ &= \Re\left(\sum_{m=1}^{\infty}\xi_m(\rho;Re)e^{im\phi}\right),\end{aligned} \tag{3.4.5}$$

where $\Re(\cdot)$ denotes the real part of an expression and χ_m and ξ_m, defined in the outer region only, represent continuous complex functions dependent on ρ and the Reynolds number.

From the representative forms of ζ_1 and $f_1(\phi)$ given above, the single-valued conditions for $\Pi_1(\rho,\phi)$ defined in equation (3.2.21) are automatically satisfied. Therefore, the pressure field up to $O(\gamma)$ is single-valued in the outer region and, using similar arguments, the corresponding pressure field in the inner region is also single-valued. Using the above substitutions, equation (3.4.2) yields the Bessel equation

$$\rho^2\xi_m''(\rho) + \rho\xi_m'(\rho) - \xi_m(\rho)\left(imA_oRe\rho^2 + m^2 + imB_oRe\right) = 0, \tag{3.4.6}$$

and the inhomogeneous Euler equation

$$\chi_m'' + \frac{1}{\rho}\chi_m'(\rho) - \frac{m^2}{\rho^2}\chi_m(\rho) = -\xi_m(\rho), \tag{3.4.7}$$

where the prime $'$ denotes differentiation with respect to ρ. For non-zero A_0 and B_0, the general solution to the Bessel equation can be written as a linear combination of Bessel functions of the first and third kind, viz

$$\xi_m(\rho) = C_m^o J_{\mu_m}(\lambda_m\rho) + D_m^o H_{\mu_m}^{(1)}(\lambda_m\rho), \tag{3.4.8}$$

with complex order and argument given by

$$\mu_m = \sqrt{m^2 + imB_oRe}, \tag{3.4.9}$$

and

$$\lambda_m \rho = \sqrt{-imA_oRe}\rho, \tag{3.4.10}$$

respectively. The Bessel functions are defined such that $|arg(\lambda_m \rho)| < \pi/2$. Variation of parameters yields the general solution for $\chi_m(\rho)$ as

$$\chi_m(\rho) = A_m^o \rho^m + B_m^o \rho^{-m} - C_m^o I_m^{(1)}(\rho) - D_m^o I_m^{(2)}(\rho), \tag{3.4.11}$$

with $I_m^{(1)}(\rho)$ and $I_m^{(2)}(\rho)$ given by

$$I_m^{(1)}(\rho) = \frac{1}{2m\rho^m} \int_1^\rho K_1^{(m)}(s,\rho) J_{\mu_m}(\lambda_m s) ds \tag{3.4.12}$$

and

$$I_m^{(2)}(\rho) = -\frac{1}{2m\rho^m} \int_\rho^\beta K_1^{(m)}(s,\rho) H_{\mu_m}^{(1)}(\lambda_m s) ds, \tag{3.4.13}$$

where

$$K_1^{(m)}(s,\rho) = s^{1-m}\rho^{2m} - s^{1+m} \tag{3.4.14}$$

represents the kernel. A_m^o, B_m^o, C_m^o and D_m^o are determined from the conditions

$$\left.\begin{array}{llll} \chi_m'(\beta) & = (2\beta - 3A_o\beta^2)\epsilon_m, & \chi_m(\beta) & = -A_o\beta^3\epsilon_m, \\ \chi_m'(1) & = (2g_0 - 3A_o)\epsilon_m, \quad \text{and} & \chi_m(1) & = E_m - A_o\epsilon_m. \end{array}\right\} \tag{3.4.15}$$

where

$$E_m = -\frac{i}{m\pi} \int_{-\pi}^{\pi} f_1(\phi) e^{-im\phi} d\phi = -\frac{b_m + ia_m}{m}, \tag{3.4.16}$$

$\epsilon_1 = 1$ and $\epsilon_m = 0$ for $m \neq 1$.

Similarly, to determine the stream function within the inner region we introduce two complex functions, defined within the inner region only, and possessing the forms

$$\tilde{\xi}_m(\rho) = C_m^i J_{\mu_m}(\lambda_m \rho) + D_m^i H_{\mu_m}^{(1)}(\lambda_m \rho), \tag{3.4.17}$$

and

$$\tilde{\chi}_m(\rho) = A_m^i \rho^m + B_m^i \rho^{-m} - C_m^i I_m^{(1)}(\rho) - D_m^i I_m^{(2)}(\rho). \tag{3.4.18}$$

The order and argument of the Bessel functions are now written in terms of the complex constants A_i and B_i and the same restriction to that given in the outer region is placed on the argument of

$\lambda_m \rho$. The functions are related to $\bar{\psi}_1$ and $\bar{\zeta}_1$ through the substitutions of the same form as equations (3.4.4) and (3.4.5). The integrals involving the Bessel functions are defined in the inner region by

$$I_m^{(1)}(\rho) = \frac{1}{2m\rho^m} \int_\lambda^\rho K_1^{(m)}(s,\rho) J_{\mu_m}(\lambda_m s) ds \tag{3.4.19}$$

and

$$I_m^{(2)}(\rho) = -\frac{1}{2m\rho^m} \int_\rho^1 K_1^{(m)}(s,\rho) H_{\mu_m}^{(1)}(\lambda_m s) ds \tag{3.4.20}$$

where the kernel is given in equation (3.4.14). The constants A_m^i, B_m^i, C_m^i and D_m^i are determined from the conditions

$$\tilde{\chi}_m'(\lambda) = \left(2\lambda\bar{U} + \frac{\alpha(g_0 - A_i(1+\lambda^2))}{\lambda^2} - 3A_i\lambda^2\right)\epsilon_m, \quad \tilde{\chi}_m(\lambda) = -(A_i\lambda^3 + \alpha\bar{U})\epsilon_m,$$

$$\tilde{\chi}_m'(1) = (2g_0 - 3A_i)\epsilon_m, \qquad \text{and} \qquad \tilde{\chi}_m(1) = E_m - A_i\epsilon_m, \tag{3.4.21}$$

and where E_m and ϵ_m are defined as before.

Applying equation (3.4.15) to equation (3.4.11) generates the following algebraic system of equations

$$\begin{array}{llll} mA_m^o\beta^{m-1} & -mB_m^o\beta^{-(m+1)} & -C_m^o I_m^{(1)'}(\beta) & = (2\beta - 3A_o\beta^2)\,\epsilon_m, \\ A_m^o\beta^m & +B_m^o\beta^{-m} & -C_m^o I_m^{(1)}(\beta) & = -A_o\beta^3\epsilon_m, \\ mA_m^o & -mB_m^o & -D_m^o I_m^{(2)'}(1) & = (2g_0 - 3A_o)\,\epsilon_m, \\ A_m^o & +B_m^o & -D_m^o I_m^{(2)}(1) & = E_m - A_o\epsilon_m. \end{array} \tag{3.4.22}$$

Equivalently,

$$\mathbf{U}\mathbf{d}_1 = \mathbf{p}_1$$

where

$$\mathbf{U} = \begin{bmatrix} m\beta^{m-1} & -m\beta^{-(m+1)} & -I_m^{(1)'}(\beta) & 0 \\ \beta^m & \beta^{-m} & -I_m^{(1)}(\beta) & 0 \\ m & -m & 0 & -I_m^{(2)'}(1) \\ 1 & 1 & 0 & -I_m^{(2)}(1) \end{bmatrix}, \quad (3.4.23)$$

$$\mathbf{d}_1 = \begin{bmatrix} A_m^o \\ B_m^o \\ C_m^o \\ D_m^o \end{bmatrix}, \quad (3.4.24)$$

and

$$\mathbf{p}_1 = \begin{bmatrix} (2\beta - 3A_o\beta^2)\epsilon_m \\ -A_o\beta^3\epsilon_m \\ (2g_0 - 3A_o)\epsilon_m \\ E_m - A_o\epsilon_m \end{bmatrix}. \quad (3.4.25)$$

Let

$$\begin{aligned} \Delta_m^o &= \left(\beta^{2m} - 1\right)\left[\beta I_m^{(1)'}(\beta) I_m^{(2)'}(1) - m^2 I_m^{(1)}(\beta) I_m^{(2)}(1)\right] \\ &\quad + m\left(\beta^{2m} + 1\right)\left[\beta I_m^{(1)'}(\beta) I_m^{(2)}(1) - I_m^{(1)}(\beta) I_m^{(2)'}(1)\right], \quad (3.4.26) \end{aligned}$$

then solving the above system of equations we find that for m=1, $\Delta_1^o C_1^o$ and $\Delta_1^o D_1^o$ are given by

$$\begin{aligned} \Delta_1^o C_1^o &= 2\beta\left[\left(I_1^{(2)'}(1) - I_1^{(2)}(1)\right)\left(\beta - 2A_o\beta^2\right) + \left(I_1^{(2)}(1) + I_1^{(2)'}(1)\right)\left(A_o\beta^4 - \beta^3\right)\right. \\ &\quad \left. + I_1^{(2)}(1)\left(2g_0 - 3A_o\right) + I_1^{(2)'}(1)\left(A_o - E_1\right)\right] \\ &= I_1^{(2)}(1)\left[4\beta^2 - 2\beta g_0(1+\beta^2)\right] + I_1^{(2)'}(1)\left[2\beta g_0(1-\beta^2) - 2\beta E_1\right], \quad (3.4.27) \end{aligned}$$

and

$$\begin{aligned} \Delta_1^o D_1^o &= -\left[\left(\beta I_1^{(1)'}(\beta) - I_1^{(1)}(\beta)\right)\left(\beta^2 E_1 + 2\beta^2(g_0 - 2A_o)\right)\right. \\ &\quad + \left(\beta I_1^{(1)'}(\beta) + I_1^{(1)}(\beta)\right)\left(E_1 + 2(A_o - g_0)\right) + 2A_0\beta^5 I_1^{(1)'}(\beta) \\ &\quad \left. + 2\beta^3 I_1^{(1)}(\beta)\left(2 - 3A_o\beta\right)\right] \\ &= I_1^{(1)}(\beta)\left[2\beta(1+\beta^2) + E_1(\beta^2 - 1) - 4g_0\beta^2\right] \\ &\quad + I_1^{(1)'}(\beta)\left[2\beta^2(1-\beta^2) - \beta E_1(1+\beta^2)\right]. \quad (3.4.28) \end{aligned}$$

The simplified form of equations (3.4.27) and (3.4.28) results from using equation (3.3.5) to replace A_o with an expression involving the slip velocity g_0.

When $m \geq 2$, we observe

$$\Delta_m^o C_m^o = -2m\beta^m E_m I_m^{(2)'}(1), \tag{3.4.29}$$

and

$$\Delta_m^o D_m^o = -mE_m \left[m\left(1-\beta^{2m}\right) I_m^{(1)}(\beta) + \beta\left(1+\beta^{2m}\right) I_m^{(1)'}(\beta) \right]. \tag{3.4.30}$$

For any given harmonic A_m^o and B_m^o are easily extracted from equation (3.4.22), viz

$$A_m^o = \frac{D_m^o}{2m}\left[mI_m^{(2)}(1) + I_m^{(2)'}(1) \right] + E_m/2 + (g_0 - 2A_o)\,\epsilon_m, \tag{3.4.31}$$

and

$$B_m^o = \frac{D_m^o}{2m}\left[mI_m^{(2)}(1) - I_m^{(2)'}(1) \right] + E_m/2 + (A_o - g_o)\,\epsilon_m. \tag{3.4.32}$$

Differentiating equations (3.4.12) and (3.4.13), $I_m^{(1)'}(\rho)$ and $I_m^{(2)'}(\rho)$ are given by

$$I_m^{(1)'}(\rho) = \frac{1}{2}\int_1^\rho K_2^{(m)}(s,\rho) J_{\mu_m}(\lambda_m s) ds, \tag{3.4.33}$$

and

$$I_m^{(2)'}(\rho) = -\frac{1}{2}\int_\rho^\beta K_2^{(m)}(s,\rho) H_{\mu_m}^{(1)}(\lambda_m s) ds, \tag{3.4.34}$$

where

$$K_2^{(m)}(s,\rho) = \left(\frac{s}{\rho}\right)^{1-m} + \left(\frac{s}{\rho}\right)^{1+m}. \tag{3.4.35}$$

Within the inner region, equations (3.4.18) and (3.4.21) generate the system of algebraic equations

$$mA_m^i \lambda^{m-1} - mB_m^i \lambda^{-(m+1)} - D_m^i I_m^{(2)'}(\lambda) = \left(2\lambda\bar{U} + \frac{\alpha\left(g_0 - A_i\left(1+\lambda^2\right)\right)}{\lambda^2} - 3A_i\lambda^2\right)\epsilon_m,$$

$$\begin{array}{llll} A_m^i\lambda^m & +B_m^i\lambda^{-m} & -D_m^i I_m^{(2)}(\lambda) & = -\left(A_i\lambda^3+\alpha\bar{U}\right)\epsilon_m, \\ mA_m^i & -mB_m^i \quad -C_m^i I_m^{(1)'}(1) & & = (2g_0-3A_i)\,\epsilon_m, \\ A_m^i & +B_m^i \quad -C_m^i I_m^{(1)}(1) & & = E_m - A_i\epsilon_m. \end{array} \tag{3.4.36}$$

Equivalently,

$$\mathbf{V}\mathbf{d}_2 = \mathbf{p}_2$$

where

$$\mathbf{V} = \begin{bmatrix} m\lambda^{m-1} & -m\lambda^{-(m+1)} & 0 & -I_m^{(2)'}(\lambda) \\ \lambda^m & \lambda^{-m} & 0 & -I_m^{(2)}(\lambda) \\ m & -m & -I_m^{(1)'}(1) & 0 \\ 1 & 1 & -I_m^{(1)}(1) & 0 \end{bmatrix}, \tag{3.4.37}$$

$$\mathbf{d}_2 = \begin{bmatrix} A_m^i \\ B_m^i \\ C_m^i \\ D_m^i \end{bmatrix}, \tag{3.4.38}$$

and

$$\mathbf{p}_2 = \begin{bmatrix} \left(2\lambda\bar{U}+\dfrac{\alpha\,(g_0-A_i\,(1+\lambda^2))}{\lambda^2}-3A_i\lambda^2\right)\epsilon_m, \\ -\left(A_i\lambda^3+\alpha\bar{U}\right)\epsilon_m, \\ (2g_0-3A_i)\,\epsilon_m \\ E_m - A_i\epsilon_m \end{bmatrix}. \tag{3.4.39}$$

From this system of equations if we define

$$\begin{aligned} \Delta_m^i &= \left(\lambda^{2m}-1\right)\left[\lambda I_m^{(2)'}(\lambda)I_m^{(1)'}(1) - m^2 I_m^{(2)}(\lambda)I_m^{(1)}(1)\right] \\ &\quad +m\left(\lambda^{2m}+1\right)\left[\lambda I_m^{(2)'}(\lambda)I_m^{(1)}(1) - I_m^{(2)}(\lambda)I_m^{(1)'}(1)\right] \end{aligned} \tag{3.4.40}$$

then for $m=1$, $\Delta_1^i C_1^i$ and $\Delta_1^i D_1^i$ are given by

$$\begin{aligned} \Delta_1^i C_1^i &= \lambda^2\left[\left(I_1^{(2)}(\lambda)-\lambda I_1^{(2)'}(\lambda)\right)(E_1+2(g_0-2A_i)) \right. \\ &\quad -\left(I_1^{(2)}(\lambda)+\lambda I_1^{(2)'}(\lambda)\right)(E_1+2(A_i-g_0)) \\ &\quad -2\lambda^2 I_1^{(2)'}(\lambda)\left(\alpha\bar{U}+A_i\lambda^3\right)-2I_1^{(2)}(\lambda)\left(\alpha(g_0-A_i)-A_i\lambda^2(\alpha+3\lambda^2)\right. \\ &\quad \left.\left.+2\lambda^3\bar{U}\right)\right], \\ &= -\lambda E_1\left(1+\lambda^2\right)I_1^{(2)'}(\lambda)-E_1\left(1-\lambda^2\right)I_1^{(2)}(\lambda), \end{aligned}$$

and

$$\begin{aligned}\Delta_1^i D_1^i &= \left[\left(I_1^{(1)'}(1)+I_1^{(1)}(1)\right)\left(\left(2\lambda^4+\alpha\lambda^2\right)\left(A_i\lambda-\bar{U}\right)-\lambda\alpha g_0\right)\right. \\ &\quad +\frac{\left(I_1^{(1)'}(1)-I_1^{(1)}(1)\right)}{\lambda}\left(\lambda\bar{U}\left(2\lambda^2-\alpha\right)+\alpha(g_0-A_i)-4A_i\lambda^4\right) \\ &\quad \left.+2\lambda I_1^{(1)'}(1)(A_i-E_1)+2\lambda I_1^{(1)}(1)\left(2g_0+A_i(\alpha-3)\right)\right], \\ &= -2\lambda E_1 I_1^{(1)'}(1).\end{aligned} \tag{3.4.41}$$

For $m \geq 2$,

$$\Delta_m^i C_m^i = -mE_m\left[m\left(1-\lambda^{2m}\right)I_m^{(2)}(\lambda)+\lambda\left(1+\lambda^{2m}\right)I_m^{(2)'}(\lambda)\right] \tag{3.4.42}$$

and

$$\Delta_m^i D_m^i = -2m\lambda^m E_m I_m^{(1)'}(1), \tag{3.4.43}$$

and A_m^i and B_m^i are determined from

$$A_m^i = \frac{C_m^i}{2m}\left[mI_m^{(1)}(1)+I_m^{(1)'}(1)\right]+E_m/2+(g_0-2A_i)\,\epsilon_m, \tag{3.4.44}$$

and

$$B_m^i = \frac{C_m^i}{2m}\left[mI_m^{(1)}(1)-I_m^{(1)'}(1)\right]+E_m/2+(A_i-g_0)\,\epsilon_m. \tag{3.4.45}$$

From equations (3.4.19) and (3.4.20), we define

$$I_m^{(1)'}(\rho) = \frac{1}{2}\int_\lambda^\rho K_2^{(m)}(s,\rho)J_{\mu_m}(\lambda_m s)ds, \tag{3.4.46}$$

and

$$I_m^{(2)'}(\rho) = -\frac{1}{2}\int_\rho^1 K_2^{(m)}(s,\rho)H_{\mu_m}^{(1)}(\lambda_m s)ds, \tag{3.4.47}$$

with $K_2^{(m)}(s,\rho)$ defined in (3.4.35). In the absence of the slip velocity, g_0, the results given in equations (3.4.26) – (3.4.32) reduce to those given by Hird and Siew [42] and also Wood [95] (when $m = 1$). The form of the first-order stream and vorticity functions can be given in closed form; however, as

solutions to large-Reynolds-number flows are required, the Bessel functions are replaced with their asymptotic expansions. Therefore, the first-order stream and vorticity functions defined through equations (3.4.4) and (3.4.5) will be given asymptotically. Clearly, the asymptotic behaviour of the Bessel functions governs the behaviour to the flow field.

Asymptotic expansions for Bessel functions have been tabulated when the relative magnitudes of the order and argument are known (see Watson [93]); however, for a given geometry, the prescribed slip velocity determines both the sign and size of the constants A_o and B_o, this in turn determines the relative sizes of the complex order and argument of the Bessel functions. The asymptotic expansions for the Bessel functions when both the order and argument are large and complex are determined by applying the WKB method to the Bessel equation. The various expansions are derived in Appendix A. In Section 3.5, we use the asymptotic expansions for the Bessel functions to generate asymptotic expansions for the first-order stream and vorticity functions. By construction, the behaviour of the stream function within the inner region is expected to be similar to that of the flow field in the outer region. Section 3.6 uses the results of Section 3.5 to determine the asymptotic expansions for the stream and vorticity functions within the inner region.

3.5 Determining $\psi_1(\rho, \phi)$ for Large Reynolds Number

For large-Reynolds-number flows, the Bessel functions $J_{\mu_m}(\lambda_m \rho)$ and $H^{(1)}_{\mu_m}(\lambda_m \rho)$ can be given asymptotically. If the relative magnitudes of the order and argument are known, asymptotic expansions for large (complex) order and argument can be generated through the method of steepest descents using Debeye's contours (see, for example, Watson [93]). If, however, no assumptions are placed on the magnitudes of these components expansions for the Bessel func-

tions are possible from known tables (see Abramowitz and Stegun [1]). Here, the slip velocity determines the size of the order and argument, therefore using tabulated results is likely to make the analysis too cumbersome. Thus, the asymptotic expansions will be generated from the WKB approximation of the Bessel equation. Once known, these expansions, through equations (3.4.4), (3.4.11), (3.4.12) and (3.4.13), will determine the first-order stream and vorticity functions. Thus, the behaviour of the stream and vorticity functions are governed by the asymptotic behaviour of the Bessel functions. The local expansions for $J_{\mu_m}(\lambda_m\rho)$ and $H^{(1)}_{\mu_m}(\lambda_m\rho)$ under various conditions are given in Appendix A and are now used to generate asymptotic expansions for the definite integrals involving these functions. As errors are easily introduced, the symbolic package MAPLE [22] is used to manipulate the various terms of the expansions given in the following sections. The use of MAPLE to retain and manipulate cumbersome expansions has been used successfully elsewhere (see Hird and Siew [42] and Siew and Hird [81]) to solve problems that would otherwise be difficult to obtain.

3.5.1 Uniform Expansions for the Integrals

The various asymptotic expansions for $J_{\mu_m}(\lambda_m\rho)$ and $H^{(1)}_{\mu_m}(\lambda_m\rho)$ given in Appendix A can be written in same form, viz

$$J_{\mu_m}(\lambda_m\rho) \sim \frac{\mathcal{A}_1(Re)}{N^{1/4}(\rho)} e^{P\sqrt{\frac{mRe}{2}}\sigma(\rho)} \left(1 + \frac{\tau_1^{(m)}(\rho)}{\sqrt{Re}} + \frac{\tau_2^{(m)}(\rho)}{Re} + \ldots\right), \quad (3.5.1)$$

and

$$H^{(1)}_{\mu_m}(\lambda_m\rho) \sim \frac{\mathcal{A}_2(Re)}{N^{1/4}(\rho)} e^{-P\sqrt{\frac{mRe}{2}}\sigma(\rho)} \left(1 - \frac{\tau_1^{(m)}(\rho)}{\sqrt{Re}} + \frac{\tau_2^{(m)}(\rho)}{Re} - \ldots\right), \quad (3.5.2)$$

where the real part of P is positive. The forms of the terms given above are defined in Appendix A and depend on the sign of the real constants A_o and B_o and their relative magnitudes. For example, when both A_o and B_o are positive

we observe

$$
\begin{aligned}
P &= 1+i, \\
N(\rho) &= A_o\rho^2 + B_o, \\
\tau_1^{(m)}(\rho) &= \frac{3\sqrt{B_o}A_o\rho^2 - 2B_o^{3/2} - 12m^2(N(\rho))^{3/2}\text{arctanh}\left(\sqrt{N(\rho)/B_o}\right)}{24\sqrt{imB_o}(N(\rho))^{3/2}}, \\
\tau_2^{(m)}(\rho) &= \frac{\left(\tau_1^{(m)}(\rho)\right)^2}{2} - \frac{A_o^2\rho^4(4m^2-1) + (1+2m^2)4A_oB_o\rho^2 + 4m^2B_o^2}{16im(N(\rho))^3} \\
\text{and} \quad \sigma(\rho) &= \int^\rho \frac{\sqrt{N(s)}}{s}ds = \sqrt{N(\rho)} + \sqrt{B_o}\ln\left(\frac{\sqrt{N(\rho)}-\sqrt{B_o}}{\sqrt{A_o}\rho}\right).
\end{aligned}
$$

In the ensuing analysis, the forms of $\mathcal{A}_1(Re)$ and $\mathcal{A}_2(Re)$ do not contribute to the asymptotic behaviour of the stream and vorticity functions and, therefore, need not be determined.

To determine asymptotic expansions for the integrals defined in equations (3.4.12) and (3.4.13) we observe that in the various expansions for $J_{\mu_m}(\lambda_m\rho)$ and $H^{(1)}_{\mu_m}(\lambda_m\rho)$, $\sigma(\rho)$ is a monotonically increasing function; this ensures that within the limits of integration, no stationary points are present in the exponentials. Hence, integration by parts is applicable and from the theory of Laplace's method we expect that the neighbourhood where the exponent is greatest will contribute the most to the large-Reynolds-number expansions for $I_m^{(1)}(\rho)$, $I_m^{(1)'}(\rho)$, $I_m^{(2)}(\rho)$ and $I_m^{(2)'}(\rho)$ given in equations (3.4.12), (3.4.33), (3.4.13) and (3.4.34). Wood [95] exploited this feature by assuming Re is large enough so that only the contributions made from the bound where the exponent is greatest are used in the asymptotic expansions for $I_m^{(1)}(\rho)$, $I_m^{(2)}(\rho)$ and their derivatives. In our expansions, the range of Reynolds number considered here is not sufficiently large to permit any such simplifications; thus, we retain the contributions from both limits of integration. From the exponential character of $J_{\mu_m}(\lambda_m\rho)$ and $H^{(1)}_{\mu_m}(\lambda_m\rho)$, we see that contributions from the upper bound will be dominant in $I_m^{(1)}(\rho)$ and $I_m^{(1)'}(\rho)$; while, contributions from the lower bound will be dominant in $I_m^{(2)}(\rho)$ and $I_m^{(2)'}(\rho)$. We now generate asymptotic

expansions for $I_m^{(1)}(\rho)$ and $I_m^{(2)}(\rho)$.

3.5.2 Expansions for $I_m^{(1)}(\rho)$ and $I_m^{(2)}(\rho)$

In equation (3.4.12), we replace the Bessel function $J_{\mu_m}(\lambda_m\rho)$ with its series form given in equation (3.5.1) and perform integration by parts successively to produce

$$I_m^{(1)}(\rho) = \frac{\mathcal{A}_1(Re)}{2m\rho^m}\left[\sqrt{\frac{2}{mRe}}\frac{t_1^{(m)}(s,\rho)}{P}\, e^{P\sqrt{\frac{mRe}{2}}\sigma(s)}\Big|_{s=1}^{s=\rho}\right.$$
$$+\frac{1}{Re}\left(\frac{1}{P}\sqrt{\frac{2}{m}}\tau_1^{(m)}(s)t_1^{(m)}(s,\rho) - \frac{2t_1^{(m)'}(s,\rho)}{P^2 m\sigma'(s)}\right) e^{P\sqrt{\frac{mRe}{2}}\sigma(s)}\Big|_{s=1}^{s=\rho}$$
$$\left.+O\left(\frac{e^{\sqrt{\frac{mRe}{2}}\sigma(\rho)}}{Re^{3/2}}\right)\right], \tag{3.5.3}$$

where

$$t_1^{(m)}(s,\rho) = \frac{K_1^{(m)}(s,\rho)}{\sigma'(s)N^{1/4}(s)} \tag{3.5.4}$$

and $'$ denotes differentiation with respect to s. Equation (3.5.3) can be written as

$$I_m^{(1)}(\rho) = \frac{\mathcal{A}_1(Re)}{\sqrt{2mRe}P}\left\{-\frac{t_1^{(m)}(1,\rho)}{\rho^m m}e^{-P\sqrt{\frac{mRe}{2}}[\sigma(\rho)-\sigma(1)]}\right.$$
$$+\frac{1}{\sqrt{Re}}\left(\left(-\frac{t_1^{(m)}(1,\rho)\tau_1^{(m)}(1)}{\rho^m m} + \frac{1}{P}\sqrt{\frac{2}{m^3}}\frac{t_1^{(m)'}(1,\rho)}{\rho^m\sigma'(1)}\right) e^{-P\sqrt{\frac{mRe}{2}}[\sigma(\rho)-\sigma(1)]}\right.$$
$$\left.\left.-\frac{1}{P}\sqrt{\frac{2}{m^3}}\frac{t_1^{(m)'}(\rho,\rho)}{\rho^m\sigma'(\rho)}\right)+\ldots\right\} e^{P\sqrt{\frac{mRe}{2}}\sigma(\rho)}, \tag{3.5.5}$$

where we note from (3.4.14) $K_1^{(m)}(\rho,\rho) = 0$. When $Re \to \infty$, or when $\sigma(\rho) - \sigma(1)$ is sufficiently large, terms containing $e^{-P\sqrt{mRe/2}[\sigma(\rho)-\sigma(1)]}$ are exponentially small and can be neglected (see Wood [95]) but for the range of

Reynolds number considered here we retained these terms. When n terms are used in (3.5.5), the remainder $r_n(\rho)$ has magnitude

$$|r_n(\rho)| = O\left(\frac{e^{\sqrt{\frac{mRe}{2}}\sigma(\rho)}}{Re^{(n+1)/2}}\right),$$

and as the last term in the approximation is $O\left(\frac{e^{\sqrt{mRe/2}\sigma(\rho)}}{Re^{n/2}}\right)$, then

$$r_n(\rho) = o\left(\frac{e^{\sqrt{mRe/2}\sigma(\rho)}}{Re^{n/2}}\right), \qquad \text{as } Re \to \infty, \text{ with } n \text{ fixed.}$$

Thus, the right hand side of equation (3.5.5) is asymptotic to $I_1^{(1)}(\rho)$ as $Re \to \infty$. We note also $r_n(\rho) \to 0$ as $n \to \infty$ ($Re > 1$ and fixed), therefore the series is also convergent. The asymptotic expansion for $I_1^{(1)}(\rho)$ uniform in the outer region is therefore given by

$$I_m^{(1)}(\rho) \sim \mathcal{K}_1^{(m)}(Re)\left\{\sum_{l=0}^{\infty} j_l^{(m)}(\rho) Re^{-l/2}\right\} e^{P\sqrt{\frac{mRe}{2}}\sigma(\rho)}, \tag{3.5.6}$$

where $\mathcal{K}_1^{(m)}(Re) = \dfrac{\mathcal{A}_1(Re)}{\sqrt{2mRe}P}$ and $j_l^{(m)}(\rho)$ $(l = 0, 1, \ldots)$ represent the coefficients given in (3.5.5) and are dependent on Re as well as ρ. The explicit form of this series is determined once the slip velocity, g_0, is known.

Again by integrating by parts, a uniform asymptotic expansion for $I_m^{(2)}(\rho)$ is easily obtained from equation (3.4.13). Thus,

$$I_m^{(2)}(\rho) \sim \mathcal{K}_2^{(m)}(Re)\left\{\sum_{l=0}^{\infty} h_l^{(m)}(\rho) Re^{-l/2}\right\} e^{-P\sqrt{\frac{mRe}{2}}\sigma(\rho)}, \tag{3.5.7}$$

where $\mathcal{K}_2^{(m)}(Re) = \dfrac{\mathcal{A}_2(Re)}{\sqrt{2mRe}P}$ and

$$\begin{aligned}
h_0^{(m)}(\rho) &= \frac{t_1^{(m)}(\beta,\rho)}{\rho^m m} e^{-P\sqrt{\frac{mRe}{2}}[\sigma(\beta)-\sigma(\rho)]}, \\
h_1^{(m)}(\rho) &= -\left(\frac{\tau_1^{(m)}(\beta) t_1^{(m)}(\beta,\rho)}{\rho^m m} - \frac{1}{P}\sqrt{\frac{2}{m^3}}\frac{t_1^{(m)'}(\beta,\rho)}{\sigma'(\beta)\rho^m}\right) e^{-P\sqrt{\frac{mRe}{2}}[\sigma(\beta)-\sigma(\rho)]} \\
&\quad -\frac{1}{P}\sqrt{\frac{2}{m^3}}\frac{t_1^{(m)'}(\rho,\rho)}{\sigma'(\rho)\rho^m},
\end{aligned}$$

$$h_2^{(m)}(\rho) = \left(\frac{t_1^{(m)}(\beta,\rho)\tau_2^{(m)}(\beta)}{\rho^m m} - \frac{1}{P}\sqrt{\frac{2}{m^3}}\frac{t_1^{(m)'}(\beta,\rho)\tau_1^{(m)}(\beta) + t_1^{(m)}(\beta,\rho)\tau_1^{(m)'}(\beta)}{\rho^m \sigma'(\beta)} \right) e^{-P\sqrt{\frac{mRe}{2}}[\sigma(\beta)-\sigma(\rho)]} + \frac{1}{P}\sqrt{\frac{2}{m^3}}\frac{t_1^{(m)'}(\rho,\rho)\tau_1^{(m)}(\rho)}{\rho^m \sigma'(\rho)},$$

and so on.

(3.5.8)

The $t_1^{(m)}(s,\rho)$ is defined in equation (3.5.4). When Re is large enough, exponentially small terms are generated and can be neglected; thus, simplifying the form of the asymptotic series expansion.

We note, by retaining the contributions from both limits of integration, the expansions for $I_m^{(1)}(\rho)$ and $I_m^{(2)}(\rho)$ satisfy the conditions $I_m^{(1)}(1) = 0$ and $I_m^{(2)}(\beta) = 0$. We now generate uniform expansions for $I_m^{(1)'}(\rho)$ and $I_m^{(2)'}(\rho)$.

3.5.3 Expansions for $I_m^{(1)'}(\rho)$ and $I_m^{(2)'}(\rho)$

In determining asymptotic expansions for $I_m^{(1)'}(\rho)$ and $I_m^{(2)'}(\rho)$ we note that Wood [95] appears to use the expansions for $I_m^{(1)}(\rho)$ and $I_m^{(2)}(\rho)$ (see equation (33) in [95]). This approach produces asymptotic expansions for $I_m^{(1)'}(\rho)$ and $I_m^{(2)'}(\rho)$ but they do not satisfy the conditions $I_m^{(1)'}(1) = 0$ and $I_m^{(2)'}(\beta) = 0$; thus, introducing avoidable errors into the solution. We, therefore, use equations (3.4.33) and (3.4.34) to give asymptotic expansions for $I_m^{(1)'}(\rho)$ and $I_m^{(2)'}(\rho)$ when the Reynolds number is large. Performing integration by parts, equations (3.4.33) and (3.4.34) give

$$I_m^{(1)'}(\rho) \sim \mathcal{K}_1^{(m)}(Re)\left\{\sum_{l=0}^{\infty} j_l^{(m)*}(\rho)Re^{-l/2}\right\} e^{P\sqrt{\frac{mRe}{2}}\sigma(\rho)}, \tag{3.5.9}$$

and

$$I_m^{(2)'}(\rho) \sim \mathcal{K}_2^{(m)}(Re)\left\{\sum_{l=0}^{\infty} h_l^{(m)*}(\rho)Re^{-l/2}\right\} e^{-P\sqrt{\frac{mRe}{2}}\sigma(\rho)}, \tag{3.5.10}$$

where

$$
\begin{aligned}
j_0^{(m)^*}(\rho) &= t_2^{(m)}(\rho,\rho) - t_2(1,\rho)e^{-P\sqrt{\frac{mRe}{2}}[\sigma(\rho)-\sigma(1)]}, \\
j_1^{(m)^*}(\rho) &= t_2^{(m)}(\rho,\rho)\tau_1^{(m)}(\rho) - \frac{1}{P}\sqrt{\frac{2}{m}}\frac{t_2^{(m)'}(\rho,\rho)}{\sigma'(\rho)} \\
&\quad + \left(\frac{1}{P}\sqrt{\frac{2}{m}}\frac{t_2^{(m)'}(1,\rho)}{\sigma'(1)} - t_2^{(m)}(1,\rho)\tau_1^{(m)}(1)\right)e^{-P\sqrt{\frac{mRe}{2}}[\sigma(\rho)-\sigma(1)]}, \\
j_2^{(m)^*}(\rho) &= -\frac{1}{P\sigma'(\rho)}\sqrt{\frac{2}{m}}\left[t_2^{(m)'}(\rho,\rho)\tau_1^{(m)}(\rho) + t_2^{(m)}(\rho,\rho)\tau_1^{(m)'}(\rho)\right] \\
&\quad + t_2^{(m)}(\rho,\rho)\tau_2^{(m)}(\rho) \\
&\quad + \left(\frac{1}{P\sigma'(1)}\sqrt{\frac{2}{m}}\left[t_2^{(m)'}(1,\rho)\tau_1^{(m)}(1) + t_2^{(m)}(1,\rho)\tau_1^{(m)'}(1)\right]\right. \\
&\quad \left. - t_2^{(m)}(1,\rho)\tau_2^{(m)}(1)\right)e^{-P\sqrt{\frac{mRe}{2}}[\sigma(\rho)-\sigma(1)]},
\end{aligned}
\tag{3.5.11}
$$

and so on. Also

$$
\begin{aligned}
h_0^{(m)^*}(\rho) &= t_2^{(m)}(\beta,\rho)e^{-P\sqrt{\frac{mRe}{2}}[\sigma(\beta)-\sigma(\rho)]} - t_2(\rho,\rho), \\
h_1^{(m)^*}(\rho) &= -\left(t_2^{(m)}(\beta,\rho)\tau_1^{(m)}(\beta) - \frac{1}{P}\sqrt{\frac{2}{m}}\frac{t_2^{(m)'}(\beta,\rho)}{\sigma'(\beta)}\right)e^{-P\sqrt{\frac{mRe}{2}}[\sigma(\beta)-\sigma(\rho)]} \\
&\quad - \frac{1}{P}\sqrt{\frac{2}{m}}\frac{t_2^{(m)'}(\rho,\rho)}{\sigma'(\rho)} + t_2^{(m)}(\rho,\rho)\tau_1^{(m)}(\rho), \\
h_2^{(m)^*}(\rho) &= \left(-\frac{1}{P\sigma'(\beta)}\sqrt{\frac{2}{m}}\left[t_2^{(m)'}(\beta,\rho)\tau_1^{(m)}(\beta) + t_2^{(m)}(\beta,\rho)\tau_1^{(m)'}(\beta)\right]\right. \\
&\quad \left. + t_2^{(m)}(\beta,\rho)\tau_2^{(m)}(\beta)\right)e^{-P\sqrt{\frac{mRe}{2}}[\sigma(\beta)-\sigma(\rho)]} \\
&\quad + \frac{1}{P\sigma'(\rho)}\sqrt{\frac{2}{m}}\left[t_2^{(m)'}(\rho,\rho)\tau_1^{(m)}(\rho) + t_2^{(m)}(\rho,\rho)\tau_1^{(m)'}(\rho)\right] \\
&\quad - t_2^{(m)}(\rho,\rho)\tau_2^{(m)}(\rho),
\end{aligned}
\tag{3.5.12}
$$

and so on. $K_1^{(m)}(Re)$ and $K_2^{(m)}(Re)$ are given in equations (3.5.6) and (3.5.7), and $t_2^{(m)}(s,\rho) = \dfrac{K_2^{(m)}(s,\rho)}{\sigma'(s)N^{1/4}(s)}$.

The expansions for $I_m^{(1)'}(\rho)$, $I_m^{(2)'}(\rho)$, $I_m^{(1)}(\rho)$ and $I_m^{(2)}(\rho)$ defined here will now be applied to equations (3.4.31), (3.4.32), (3.4.29) and (3.4.30) to generate

expansions for the complex coefficients A_m^o, B_m^o, C_m^o and D_m^o in powers of $Re^{-1/2}$. The explicit nature of the these expansions will depend on the value of the slip velocity.

3.5.4 Expansions for A_m^o, B_m^o, C_m^o and D_m^o

Before asymptotic expansions for A_m^o, B_m^o, C_m^o and D_m^o can be determined, the expansions for Δ_m^o, $\Delta_m^o C_m^o$ and $\Delta_m^o D_m^o$ must be found. From the expression for Δ_m^o given in equation (3.4.26) together with the asymptotic behaviour of $I_m^{(1)}(\rho)$, $I_m^{(2)}(\rho)$ and their derivatives given in Sections 3.5.2 and 3.5.3, the asymptotic expansion for Δ_m^o when Reynolds number is large is given by

$$\Delta_m \sim K_1^{(m)}(Re)K_2^{(m)}(Re)\left\{\sum_{l=0}^{\infty}\delta_l^{(m)}Re^{-l/2}\right\}e^{P\sqrt{\frac{mRe}{2}}[\sigma(\beta)-\sigma(1)]}. \qquad (3.5.13)$$

From equations (3.4.26), (3.5.6), (3.5.7), (3.5.9) and (3.5.10), $\delta_l^{(m)}$ $(l=0,1,\ldots)$ are given by

$$\begin{aligned}
\delta_0^{(m)} &= \left(\beta^{2m}-1\right)\left[\beta j_0^{(m)^*}(\beta)h_0^{(m)^*}(1) - m^2 j_0^{(m)}(\beta)h_0^{(m)}(1)\right] \\
&\quad +m\left(\beta^{2m}+1\right)\left[\beta j_0^{(m)^*}(\beta)h_0^{(m)}(1) - j_0^{(m)}(\beta)h_0^{(m)^*}(1)\right], \\
\delta_1^{(m)} &= \left(\beta^{2m}-1\right)\left[\beta\left(j_0^{(m)^*}(\beta)h_1^{(m)^*}(1) + j_1^{(m)^*}(\beta)h_0^{(m)^*}(1)\right)\right. \\
&\quad \left.-m^2\left(j_0^{(m)}(\beta)h_1^{(m)}(1) + j_1^{(m)}(\beta)h_0^{(m)}(1)\right)\right] \\
&\quad +m\left(\beta^{2m}+1\right)\left[\beta\left(j_0^{(m)^*}(\beta)h_1^{(m)}(1) + j_1^{(m)^*}(\beta)h_0^{(m)}(1)\right)\right. \\
&\quad \left.-j_0^{(m)}(\beta)h_1^{(m)^*}(1) - j_1^{(m)}(\beta)h_0^{(m)^*}(1)\right], \\
\delta_2^{(m)} &= \left(\beta^{2m}-1\right)\left[\beta\left(j_0^{(m)^*}(\beta)h_2^{(m)^*}(1) + j_1^{(m)^*}(\beta)h_1^{(m)^*}(1)\right.\right. \\
&\quad \left.+j_2^{(m)^*}(\beta)h_0^{(m)^*}(1)\right) \\
&\quad \left.-m^2\left(j_0^{(m)}(\beta)h_2^{(m)}(1) + j_1^{(m)}(\beta)h_1^{(m)}(1) + j_2^{(m)}(\beta)h_0^{(m)}(1)\right)\right] \\
&\quad +m\left(\beta^{2m}+1\right)\left[\beta\left(j_0^{(m)^*}(\beta)h_2^{(m)}(1) + j_1^{(m)^*}(\beta)h_1^{(m)}(1)\right.\right. \\
&\quad \left.+j_2^{(m)^*}(\beta)h_0^{(m)}(1)\right) \\
&\quad \left.-j_0^{(m)}(\beta)h_2^{(m)^*}(1) - h_1^{(m)^*}(1)j_1^{(m)}(\beta) - h_0^{(m)^*}(1)j_2^{(m)}(\beta)\right],
\end{aligned}$$

and so on. (3.5.14)

Also from the way $\Delta_m^o C_m^o$ and $\Delta_m^o D_m^o$, as given in equations (3.4.29) and (3.4.30), are dependent on $I_m^{(1)}(\rho)$, $I_m^{(2)}(\rho)$ and their derivatives, we have the expansions

$$\Delta_m^o C_m^o \sim K_2^{(m)}(Re)\left\{\sum_{l=0}^{\infty}\tilde{c}_l^{(m)}Re^{-l/2}\right\}e^{-P\sqrt{\frac{mRe}{2}}\sigma(1)}, \tag{3.5.15}$$

and

$$\Delta_m^o D_m^o \sim K_1^{(m)}(Re)\left\{\sum_{l=0}^{\infty}\tilde{d}_l^{(m)}Re^{-l/2}\right\}e^{P\sqrt{\frac{mRe}{2}}\sigma(\beta)}, \tag{3.5.16}$$

where the coefficients $\tilde{c}_l^{(m)}$ and $\tilde{d}_l^{(m)}$ for a given harmonic, m, are easily determined from equations (3.4.27)-(3.4.30), viz

$$\begin{aligned}
\tilde{c}_l^{(1)} &= h_l^{(1)}(1)\left[4\beta^2 - 2\beta g_0\left(1+\beta^2\right)\right] + h_l^{(1)^*}(1)\left[2\beta g_0\left(1-\beta^2\right) - 2\beta E_1\right], \\
&\qquad\qquad \text{for, } l = 0,1,2,\ldots, \\
\tilde{c}_l^{(m)} &= -2m\beta^m E_m h_l^{(m)^*}(1), \qquad \text{when } m>1, \text{ and } l = 0,1,2,\ldots, \\
\tilde{d}_l^{(1)} &= \left[2\beta\left(1+\beta^2\right) + E_1\left(\beta^2-1\right) - 4g_0\beta^2\right] j_l^{(1)}(\beta) \\
&\quad + \left[2\beta^2\left(1-\beta^2\right) - \beta E_1\left(1+\beta^2\right)\right] j_l^{(1)^*}(\beta),
\end{aligned}$$

and

$$\begin{aligned}
\tilde{d}_l^{(m)} &= -mE_m\left[m\left(1-\beta^{2m}\right) j_l^{(m)}(\beta) + \beta\left(1+\beta^{2m}\right) j_l^{(m)^*}(\beta)\right] \\
&\qquad\qquad \text{for } m>1 \text{ and } l = 0,1,2,\ldots,
\end{aligned} \tag{3.5.17}$$

and equations (3.5.6), (3.5.7), (3.5.9) and (3.5.10) determine $j_l^{(m)}(\beta)$, $j_l^{(m)^*}(\beta)$, $h_l^{(m)}(1)$ and $h_l^{(m)^*}(1)$. Using (3.5.13), (3.5.15) and (3.5.16), asymptotic series expansions for C_m^o and D_m^o in powers of $1/\sqrt{Re}$ are generated, viz

$$\begin{aligned}
C_m^o \sim\ & \\
& \frac{1}{K_1^{(m)}(Re)}\left\{\frac{\tilde{c}_0^{(m)}}{\delta_0^{(m)}} + \frac{1}{\sqrt{Re}}\left(\frac{\tilde{c}_1^{(m)}}{\delta_0^{(m)}} - \frac{\delta_1^{(m)}\tilde{c}_0^{(m)}}{\left(\delta_0^{(m)}\right)^2}\right)\right. \\
& \left. + \frac{1}{Re}\left(\tilde{c}_0^{(m)}\left[-\frac{\delta_2^{(m)}}{\left(\delta_0^{(m)}\right)^2} + \frac{\left(\delta_1^{(m)}\right)^2}{\left(\delta_0^{(m)}\right)^3}\right] - \frac{\tilde{c}_1^{(m)}\delta_1^{(m)}}{\left(\delta_0^{(m)}\right)^2} + \frac{\tilde{c}_2^{(m)}}{\delta_0^{(m)}}\right) + \ldots\right\} e^{-P\sqrt{\frac{mRe}{2}}\sigma(\beta)}
\end{aligned} \tag{3.5.18}$$

and

$$D_m^o \sim$$
$$\frac{1}{K_2^{(m)}(Re)}\left\{\frac{\tilde{d}_0^{(m)}}{\delta_0^{(m)}}+\frac{1}{\sqrt{Re}}\left(\frac{\tilde{d}_1^{(m)}}{\delta_0^{(m)}}-\frac{\delta_1^{(m)}\tilde{d}_0^{(m)}}{\left(\delta_0^{(m)}\right)^2}\right)\right.$$
$$\left.+\frac{1}{Re}\left(\tilde{d}_0^{(m)}\left[-\frac{\delta_2^{(m)}}{\left(\delta_0^{(m)}\right)^2}+\frac{\left(\delta_1^{(m)}\right)^2}{\left(\delta_0^{(m)}\right)^3}\right]-\frac{\tilde{d}_1^{(m)}\delta_1^{(m)}}{\left(\delta_0^{(m)}\right)^2}+\frac{\tilde{d}_2^{(m)}}{\delta_0^{(m)}}\right)+\ldots\right\}e^{P\sqrt{\frac{mRe}{2}}\sigma(1)}. \tag{3.5.19}$$

Finally, the expansions for A_m^o and B_m^o are easily found through equations (3.4.31) and (3.4.32), viz

$$A_m^o \sim \sum_{l=0}^{\infty}\tilde{a}_l^{(m)}Re^{-l/2} \quad \text{and} \quad B_m^o \sim \sum_{l=0}^{\infty}\tilde{b}_l^{(m)}Re^{-l/2}. \tag{3.5.20}$$

The coefficients $\tilde{a}_l^{(m)}$ and $\tilde{b}_l^{(m)}$ are determined by substituting the expansions for D_m^o, $I_m^{(2)}(1)$, $I_m^{(2)'}(1)$ into equations (3.4.31) and (3.4.32). For example, $\tilde{a}_0^{(m)}$, $\tilde{a}_1^{(m)}$, $\tilde{b}_0^{(m)}$ and $\tilde{b}_1^{(m)}$ are given by

$$\begin{aligned}
\tilde{a}_0^{(m)} &= \frac{\tilde{d}_0^{(m)}}{2m\delta_0^{(m)}}\left[mh_0^{(m)}(1)+h_0^{(m)^*}(1)\right]+\frac{E_m}{2}+(g_0-2A_o)\epsilon_m,\\
\tilde{a}_1^{(m)} &= \frac{\tilde{d}_0^{(m)}}{2m\delta_0^{(m)}}\left[mh_1^{(m)}(1)+h_1^{(m)^*}(1)\right]\\
&\quad+\frac{1}{2m}\left(\frac{\tilde{d}_1^{(m)}}{\delta_0^{(m)}}-\frac{\delta_1^{(m)}\tilde{d}_0^{(m)}}{\left(\delta_0^{(m)}\right)^2}\right)\left[mh_0^{(m)}(1)+h_0^{(m)^*}(1)\right],\\
\tilde{b}_0^{(m)} &= \frac{\tilde{d}_0^{(m)}}{2m\delta_0^{(m)}}\left[mh_0^{(m)}(1)-h_0^{(m)^*}(1)\right]+\frac{E_m}{2}+(A_o-g_0)\epsilon_m,\\
\text{and } \tilde{b}_1^{(m)} &= \frac{\tilde{d}_0^{(m)}}{2m\delta_0^{(m)}}\left[mh_1^{(m)}(1)-h_1^{(m)^*}(1)\right]\\
&\quad+\frac{1}{2m}\left(\frac{\tilde{d}_1^{(m)}}{\delta_0^{(m)}}-\frac{\delta_1^{(m)}\tilde{d}_0^{(m)}}{\left(\delta_0^{(m)}\right)^2}\right)\left[mh_0^{(m)}(1)-h_0^{(m)^*}(1)\right].
\end{aligned} \tag{3.5.21}$$

Thus, for any harmonic, asymptotic series expansions in powers of $1/\sqrt{Re}$ for A_m^o, B_m^o, C_m^o and D_m^o can be generated. These, together with the asymptotic

expansions for $I_m^{(1)}(\rho)$ and $I_m^{(2)}(\rho)$, will be used to generate the expansions uniform within the entire outer region for the first-order stream and vorticity functions. We are now able to generate asymptotic expansions for the first-order stream and vorticity functions for the flow within the outer region.

3.5.5 Asymptotic Expansions for $\psi_1(\rho, \phi; Re)$

From Section 3.4, $\psi_1(\rho, \phi; Re)$ can be decomposed into two distinct parts

$$\psi_1(\rho, \phi; Re) = \psi_{IR}(\rho, \phi; Re) - \psi_R(\rho, \phi; Re),$$

where

$$\begin{aligned} \psi_R(\rho, \phi; Re) &= \Re\left\{\sum_{m=1}^{\infty}\left(C_m^o I_m^{(1)}(\rho) + D_m^o I_m^{(2)}(\rho)\right)e^{im\phi}\right\} \\ &= \Re\left\{\sum_{m=1}^{\infty} C_m^o I_m^{(1)}(\rho)e^{im\phi}\right\} + \Re\left\{\sum_{m=1}^{\infty} D_m^o I_m^{(2)}(\rho)e^{im\phi}\right\} \\ &= \psi_{R_1}^{(m)}(\rho, \phi; Re) + \psi_{R_2}^{(m)}(\rho, \phi; Re) \end{aligned} \tag{3.5.22}$$

and

$$\psi_{IR}(\rho, \phi; Re) = A_o\rho^3\cos\phi + \Re\left\{\sum_{m=1}^{\infty}\left(A_m^o\rho^m + B_m^o\rho^{-m}\right)e^{im\phi}\right\}. \tag{3.5.23}$$

Clearly, $\psi_R(\rho, \phi; Re)$ represents the component of the first-order stream function influenced most by the vorticity function. Furthermore, from the expansions for C_m^o, D_m^o, $I_m^{(1)}(\rho)$ and $I_m^{(2)}(\rho)$ given in equations (3.5.18), (3.5.19), (3.5.6) and (3.5.7) we observe

$$\begin{aligned} C_m^o I_m^{(1)}(\rho) \sim \Bigg\{ & \frac{j_0^{(m)}(\rho)\tilde{c}_0^{(m)}}{\delta_0^{(m)}} \\ & + \frac{1}{\sqrt{Re}}\left(\frac{j_1^{(m)}(\rho)\tilde{c}_0^{(m)}}{\delta_0^{(m)}} + j_0^{(m)}(\rho)\left[\frac{\tilde{c}_1^{(m)}}{\delta_0^{(m)}} - \frac{\delta_1^{(m)}\tilde{c}_0^{(m)}}{\left(\delta_0^{(m)}\right)^2}\right]\right) + \ldots \Bigg\} e^{-P\sqrt{\frac{mRe}{2}}[\sigma(\beta)-\sigma(\rho)]} \end{aligned} \tag{3.5.24}$$

and

$$D_m^o I_m^{(2)}(\rho) \sim \left\{ \frac{h_0^{(m)}(\rho)\tilde{d}_0^{(m)}}{\delta_0^{(m)}} \right.$$

$$+\frac{1}{\sqrt{Re}}\left(\frac{h_1^{(m)}(\rho)\tilde{d}_0^{(m)}}{\delta_0^{(m)}}+h_0^{(m)}(\rho)\left[\frac{\tilde{d}_1^{(m)}}{\delta_0^{(m)}}-\frac{\delta_1^{(m)}\tilde{d}_0^{(m)}}{\left(\delta_0^{(m)}\right)^2}\right]\right)+\ldots\Bigg\}e^{-P\sqrt{\frac{mRe}{2}}[\sigma(\rho)-\sigma(1)]}. \tag{3.5.25}$$

Thus, while $\psi_{R_1}^{(m)}(\rho,\phi;Re)$ represents the term significant in a neighbourhood of distance $O(1/\sqrt{Re})$ from the boundary $\rho=\beta$ and decaying exponentially away, $\psi_{R_2}^{(m)}(\rho,\phi;Re)$ decays exponentially away from the boundary $\rho=1$. The expansion for $\psi_{IR}(\rho,\phi;Re)$ when Reynolds number is large is given by

$$\begin{aligned}\psi_{IR}(\rho,\phi;Re)\sim\\ &A_o\rho^3\cos\phi+\Re\left\{\sum_{m=1}^{\infty}\left(\tilde{a}_0^{(m)}\rho^m+\tilde{b}_0^{(m)}\rho^{-m}\right)e^{im\phi}\right\}\\ &+\Re\left\{\sum_{l,m=1}^{\infty}\left(\tilde{a}_l^{(m)}\rho^m+\tilde{b}_l^{(m)}\rho^{-m}\right)e^{im\phi}Re^{-l/2}\right\}.\end{aligned}$$

Therefore, using the expansions for $\psi_R(\rho,\phi;Re)$ and $\psi_{IR}(\rho,\phi;Re)$, the first-order stream function can be written as

$$\psi_1(\rho,\phi;Re)\sim\sum_{l=0}^{\infty}\psi_{1l}(\rho,\phi)Re^{-l/2} \tag{3.5.26}$$

where, for example, $\psi_{10}(\rho,\phi)$ and $\psi_{11}(\rho,\phi)$ are given by

$$\begin{aligned}\psi_{10}(\rho,\phi) &= A_o\rho^3\cos\phi+\Re\left\{\sum_{m=1}^{\infty}\left[\tilde{a}_0^{(m)}\rho^m+\tilde{b}_0^{(m)}\rho^{-m}\right.\right.\\ &\left.\left.-\frac{\tilde{c}_0^{(m)}j_0^{(m)}(\rho)}{\delta_0^{(m)}}e^{-P\sqrt{\frac{mRe}{2}}[\sigma(\beta)-\sigma(\rho)]}-\frac{\tilde{d}_0^{(m)}h_0^{(m)}(\rho)}{\delta_0^{(m)}}e^{-P\sqrt{\frac{mRe}{2}}[\sigma(\rho)-\sigma(1)]}\right]e^{im\phi}\right\}\end{aligned}$$

and

$$\begin{aligned}\psi_{11}(\rho,\phi) &= \Re\left\{\sum_{m=1}^{\infty}\left[\tilde{a}_1^{(m)}\rho^m+\tilde{b}_1^{(m)}\rho^{-m}\right.\right.\\ &-\left(\frac{\tilde{c}_0^{(m)}j_1^{(m)}(\rho)}{\delta_0^{(m)}}+\left[\frac{\tilde{c}_1^{(m)}}{\delta_0^{(m)}}-\frac{\delta_1^{(m)}\tilde{c}_0^{(m)}}{\left(\delta_0^{(m)}\right)^2}\right]j_0^{(m)}(\rho)\right)e^{-P\sqrt{\frac{mRe}{2}}[\sigma(\beta)-\sigma(\rho)]}\\ &\left.\left.-\left(\frac{\tilde{d}_0^{(m)}h_1^{(m)}(\rho)}{\delta_0^{(m)}}+h_0^{(m)}(\rho)\left[\frac{\tilde{d}_1^{(m)}}{\delta_0^{(m)}}-\frac{\tilde{d}_0^{(m)}\delta_1^{(m)}}{\left(\delta_0^{(m)}\right)^2}\right]\right)e^{-P\sqrt{\frac{mRe}{2}}[\sigma(\rho)-\sigma(1)]}\right]e^{im\phi}\right\}.\end{aligned} \tag{3.5.27}$$

We note that the first-order stream function defined in equation (3.4.4) is determined so that the boundary conditions on the bounding surfaces, given in (3.2.14), are satisfied. Hence, the asymptotic series expansions for $\psi_1(\rho, \phi; Re)$ generated can be used, in turn, to generate the behaviour of the stream function within the entire outer region. Wood [95] uses an asymptotic expansion to obtain the behaviour of the stream function within laminar boundary layers. The resultant expansions correspond to those generated using the boundary layer approximation formulated by Prandtl (see Chipman and Duck [24]). We now proceed to generate the asymptotic series expansion for $\zeta_1(\rho, \phi; Re)$.

3.5.6 Asymptotic Expansions for $\zeta_1(\rho, \phi; Re)$

Using the asymptotic expansions for the Bessel functions, $J_{\mu_m}(\lambda_m \rho)$ and $H^{(1)}_{\mu_m}(\lambda_m \rho)$ and those for the complex coefficients C^o_m and D^o_m given in Section 3.5.4, $\zeta_1(\rho, \phi; Re)$ given by

$$\begin{aligned} \zeta_1(\rho, \phi; Re) &= \Re\left\{ \sum_{m=1}^{\infty} \xi_m(\rho; Re) e^{im\phi} \right\} \\ &= \Re\left\{ \sum_{m=1}^{\infty} \left(C^o_m J_{\mu_m}(\lambda_m \rho) + D^o_m H^{(1)}_{\mu_m}(\lambda_m \rho) \right) e^{im\phi} \right\} \end{aligned}$$

has the asymptotic expansion

$$\zeta_1(\rho, \phi; Re) \sim \sum_{l=1}^{\infty} \zeta_{1l}(\rho, \phi) Re^{(2-l)/2}, \tag{3.5.28}$$

where $\zeta_{11}(\rho, \phi)$ and $\zeta_{12}(\rho, \phi)$, for example, are given by

$$\begin{aligned} \zeta_{11}(\rho, \phi) = \Re\Bigg\{ \sum_{m=1}^{\infty} T^{(m)}(\rho) \Bigg(& \frac{\tilde{c}^{(m)}_0}{\delta^{(m)}_0} e^{-P\sqrt{\frac{mRe}{2}}[\sigma(\beta)-\sigma(\rho)]} \\ & + \frac{\tilde{d}^{(m)}_0}{\delta^{(m)}_0} e^{-P\sqrt{\frac{mRe}{2}}[\sigma(\rho)-\sigma(1)]} \Bigg) e^{im\phi} \Bigg\} \end{aligned}$$

and

$$\zeta_{12}(\rho, \phi) = \Re\left\{ \sum_{m=1}^{\infty} T^{(m)}(\rho) \left(\left(\frac{\tilde{c}^{(m)}_0 \tau^{(m)}_1(\rho)}{\delta^{(m)}_0} + \frac{\tilde{c}^{(m)}_1}{\delta^{(m)}_0} - \frac{\delta^{(m)}_1 \tilde{c}^{(m)}_0}{\left(\delta^{(m)}_0\right)^2} \right) e^{-P\sqrt{\frac{mRe}{2}}[\sigma(\beta)-\sigma(\rho)]} \right.\right.$$

$$+\left(\frac{-\tilde{d}_0^{(m)}\tau_1^{(m)}(\rho)}{\delta_0^{(m)}}+\frac{\tilde{d}_1^{(m)}}{\delta_0^{(m)}}-\frac{\delta_1^{(m)}\tilde{d}_0^{(m)}}{\left(\delta_0^{(m)}\right)^2}\right)e^{-P\sqrt{\frac{mRe}{2}}[\sigma(\rho)-\sigma(1)]}\Bigg)\Bigg\}. \tag{3.5.29}$$

Where $T^{(m)}(\rho)=\dfrac{\sqrt{2m}P}{N^{1/4}(\rho)}$. Here, we observe that $\zeta_1(\rho,\phi;Re)$ comprises of terms that decay away from the boundary $\rho=\beta$ and terms that decay exponentially away from the boundary $\rho=1$. This is to be expected from the asymptotic expansions for the two Bessel functions. The exact nature of the vorticity within the outer region is known once the Fourier coefficients a_m and b_m are determined. We now use the results generated for the outer region to produce asymptotic expansions for the inner region.

3.6 Determining $\bar{\psi}_1(\rho,\phi)$ for Large Reynolds Number

The asymptotic methods used to determine $\psi_1(\rho,\phi)$ in the outer region can also be used to determine the stream function within the inner region. Consequently, we do not reproduce all of the intermediate expansions necessary to determine the first-order stream and vorticity functions.

Instead of solving equation (3.4.3) directly, the coupled equations given in (3.4.17) and (3.4.18) are solved for large Reynolds number. Asymptotic expansions for $J_{\mu_m}(\lambda_m\rho)$ and $H^{(1)}_{\mu_m}(\lambda_m\rho)$ defined within the inner region will possess the same form as the corresponding expansions for the outer region shown in Appendix A. The expansions now contain A_i and B_i instead of A_o and B_o. The choice of the expansions used are this time determined from the following bounds

$$\frac{1}{\rho}\left|\frac{B_i}{A_i}\right|^{1/2} > 1 \quad \text{when} \quad |g_0| < \frac{2\lambda|\bar{U}|}{1+\lambda^2}, \text{ for } \lambda \le \rho \le 1, \tag{3.6.1}$$

$$\text{and} \quad \frac{1}{\rho}\left|\frac{B_i}{A_i}\right|^{1/2} < 1 \quad \text{when} \quad |g_0| > \frac{|\bar{U}|(1+\lambda^2)}{2\lambda}, \text{ for } 1 \le \rho \le \beta. \tag{3.6.2}$$

From the analysis of the outer region, g_0 must take on positive values. Furthermore, bounds can be given for the various combinations of the signs of A_i and B_i, viz

$$A_i > 0, B_i > 0 \quad \text{when} \quad \lambda\bar{U} < g_0 < \frac{\bar{U}}{\lambda}, \tag{3.6.3}$$

$$A_i > 0, B_i < 0 \quad \text{when} \quad g_0 > \frac{\bar{U}}{\lambda}, \tag{3.6.4}$$

and

$$A_i < 0, B_i > 0 \quad \text{when} \quad g_0 < \lambda\bar{U}. \tag{3.6.5}$$

The bounds in (3.6.1) and (3.6.2) ensure that the unperturbed azimuthal velocity does not vanish within the inner region.

The asymptotic expansions for $I_m^{(1)}(\lambda_\mu\rho)$, $I_m^{(2)}(\lambda_\mu\rho)$ and their derivatives defined in equations (3.4.19), (3.4.20), (3.4.46) and (3.4.47) are easily given from those generated in Sections 3.5.2 and 3.5.3; thus, we have

$$I_m^{(1)}(\rho) \sim \mathcal{K}_1^{(m)}(Re)\left\{\sum_{l=0}^{\infty} j_l^{(m)}(\rho)Re^{-l/2}\right\} e^{P\sqrt{\frac{mRe}{2}}\sigma(\rho)}, \tag{3.6.6}$$

$$I_m^{(2)}(\rho) \sim \mathcal{K}_2^{(m)}(Re)\left\{\sum_{l=0}^{\infty} h_l^{(m)}(\rho)Re^{-l/2}\right\} e^{-P\sqrt{\frac{mRe}{2}}\sigma(\rho)}, \tag{3.6.7}$$

$$I_m^{(1)'}(\rho) \sim \mathcal{K}_1^{(m)}(Re)\left\{\sum_{l=0}^{\infty} j_l^{(m)^*}(\rho)Re^{-l/2}\right\} e^{P\sqrt{\frac{mRe}{2}}\sigma(\rho)}, \tag{3.6.8}$$

and

$$I_m^{(2)'}(\rho) \sim \mathcal{K}_2^{(m)}(Re)\left\{\sum_{l=0}^{\infty} h_l^{(m)^*}(\rho)Re^{-l/2}\right\} e^{-P\sqrt{\frac{mRe}{2}}\sigma(\rho)}, \tag{3.6.9}$$

where $j_l^{(m)}(\rho)$, $h_l^{(m)}(\rho)$, $j_l^{(m)^*}(\rho)$ and $h_l^{(m)^*}(\rho)$ given in equations (3.5.5), (3.5.8), (3.5.11) and (3.5.12) are still valid if 1 is replaced with λ and β is replaced with 1. The expansions given in (3.6.6)−(3.6.9) are used in conjunction with equations (3.4.40)−(3.4.45) to obtain asymptotic expansions for A_m^i, B_m^i, C_m^i and D_m^i. By comparing expressions for these complex constants with those for A_m^o, B_m^o, C_m^o and D_m^o, we see C_m^i and D_m^i will possess the same asymptotic form as C_m^o and D_m^o given in equations (3.5.18) and (3.5.19), noting the variation in the exponent that will exist; however, A_m^i and B_m^i cannot be determined from their counterpart in the outer region as A_m^i and B_m^i are dependent on C_m^i,

$I_m^{(1)}(1)$ and $I_m^{(1)'}(1)$ whereas A_m^o and B_m^o depend on D_m^o, $I_m^{(2)}(1)$ and $I_m^{(2)'}(1)$. Here $\tilde{a}_0^{(m)}$, $\tilde{a}_1^{(m)}$, $\tilde{b}_0^{(m)}$ and $\tilde{b}_1^{(m)}$, for example, are given by

$$\tilde{a}_0^{(m)} = \frac{\tilde{c}_0^{(m)}}{2m\delta_0^{(m)}}\left[mj_0^{(m)}(1) + j_0^{(m)^*}(1)\right] + \frac{E_m}{2} + (g_0 - 2A_i)\epsilon_m, \quad (3.6.10)$$

$$\tilde{a}_1^{(m)} = \frac{\tilde{c}_0^{(m)}}{2m\delta_0^{(m)}}\left[mj_1^{(m)}(1) + j_1^{(m)^*}(1)\right] + \frac{1}{2m}\left(\frac{\tilde{c}_1^{(m)}}{\delta_0^{(m)}} - \frac{\delta_1^{(m)}\tilde{c}_0^{(m)}}{\left(\delta_0^{(m)}\right)^2}\right)\left[mj_0^{(m)}(1) + j_0^{(m)^*}(1)\right], \quad (3.6.11)$$

$$\tilde{b}_0^{(m)} = \frac{\tilde{c}_0^{(m)}}{2m\delta_0^{(m)}}\left[mj_0^{(m)}(1) - j_0^{(m)^*}(1)\right] + \frac{E_m}{2} + (A_i - g_0)\epsilon_m, \quad (3.6.12)$$

$$\text{and } \tilde{b}_1^{(m)} = \frac{\tilde{c}_0^{(m)}}{2m\delta_0^{(m)}}\left[mj_1^{(m)}(1) - j_1^{(m)^*}(1)\right] + \frac{1}{2m}\left(\frac{\tilde{c}_1^{(m)}}{\delta_0^{(m)}} - \frac{\delta_1^{(m)}\tilde{c}_0^{(m)}}{\left(\delta_0^{(m)}\right)^2}\right)\left[mj_0^{(m)}(1) - j_0^{(m)^*}(1)\right], \quad (3.6.13)$$

for $m = 1, 2, \ldots$.

The asymptotic expansions for $\bar{\psi}_1(\rho, \phi)$ has a similar asymptotic form as $\psi_1(\rho, \phi)$, the only difference being that $\sigma(\beta) - \sigma(\rho)$ and $\sigma(\rho) - \sigma(1)$ are replaced with $\sigma(1) - \sigma(\rho)$ and $\sigma(\rho) - \sigma(\lambda)$ respectively. $\bar{\psi}_1(\rho, \phi; Re)$, is therefore given by

$$\bar{\psi}_1(\rho, \phi; Re) \sim \sum_{l=0}^{\infty} \psi_{1l}(\rho, \phi) Re^{-l/2} \quad (3.6.14)$$

where, for example, $\psi_{10}(\rho, \phi)$ and $\psi_{11}(\rho, \phi)$ are given by

$$\psi_{10}(\rho, \phi) = A_i\rho^3\cos\phi + \Re\left\{\sum_{m=1}^{\infty}\left[\tilde{a}_0^{(m)}\rho^m + \tilde{b}_0^{(m)}\rho^{-m} - \frac{\tilde{c}_0^{(m)}j_0^{(m)}(\rho)}{\delta_0^{(m)}}e^{-P\sqrt{\frac{mRe}{2}}[\sigma(1)-\sigma(\rho)]} - \frac{\tilde{d}_0^{(m)}h_0^{(m)}(\rho)}{\delta_0^{(m)}}e^{-P\sqrt{\frac{mRe}{2}}[\sigma(\rho)-\sigma(\lambda)]}\right]e^{im\phi}\right\}$$

and

$$\psi_{11}(\rho, \phi) = \Re\left\{\sum_{m=1}^{\infty}\left[\tilde{a}_1^{(m)}\rho^m + \tilde{b}_1^{(m)}\rho^{-m} - \left(\frac{\tilde{c}_0^{(m)}j_1^{(m)}(\rho)}{\delta_0^{(m)}} + \left[\frac{\tilde{c}_1^{(m)}}{\delta_0^{(m)}} - \frac{\delta_1^{(m)}\tilde{c}_0^{(m)}}{\left(\delta_0^{(m)}\right)^2}\right]j_0^{(m)}(\rho)\right)e^{-P\sqrt{\frac{mRe}{2}}[\sigma(1)-\sigma(\rho)]}\right.\right.$$

$$- \left(\frac{\tilde{d}_0^{(m)} h_1^{(m)}(\rho)}{\delta_0^{(m)}} + h_0^{(m)}(\rho) \left[\frac{\tilde{d}_1^{(m)}}{\delta_0^{(m)}} - \frac{\tilde{d}_0^{(m)} \delta_1^{(m)}}{\left(\delta_0^{(m)}\right)^2} \right] \right) e^{-P\sqrt{\frac{mRe}{2}}[\sigma(\rho)-\sigma(\lambda)]} \Bigg] e^{im\phi} \Bigg\}. \tag{3.6.15}$$

The stream function contains terms that decay away from $\rho = 1$ and $\rho = \lambda$.

Finally, the vorticity defined within the inner region is easily determined, viz

$$\begin{aligned} \bar{\zeta}_1(\rho, \phi; Re) &= \Re \left\{ \sum_{m=1}^{\infty} \tilde{\xi}_m(\rho; Re) e^{im\phi} \right\} \\ &= \Re \left\{ \sum_{m=1}^{\infty} \left(C_m^i J_{\mu_m}(\lambda_m \rho) + D_m^i H_{\mu_m}^{(1)}(\lambda_m \rho) \right) e^{im\phi} \right\}. \end{aligned}$$

This has the asymptotic expansion

$$\bar{\zeta}_1(\rho, \phi; Re) \sim \sum_{l=1}^{\infty} \zeta_{1l}(\rho, \phi) Re^{(2-l)/2}. \tag{3.6.16}$$

From equations (3.5.29) we have

$$\zeta_{11}(\rho, \phi) = \Re \left\{ \sum_{m=1}^{\infty} T^{(m)}(\rho) \left(\frac{\tilde{c}_0^{(m)}}{\delta_0^{(m)}} e^{-P\sqrt{\frac{mRe}{2}}[\sigma(1)-\sigma(\rho)]} + \frac{\tilde{d}_0^{(m)}}{\delta_0^{(m)}} e^{-P\sqrt{\frac{mRe}{2}}[\sigma(\rho)-\sigma(\lambda)]} \right) e^{im\phi} \right\}$$

and

$$\begin{aligned} \zeta_{12}(\rho, \phi) = \Re \Bigg\{ \sum_{m=1}^{\infty} T^{(m)}(\rho) \Bigg(\left(\frac{\tilde{c}_0^{(m)} \tau_1^{(m)}(\rho)}{\delta_0^{(m)}} + \frac{\tilde{c}_1^{(m)}}{\delta_0^{(m)}} - \frac{\delta_1^{(m)} \tilde{c}_0^{(m)}}{\left(\delta_0^{(m)}\right)^2} \right) e^{-P\sqrt{\frac{mRe}{2}}[\sigma(1)-\sigma(\rho)]} \\ + \left(-\frac{\tilde{d}_0^{(m)} \tau_1^{(m)}(\rho)}{\delta_0^{(m)}} + \frac{\tilde{d}_1^{(m)}}{\delta_0^{(m)}} - \frac{\delta_1^{(m)} \tilde{d}_0^{(m)}}{\left(\delta_0^{(m)}\right)^2} \right) e^{-P\sqrt{\frac{mRe}{2}}[\sigma(\rho)-\sigma(\lambda)]} \Bigg) \Bigg\}. \end{aligned} \tag{3.6.17}$$

From the expansions for the first-order vorticity function generated in each region, we see that this vorticity function is discontinuous across the membrane (i.e., $\rho = 1$).

3.7 Using Darcy's Law to get $f(\phi;\gamma)$

As the pressure difference across the membrane governs the flow through, the radial velocity along the membrane will be estimated from Darcy's law. For the laminar flow of an isotropic fluid through a porous medium this is given by (see Scheidegger [79, page 74])

$$f(\phi;\gamma) = -\kappa\left(\Pi(\phi;\gamma) - P(\phi;\gamma)\right)$$

where κ is given by the ratio of the permeability of the membrane and the dynamic viscosity of the fluid. Using the perturbation schemes given in equations (3.1.2) and (3.1.7), the radial velocity of $O(\gamma^n)$ is given by

$$f_n(\phi) = -\kappa\left(\Pi_n(\phi) - P_n(\phi)\right), \quad n = 1, 2, \ldots.$$

To determine $f_1(\phi)$, we use equation (3.4.1) and solve the system of equations

$$\sum_{m=1}^{\infty} a_m \cos m\phi + b_m \sin m\phi = -\kappa\left(\Pi_1(\phi) - P_1(\phi)\right). \tag{3.7.1}$$

Once the pressure distributions in each region are known, (3.7.1) generates a system of linear equations, from which the $2m$ Fourier coefficients are determined. We now endeavour to determine the pressure field within each region.

3.8 The Pressure Distributions

We begin by stating the momentum equations for the $\rho\phi$-plane obtained by applying the transformation given in equation (2.2.6) to equation (2.2.20)

$$\sqrt{J}v_\rho\frac{\partial v_\rho}{\partial\rho} + \frac{\sqrt{J}}{\rho}v_\phi\frac{\partial v_\rho}{\partial\phi} + \frac{Jv_\phi}{\rho}\left(v_\rho\frac{\partial}{\partial\phi}\left(\frac{1}{\sqrt{J}}\right) - v_\phi\frac{\partial}{\partial\rho}\left(\frac{\rho}{\sqrt{J}}\right)\right) = -\sqrt{J}\frac{\partial p}{\partial\rho} - \frac{\sqrt{J}}{Re\rho}\frac{\partial}{\partial\phi}\left(\frac{J}{\rho}\left(\frac{\partial}{\partial\rho}\left(\frac{\rho v_\phi}{\sqrt{J}}\right) - \frac{\partial}{\partial\phi}\left(\frac{v_\rho}{\sqrt{J}}\right)\right)\right),$$

and

$$\sqrt{J}v_\rho\frac{\partial v_\phi}{\partial\rho} + \frac{\sqrt{J}}{\rho}v_\phi\frac{\partial v_\phi}{\partial\phi} + \frac{Jv_\rho}{\rho}\left(v_\phi\frac{\partial}{\partial\rho}\left(\frac{\rho}{\sqrt{J}}\right) - v_\rho\frac{\partial}{\partial\phi}\left(\frac{1}{\sqrt{J}}\right)\right) = \tag{3.8.1}$$

$$-\frac{\sqrt{J}}{\rho}\frac{\partial p}{\partial \phi}+\frac{\sqrt{J}}{Re}\frac{\partial}{\partial \rho}\left(\frac{J}{\rho}\left(\frac{\partial}{\partial \rho}\left(\frac{\rho v_\phi}{\sqrt{J}}\right)-\frac{\partial}{\partial \phi}\left(\frac{v_\rho}{\sqrt{J}}\right)\right)\right), \tag{3.8.2}$$

then using equations (2.2.10) and (2.2.11), the momentum equations can be written in the form

$$J\frac{\partial p}{\partial \rho} = -\frac{J}{Re\rho}\frac{\partial \zeta}{\partial \phi}-Jv_\rho\frac{\partial v_\rho}{\partial \rho}-\frac{Jv_\phi}{\rho}\frac{\partial v_\rho}{\partial \phi}+\frac{v_\phi}{\rho}\left(Jv_\phi-\frac{\rho v_\phi}{2}\frac{\partial J}{\partial \rho}+\frac{v_\rho}{2}\frac{\partial J}{\partial \phi}\right) \tag{3.8.3}$$

and

$$J\frac{\partial p}{\partial \phi} = \frac{J\rho}{Re}\frac{\partial \zeta}{\partial \rho}-J\rho v_\rho\frac{\partial v_\phi}{\partial \rho}-Jv_\phi\frac{\partial v_\phi}{\partial \phi}-v_\rho\left(Jv_\phi-\frac{\rho v_\phi}{2}\frac{\partial J}{\partial \rho}+\frac{v_\rho}{2}\frac{\partial J}{\partial \phi}\right). \tag{3.8.4}$$

Perturbing equations (3.8.3) and (3.8.4) determine the pressure terms for various orders of γ. The pressure field up to $O(\gamma)$ will now be determined in the outer region.

3.8.1 $\Pi_0(\rho)$ and $\Pi_1(\rho,\phi)$

In the outer region, the pressure is denoted by $\Pi(\rho,\phi;\gamma)$. This can be determined by applying the perturbation scheme in equation (3.1.7) to the modified momentum equations given in (3.8.3) and (3.8.4). Thus, replacing the pressure term in (3.8.3) and (3.8.4) with $\Pi(\rho,\phi)$ and perturbing yields

$$\frac{d\Pi_0}{d\rho}=\frac{\left(v_\phi^{(0)}\right)^2}{\rho}, \quad \text{and} \quad \frac{d\Pi_0}{d\phi}=0, \tag{3.8.5}$$

and

$$\frac{\partial \Pi_1}{\partial \rho}+4\rho\cos\phi\frac{\partial \Pi_0}{\partial \rho} = -\frac{1}{Re\rho}\frac{\partial \zeta_1}{\partial \phi}-\frac{v_\phi^{(0)}}{\rho}\frac{\partial v_\rho^{(1)}}{\partial \phi}+\frac{2v_\phi^{(1)}v_\phi^{(0)}}{\rho}+2\left(v_\phi^{(0)}\right)^2\cos\phi, \tag{3.8.6}$$

$$\frac{\partial \Pi_1}{\partial \phi} = \frac{\rho}{Re}\frac{\partial \zeta_1}{\partial \rho}-\rho v_\rho^{(1)}\frac{\partial v_\phi^{(0)}}{\partial \rho}-v_\phi^{(0)}\frac{\partial v_\phi^{(1)}}{\partial \phi}-v_\rho^{(1)}v_\phi^{(0)}, \tag{3.8.7}$$

$$\frac{\partial \Pi_2}{\partial \rho} + 4\rho\cos\phi\frac{\partial \Pi_1}{\partial \rho} + \left(2\rho^2\cos 2\phi + 4\rho^2\right)\frac{\partial \Pi_0}{\partial \rho} =$$
$$-\frac{1}{Re\rho}\frac{\partial \zeta_2}{\partial \phi} - \frac{4\cos\phi}{Re}\frac{\partial \zeta_1}{\partial \phi} - v_\rho^{(1)}\frac{\partial v_\rho^{(1)}}{\partial \rho} - 4\cos\phi v_\phi^{(0)}\frac{\partial v_\rho^{(1)}}{\partial \phi}$$
$$-\frac{v_\phi^{(1)}}{\rho}\frac{\partial v_\rho^{(1)}}{\partial \phi} - \frac{v_\phi^{(0)}}{\rho}\frac{\partial v_\rho^{(2)}}{\partial \phi} + \frac{2v_\phi^{(2)}v_\phi^{(0)}}{\rho} + 4\cos\phi v_\phi^{(1)}v_\phi^{(0)}$$
$$+\frac{\left(v_\phi^{(1)}\right)^2}{\rho} - 2\sin\phi v_\rho^{(1)}v_\phi^{(0)}, \tag{3.8.8}$$

and

$$\frac{\partial \Pi_2}{\partial \phi} + 4\rho\cos\phi\frac{\partial \Pi_1}{\partial \phi} =$$
$$\frac{\rho}{Re}\frac{\partial \zeta_2}{\partial \rho} + \frac{4\rho^2\cos\phi}{Re}\frac{\partial \zeta_1}{\partial \rho} - \rho v_\rho^{(1)}\frac{\partial v_\phi^{(1)}}{\partial \rho} - 4\rho^2\cos\phi v_\rho^{(1)}\frac{\partial v_\phi^{(0)}}{\partial \rho}$$
$$-\rho v_\rho^{(2)}\frac{\partial v_\phi^{(0)}}{\partial \rho} - 4\rho\cos\phi v_\phi^{(0)}\frac{\partial v_\phi^{(1)}}{\partial \phi} - v_\phi^{(1)}\frac{\partial v_\phi^{(1)}}{\partial \phi} - v_\phi^{(0)}\frac{\partial v_\phi^{(2)}}{\partial \phi}$$
$$-2\cos\phi v_\rho^{(1)} - v_\rho^{(1)}v_\phi^{(1)} - v_\rho^{(2)}v_\phi^{(0)}. \tag{3.8.9}$$

Equation (2.2.11) is used to determine the velocity components of various orders, viz

$$\left.\begin{aligned}
v_\phi^{(0)} &= -\frac{\partial \psi_0}{\partial \rho} \\
&= A_o\rho + B_o/\rho, \\
v_\phi^{(1)} &= -\frac{\partial \psi_1}{\partial \rho} - 2\rho\cos\phi\frac{\partial \psi_0}{\partial \rho} \\
&= 2\rho\cos\phi(A_o\rho + B_o/\rho) - \frac{\partial \psi_1}{\partial \rho}, \\
v_\phi^{(2)} &= -\frac{\partial \psi_2}{\partial \rho} - 2\rho\cos\phi\frac{\partial \psi_1}{\partial \rho} + \left(1+\rho^2\right)(A_o\rho + B_o/\rho),
\end{aligned}\right\} \tag{3.8.10}$$

and so on. Also, we have

$$\left.\begin{aligned} v_\rho^{(0)} &= 0, \\ v_\rho^{(1)} &= \frac{1}{\rho}\frac{\partial \psi_1}{\partial \phi}, \\ v_\rho^{(2)} &= \frac{1}{\rho}\frac{\partial \psi_2}{\partial \phi} + 2\cos\phi \frac{\partial \psi_1}{\partial \phi}, \end{aligned}\right\} \tag{3.8.11}$$

and so on. As we are confining our attention to the first-order solutions, we need only determine the pressure up to $O(\gamma)$. The zeroth-order equation for pressure simply states that in Couette flow between two rotating cylinders the centrifugal acceleration is balanced by the radial pressure gradient. This pressure is easily determined via equation (3.8.11)

$$\Pi_0(\rho) = \frac{(A_o\rho)^2}{2} + 2A_oB_o\ln\rho - \frac{B_o^2}{4\rho^4} + \text{const}, \tag{3.8.12}$$

the leading order results, together with equation (3.8.10), reduce the second equation in (3.8.7) to

$$\frac{\partial \Pi_1}{\partial \phi} = \frac{\rho}{Re}\frac{\partial \zeta_1}{\partial \rho} - 2A_o\frac{\partial \psi_1}{\partial \phi} - (A_o\rho + B_o/\rho)\frac{\partial v_\phi^{(1)}}{\partial \phi}.$$

Upon integrating and noting from equation (3.4.5) that

$$\int^\phi \frac{\partial \zeta_1}{\partial \rho} ds = -\Re\left\{\sum_{m=1}^{\infty} \frac{i\xi_m'(\rho; Re)}{m} e^{im\phi}\right\},$$

$\Pi_1(\rho, \phi; Re)$ is given by

$$\begin{aligned} \Pi_1(\rho, \phi; Re) = -\frac{\rho}{Re}\Re\left\{\sum_{m=1}^{\infty} \frac{i\xi_m'(\rho; Re)}{m} e^{im\phi}\right\} \\ -2A_o\psi_1(\rho, \phi) - (A_o\rho + B_o/\rho)v_\phi^{(1)}(\rho, \phi) + s(\rho), \end{aligned} \tag{3.8.13}$$

where $s(\rho)$ is an arbitrary function of ρ. At $\rho = 1$ we see from equations (3.4.4) and (3.4.15) that

$$\psi_1(\rho, \phi) = A_o\cos\phi + \Re\left(\sum_{m=1}^{\infty} \chi_m(1)e^{im\phi}\right)$$

$$= \Re\left\{\sum_{m=1}^{\infty} E_m e^{im\phi}\right\}$$
$$= -\sum_{m=1}^{\infty} \frac{b_m \cos m\phi - a_m \sin m\phi}{m},$$

and $v_\phi^{(m)}(1,\phi) = 0$, $m = 1, 2, \ldots$. Thus $\Pi_1(1,\phi;Re)$ is given by

$$\Pi_1(1,\phi;Re) = -\frac{1}{Re}\Re\left\{\sum_{m=1}^{\infty} \frac{i\xi_m'(1;Re)}{m} e^{im\phi}\right\} + 2A_o \sum_{m=1}^{\infty} \frac{b_m \cos m\phi - a_m \sin m\phi}{m} + \text{const} \tag{3.8.14}$$

where $\xi_m'(1;Re)$ also contains the coefficients a_m and b_m. The pressure distribution given above is the same as that given by Hird and Siew [42] for the no-slip case. This is apparent as the contribution made by the slip velocity is only present in the zeroth-order pressure. It is now a trivial exercise to produce the pressure field within the inner region.

3.8.2 $P_0(\rho)$ and $P_1(\rho,\phi)$

Perturbing equations (3.8.3) and (3.8.4) to generate the inner pressure terms yields the same form as given in equations (3.8.12) and (3.8.13) with only minor differences in the terms used, thus

$$P_0(\rho) = \frac{(A_i\rho)^2}{2} + 2A_iB_i \ln\rho - \frac{B_i^2}{4\rho^4} + \text{const} \tag{3.8.15}$$

and

$$P_1(\rho,\phi;Re) = -\frac{\rho}{Re}\Re\left\{\sum_{m=1}^{\infty} \frac{i\tilde{\xi}_m'(\rho;Re)}{m} e^{im\phi}\right\} - 2A_i\bar{\psi}_1(\rho,\phi) - (A_i\rho + B_i/\rho)v_\phi^{(1)}(\rho,\phi) + s(\rho), \tag{3.8.16}$$

where

$$P_1(1,\phi;Re) = -\frac{1}{Re}\Re\left\{\sum_{m=1}^{\infty} \frac{i\tilde{\xi}_m'(1;Re)}{m} e^{im\phi}\right\}$$

$$+2A_i \sum_{m=1}^{\infty} \frac{b_m \cos m\phi - a_m \sin m\phi}{m} + \text{const.} \tag{3.8.17}$$

Equations (3.8.14) and (3.8.17) are now inserted into equation (3.7.1) to produce a system of $2m$ equations. The solution to this system determines the coefficients a_m and b_m and therefore the flow field in both regions is completely determined.

Chapter 4

Results for Model One

We now use a number of examples to determine the parameters that influence the flow through the membrane.

4.1 Bounds for the Geometric and Perturbative Parameters

The dimensions of the apparatus described by Overend et al [68] are given by

$$c = 0.019\text{m}, \quad a = 0.024\text{m}, \quad \text{and} \quad b = 0.094\text{m}.$$

For varying eccentricity ratios, $\bar{\epsilon}$, the corresponding values for γ are given in Table 4.1. Within the flow field the stream function has been determined

$\bar{\epsilon}$	$\lvert\gamma\rvert$	$\lvert 1/\gamma\rvert$	$1/\gamma^2$
0.10	0.02054	48.7	2372.0
0.20	0.04188	23.9	571.0
0.30	0.06494	15.4	237.0
0.40	0.09092	11.0	121.0
0.50	0.12153	8.2	64.0

Table 4.1: Values of γ for various $\bar{\epsilon}$.

asymptotically, i.e.,

$$\psi(\rho,\phi;Re;\gamma) \sim \psi_0(\rho) + \gamma\left(\psi_{10}(\rho,\phi) + \frac{\psi_{11}(\rho,\phi)}{\sqrt{Re}} + \frac{\psi_{12}(\rho,\phi)}{Re} + \ldots\right) + \ldots$$

where the form of these terms vary across the membrane. If γ is assumed small enough so that the stream function possesses an error of $O(\gamma^2)$ then we need only retain terms up to $O(\gamma/\sqrt{Re})$ as it is unlikely that γ/Re will be $O(\gamma^2)$. Thus, for small γ, the stream function within each region is given by

$$\psi(\rho,\phi;Re;\gamma) \sim \psi_0(\rho) + \gamma\left(\psi_{10}(\rho,\phi) + \frac{\psi_{11}(\rho,\phi)}{\sqrt{Re}}\right) + O(\gamma^2) \tag{4.1.1}$$

and since $\zeta = -J(\rho,\phi)\nabla^2\psi$, the vorticity in each region is approximated using

$$\zeta(\rho,\phi;Re;\gamma) \sim \zeta_0 + \gamma\sqrt{Re}\zeta_{11}(\rho,\phi) + O(\gamma^2). \tag{4.1.2}$$

These expansions hold when

$$\frac{1}{|\gamma|} < Re < \frac{1}{\gamma^2}. \tag{4.1.3}$$

To ensure γ remains small, we would only consider flows where the eccentricity ratio is not more than 0.2. However, qualitative results are produced here using the approximation in (4.1.1) when the value of γ is beyond the range where (4.1.1) is likely to hold and agree with the physics of the problem. The third and fourth columns in Table 4.1 give the lower and upper bounds for Re, as defined in (4.1.3), for a given eccentricity ratio. From rheograms of Newtonian and non-Newtonian fluids supplied by the Curtin University Slurry Research Group we may say that $50 \leq Re \leq 1000$ represents a typical range for the Reynolds number. The types of fluids that yield a Reynolds number within this range include silicon-based slurries, aqueous solutions of glycerol (of at most 50% by weight), aqueous solutions of sucrose (of at most 50% by weight) and oils such as olive, linseed and light machine oil.

Before determining the flow field, the slip velocity must be determined. Our analysis shows that the slip velocity, g_0 must be positive and once known

$\bar{\epsilon}$	$\bar{U}$	$\frac{2\beta}{\beta^2+1}$	$\frac{\beta^2+1}{2\beta}$	$\frac{2\lambda\bar{U}}{1+\lambda^2}$	$\frac{\bar{U}(1+\lambda^2)}{2\lambda}$
0.10	2.0	0.4833	2.0690	1.9465	2.0558
0.10	5.0	0.4833	2.0690	4.8642	5.1395
0.20	1.0	0.4911	2.0361	0.9728	1.0279
0.20	5.0	0.4911	2.0361	4.8642	5.1396
0.30	2.0	0.5048	1.9811	1.9465	2.0558
0.40	2.0	0.5247	1.9057	1.9465	2.0558
0.40	5.0	0.5247	1.9057	4.8642	5.1395

Table 4.2: A few bounds used for the expansions.

the sign and magnitude of A_o, B_o, A_i and B_i are determined. Thus the size of g_0 determines the correct asymptotic expansion for the Bessel functions, $I_m^{(1)}(\rho)$, $I_m^{(2)}(\rho)$ and their derivatives and ultimately the asymptotic form for $\psi_1(\rho,\phi)$ within each region. Table 4.2 quantifies the bounds used to select the appropriate expansions for various values of $\bar{\epsilon}$ and $\bar{U}$. From Table 4.2 and using equations (A.0.25)−(A.0.29) and (3.6.1)−(3.6.5), we choose

$$g_0 = 0.4;$$

thus, expansions corresponding to

$$\frac{1}{\rho}\left|\frac{B_i}{A_i}\right|^{1/2} > 1, \quad \text{and} \quad A_i < 0, B_i > 0$$

$$\text{and} \quad \frac{1}{\rho}\left|\frac{B_o}{A_o}\right|^{1/2} < 1, \quad \text{and} \quad A_o > 0, B_o > 0$$

are used to determine the flow field within the inner and outer regions. This value for the slip velocity allows the eccentricity ratio to vary up to 0.5 and thus Table 4.1 gives the desired range for Reynolds number, namely $50 \leq Re \leq 1000$. Furthermore, we will also consider the relative rotational speed of the inner cylinder to vary in the range $1.0 - 5.0$ as this represents the range used

in the modified viscometer. In the following problems, we use the first two harmonics to model the radial velocity $f_1(\phi)$. Consequently, to determine the Fourier coefficients a_1, a_2, b_1 and b_2 through use of Darcy's law, a 4×4 system of equations generated in equation (3.7.1) must be solved. We now consider a few examples.

4.2 A Number of Problems

To define a given problem, we use the parameter set $\{Re, \bar{\epsilon}, \bar{U}, \kappa\}$. The approximations used for the stream and vorticity functions given in equations (4.1.1) and (4.1.2) are valid for small γ ($\bar{\epsilon}$). For small eccentricity flows, no eddies are observed within the flow field; therefore, no contour plots are given as they add little to the understanding of the flow field developed using our analytic model. However, by graphing the radial velocity $f_1(\phi)$, the effect induced by a change in eccentricity, Reynolds number, rotational speed and permeability can be observed. To this end, we consider the flow fields produced from the following problems

1. $\{1000, 0.1, 2.0, 0.8\}$,
2. $\{500, 0.1, 2.0, 0.8\}$,
3. $\{500, 0.2, 2.0, 0.8\}$,
4. $\{100, 0.2, 2.0, 0.8\}$,
5. $\{200, 0.3, 2.0, 0.8\}$,
6. $\{200, 0.3, 2.0, 0.2\}$,
7. $\{50, 0.4, 2.0, 0.8\}$, and
8. $\{50, 0.4, 5.0, 0.8\}$.

These problems produce radial velocity profiles v_1–v_8, respectively. The Fourier coefficients obtained for these cases are given in Table 4.3 and show that to the

degree of accuracy given in Table 4.3 the radial velocity through the membrane is captured in the first-order harmonic only. Although the values of eccentricity ratio used to get v_7 and v_8 are beyond the range where equations (4.1.1) and (4.1.2) are expected to give reliable results, we will see that the results produced give qualitative agreement with the physics of the problem.

$\bar{\epsilon}$	Re	$\bar{U}$	κ	a_1	b_1	a_2	b_2
0.10	1000.0	2.0	0.8	0.0475610	0.3318436	0.0	0.0
0.10	500.0	2.0	0.8	0.0492467	0.3407413	0.0	0.0
0.20	500.0	2.0	0.8	0.0481617	0.3343417	0.0	0.0
0.20	100.0	2.0	0.8	0.1005177	0.3385143	0.0	0.0
0.30	200.0	2.0	0.8	0.0728399	0.3282503	0.0	0.0
0.30	200.0	2.0	0.2	0.1548334	0.2414975	0.0	0.0
0.40	50.0	2.0	0.8	0.1061699	0.3150471	0.0	0.0
0.40	50.0	5.0	0.8	0.0203755	0.1222531	0.0	0.0

Table 4.3: Fourier coefficients a_1, b_1, a_2 and b_2.

The flow through the membrane is expected to be influenced by the position of the membrane and inner cylinder within the flow domain. Fig. 4.1 gives the velocity profiles v_2 and v_3. Clearly, both the speed and flow through the membrane increase with increasing eccentricity. The Reynolds number also influences both the regions of entry (negative velocity) and exit (positive velocity) into the annulus and the speed of the fluid through the membrane. Fig. 4.2 uses velocity profiles v_3 and v_4 to show that when the Reynolds number decreases from 500 to 100, the speed of the fluid passing through the membrane increases and there is also a slight phase shift in the regions of entry and exit. The increase in flux across the membrane is unexpected, we suspect that the terms possessing negative (real) exponents appearing in the expansions for the integrals given in Section 3.5.2 and 3.5.3 are responsible for this since their magnitudes increase as the Reynolds number decreases. The relative rotational

speed of the inner cylinder affects the flux through the membrane. This is seen from Fig. 4.3 using velocity profiles v_7 and v_8. As the rotational speed $\bar{U}$ increases both the speed and amount of fluid flowing through the membrane are retarded. Although the results given by Hird and Siew [42] also show the retardation of flow through the membrane as the rotor speed is increased, as a no-slip condition was imposed along the membrane, this effect could not be demonstrated by the velocity profiles. Note that even though the eccentricity used in problems 7 and 8 is large the results obtained are qualitatively correct since, physically, increasing the centrifugal acceleration of the fluid within the annulus will retard the amount of fluid entering the annulus.

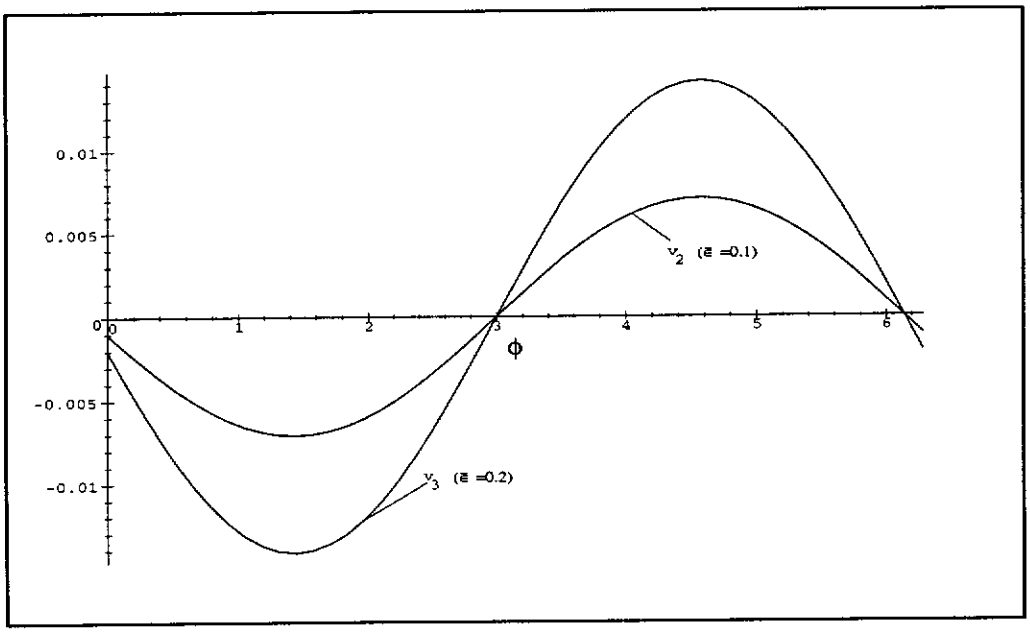

Figure 4.1: Velocity profiles v_2 and v_3:effect of eccentricity.

To study the effects of varying the permeability of the membrane, consider Fig. 4.4; this gives the velocity profiles v_5 and v_6. As the permeability of the membrane decreases, both the speed and the amount of fluid flowing through the membrane also decrease.

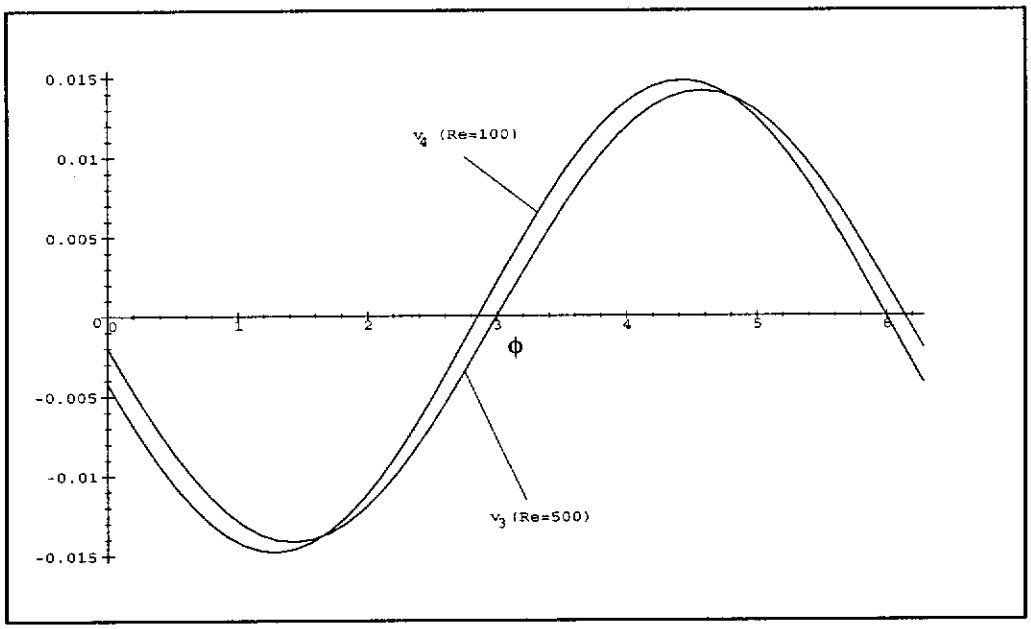

Figure 4.2: Velocity profiles v_3 and v_4:effect of Reynolds number.

4.3 Summary

For the problems considered here, the eccentricity and relative rotational speed of the rotor have the greatest influence on both the speed and the amount of fluid flowing through the membrane. The use of a permeable membrane to model the two-dimensional flow around a slotted sleeve allows an analytical treatment of the model; however, we are restricted to small eccentricity. To extend our range of eccentricity and improve our analytic model we could solve the equations of $O(\gamma^2)$ given in (3.2.17)−(3.2.20). The analytical treatment becomes increasingly more difficult with little gain. The eccentricity will still be small and we are still using a membrane to model the slotted sleeve. In short, to gain a deeper understanding of the role that the slotted sleeve plays in the flow field, we must look at large-eccentricity problems and use a slotted boundary; thus, the flow field must be modelled numerically.

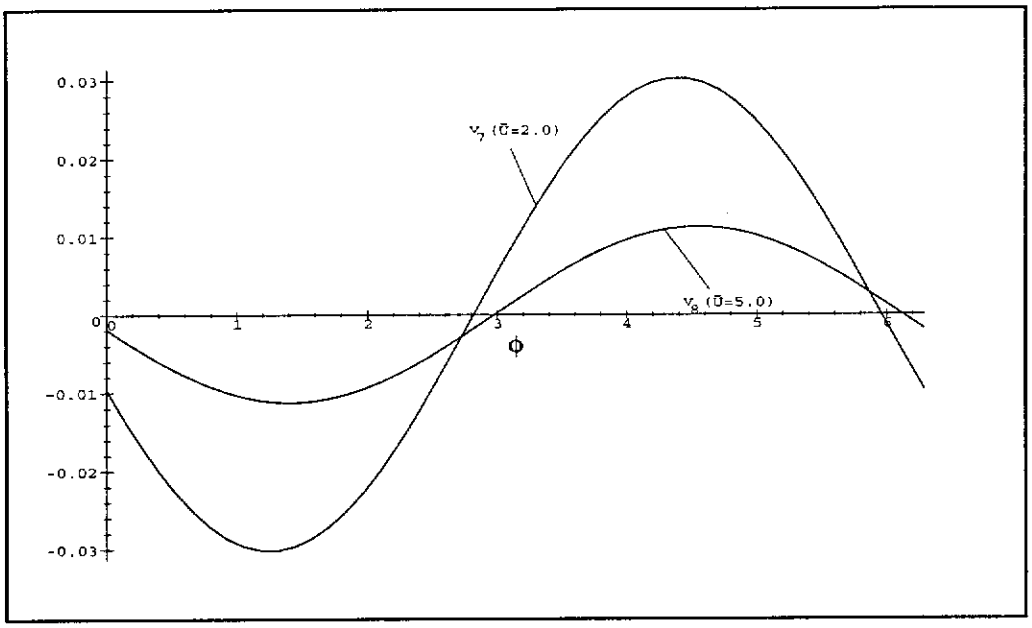

Figure 4.3: Velocity profiles v_7 and v_8:effect of rotational speed.

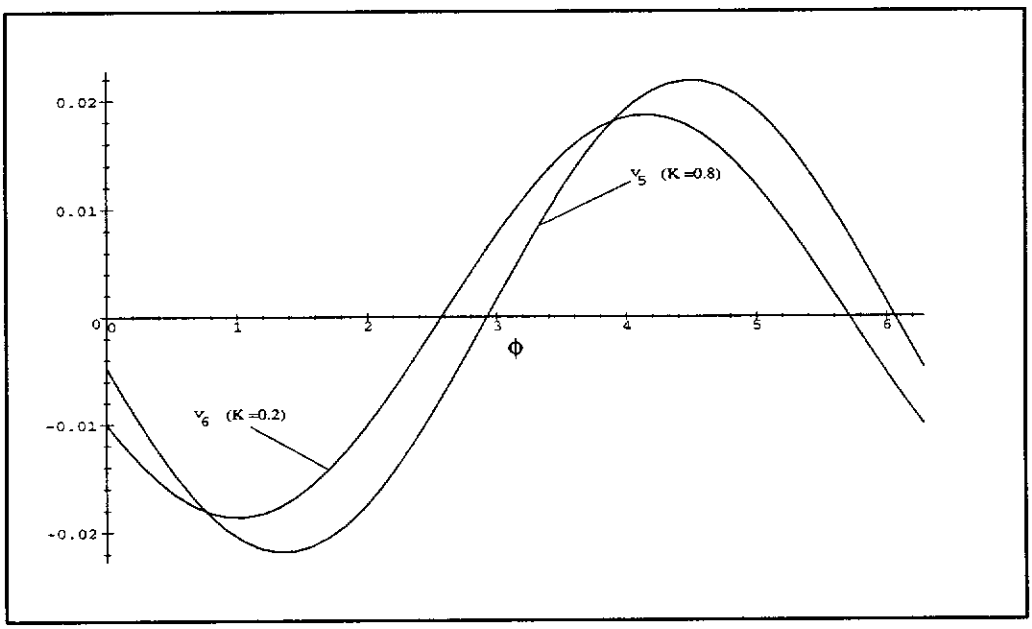

Figure 4.4: Velocity profiles v_5 and v_6:effect of permeability.

Chapter 5

Model Two: A Finite Volume Method for Newtonian Fluids

Here we replace the slurry by a Newtonian fluid and apply the exponentially fitted finite volume method given by Miller and Wang [60] to determine the flow field for moderate to high Reynolds number. This model is designed to estimate the flow patterns of silicon-based slurries and fluids such as olive oil, and some aqueous solutions of glycerol and sucrose. The numerical approach allows a wider class of problems to be considered than the analytic approach used in the first model. Unstructured meshes based on the Delaunay triangles and Voronoi tessellations are used to decompose the flow field. We note, however, that the slotted sleeve introduces additional complications due to the corner singularities present (see Moffatt [63] and Crochet et al [28]). These singularities are treated by using a slotted sleeve of zero thickness together with local refinement around the slotted sleeve. To determine the steady-state flow field (if one exists), the transient problem is solved by introducing boundary conditions for the vorticity along the solid boundaries and solving the governing equations in succession. The long-term solution represents the steady-state solution.

5.1 Discretisation and Assembly

As a complete discussion of the following finite volume method can be found in [60] we give only a brief account of it here. To discretise the governing equations given in (2.3.1), we introduce the Delaunay triangulation, T_h, with mesh parameter h, and its dual the Voronoi (Dirichlet) tessellation, D_h, of the domain Ω (see Fig. 5.1). Each vertex, $\boldsymbol{x}_i$, of T_h is associated with a convex set, d_i, whose boundary, ∂d_i, is a Voronoi polygon with vertices being the circum-centres of all triangles with common vertex $\boldsymbol{x}_i$. We use N_v and N_e to denote the numbers of nodes and edges in T_h not on $\partial\Omega_1$, $\partial\Omega_2$ or $\partial\Omega_3$. The convex set, d_i, represents the locus of points closer to node $\boldsymbol{x}_i$ than any other node and the Delaunay triangulation of Ω can be constructed from the Voronoi tessellations by generating the largest empty circle centred at each of the vertices of the Voronoi polygons (see Okabe et al [67]). McNeal [55] appears to be the first worker to apply Delaunay triangulations and Voronoi tessellations to conservation equations. The governing equations given in (2.3.1) satisfies both the conservation of mass and the conservation linear momentum of the fluid. The finite volume method applies these equations to each control volume and consequently the equations of conservation are, approximately, maintained by the method. In two-dimensions, each control volume has cross-sectional area $|d_i|$ and unit height. Integrating (2.3.1) over each tessellation (i.e., d_i) yields

$$\int_{d_i} \frac{\partial \zeta}{\partial t} - \nabla \cdot \left(\frac{1}{Re} \nabla \zeta - \zeta \mathbf{v} \right) dA = 0,$$

and

$$\int_{d_i} \nabla^2 \psi + \zeta dA = 0.$$

Applying Green's formula, we obtain

$$\frac{\partial \zeta_i}{\partial t} |d_i| - \int_{\partial d_i} \left(\frac{1}{Re} \nabla \zeta - \zeta \mathbf{v} \right) \cdot \mathbf{n} ds = 0, \tag{5.1.1}$$

and

$$\int_{\partial d_i} \nabla \psi \cdot \mathbf{n} ds + \zeta_i |d_i| = 0, \tag{5.1.2}$$

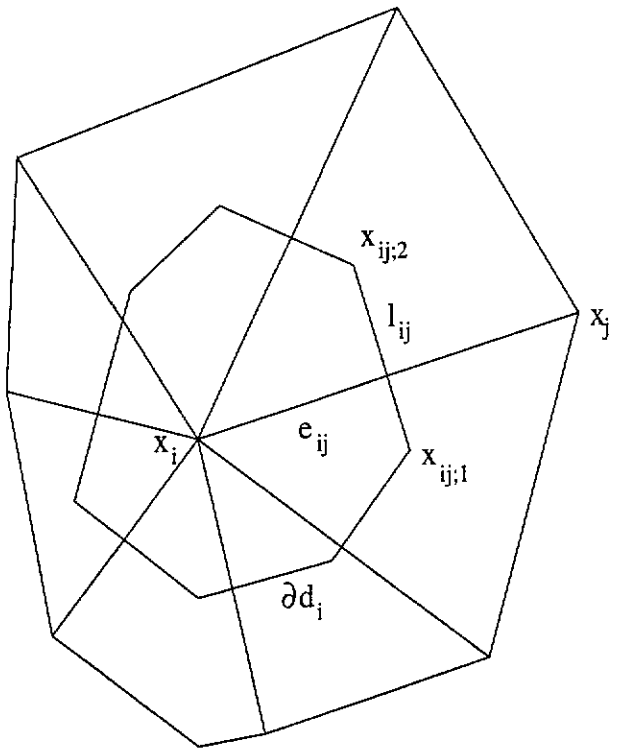

Figure 5.1: The Voronoi tessellation and Delaunay triangulation around a mesh node.

where ζ is assumed piecewise constant over each tessellation and $\zeta_i = \zeta(\boldsymbol{x}_i, t)$. If I_i represents the index set of neighbouring nodes to the interior node $\boldsymbol{x}_i$ then (5.1.1) can be written as

$$\frac{\partial \zeta_i}{\partial t}|d_i| - \sum_{j \epsilon I_i} \int_{l_{ij}} \left(\frac{1}{Re} \frac{d\zeta}{d\mathrm{e}_{ij}} - \zeta \mathbf{v} \cdot \mathrm{e}_{ij} \right) ds = 0, \quad i = 1, \ldots, N_v, \tag{5.1.3}$$

where l_{ij} denotes the edge of ∂d_i (with length $|l_{ij}|$) normal to edge e_{ij} joining $\boldsymbol{x}_i$ and $\boldsymbol{x}_j$, and e_{ij} is the unit vector. The integrand in (5.1.3) can be linearised by approximating $\mathbf{v} \cdot \mathrm{e}_{ij}$ along each edge e_{ij}, i.e.,

$$\mathbf{v} \cdot \mathrm{e}_{ij} = \frac{d\psi}{dl_{ij}} \approx \frac{\psi_{ij;2} - \psi_{ij;1}}{|l_{ij}|} = \bar{v}_{ij},$$

where $\psi_{ij;2}$ and $\psi_{ij;1}$ represent the nodal values of ψ at the end-points of l_{ij} which are estimated from the nodal values of the vertices of the triangles with circumcentres at $\boldsymbol{x}_{ij;2}$ and $\boldsymbol{x}_{ij;1}$ (see Fig. 5.1). We now use a control region approximation (see McCartin [58]) by assuming the (now linear) integrand in (5.1.3) is constant along all perpendiculars to l_{ij}; hence a constant approxi-

mation to the integrand is found by considering the following boundary value problem

$$\frac{d}{d\mathbf{e}_{ij}}\left(\frac{1}{Re}\frac{d\zeta}{d\mathbf{e}_{ij}} - \bar{v}_{ij}\zeta\right) = 0,$$

$$\zeta(\boldsymbol{x}_i, t) = \zeta_i, \quad \zeta(\boldsymbol{x}_j, t) = \zeta_j,$$

or equivalently,

$$\frac{d}{ds}\left(\frac{1}{Re}\frac{d\zeta}{ds} - \bar{v}_{ij}\zeta\right) = 0,$$

$$\zeta(0) = \zeta_i, \quad \zeta(|e_{ij}|) = \zeta_j.$$

Thus, along each edge $\mathbf{e}_{ij}$,

$$\zeta(s) = -\frac{C_1}{\bar{v}_{ij}} + C_2 e^{\bar{v}_{ij}(Re)s}$$

where

$$C_2 = \frac{\zeta_j - \zeta_i}{e^{\bar{v}_{ij}Re|e_{ij}|} - 1},$$

and

$$C_1 = \frac{1}{Re}\frac{d\zeta}{d\mathbf{e}_{ij}} - \zeta\bar{v}_{ij} = \frac{1}{Re|e_{ij}|}[B(Re\bar{v}_{ij}|e_{ij}|)\zeta_j - B(-Re\bar{v}_{ij}|e_{ij}|)\zeta_i]. \quad (5.1.4)$$

$B(x)$ represents the Bernoulli function defined by

$$B(x) = \begin{cases} \dfrac{x}{e^x - 1} & x \neq 0 \\ 1 & x = 0 \end{cases}$$

and possesses the asymptotic forms

$$B(x) \sim 1 - x/2 + x^2/12 + O(x^3) \text{ as } x \to 0,$$

$$B(x) \sim 0 \text{ as } x \to +\infty, \text{ and}$$

$$B(x) \sim -x \text{ as } x \to -\infty.$$

Using (5.1.3) and (5.1.4), the flux integrals along each face of d_i (i.e., l_{ij}) can be approximated to yield the system of algebraic equations

$$\frac{\partial\zeta_i}{\partial t}|d_i| + \sum_{j\epsilon I_i}\sigma_{ij}\left[B\left(-Re\bar{v}_{ij}|e_{ij}|\right)\zeta_i - B\left(Re\bar{v}_{ij}|e_{ij}|\right)\zeta_j\right] = 0,$$

where $\sigma_{ij} = \dfrac{|l_{ij}|}{Re|e_{ij}|}$.

To discretise the time component, we use the fully implicit backward-Euler scheme. Therefore, for a given time sub-interval $[t_{k-1}, t_k] \in (0,\mathrm{T}]$, the system of linear equations generated to determine the vorticity at an interior node $\boldsymbol{x}_i$ at time step k (ζ_i^k) is given by

$$\zeta_i^k + \sum_{j \in I_i} \frac{\Delta t_k \sigma_{ij}}{|d_i|} \left[B\left(-Re\bar{v}_{ij}^k |e_{ij}|\right) \zeta_i^k - B\left(Re\bar{v}_{ij}^k |e_{ij}|\right) \zeta_j^k \right] = \zeta_i^{k-1}, \quad i = 1, \ldots, N_v,$$

where $\Delta t_k = t_k - t_{k-1}$. Written in matrix notation

$$\left(I + C^k\right) Z^k + W^k = Z^{k-1}, \tag{5.1.5}$$

where I is the identity matrix,

$$c_{ii}^k = \Delta t_k \sum_{j \in I_i} \frac{\sigma_{ij}}{|d_i|} B\left(\frac{\psi_{ij;1}^k - \psi_{ij;2}^k}{\sigma_{ij}}\right), \tag{5.1.6}$$

$$c_{ij}^k = -\Delta t_k \frac{\sigma_{ij}}{|d_i|} B\left(\frac{\psi_{ij;2}^k - \psi_{ij;1}^k}{\sigma_{ij}}\right) \quad \text{if } \boldsymbol{x}_j \notin \partial\Omega_1 \cup \partial\Omega_2 \cup \partial\Omega_3, \tag{5.1.7}$$

$$w_i^k = \begin{cases} -\sum_{j \in I_i} \Delta t_k \frac{\sigma_{ij}}{|d_i|} B\left(\frac{\psi_{ij;2}^k - \psi_{ij;1}^k}{\sigma_{ij}}\right) \zeta_1^j & \text{if } \boldsymbol{x}_j \in \partial\Omega_1 \\ -\sum_{j \in I_i} \Delta t_k \frac{\sigma_{ij}}{|d_i|} B\left(\frac{\psi_{ij;2}^k - \psi_{ij;1}^k}{\sigma_{ij}}\right) \zeta_2^j & \text{if } \boldsymbol{x}_j \in \partial\Omega_2 \\ -\sum_{j \in I_i} \Delta t_k \frac{\sigma_{ij}}{|d_i|} B\left(\frac{\psi_{ij;2}^k - \psi_{ij;1}^k}{\sigma_{ij}}\right) \zeta_{3,q}^j & \text{if } \boldsymbol{x}_j \in \partial\Omega_3^q \\ 0 & \text{if } \boldsymbol{x}_j \notin \partial\Omega_1 \cup \partial\Omega_2 \cup \partial\Omega_3, \end{cases} \tag{5.1.8}$$

$$\text{and} \quad z_i^k = \zeta_i^k. \tag{5.1.9}$$

Here ζ_1^j, ζ_2^j and $\zeta_{3,q}^j$ represent the vorticity at node $\boldsymbol{x}_j$ along the no-slip boundaries and can be estimated at each time step through equations (5.2.4), (5.2.5) and (5.2.6) as shown in Section 5.2. We observe that $c_{ii}^k > 0$ and $c_{ij}^k \leq 0$ $(i \neq j)$ and is easily shown to be irreducible with column diagonal dominance (see Miller and Wang [61]). Thus C^k is an asymmetric M-matrix (see Varga [90]).

The Poisson equation in (5.1.2) can be discretised in the same manner used to discretise the advection-diffusion equation. Thus, at each time step (5.1.2) is approximated by the system of linear equations

$$\sum_{j\epsilon I_i} \frac{|l_{ij}|}{|e_{ij}||d_i|}\left(\psi_i^k - \psi_j^k\right) = \zeta_i^k, \quad i = 1, \ldots, N_v,$$

or equivalently

$$A\Psi^k + B^k = Z^k, \tag{5.1.10}$$

where

$$a_{ii} = \sum_{j\in I_i} \frac{|l_{ij}|}{|e_{ij}||d_i|}, \tag{5.1.11}$$

$$a_{ij} = -\frac{|l_{ij}|}{|e_{ij}||d_i|} \text{ if } \boldsymbol{x}_j \notin \partial\Omega_1 \cup \partial\Omega_2 \cup \partial\Omega_3 \tag{5.1.12}$$

$$\text{and} \quad b_i^k = \begin{cases} -\sum_{j\in I_i} \frac{|l_{ij}|}{|e_{ij}||d_i|} K_2 & \text{if } \boldsymbol{x}_j \in \partial\Omega_2 \\ -\sum_{j\in I_i} \frac{|l_{ij}|}{|e_{ij}||d_i|} K_3^q & \text{if } \boldsymbol{x}_j \in \partial\Omega_3^q, q = 1, \ldots, s \\ 0 & \text{if } \boldsymbol{x}_j \notin \partial\Omega_2 \cup \partial\Omega_3. \end{cases} \tag{5.1.13}$$

Matrix A given above is an asymmetric M-matrix but it can be written as a symmetric M-matrix. A consequence of both A and C^k being M-matrices is that the convergence of most of the classical iterative schemes (i.e., Jacobi, Gauss-Seidel and sucessive under relaxation) is ensured when applied to these sparse matrices.

5.2 Estimating the Dirichlet Boundary Conditions

At each time step we decouple the system of equations given in (5.1.5) and (5.1.10) using a Picard-type scheme. However, before these systems can be solved, the Dirichlet boundary conditions for ψ and ζ along the no-slip boundaries must be generated. Here we give a means of estimating these conditions.

5.2.1 Estimates for K_2 and K_3^q

By construction, the stream function value along $\partial\Omega_1$ is set to zero, but K_2 and K_3^q must be determined a posteriori. Given a Delaunay triangulation, K_2 and K_3^q are estimated from the interior nodal values of the stream function. To determine K_q^s $q = 1, \ldots, s$, a dense covering of nodes is placed around each element and the Dirichlet boundary conditions are estimated from these surrounding nodes. If $2n$ nodes surround element q then K_3^q is estimated from

$$K_3^q \approx \frac{1}{2n} \sum_{j=1}^{n} (\psi_{j,q+1} + \psi_{j,q-1}) = \bar{K}_3^q, \qquad q = 1, 2, \ldots, s \tag{5.2.1}$$

where $\psi_{j,q+1}$ and $\psi_{j,q-1}$ represent the j^{th} nodal value above and below surface element $\partial\Omega_3^q$ respectively.

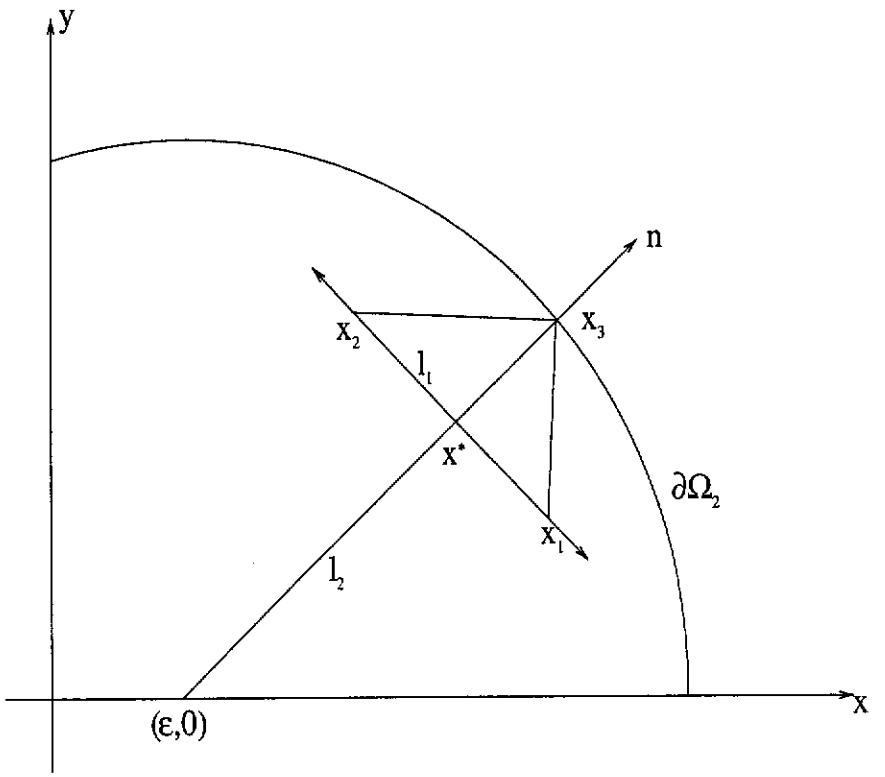

Figure 5.2: Interpolating to get ψ on $\partial\Omega_2$.

Next, consider a Delaunay triangle with vertices $\boldsymbol{x}_1$, $\boldsymbol{x}_2$, and $\boldsymbol{x}_3$ and only one vertex lying on $\partial\Omega_2$ ($\boldsymbol{x}_3$ say) (see Fig. 5.2). To approximate ψ on $\partial\Omega_2$

we use a linear approximation at each such boundary node, $\psi_{j,b_2}, j = 1, \ldots, \alpha$, given by

$$\psi_{j,b_2} = \psi_{j,b_2-1} + \delta_j \left.\frac{\partial \psi}{\partial \mathbf{n}}\right|_{\partial\Omega_2} + O(\delta_j^2), \quad j = 1, \ldots, \alpha.$$

ψ_{j,b_2-1} is an adjacent point at a distance of δ_j from the boundary in the normal direction and is given by

$$\psi_{j,b_2-1} \approx S(\boldsymbol{x}^*)\psi(\boldsymbol{x}_2) + (1 - S(\boldsymbol{x}^*))\psi(\boldsymbol{x}_1), \tag{5.2.2}$$

where $S(\boldsymbol{x}^*) = \dfrac{\|\boldsymbol{x}_1 - \boldsymbol{x}^*\|_2}{\|\boldsymbol{x}_1 - \boldsymbol{x}_2\|_2}$ and $\|\cdot\|_2$ represents the Euclidean norm. The nature of $\boldsymbol{x}^* = (x^*, y^*)$ depends on the orientation of the Delaunay triangle. If the slopes of l_1 and l_2, given in Fig. 5.2, are denoted by m_1 and m_2 respectively then we find

$$x^* = \frac{m_1 x_1 - y_1 - m_2 \varepsilon}{m_1 - m_2},$$

and

$$y^* = m_2(x^* - \varepsilon)$$

when both m_1 and m_2 are distinct and finite. However,

$$x^* = x_1 \quad \text{and} \quad y^* = m_2(x_1 - \varepsilon)$$

when m_1 becomes unbounded, and

$$x^* = x_3 \quad \text{and} \quad y^* = y_1 + m_1(x_3 - x_1)$$

when m_2 becomes unbounded. Furthermore, to ensure the correct triangle is used to determine $\boldsymbol{x}^*$, l_2 must lie between $\boldsymbol{x}_1$ and $\boldsymbol{x}_2$. Hence the correct triangle satisfies the conditions

$$S(\boldsymbol{x}^*) < 1 \quad \text{and} \quad \|\boldsymbol{x}_2 - \boldsymbol{x}^*\|_2 < \|\boldsymbol{x}_1 - \boldsymbol{x}_2\|_2 .$$

Consequently, there is no guarantee that estimates for ψ_{j,b_2} can be found for every boundary node. If m ($\leq \alpha$) estimates are obtained, we use the arithmetic mean of ψ_{j,b_2}, viz

$$K_2 \approx \frac{1}{m} \sum_{j=1}^{m} (\psi_{j,b_2-1} - \delta_j) = \bar{K}_2, \tag{5.2.3}$$

to estimate K_2. The triangulations used to generated the flow fields displayed in Chapter 6 ensure that about 95% of the boundary nodes are used in this averaging process.

5.2.2 Approximating ζ on the No-Slip Boundaries

Although the equations given in (2.3.1) are coupled and have been solved as such (see Campion-Renson and Crochet [18], Glowinski and Pironneau [34] and Gresho [35]), many workers have had success decoupling these by approximating the vorticity along no-slip surfaces from a discretisation of the Poisson equation (see Dhatt et al [29], Gupta and Manohar [38], Mukhopadhyay and Basu [64]) and Miller and Wang [60]), we follow the approach given in [60]. Using the Poisson equation in (2.3.1), an integration over any region $R \subset \Omega$ gives

$$-\int_R \nabla^2 \psi dA = -\int_{\partial R} \frac{d\psi}{d\mathbf{n}} ds = \int_R \zeta dA.$$

In particular, for a mesh point $\boldsymbol{x}_b$ on $\partial\Omega$ it follows that

$$\int_{d_b} \zeta dA = -\sum_{j \in I_b} \int_{l_{bj}} \frac{\partial \psi}{\partial \mathrm{e}_{bj}} ds + \int_{\partial d_b \cap \partial\Omega} \frac{\partial \psi}{\partial \mathbf{n}} ds.$$

As e_{bj} represents a directed interior edge from $\boldsymbol{x}_b$ to $\boldsymbol{x}_j$, we can estimate $\dfrac{\partial \psi}{\partial \mathrm{e}_{bj}}$ by

$$\frac{\partial \psi}{\partial \mathrm{e}_{bj}} \approx \frac{\psi_j^k - \psi_b}{|\mathrm{e}_{bj}|},$$

where ψ_b represents the given Dirichlet condition along boundary $\partial\Omega$. So, at each time step the vorticity on boundary $\partial\Omega$ is approximated by

$$\zeta^b \approx -\frac{1}{|d_b|}\left[\sum_{j \in I_b, \boldsymbol{x}_j \notin \partial\Omega} \frac{(\psi_j^k - \psi_b)|l_{bj}|}{|e_{bj}|} + \int_{\partial d_b \cap \partial\Omega} \frac{\partial \psi}{\partial \mathbf{n}} ds\right].$$

Therefore, using the Neumann and Dirichlet conditions given in (2.1.14) and (2.1.15), the vorticity at node $\boldsymbol{x}_b$ on boundary $\partial\Omega_i$ $(i = 1, 2, 3)$, namely ζ_i^b, is

approximated by

$$\zeta_1^b \approx -\frac{1}{|d_b|}\left[\sum_{j\in I_b, \boldsymbol{x}_j\notin\partial\Omega_1}\psi_j^k\frac{|l_{bj}|}{|e_{bj}|}+\int_{\partial d_b\cap\partial\Omega_1}\bar{U}ds\right], \tag{5.2.4}$$

$$\zeta_2^b \approx -\frac{1}{|d_b|}\left[\sum_{j\in I_b, \boldsymbol{x}_j\notin\partial\Omega_2}\left(\psi_j^k-K_2\right)\frac{|l_{bj}|}{|e_{bj}|}-\int_{\partial d_b\cap\partial\Omega_2}ds\right], \tag{5.2.5}$$

$$\text{and}\quad \zeta_{3,q}^b \approx -\frac{1}{|d_b|}\left[\sum_{j\in I_b, \boldsymbol{x}_j\notin\partial\Omega_3^q}\left(\psi_j^k-K_3^q\right)\frac{|l_{bj}|}{|e_{bj}|}\right],\quad q=1,\ldots,s, \tag{5.2.6}$$

where exact integration is performed on the integrals along $\partial\Omega_1$ and $\partial\Omega_2$ and where K_2 and K_3^q are estimated at each time step using equations (5.2.3) and (5.2.1). At the ends of each surface element forming the slotted sleeve, the vorticity is known to possess an algebraic singularity. From the approximation given in (5.2.6), the behaviour of the vorticity at these singular points is estimated from the neighbouring stream function values. Once the Dirichlet boundary conditions for the field variables are found, the governing equations can be decoupled at each time step and solved in sequence. The iterative scheme used to linearise the system of equations is now described.

5.3 Decoupling the Governing Equations

One disadvantage of using the stream function-vorticity formulation for multi-connected domains is that the stream function may be completely specified on only one boundary. The additive constants at the remaining boundaries must be determined as part of the solution process. The constants are often determined by imposing the condition that the pressure field is single-valued within the domain. This condition introduces an extra equation involving the stream function and vorticity from which the constants can be determined, see for example Gunzburger and Peterson [37]. Here, we use a Gauss-Seidel iterative method to solve the coupled equations (5.1.5) and (5.1.10) with the boundary conditions (5.2.1), (5.2.3), (5.2.4), (5.2.5) and (5.2.6) (see Gupta and Manohar

[38] for an outline of the scheme). In order to incorporate equations (5.2.1) and (5.2.3) into the iterative scheme, the discretised Poisson equation together with (5.2.1) and (5.2.3) are solved iteratively until self-consistent stream function and Dirichlet boundary values are obtained. The Dirichlet boundary values are smoothed between iterations to aid in the rate of convergence. Intuitively, this additional iterative scheme should not significantly affect the stability of the Gauss-Seidel scheme as we have smoothed the boundary values of ψ before the vorticity vector is updated. However, the rate of convergence is expected to be affected as the accuracy of $\bar{K}_2$ and $\bar{K}_3^q$ is dependent on how far the current vorticity field is from the steady-state solution.

The solution to the Couette flow between the rotor and bowl is used to generate the initial estimates for the vorticity field and the stream function on $\partial\Omega_2$ and $\partial\Omega_3$. Three iterative schemes, referred to as the outer, middle and inner iterations respectively, are then used to obtain steady-state solution fields. The outer iteration generates the sequence of solution fields converged at each time step, eventually reaching the steady-state solution. The middle iteration solves the discretised Poisson and vorticity transport equations through the use of the estimates for the vorticity along the solid boundaries given in (5.2.4), (5.2.5) and (5.2.6). The boundary estimates for ζ are updated using a weighted average and convergence is reached when the difference between two successive estimates (in the maximum norm) is smaller than a given tolerance. When convergence is reached, the solution fields for a given time step are known. The inner iteration solves the discretised Poisson equation and updates $\bar{K}_2$ and $\bar{K}_3^q$ until self-consistent solutions are obtained. The converged results represent an intermediate set of values of the middle iteration. If superscript k is used to represent the k^{th} time step, superscript j is used to represent the j^{th} iterative step in the middle iteration and superscript i is used to represent the i^{th} step of the inner iteration then the modified Gauss-Seidel

iterative scheme is:

1. Choose tolerances ϵ_0, ϵ_1 and ϵ_2, and smoothing parameters δ_1, $\delta_2 \in [0,1)$. Use the Couette flow to get the initial $Z^{j,k}$, $\bar{K}_2^{i,j,k}$ and $\bar{K}_3^{i,j,k}$ distributions and put $i,j,k=0$.

2. Solve (5.1.10) i.e.,

$$A\Psi^{i+1,j+1,k+1} + B^{i+1,j+1,k+1} = Z^{j,k}$$

iteratively using the CGS until

$$\|\Psi^{i+1,n} - \Psi^{i+1,n-1}\|_\infty < \epsilon_0.$$

$\Psi^{i+1,n}$ denotes the estimate for $\Psi^{i+1,j+1,k+1}$ after n iterations of the CGS method.

3. Update $\bar{K}_2^{i+1,j+1,k+1}$ and $\bar{K}_3^{i+1,j+1,k+1}$ using (5.2.3) and (5.2.1) and the smoothing parameter δ_1 i.e.,

$$\left.\begin{aligned} \bar{K}_2^{i+1,j+1,k+1} &:= (1-\delta_1)\bar{K}_2^{i+1,j+1,k+1} + \delta_1 \bar{K}_2^{i,j+1,k+1} \\ \bar{K}_3^{i+1,j+1,k+1} &:= (1-\delta_1)\bar{K}_3^{i+1,j+1,k+1} + \delta_1 \bar{K}_3^{i,j+1,k+1}. \end{aligned}\right\}$$

4. Put $i = i+1$ and repeat steps $2-3$ until the following convergence criteria are met

$$|\bar{K}_2^{i+1,j+1,k+1} - \bar{K}_2^{i,j+1,k+1}| < \epsilon_1 \quad \text{and} \quad \|\bar{K}_3^{i+1,j+1,k+1} - \bar{K}_3^{i,j+1,k+1}\|_\infty < \epsilon_1.$$

5. Put $\Psi^{j+1,k+1} = \Psi^{i+1,j+1,k+1}$, $\bar{K}_2^{j+1,k+1} = \bar{K}_2^{i+1,j+1,k+1}$ and $\bar{K}_3^{j+1,k+1} = \bar{K}_3^{i+1,j+1,k+1}$, and approximate vorticity at the no-slip surfaces, $Z_b^{j+1,k+1}$, using (5.2.4), (5.2.5) and (5.2.6). Modify the values using the smoothing parameter δ_2, i.e.,

$$Z_b^{j+1,k+1} := (1-\delta_2)Z_b^{j+1,k+1} + \delta_2 Z_b^{j,k+1}.$$

6. Solve (5.1.5) i.e.,

$$\left(I + C^{j+1,k+1}\right) Z^{j+1,k+1} + W^{j+1,k+1} = Z^k$$

iteratively using the CGS until

$$\|Z^{j+1,n} - Z^{j+1,n-1}\| < \epsilon_0.$$

$Z^{j+1,n}$ denotes the estimate for $Z^{j+1,k+1}$ after n iterations of the CGS method.

7. Put $j = j+1$, $i = 0$ and repeat steps $2-6$ until the following convergence criterion is met

$$\|Z^{j+1,k+1} - Z^{j,k+1}\|_\infty < \epsilon_2.$$

8. Use $Z^{j+1,k+1}$, $Z_b^{j+1,k+1}$, $\Psi^{j+1,k+1}$, $\bar{K}_2^{j+1,k+1}$ and $\bar{K}_3^{j+1,k+1}$ to define the nodal values of vorticity and stream function at time step $k+1$ $\left(\tilde{Z}^{k+1}, \tilde{\Psi}^{k+1}\right)$.

9. Put $k = k+1, i, j = 0$ and repeat steps $2-8$ until

$$\|\tilde{Z}^{k+1} - \tilde{Z}^k\|_\infty < \epsilon_3. \tag{5.3.1}$$

Here $\|\cdot\|_\infty$ represents the maximum norm. If the convergence criterion (5.3.1) is satisfied after k steps, the program is continued for another k time steps before the program terminates. This technique is used to avoid instances when spurious steady-state solutions are reached quickly as are known to occur when the mesh is not fine enough. The solution fields obtained when convergence is first met are compared with the solution fields after the extended period of time before contour plots are produced. The Gauss-Seidel approach reduces the number of iterations as the nodal values reach the steady-state solution; further, it is not neccessary at the beginning of the procedure to solve the coupled system exactly at each time step as this is equivalent to restarting the

iterative procedure at the next time step with an initial guess closer to the steady-state solution.

We note that the use of the smoothing parameters δ_1 and δ_2 as an aid to obtain steady-state solutions to coupled systems is not widely accepted. According to Gupta and Manohar [38] their use is essential for the convergence of the iterative scheme; however, Crochet et al [28, pages 138–139] state that the use of a smoothing parameter is questionable but rather the choice of the tolerances and initial guess influence the rate of convergence more than the need to use a smoothing parameter. We found the use of smoothing parameters for the Dirichlet boundary conditions for the two field variables a necessary feature of the iterative scheme. The amount of smoothing done on the (Dirichlet) vorticity values has the greater influence on the stability of the solution process.

The sparsity of the matrices created makes the use of iterative schemes advantageous and since both A and C^k are M-matrices iterative schemes such as Jacobi, Gauss-Seidel and SOR (for under-relaxation) are guaranteed to converge if employed. However, Conjugate Gradients methods (with preconditioning) are superior to these classical techniques and will be used here. The system given in (5.1.5) may be solved using the ICCG scheme (if A is represented as a symmetric M-matrix) (see Meijerink and van der Vorst [59]) while (5.1.10) is solved using the Conjugate Gradients Squared method (CGS) given by Sonneveld [83]. To improve the spectral properties we precondition matrices A and C^k using incomplete LU factorisation (with no fill-in). The numerical stability of the CGS using this precondioning method when the coefficient matrix is an M-matrix has been proved (see Meijerink and van der Vorst [59]). Hence, if we write

$$M\mathbf{x} = \mathbf{b}$$

to represent the system to be solved at steps 2 and 6 given above, then instead of solving the original system we solve the preconditioned system

$$\tilde{A}\tilde{\mathbf{x}} = \tilde{\mathbf{b}} \tag{5.3.2}$$

where the preconditioned matrix $\tilde{A} = L^{-1}MU^{-1}$, $\mathbf{x} = U^{-1}\tilde{\mathbf{x}}$ and $\tilde{\mathbf{b}} = L^{-1}\mathbf{b}$. Here L represents the lower triangular matrix of M, with $l_{ii} = 1$ and U represents the upper triangular matrix of M. L and U are defined so that $M \approx LU$ and the structure (i.e., the non-zero pattern) of M is retained in these matrices. To solve (5.3.2), the Conjugate Gradients Squared algorithm given by Sonneveld [83] is used. We note that each time the system in step 6 is solved, a new coefficent matix C^k (and therefore a new preconditioned matrix) must be found. This, however, is not required for step 2; once the preconditioned matrix for A is found, it is retained for later use. At all stages of the solution process, the CGS is used to solve the system of equations until

$$\|\mathbf{x}^{n+1} - \mathbf{x}^n\| < 10^{-6}.$$

Given the intended application of the apparatus, the torque exerted on the rotor about its centre is estimated at the end of each time step. If T represents the dimensionless torque exerted on the rotor then using polar coordinates T is given by

$$T = \int_0^{2\pi} \tau_{r\theta}|_{\partial\Omega_1}\, d\theta,$$

where the dimensionless shear stress, $\tau_{r\theta}$, along the rotor is given by

$$\tau_{r\theta}|_{\partial\Omega_1} = \left(\zeta - \frac{2v_\theta}{r}\right)\Big|_{\partial\Omega_1},$$

hence,

$$T = \int_0^{2\pi} \zeta|_{\partial\Omega_1}\, d\theta - \frac{4\pi\bar{U}}{c}. \tag{5.3.3}$$

The trapezoidal rule is then used to evaluate T from the vorticity data along the rotor.

Chapter 6

Results for Model Two

To determine the flow field in Ω, the necessary codes used to implement the numerical scheme were written in FORTRAN using double precision in all computations and run on an SGI INDY workstation. Also, for the problems considered here, a non-dimensional time step of 0.1 and a tolerance of 10^{-4} for ϵ_1, ϵ_2, and ϵ_3 are used, and values of 0.80 and 0.95 are used for the smoothing parameters δ_1 and δ_2 respectively. The iterative scheme described in Section 5.3 to decouple the governing equations is cumbersome to implement and computationally expensive if all of the entries of the sparse matrices (i.e., A, C^k and their corresponding preconditioned matrices) are manipulated. We, therefore, use an efficient row-indexed sparse storage technique (see Press et al [72]) to store only the non-zero coefficients of these matrices and to perform all matrix operations needed in the solution scheme. This technique will reduce the amount of memory needed in the solution process but the programming involved becomes unwieldy.

When considering the two-dimensional model, the dimensions used represent the dimensions of the viscometer used in practice. In MKS units $a = 0.024$m, $b = 0.093$m and $c = 0.019$m. Furthermore, 10 surface elements ($s = 10$) are used to represent the surface of the slotted sleeve. The sleeve used in practice is designed to facilitate the entrainment of the slurry onto the rotor, consequently the sleeve possesses large slots. Typically, only one-third

of the sleeve is solid so a ratio of 1 : 2 for the surface to slot length is used in the current model.

In the numerical scheme, Ω is initially partitioned into three disjoint regions; these regions cover the domain around the rotor (region $R1$), the domain around the slotted sleeve (region $R2$) and the domain of Ω a small distance from the slotted sleeve to the outer boundary (region $R3$). Mesh nodes within $R1$ and $R3$ are generated using polar coordinates by incrementing the polar angle and radial distance through a prescribed number of intervals. Mesh nodes in $R2$ are structured so that n nodes (equally spaced) lie along each surface element and p nodes (equally spaced) are placed along each slot. This sequence of nodes is repeated a small distance both above and below the sleeve a given number of times. For flows at large Reynolds numbers, boundary layers on both sides of each surface element are expected to exist, therefore, such a dense distribution of nodes around the sleeve is required to capture the shear layers around the slotted sleeve. The location of the nodes in $R2$ is important in estimating K_3^q, as well as modelling the flow through the sleeve; therefore, the nodes in this mesh are not moved. However, the placement of the nodes in $R1$ and $R3$ is not important in estimating K_2 and K_3^q, these nodes are simply used to cover their respective domains. The nodes in Ω are triangulated and the resulting mesh is smoothed by moving each interior node to the average of its neighbouring nodes. Smoothing the mesh so as to maximise the minimum angle and minimise the maximum angle is seen to yield more accurate results (see Miller and Wang [60]). This mesh can be refined, if necessary, by adding a midpoint for each edge. Fig. 6.1 shows a typical sequence of meshes following the initial triangulation, smoothing and edge refinement of a mesh.

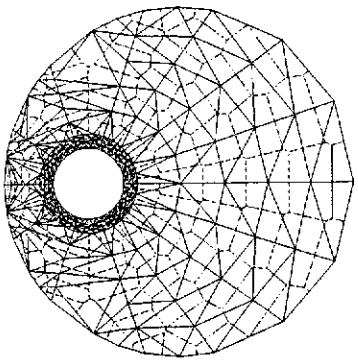

(a) Initial mesh.

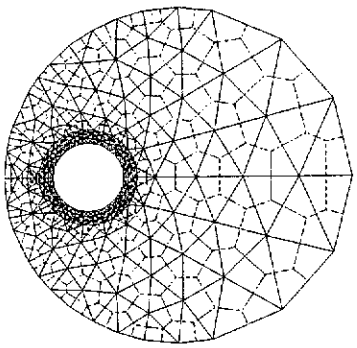

(b) Smoothed mesh.

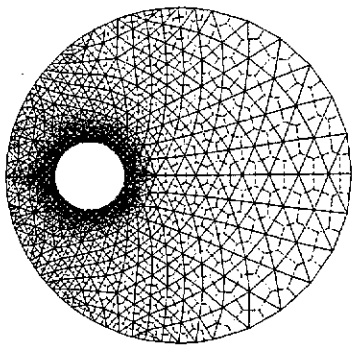

(c) Refined mesh.

Figure 6.1: Mesh smoothing and refinement.

To test that the finite volume method has been implemented correctly, the following transient boundary value problem, defined on a unit circle, is solved

$$\frac{\partial \zeta}{\partial t} - \nabla . \left(\frac{1}{100} \nabla \zeta - \mathbf{v} \zeta \right) = f(x, y; t), \quad \zeta = 0 \text{ on } \partial\Omega,$$

where

$$\mathbf{v} = [1, 1] \text{ and } f(x, y; t) = -\left(\frac{1 - x^2 - y^2}{4} \right) e^{-t} + \left(\frac{1}{100} - \frac{x + y}{2} \right) \left(1 + e^{-t} \right).$$

The analytic solution is

$$\zeta = \left(\frac{1 - x^2 - y^2}{4} \right) \left(1 + e^{-t} \right).$$

Using a time step of 0.1 the test problem is solved using meshes of varying density. The relative errors using both the maximum and Euclidean norms for

each mesh are given in Table 6.1. Clearly, the numerical solution becomes more

nodes on $\partial\Omega$	nodes in Ω	h	$\frac{\|\zeta - \zeta_h\|_\infty}{\|\zeta_h\|_\infty}$	$\frac{\|\zeta - \zeta_h\|_2}{\|\zeta_h\|_2}$
6	6	1.0000	1.8801	2.0234
16	33	0.5176	0.9644	0.7998
36	161	0.2959	0.3770	0.2914
84	689	0.2158	0.2031	0.0111

Table 6.1: Relative errors for the test problem.

accurate as the mesh is refined. This is only a partial check of the algorithm since the analytic solution is independent of Reynolds number. In addition to solving the above test problem, the flow bounded between two eccentric cylinders corresponding to the geometry considered by San Andres and Szeri [78] is solved. Specifically, in their Fig. 14 they considered the case when the inner cylinder is stationary and used Reynolds numbers of 10, 20 and 30 and an eccentricity of 0.5. There exists a discrepancy between the results produced by San Andres and Szeri [78] and those produced by Ballal and Rivlin [5] regarding the location of the separation and reattachment points as Reynolds number is increased. The results obtained using our numerical scheme agree with those given by Ballal and Rivlin [5] in that the separation and reattachment points both move in the direction opposite to the rotation of the outer cylinder.

To study the flow around the slotted sleeve, we consider cases when the cylinders rotate in the same sense (case one) and in opposite senses (case two). For case one, 0.5 and 0.7 are used for the eccentricity, $\bar{\epsilon}$, and the rotational speed of the rotor, $\bar{U}$, is varied up to 10.0. For case two, eccentricities of 0.2, 0.5, and 0.7, together with rotational speeds of the rotor up to -20.0 are used. For both cases, the Reynolds number, Re, varies from 50 to 1000.

From here on, the parameter set $\{Re, \bar{\epsilon}, \bar{U}\}$ is used to define a given prob-

lem, where the eccentricity is defined as the ratio of displacement centres to the mean radial clearance between the sleeve and outer cylinder, i.e., $\bar{\epsilon} = a\epsilon/(b-a)$. The contour plots are generated using MATLAB [57]; however, due to the memory limitations of the computer available to us, only contour plots obtained from meshes containing approximately 1300 nodes are given here.

Qualitative agreement between coarse and fine meshes is established by solving the problems $\{500.0, 0.2, 5.0\}$ and $\{500.0, 0.2, -3.0\}$ using the four meshes given in Fig. 6.2, Fig. 6.3, Fig. 6.4 and Fig. 6.5. The first mesh contains 1311 nodes and 2531 triangular elements. The second mesh contains 2503 nodes and 4863 triangular elements. The third mesh contains 5000 nodes and 9840 triangular elements, and the finest mesh contains 9703 nodes and 19151 triangular elements. The maximum (nodal) stream function, $|\psi|$, and the Dirichlet conditions along the slotted sleeve and the outer cylinder for these two problems are given in Tables 6.2 and 6.3 respectively. From the results given in Tables 6.2 and 6.3, we can be confident that the contour plots obtained using a coarse mesh will have the same global features as the flow fields generated using much finer meshes.

mesh	$\psi\|_{\partial\Omega_2}$	max$\|\psi\|$	$\psi\|_{\partial\Omega_3^1}$	$\psi\|_{\partial\Omega_3^2}$	$\psi\|_{\partial\Omega_3^3}$	$\psi\|_{\partial\Omega_3^4}$	$\psi\|_{\partial\Omega_3^5}$
1	-4.3964	4.3964	-0.6560	-0.6649	-0.6807	-0.7013	-0.7199
2	-4.4519	4.4519	-0.6799	-0.6902	-0.7089	-0.7342	-0.7477
3	-4.6420	4.6420	-0.6755	-0.6851	-0.7047	-0.7286	-0.7468
4	-4.6143	4.6143	-0.6763	-0.6857	-0.7041	-0.7290	-0.7463

mesh	$\psi\|_{\partial\Omega_3^6}$	$\psi\|_{\partial\Omega_3^7}$	$\psi\|_{\partial\Omega_3^8}$	$\psi\|_{\partial\Omega_3^9}$	$\psi\|_{\partial\Omega_3^{10}}$
1	-0.7252	-0.7120	-0.6877	-0.6655	-0.6533
2	-0.7437	-0.7351	-0.7120	-0.6968	-0.6859
3	-0.7494	-0.7379	-0.7155	-0.6933	-0.6785
4	-0.7492	-0.7381	-0.7157	-0.6939	-0.6793

Table 6.2: Results for $\{500.0, 0.2, 5.0\}$ using successively finer meshes.

As steady-state (i.e., converged) solutions are required, the long-term behaviour of the solution fields is examined. The discretised systems of equations are solved using a CGS scheme together with preconditioning. Therefore, a convergence criterion based on the difference in solution vectors at successive time steps is adequate. The problem $\{1000.0, 0.5, 10.0\}$ is solved using the mesh shown in Fig. 6.7 and Fig. 6.6 displays the time history of the maximum norm of the absolute error in both the stream and vorticity functions at successive time steps. Over the time taken to reach the steady-state solution, the error in successive vorticity iterates is always larger than that in the stream function iterates. This is true for all the problems solved here and so a convergence criterion based on vorticity also ensures accuracy in the stream function. This has also been pointed out by Gupta and Manohar [38]. Furthermore, the torque exerted on the rotor in all the problems considered here reaches steady-state quickly, Fig. 6.6(b) shows one example.

mesh	$\psi\|_{\partial\Omega_2}$	$\max\|\psi\|$	$\psi\|_{\partial\Omega_3^1}$	$\psi\|_{\partial\Omega_3^2}$	$\psi\|_{\partial\Omega_3^3}$	$\psi\|_{\partial\Omega_3^4}$	$\psi\|_{\partial\Omega_3^5}$
1	-1.8996	0.4486	0.3028	0.2625	0.2126	0.1871	0.2004
2	-1.9788	0.3753	0.2844	0.2459	0.1997	0.1729	0.1807
3	-2.1012	0.3315	0.2784	0.2371	0.1835	0.1679	0.1767
4	-2.1507	0.3445	0.2723	0.2330	0.1841	0.1653	0.1691

mesh	$\psi\|_{\partial\Omega_3^6}$	$\psi\|_{\partial\Omega_3^7}$	$\psi\|_{\partial\Omega_3^8}$	$\psi\|_{\partial\Omega_3^9}$	$\psi\|_{\partial\Omega_3^{10}}$
1	0.2696	0.2917	0.3087	0.3176	0.3195
2	0.2245	0.2606	0.2678	0.2927	0.2984
3	0.2018	0.2432	0.2559	0.2761	0.2739
4	0.2043	0.2482	0.2499	0.2728	0.2763

Table 6.3: Results for $\{500.0, 0.2, -3.0\}$ using successively finer meshes.

As the flow around the slotted sleeve is expected to be complex, the qualitative behaviour around the sleeve is captured by placing 5 nodes ($n = 5$) and 7 nodes ($p = 7$) on each surface element and slot respectively. This distribution of nodes is repeated above and below the sleeve producing 7 circles of nodes around, and on, the sleeve using a total of 840 nodes distributed through a small radial distance. This dense covering ensures that, for the range of Reynolds number considered, nodes are placed within the boundary layers present near the surface elements of the sleeve. This covering also represents an adequate model to estimate the behaviour of the vorticity near the corner singularities. We anticipate the flow in the main region will not be as intricate as that around the sleeve; hence, this region is not densely covered. The meshes used to generate the contour plots given here for eccentricities of $0.2, 0.5$ and 0.7 are shown in Fig. 6.2, Fig. 6.7 and Fig. 6.8 and are referred to as mesh A, mesh B and mesh C respectively. We now discuss case one, when

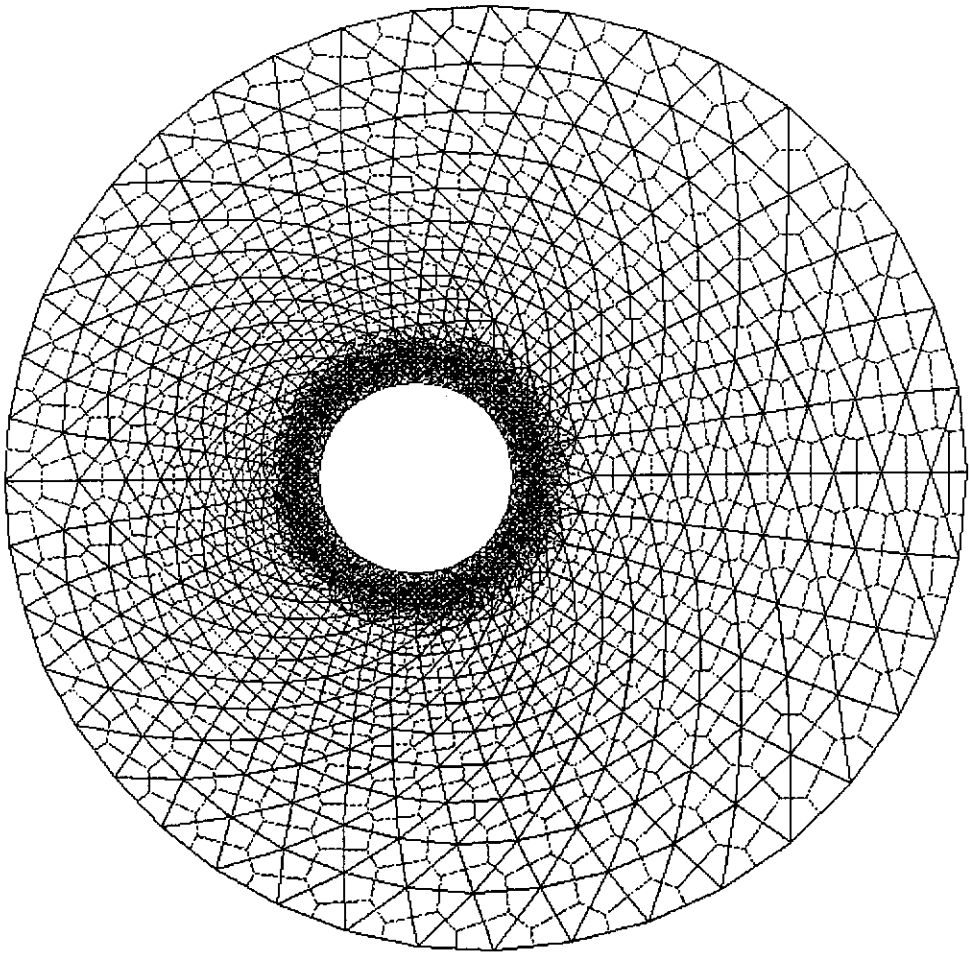

Figure 6.2: Mesh A (1311 nodes).

the bounding cylinders rotate in the same sense.

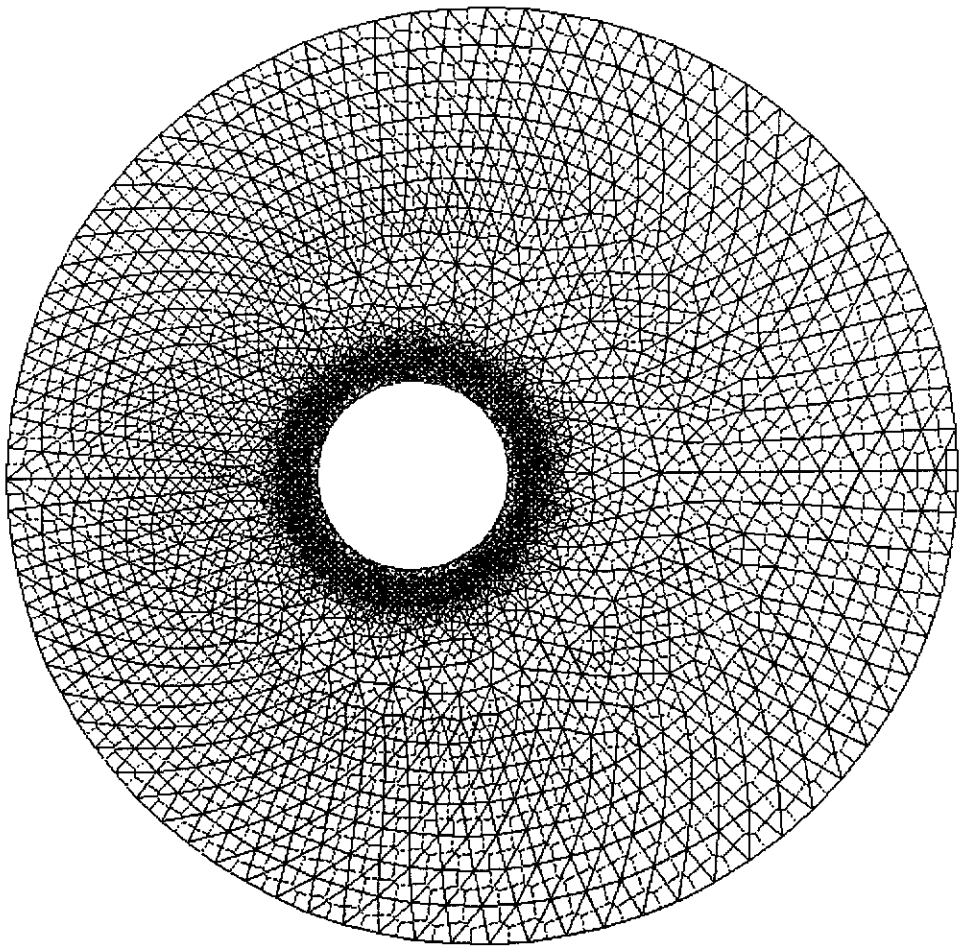

Figure 6.3: A mesh containing 2503 nodes.

6.1 Case One:The Bounding Cylinders Rotate in the Same Direction

For the problems discussed in this section, the flow field is determined by computing the streamlines. However, we note that the contour levels shown are not uniform, this is done to highlight the main features without unnecessarily cluttering the flow field.

When the modified viscometer is placed within the bowl, increasing the rotational speed of the rotor can cause the generation of eddies within the flow

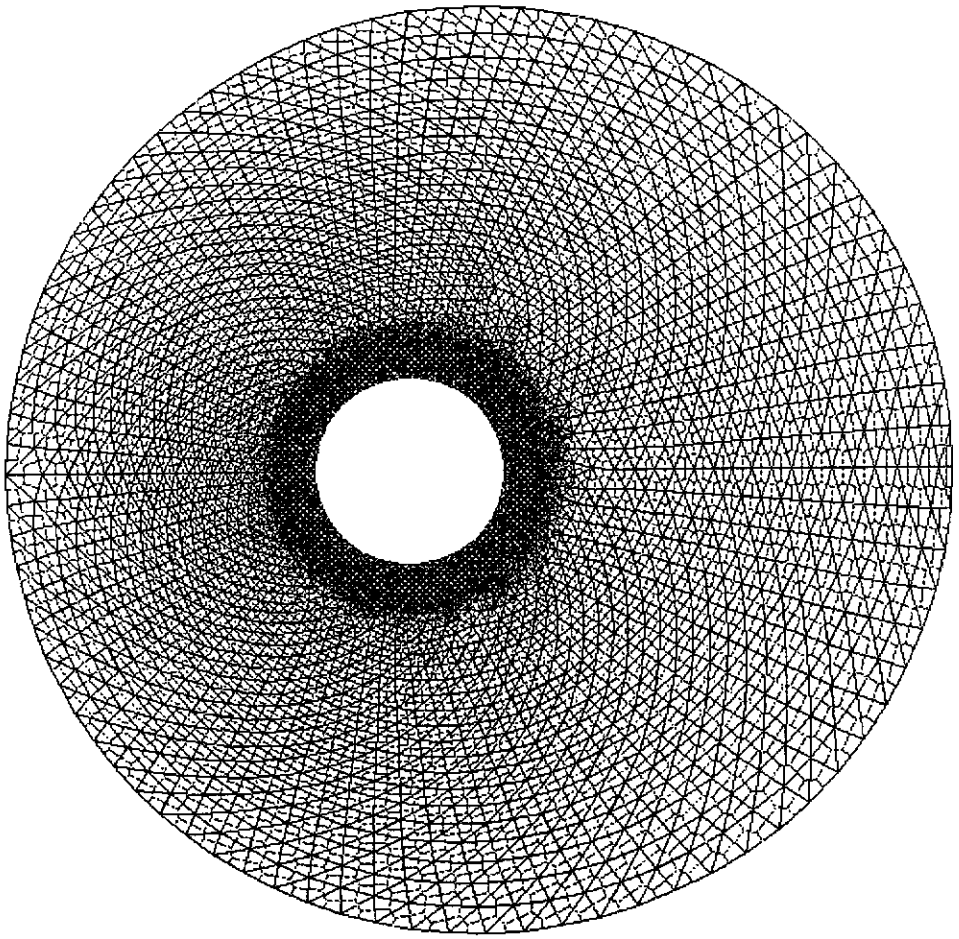

Figure 6.4: A mesh containing 5000 nodes.

domain. Fig. 6.9 gives the contour plots when problems $\{500.0, 0.7, 1.7\}$ and $\{500.0, 0.7, 2.0\}$ are solved. For small $\bar{U}$ no eddies are present and the interaction of the fluid around the sleeve can clearly be seen. The amount of flow through the sleeve depends on the eccentricity of the system. As $\bar{U}$ increases, a critical value is reached when a pair of eddies are formed within the flow domain. The critical value is dependent on the eccentricity. For example, when eccentricities of 0.5 and 0.7 are used, no eddies are observed when $\bar{U}$ is below 7.0 and 2.0 respectively. When eddies exist, the eddy closest to the sleeve (i.e., the primary eddy) rotates clockwise and represents the dominant eddy within

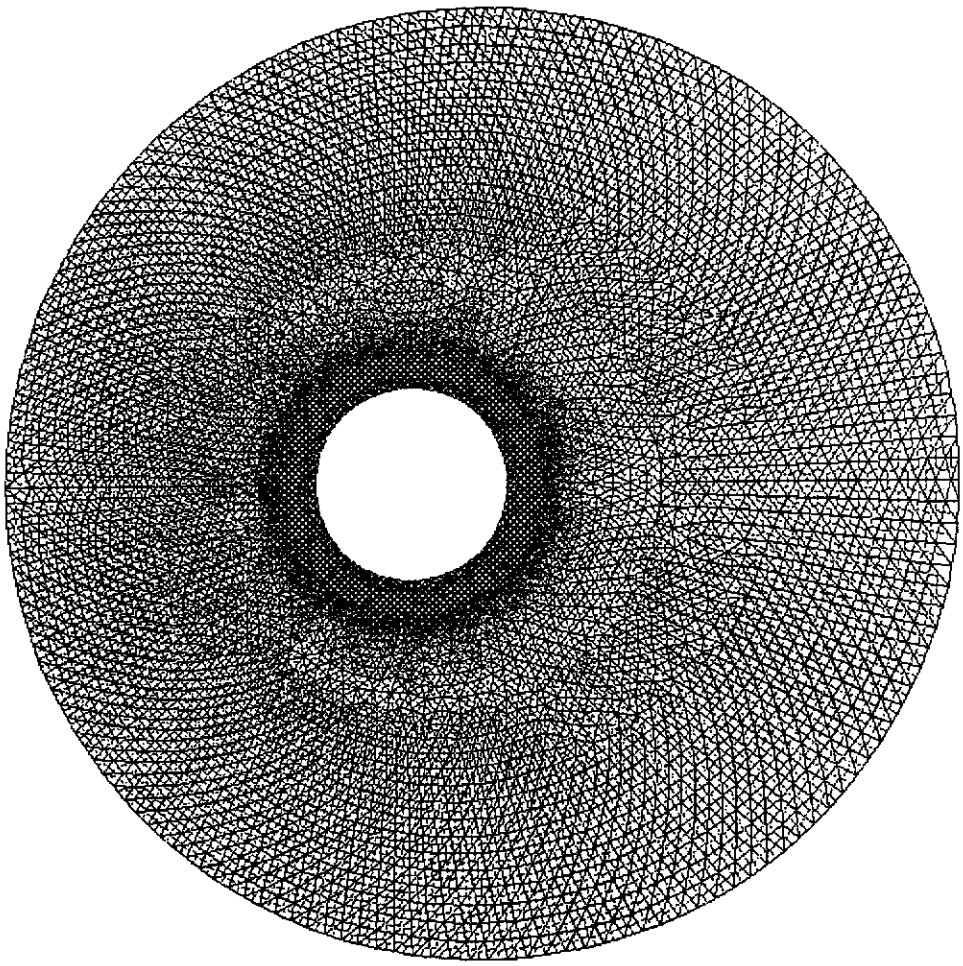

Figure 6.5: A mesh containing 9703 nodes.

the system. The eddy located near the outer cylinder (the secondary eddy) rotates in a counter-clockwise direction. From Fig. 6.9, the flow through the slotted sleeve is restricted when these eddies are present. Increasing the speed of the rotor does not affect, qualitatively, the flow field or inhibit further the flow through the slotted sleeve, only the computed values for the stream function, vorticity and torque are affected. By solving problems $\{500.0, 0.7, 2.0\}$, $\{500.0, 0.7, 5.0\}$ and $\{500.0, 0.7, 10.0\}$, Table 6.4 gives the torque exerted along the rotor (T), the centre of the primary eddy as well as the stream function (ψ_c) and vorticity (ζ_c) there. Increasing $\bar{U}$ decreases both the torque exerted

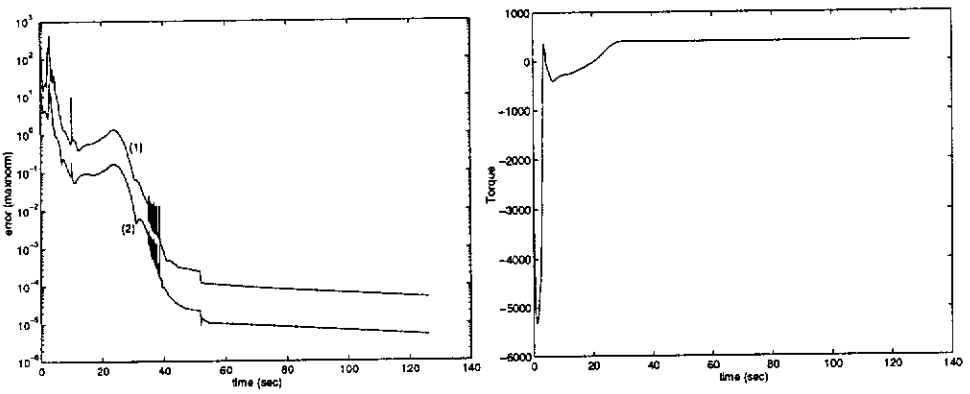

Figure 6.6: (a) Absolute errors for (1): $\|\tilde{Z}^{k+1} - \tilde{Z}^k\|_\infty$ and (2): $\|\tilde{\Psi}^{k+1} - \tilde{\Psi}^k\|_\infty$. (b) Torque along the rotor when $Re = 1000, \bar{U} = 10.0$ and $\bar{\epsilon} = 0.5$.

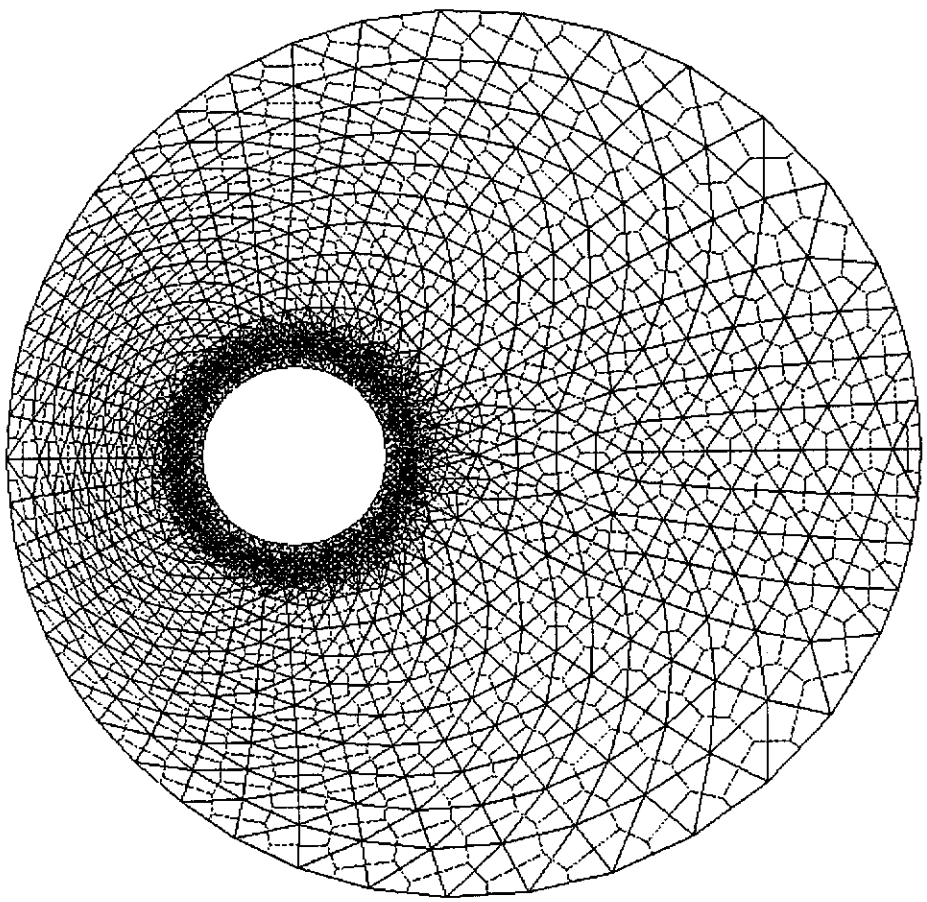

Figure 6.7: Mesh B (1340 nodes).

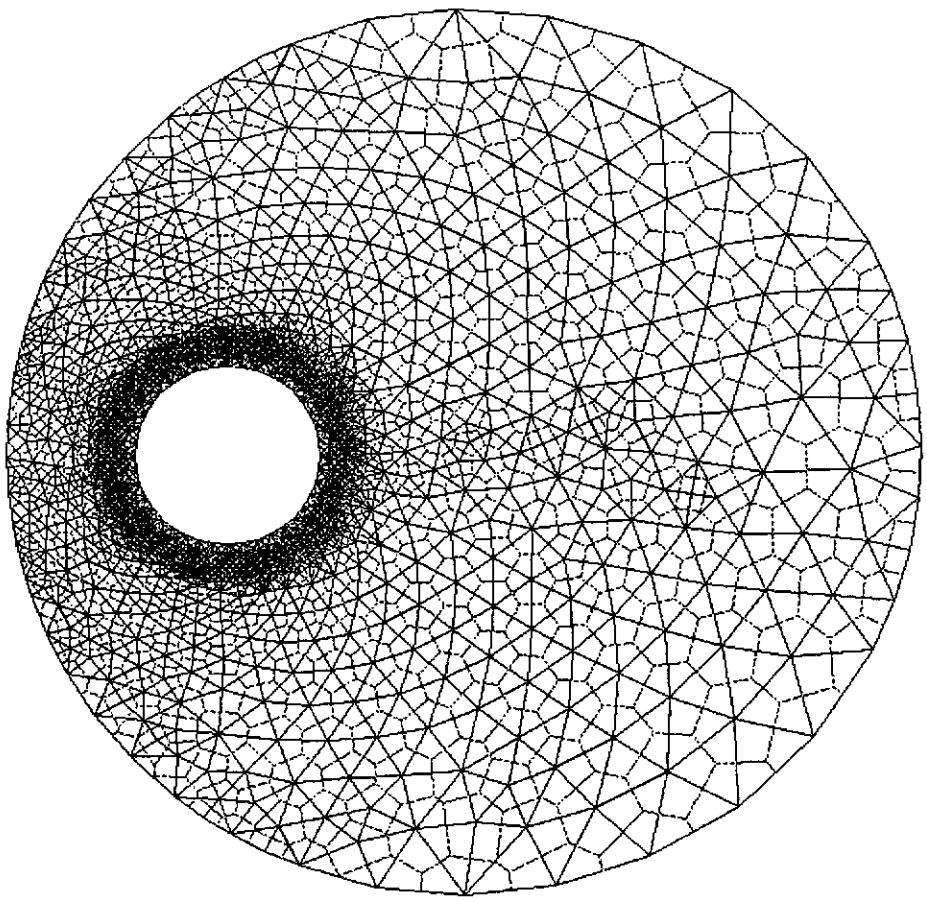

Figure 6.8: Mesh C (1352 nodes).

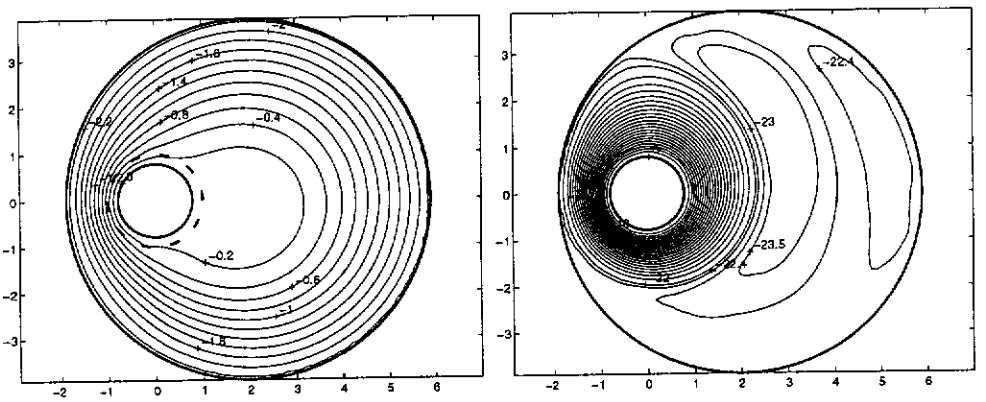

$(a)\bar{U} = 1.7$ $(b)\bar{U} = 2.0$

Figure 6.9: Contour plots for $Re = 500, \bar{\epsilon} = 0.7$ and various $\bar{U}$.

on the rotor and the stream function at the centre of the primary eddy while the vorticity there increases.

$\bar{U}$	(x_c, y_c)	ψ_c	ζ_c	T
2.0	(2.20, 2.29)	-24.21	-7.63	1470.85
5.0	(2.20, 2.29)	-24.58	-7.50	1216.37
10.0	(2.20, 2.29)	-25.49	-7.07	858.48

Table 6.4: Values ψ and ζ at (x_c, y_c) and torque along the rotor for $Re = 500.0$, $\bar{\epsilon} = 0.70$ and various $\bar{U}$.

Varying the eccentricity of the system influences both the presence of eddies and their location. Consider problems $\{500.0, 0.5, 10.0\}$ and $\{500.0, 0.7, 10.0\}$, their solution fields are given in Fig. 6.10. For small eccentricities, and sufficiently large $\bar{U}$, the centrifugal force produced by the rotor enables circular flow to extend far into the main body of the domain. As the eccentricity is increased, the effect of this inertial force is reduced and the eddies produced cover a larger area of fluid. Furthermore, the centre of the primary eddy moves in the direction of rotation of the rotor. This is confirmed from the results given in the third line of Tables 6.4 and 6.5 which also show both ψ_c and the torque T increase while ζ_c decreases with increasing eccentricity.

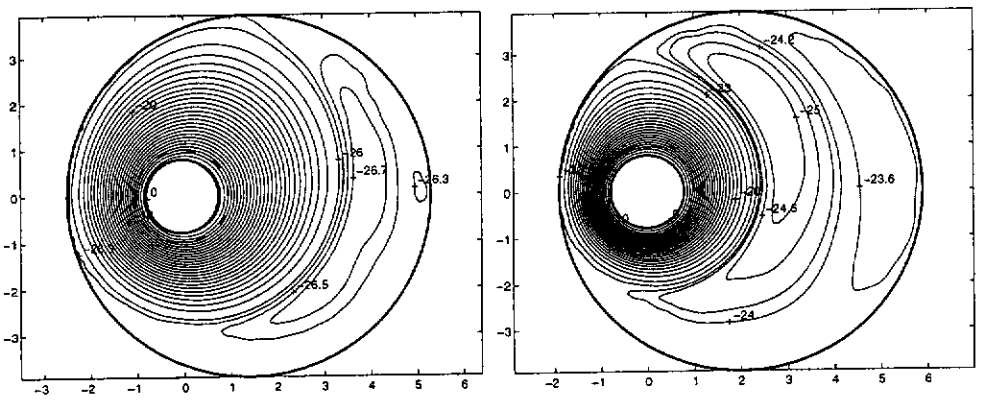

$(a)\bar{\epsilon} = 0.5$ $(b)\bar{\epsilon} = 0.7$

Figure 6.10: Contour plots for $Re = 500, \bar{U} = 10.0$ and various $\bar{\epsilon}$.

To study the effect of Reynolds number on the flow field, problems {50.0, 0.5, 10.0}, {100.0, 0.5, 10.0}, {500.0, 0.5, 10.0}, and {1000.0, 0.5, 10.0} are solved. Fig. 6.11 plots the stream function obtained for the extreme values of the Reynolds number. These results, together with the contour plot given in Fig. 6.10 for the case Re=500.0, suggest that the position of the primary eddy is unaffected by the change in Reynolds number. This is verified in Table 6.5 which also shows that ζ_c and the torque T increase while ψ_c decreases as the Reynolds number is increased. Although, on physical grounds, the secondary eddy must exist, there is insufficient detail from the results given to discuss its behaviour.

Re	(x_c, y_c)	ψ_c	ζ_c	T
50.0	(3.93, 0.00)	-23.66	-3.81	256.32
100.0	(3.93, 0.00)	-25.94	-3.80	354.21
500.0	(3.93, 0.00)	-26.92	-3.64	396.45
1000.0	(3.93, 0.00)	-27.00	-3.62	399.72

Table 6.5: Values of ψ and ζ at (x_c, y_c) and torque along the rotor for $\bar{\epsilon} = 0.5$, $\bar{U} = 10.0$ and various Reynolds numbers.

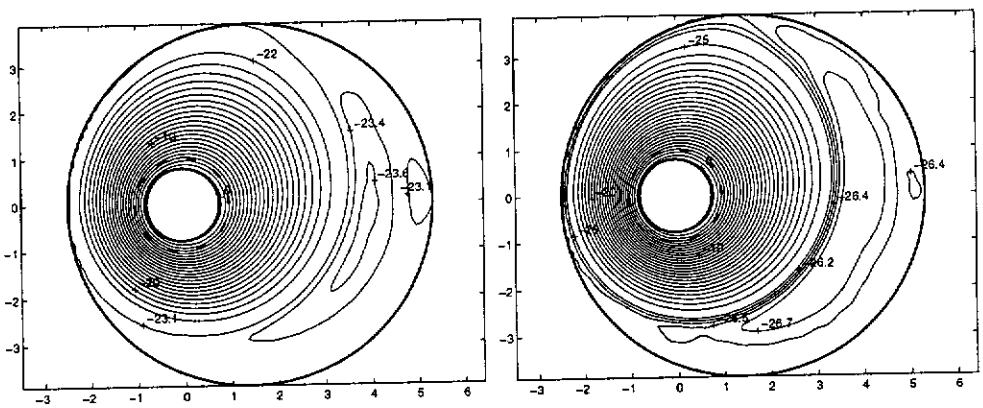

$(a) Re = 50.0$ $(b) Re = 1000.0$

Figure 6.11: Contour plots for $\bar{\epsilon} = 0.5$, $\bar{U} = 10.0$ and various Reynolds numbers.

6.1.1 The Vorticity Distribution

To investigate the development of vorticity within the flow domain as the Reynolds number is increased, we identify two lines located $\pm 42^o$ from the horizontal and passing through the centre of the bowl and also the horizontal line connecting the rotor to the bowl and passing through the main flow domain. The vorticity obtained by solving the problems $\{50.0, 0.5, 10.0\}$ and $\{1000.0, 0.5, 10.0\}$ are plotted along each of the three lines. The plots are given in Fig. 6.12. In each case the values of $|\zeta|$ is larger for the larger Reynolds number. From Fig. 6.12(a), it is clear that the rotor, sleeve and bowl are sources of vorticity. This vorticity decays quickly away from the sleeve and the bowl but varies only slightly across the wide-gap region. For the lines located diagonally across the apparatus the effect of the slotted sleeve is seen. In Figs. 6.12(b) and 6.12(c) the peak indicates when, along a given line, the vorticity is close to the slotted sleeve. From these results we can conclude that the vorticity generated along the slotted sleeve is diffused away from the sleeve and into the main flow field.

The high-Reynolds-number flow between two eccentric rotating cylinders possesses a viscous boundary layer along each boundary. Away from the

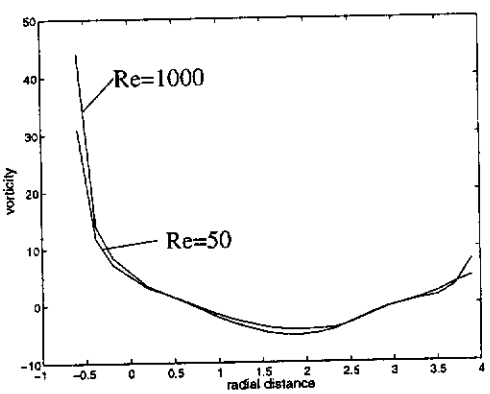

(a) $\theta = 0^o$

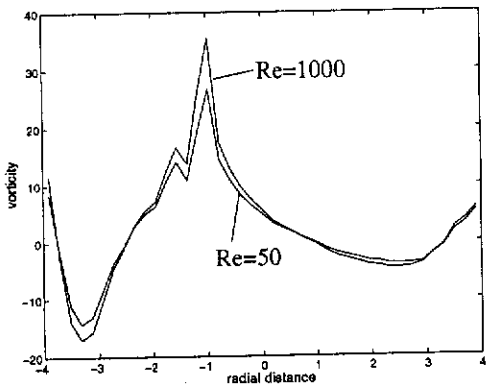

(b) $\theta = 42^o$

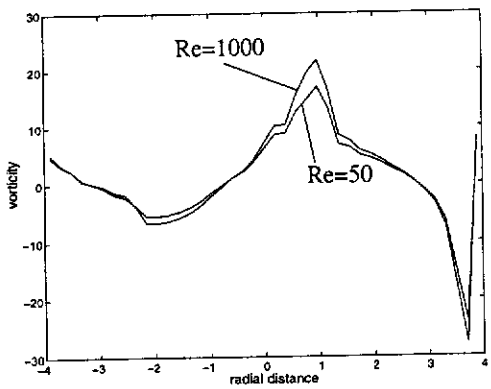

(c) $\theta = -42^o$

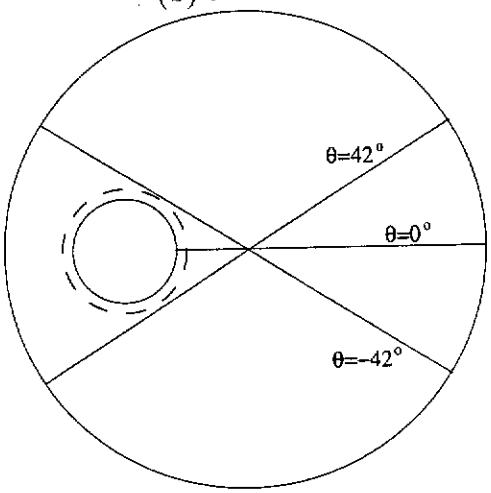

(d) The three lines across Ω.

Figure 6.12: Vorticity along three lines.

boundary layers the flow field consists of closed streamlines and, hence, the voriticity must be, nearly, constant in this region (see Batchelor [9]). We anticipate that an inviscid core will only be present in the limited case when there is no flow through the slotted sleeve (i.e., as $\bar{\epsilon} \rightarrow 0$), as the sleeve is a source of vorticity, and for problems ($\bar{\epsilon} \neq 0$) when the prescribed tangential velocities do not produce a stagnation point along the bounding cylinders.

6.2 Case Two:The Bounding Cylinders Rotate in Opposite Directions

For each problem considered, a pair of contour plots is used to examine the flow field. The first contour plot is used to illustrate the entire flow field using a contour spacing of 0.2 and the second contour plot describes the flow around the sleeve in more detail using a streamline spacing of 0.1.

Consider the problems $\{500.0, 0.2, -5.0\}$, $\{500.0, 0.5, -5.0\}$ and $\{500.0, 0.7, -5.0\}$ whose solution fields are given in Fig. 6.13. An eddy, rotating counter-clockwise, is generated for an eccentricity as small as 0.2. From Fig. 6.13, the presence of the eddy does not restrict the flow through the slotted sleeve which is predominently through the side closest to the eddy. As the eccentricity is increased, the amount of fluid flowing through the contraction (i.e., the region where the slotted sleeve is closest to the bowl) is reduced and more fluid now enters the annulus from the side closest to the eddy which is now moving in the direction of the rotation of the bowl. This is verified from Table 6.6 which gives the torque, T, the eddy centre as well as the stream function (ψ_c) and vorticity (ζ_c) values there. In addition to the movement of the eddy, the flow through the sleeve increases with increasing eccentricity. According to Table 6.6, the vorticity at the eddy centre decreases, while the stream function at the eddy centre increases with increasing eccentricity. Fig.

6.13 shows the presence of stagnation points and suggests that the flow within the annular region is bidirectional.

$\bar{\epsilon}$	(x_c, y_c)	ψ_c	ζ_c	T
0.2	$(1.27, -0.87)$	0.75	1.20	233.05
0.5	$(2.25, -0.36)$	1.24	0.80	227.60
0.7	$(2.81, -0.21)$	1.43	0.67	236.41

Table 6.6: Values of ψ and ζ at (x_c, y_c) and torque along the rotor using meshes A, B and C.

The effect of the rotational speed of the rotor is studied by considering the problems $\{500.0, 0.7, -5.0\}$, $\{500.0, 0.7, -10.0\}$ and $\{500.0, 0.7, -20.0\}$. From Fig. 6.14 we see that as the rotational speed of the rotor is increased (i.e., $|\bar{U}|$ is increased), the flow through the slotted sleeve and through the contraction become restricted causing the eddy centre to move in the direction of the rotation of the rotor. Table 6.7 confirms the motion of the eddy and also shows that ψ_c, ζ_c as well as the torque, T, increase with increasing rotational speed.

$\bar{U}$	(x_c, y_c)	ψ_c	ζ_c	T
-5.0	$(2.81, -0.21)$	1.43	0.67	236.41
-10.0	$(2.85, -0.50)$	2.28	0.71	449.81
-20.0	$(2.91, -0.94)$	5.09	0.99	839.14

Table 6.7: Values of ψ and ζ at (x_c, y_c) and torque along the rotor for $Re = 500.0$, $\bar{\epsilon} = 0.7$ and various $\bar{U}$.

Problems $\{50.0, 0.5, -10.0\}$, $\{100.0, 0.5, -10.0\}$, $\{500.0, 0.5, -10.0\}$ and $\{1000.0, 0.5, -10.0\}$ are solved in order to study the effect of the Reynolds number on the flow field. The contour plots for the extreme values of the Reynolds

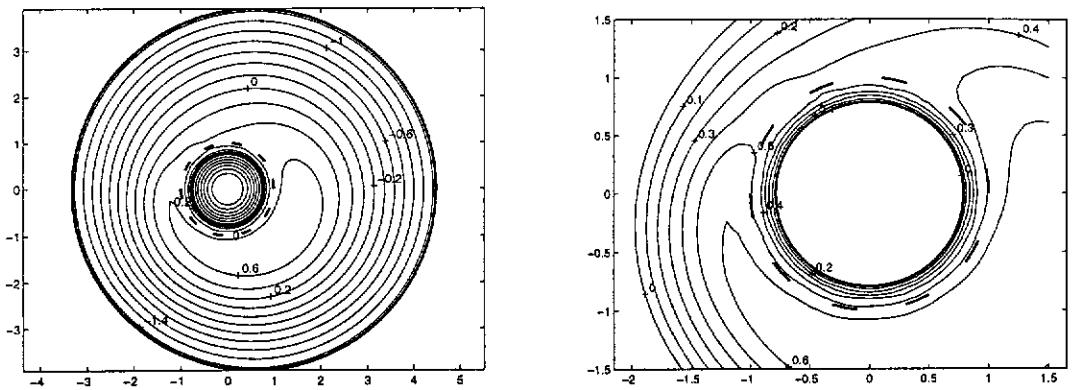

$(a)\bar{\epsilon} = 0.2$

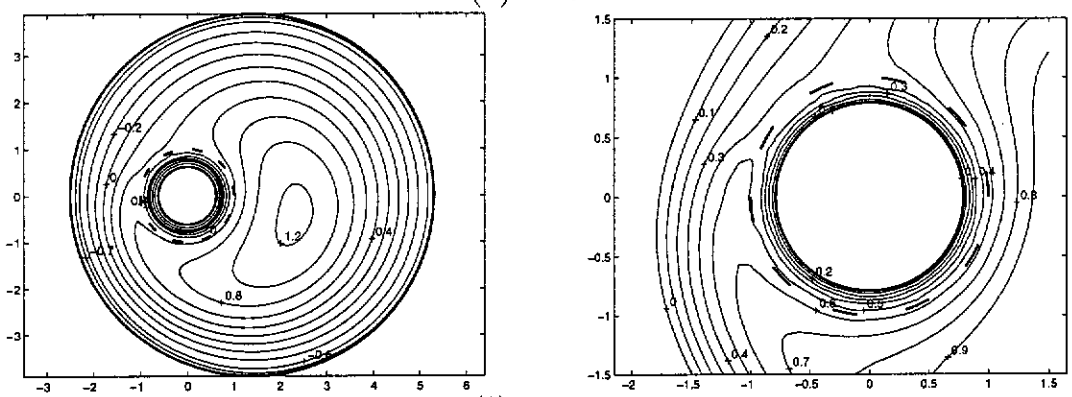

$(b)\bar{\epsilon} = 0.5$

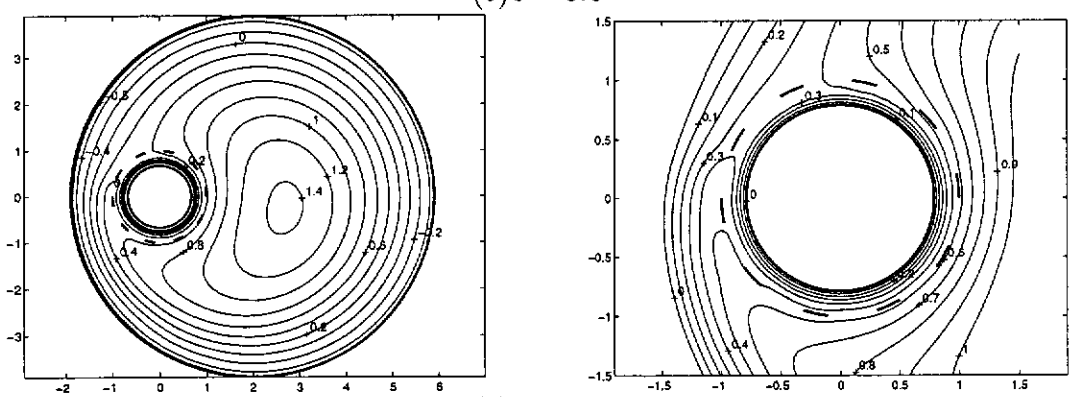

$(c)\bar{\epsilon} = 0.7$

Figure 6.13: Contour plots in the entire flow field and around the sleeve for $Re = 500, \bar{U} = -5.0$ and various $\bar{\epsilon}$.

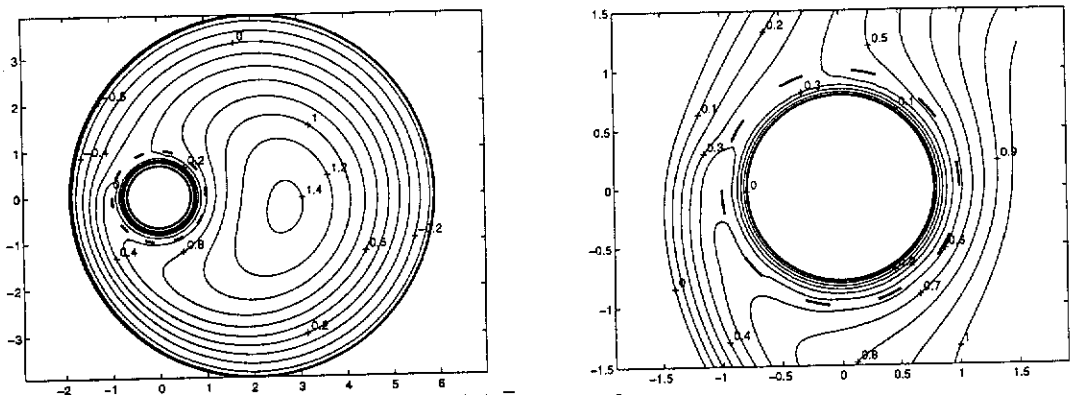

$(a)\bar{U} = -5.0$

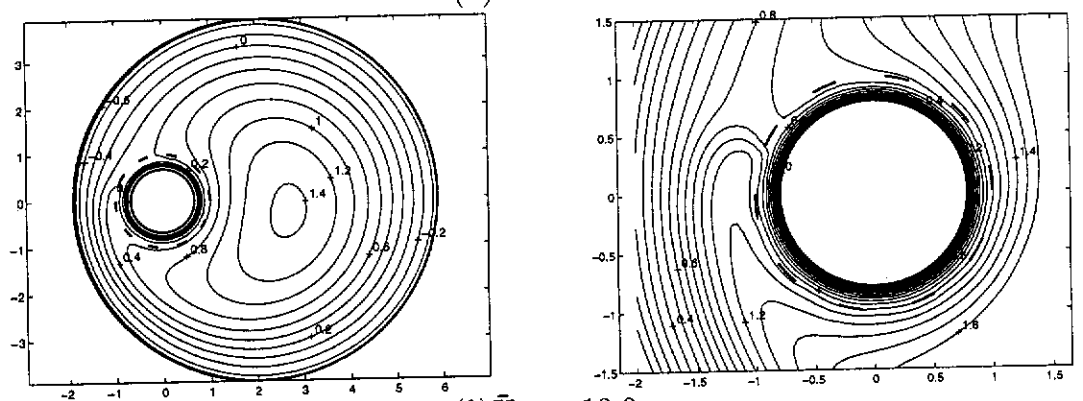

$(b)\bar{U} = -10.0$

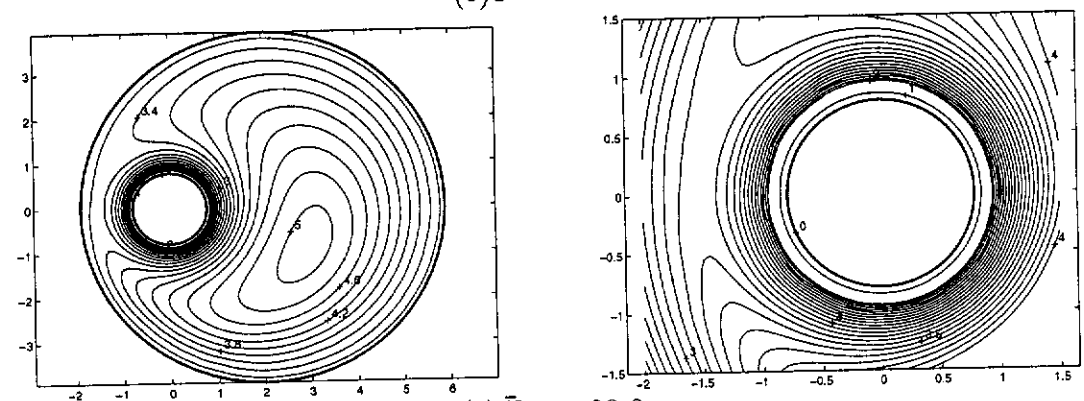

$(c)\bar{U} = -20.0$

Figure 6.14: Contour plots in the entire flow field and around the sleeve for $Re = 500, \bar{\epsilon} = 0.7$ and various $\bar{U}$.

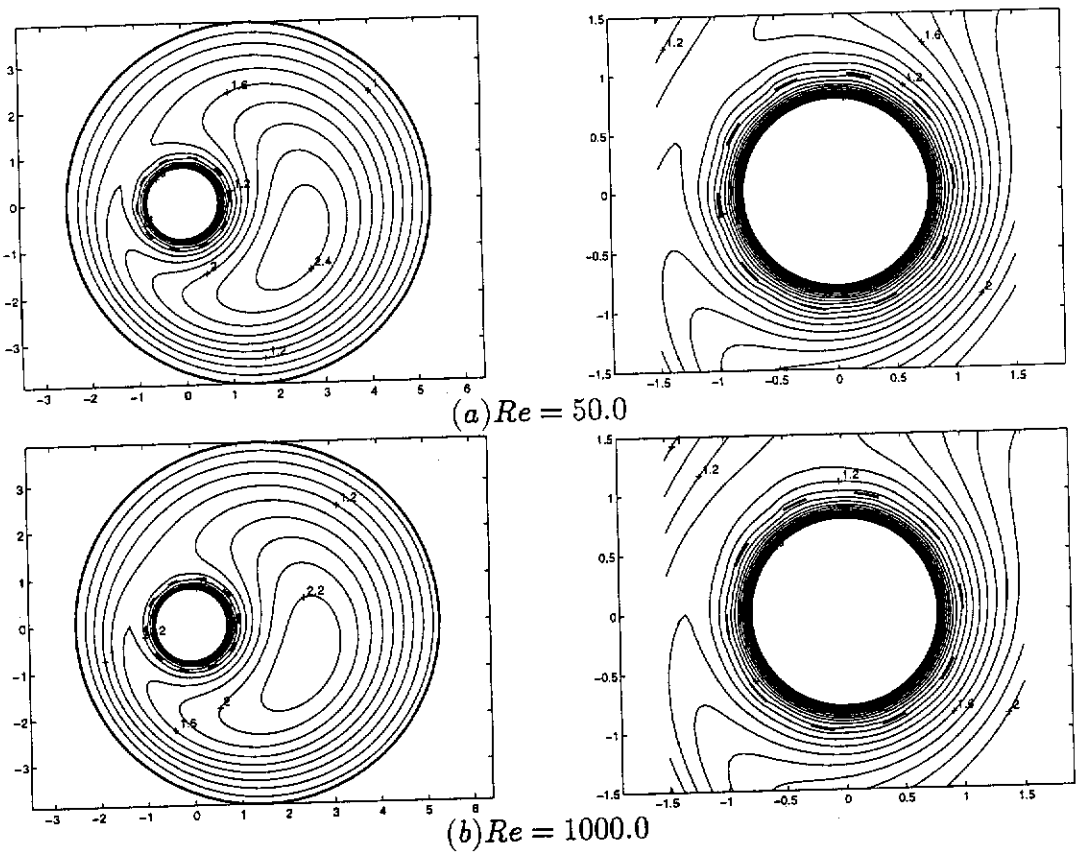

Figure 6.15: Contour plots in the entire flow field and around the slotted sleeve for $\bar{\epsilon} = 0.5$, $\bar{U} = -10.0$ and various Reynolds numbers.

number are displayed in Fig. 6.15 which indicates that the Reynolds number has little effect on the flow field. Table 6.8 shows that although the eddy centre is approximately independent of the Reynolds number, the computed values of the stream function and vorticity are changed by this parameter.

6.2.1 The Vorticity Distribution

The same lines as for case one are used to study the vorticity in the flow domain, see Fig. 6.12(d). From problems $\{50.0, 0.5, -10.0\}$ and $\{1000.0, 0.5, -10.0\}$, the vorticity along the horizontal axis, along $\theta = 42^{\circ}$ and along $\theta = -42^{\circ}$ are given in Fig. 6.16. These figures clearly show that the vorticity generated along the slotted sleeve is concentrated in a small neighbourhood about the

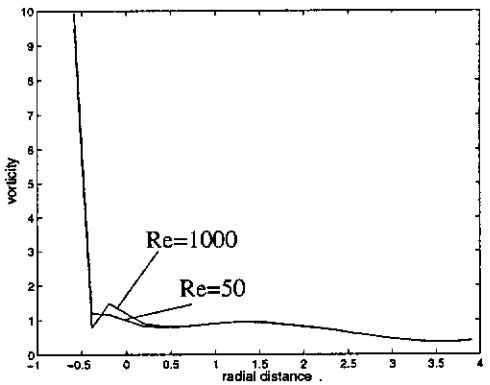

(a) $\theta = 0^o$

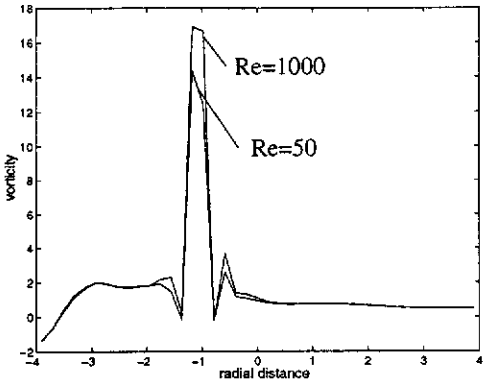

(b) $\theta = 42^o$

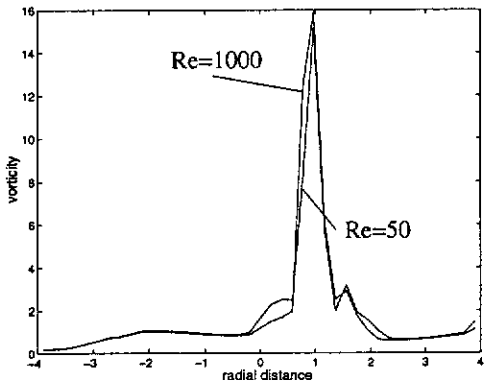

(c) $\theta = -42^o$

Figure 6.16: Vorticity along three lines.

Re	(x_c, y_c)	ψ_c	ζ_c	T
50.0	$(2.39, -0.71)$	2.52	0.96	456.16
100.0	$(2.39, -0.71)$	2.47	0.95	442.49
500.0	$(2.39, -0.71)$	2.37	0.91	430.73
1000.0	$(2.39, -0.71)$	2.35	0.90	430.01

Table 6.8: Values of ψ and ζ at (x_c, y_c) and torque along the rotor for $\bar{\epsilon} = 0.5$, $\bar{U} = -10.0$ and various Reynolds numbers.

sleeve. Consequently, the vorticity generated along the no-slip surfaces is not diffused into the main flow domain. This is in contrast to the case when the bounding cylinders rotate with the same sense (cf. Fig. 6.12).

6.3 Summary

The flow between two eccentric rotating cylinders with a slotted sleeve placed around the inner cylinder was determined numerically using the exponentially fitted finite volume method of Miller and Wang [60]. The flow field was determined for various Reynolds numbers, eccentricities and rotational rates when the cylinders rotate in the same sense (case one) and in opposite senses (case two).

For case one, the flow field was characterised, for sufficiently large eccentricity and rotational rate, by the presence of two counter-rotating eddies within the main flow domain. The dominant eddy rotates clockwise while the sub-dominant eddy located along the outer cylinder rotates counter-clockwise. The presence of these eddies restricted the flow through the slotted sleeve. Increasing the rotational speed of the inner cylinder had little effect on the flow field; however, as the eccentricity increased, the eddies moved in the direction of rotation of the bounding cylinders.

For case two, it was shown that eddies occur within the flow field for eccentricities as small as 0.2. As the eccentricity increased the eddy was seen to move in the direction of the rotation of the outer cylinder and the presence of the eddy promoted the flow through the slotted sleeve. When the rotational speed of the inner cylinder increased, the eddy moved in the direction of the inner cylinder.

No inviscid core was observed for either case one or case two for the high-Reynolds-number flow. In case one, the presence of the slotted sleeve allowed the vorticity generated there to be diffused into the main flow domain; however, little diffusion occured in case two.

Finally, we note that for the high-Reynolds-number flow between two eccentric rotating cylinders, Chipman and Duck [24] show that the existence of a stagnation point on the bounding cylinders is dependent on the relative rotational rate of the cylinders and the eccentricity of the system. For example, from their Fig. 3b, a stagnation point along the boundary layer on the inner cylinder occurs when $\bar{U} \approx 5.0$ and $\bar{\epsilon} \approx 0.35$ and a stagnation point located on the outer cylinder is found when $|\bar{U}| \approx 1.0$ and $\bar{\epsilon} \approx 0.35$. No Reynolds numbers are given at these instances as the the existence of a critical Reynolds number above which the flow in the boundary layers fails to be unidirectional is currently an open problem. Furthermore, according to Rosenhead [76, pages 505–506], this stagnation-point boundary-layer flow can also cause centrifugal instability. The connection between Reynolds number and centrifugal instability has been demonstrated experimentally. For example, in the experimental work of Versteegen and Jankowski [91] conditions for the generation of Taylor vorticies are given. For example, from their Fig. 7 instability first occurs when, using our parameters, $Re \approx 300.0$ and $\bar{U} \approx 2.0$ for an eccentricity of 0.5. Although no direct comparison can be made with the results given in [91] or [24], the problems considered here are well beyond the conditions stated above,

albeit using a relatively coarse mesh, we suspect the presence of the slotted sleeve may have a stabilising effect. The stability of the model considered here needs to be investigated in order to understand fully the role of the slotted sleeve on the flow field.

Chapter 7

Model Three: Determining the Flow Fields generated by Pseudoplastic Fluids

Most slurries are heterogeneous mixtures possessing viscoplastic behaviour; however, there are circumstances when slurries can be modelled successfully using a homogeneous pseudoplastic fluid that does not possess a yield stress. For example, if the concentration of the particles in a slurry is low, no yield stress will be present and the slurry is pseudoplastic in behaviour. Also, Logos and Nguyen [54] have shown for coal-water slurries, that the rheological behaviour of a slurry can be influenced by the size distribution of the suspended particles: the addition of coarse particles to a slurry can cause its rheological behaviour to be changed from viscoplastic to pseudoplastic. By using pseudoplastic fluids, the influence of the non-linear viscosity effects on the flow field can be studied without the need to determine a yield surface. From the work of Phan-Thien et al [71], locating the regions of low shear rate may indicate where the particles in a slurry are likely to agglomerate within the actual viscometer. Equation (2.1.13), together with the boundary conditions on the stream function given in (2.1.14) and (2.1.15) and boundary conditions for the vorticity at no-slip boundaries, govern the laminar flow of an incompressible pseudoplastic fluid in the flow domain shown in Fig. 2.1. To ensure the apparent viscos-

ity $h(\dot{\gamma})$ remains bounded, the bi-viscosity model introduced by Tanner and Milthorpe [87] is used. For power law fluids, the stress and vorticity functions become unbounded at re-entrant corners and strategies used in an attempt to obtain reliable results include establishing the behaviour of these functions via asymptotic means and local mesh refinement (see Crochet et al [28] and Hendriksen and Hassager [40]). As in the second model, where Newtonian fluids are used, we employ the simple strategy of assuming the slotted sleeve has zero thickness and refine the mesh around the sleeve to determine the vorticity and apparent viscosity along the sleeve. We now outline the discretisation and assembly of the governing equations and describe a scheme used to obtain steady-state (i.e., long-term) solutions.

7.1 Discretising the Governing Equations

The method used in the second model to decomposed the flow field Ω is used here, that is, by constructing the Delaunay triangulation (T_h) and Voronoi tessellation (D_h) of the domain. Integrating the first equation in (2.1.13) over each tessellation (d_i) and applying Green's theorem yields

$$\int_{d_i} \frac{\partial \zeta}{\partial t} dA - \int_{\partial d_i} \mathbf{F}_1 \cdot \mathbf{n} ds = \int_{\partial d_i} \mathbf{f} \cdot \mathbf{t} ds, \tag{7.1.1}$$

where

$$\mathbf{F}_1 = Sh\nabla\zeta - [\mathbf{v} + S\nabla h]\,\zeta, \tag{7.1.2}$$

and

$$\mathbf{f} = 2S\,(\nabla h \cdot \nabla)\,\mathbf{v}. \tag{7.1.3}$$

Writing $\mathbf{f}\cdot\mathbf{t} = \mathbf{F}_2\cdot\mathbf{n}$ and assuming ζ is piecewise constant over each tessellation, equation (7.1.1) can be written as

$$\frac{\partial \zeta_i}{\partial t}|d_i| - \sum_{j \in I_i} \int_{l_{ij}} (\mathbf{F}_1 + \mathbf{F}_2) \cdot \mathbf{n} ds = 0, \qquad i = 1, 2, \ldots, N_\nu \tag{7.1.4}$$

where $\mathbf{F_2} = (\mathbf{f} \times \mathbf{k})$, $\zeta_i = \zeta(\boldsymbol{x}_i, t)$, $|d_i|$ denotes the area of d_i and I_i represents the index set of neighbouring nodes to the interior node $\boldsymbol{x}_i$. Also, N_ν denotes the number of interior nodes in T_h. The notation used here to denote the edges and nodes of the dual meshes is consistent with the notation used in the second model (see Fig. 5.1). As the integrations in (7.1.4) are performed along the sides of a control volume, we introduce a coordinate system, local to each side l_{ij}, defined by the unit outward and tangential vectors $\mathbf{n}$ and $\mathbf{t}$ respectively (see Fig. 7.1). Thus, along each l_{ij}, $\mathbf{F_1}$ and $\mathbf{F_2}$ are given by

$$\mathbf{F_1} = \left[Sh\frac{\partial \zeta}{\partial n} - \left(u + S\frac{\partial h}{\partial n}\right)\zeta, Sh\frac{\partial \zeta}{\partial t} - \left(v + S\frac{\partial h}{\partial t}\right)\zeta, 0 \right] \tag{7.1.5}$$

and

$$\mathbf{F_2} = (\mathbf{f} \times \mathbf{k}) = 2S\left[\frac{\partial h}{\partial n}\frac{\partial v}{\partial n} + \frac{\partial h}{\partial t}\frac{\partial v}{\partial t}, -\frac{\partial h}{\partial n}\frac{\partial u}{\partial n} - \frac{\partial h}{\partial t}\frac{\partial u}{\partial n}, 0 \right] \tag{7.1.6}$$

where u and v denote the velocity in the directions of $\mathbf{n}$ and $\mathbf{t}$ respectively. Also within the flow domain, we have

$$h(\dot{\gamma}) = k_1 (\dot{\gamma})^{\alpha - 1} \tag{7.1.7}$$

where

$$\dot{\gamma}^2 = \zeta^2 - 4\frac{\partial(u_x, u_y)}{\partial(x, y)}, \tag{7.1.8}$$

with $\mathbf{v} = [u_x, u_y]$.

As in the previous model, the velocity normal to the face l_{ij} (i.e., u in the current model) is assumed constant along all perpendiculars to l_{ij}. For an incompressible fluid, this implies

$$\frac{\partial u}{\partial n} = 0, \quad \frac{\partial u}{\partial t} = 0 \quad \text{and} \quad \frac{\partial v}{\partial t} = 0 \tag{7.1.9}$$

along each l_{ij}. Using equations (7.1.5), (7.1.6) and (7.1.9), equation (7.1.4) simplifies to

$$\frac{\partial \zeta_i}{\partial t}|d_i| - \sum_{j \in I_i} \int_{l_{ij}} Sh\frac{\partial \zeta}{\partial \mathbf{n}} - \left(u - S\frac{\partial h}{\partial \mathbf{n}}\right)\zeta ds = 0, \qquad i = 1, 2, \ldots, N_\nu. \tag{7.1.10}$$

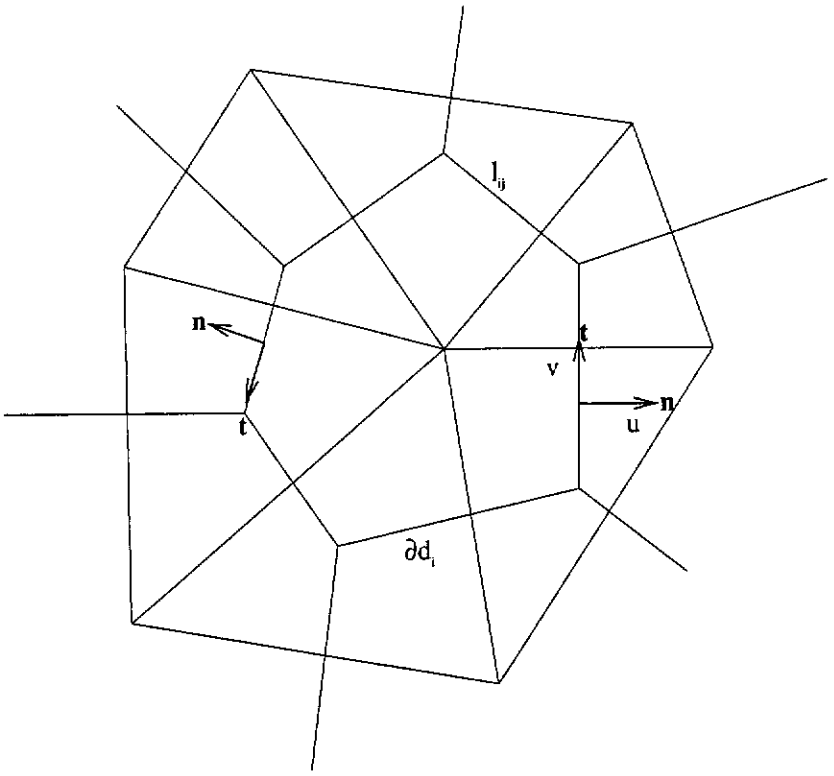

Figure 7.1: The local coordinate system around a Voronoi polygon.

To estimate $\dot{\gamma}$ and, therefore, $h(\dot{\gamma})$, we use the mean square of $\dot{\gamma}$ over each side of the tessellation, viz

$$\begin{aligned} < \dot{\gamma}_i^2 > &= \frac{1}{|d_i|} \int_{d_i} \dot{\gamma}^2 dA \\ &= < \zeta_i^2 > - \frac{4}{|d_i|} \sum_{j \in I_i} \int_{l_{ij}} u_x \frac{\partial u_y}{\partial s} ds, \qquad i = 1, 2, \ldots, N_\nu. \end{aligned} \tag{7.1.11}$$

By assuming $h(\dot{\gamma})$ is piecewise constant over each tessellation and applying the approximations

$$u = \frac{\partial \psi}{\partial \mathrm{t}} \approx \frac{\psi_{ij;2} - \psi_{ij;1}}{|l_{ij}|} = \bar{u}_{ij} \tag{7.1.12}$$

and

$$\frac{\partial h}{\partial \mathrm{n}} \approx \frac{h_j - h_i}{|e_{ij}|} = \bar{h}_{ij}, \tag{7.1.13}$$

where $\psi_{ij;2}$ and $\psi_{ij;1}$ represent the nodal values of ψ at $\boldsymbol{x}_{ij;2}$ and $\boldsymbol{x}_{ij;1}$ given in

Fig. (5.1), equation (7.1.10) becomes

$$\frac{\partial \zeta_i}{\partial t}|d_i| - \sum_{j\in I_i}\int_{l_{ij}} Sh_i \frac{\partial \zeta}{\partial n} - \left(\bar{u}_{ij} - S\bar{h}_{ij}\right)\zeta ds = 0, \qquad i = 1, 2, \ldots, N_\nu. \quad (7.1.14)$$

This is approximated by

$$\frac{\partial \zeta_i}{\partial t}|d_i| - \sum_{j\in I_i}\frac{Sh_i|l_{ij}|}{|e_{ij}|}\left[B\left(\frac{\bar{u}_{ij} - S\bar{h}_{ij}}{Sh_i}|e_{ij}|\right)\zeta_j - B\left(-\frac{\bar{u}_{ij} - S\bar{h}_{ij}}{Sh_i}|e_{ij}|\right)\zeta_i\right] = 0 \quad (7.1.15)$$

where

$$Sh_i\frac{\partial \zeta}{\partial n} - \left(\bar{u}_{ij} - S\bar{h}_{ij}\right)\zeta = \frac{Sh_i}{|e_{ij}|}\left[B\left(\frac{\bar{u}_{ij} - S\bar{h}_{ij}}{Sh_i}|e_{ij}|\right)\zeta_j - B\left(-\frac{\bar{u}_{ij} - S\bar{h}_{ij}}{Sh_i}|e_{ij}|\right)\zeta_i\right] \quad (7.1.16)$$

(cf. equation (5.1.4)) and $B(x)$ represents the Bernoulli function defined in equation (5.1). We now introduce the implicit time discretisation

$$\frac{\partial \zeta_i}{\partial t} = \frac{\zeta_i^k - \zeta_i^{k-1}}{\Delta t_k} \quad \text{and} \quad \zeta_i = c\zeta_i^k + (1-c)\zeta_i^{k-1}. \quad (7.1.17)$$

The backward-Euler and Crank-Nicholson schemes correspond to $c = 1$ and $c = 1/2$ respectively. Therefore, for a given time sub-interval $[t_{k-1}, t_k] \in (0,\mathrm{T}]$, the system of linear equations generated to determine the vorticity at an interior node $\boldsymbol{x}_i$ at time step k (ζ_i^k) is given by

$$\begin{aligned}\zeta_i^k + \sum_{j\in I_i}\frac{c\sigma_{ij}^k\Delta t_k}{|d_i|}\left[B\left(-\frac{\bar{u}_{ij}^k - S\bar{h}_{ij}^k}{Sh_i^k}|e_{ij}|\right)\zeta_i^k - B\left(\frac{\bar{u}_{ij}^k - S\bar{h}_{ij}^k}{Sh_i^k}|e_{ij}|\right)\zeta_j^k\right] &= \zeta_i^{k-1} \\ + \sum_{j\in I_i}\frac{(c-1)\sigma_{ij}^k\Delta t_k}{|d_i|}\left[B\left(-\frac{\bar{u}_{ij}^k - S\bar{h}_{ij}^k}{Sh_i^k}|e_{ij}|\right)\zeta_i^{k-1} - B\left(\frac{\bar{u}_{ij}^k - S\bar{h}_{ij}^k}{Sh_i^k}|e_{ij}|\right)\zeta_j^{k-1}\right]\end{aligned} \quad (7.1.18)$$

where $\sigma_{ij}^k = \dfrac{Sh_i^k|l_{ij}|}{|e_{ij}|}$ and $\Delta t_k = t_k - t_{k-1}$. Using matrix notation, (7.1.18) is given by

$$\left(I + cD^k\right)Z^k + E^k = \left(I + [c-1]D^k\right)Z^{k-1}, \quad (7.1.19)$$

where I is the identity matrix,

$$d_{ii}^k = \Delta t_k \sum_{j\in I_i}\frac{\sigma_{ij}^k}{|d_i|}B\left(-\frac{\bar{u}_{ij}^k - S\bar{h}_{ij}^k}{Sh_i^k}|e_{ij}|\right), \quad (7.1.20)$$

$$d_{ij}^k = -\Delta t_k \frac{\sigma_{ij}^k}{|d_i|} B\left(\frac{\bar{u}_{ij}^k - S\bar{h}_{ij}^k}{Sh_i^k}|e_{ij}|\right) \quad \text{if } \boldsymbol{x}_j \notin \partial\Omega_1 \cup \partial\Omega_2 \cup \partial\Omega_3, \tag{7.1.21}$$

$$e_i^k = \begin{cases} -\sum_{j\in I_i} \Delta t_k \frac{\sigma_{ij}^k}{|d_i|} B\left(\frac{\bar{u}_{ij}^k - S\bar{h}_{ij}^k}{Sh_i^k}|e_{ij}|\right)\zeta_1^j & \text{if } \boldsymbol{x}_j \in \partial\Omega_1 \\ -\sum_{j\in I_i} \Delta t_k \frac{\sigma_{ij}^k}{|d_i|} B\left(\frac{\bar{u}_{ij}^k - S\bar{h}_{ij}^k}{Sh_i^k}|e_{ij}|\right)\zeta_2^j & \text{if } \boldsymbol{x}_j \in \partial\Omega_2 \\ -\sum_{j\in I_i} \Delta t_k \frac{\sigma_{ij}^k}{|d_i|} B\left(\frac{\bar{u}_{ij}^k - S\bar{h}_{ij}^k}{Sh_i^k}|e_{ij}|\right)\zeta_{3,q}^j & \text{if } \boldsymbol{x}_j \in \partial\Omega_3^q \\ 0 & \text{if } \boldsymbol{x}_j \notin \partial\Omega_1 \cup \partial\Omega_2 \cup \partial\Omega_3, \end{cases} \tag{7.1.22}$$

$$\text{and} \quad z_i^k = \zeta_i^k. \tag{7.1.23}$$

Here ζ_1^j, ζ_2^j and $\zeta_{3,q}^j$ represent the vorticity at node $\boldsymbol{x}_j$ along the no-slip boundaries and can be estimated at each time step. The approximations for these terms are given in equations (5.2.4), (5.2.5) and (5.2.6).

The Poisson equation in (2.1.13) can be discretised to determine the stream function field at each time step. The discretised system is given in equation (5.1.10); however, for convenience, the discretisation is rewritten below

$$A\Psi^k + B^k = Z^k, \tag{7.1.24}$$

where

$$a_{ii} = \sum_{j\in I_i} \frac{|l_{ij}|}{|e_{ij}||d_i|}, \tag{7.1.25}$$

$$a_{ij} = -\frac{|l_{ij}|}{|e_{ij}||d_i|} \text{ if } \boldsymbol{x}_j \notin \partial\Omega_1 \cup \partial\Omega_2 \cup \partial\Omega_3 \tag{7.1.26}$$

$$\text{and} \quad b_i^k = \begin{cases} -\sum_{j\in I_i} \frac{|l_{ij}|}{|e_{ij}||d_i|} K_2 & \text{if } \boldsymbol{x}_j \in \partial\Omega_2 \\ -\sum_{j\in I_i} \frac{|l_{ij}|}{|e_{ij}||d_i|} K_3^q & \text{if } \boldsymbol{x}_j \in \partial\Omega_3^q, q = 1, \ldots, s \\ 0 & \text{if } \boldsymbol{x}_j \notin \partial\Omega_2 \cup \partial\Omega_3. \end{cases} \tag{7.1.27}$$

From equation (7.1.11), we have a means of estimating the apparent viscosity in the flow field at each time step. As the velocity components u_x and u_y need to

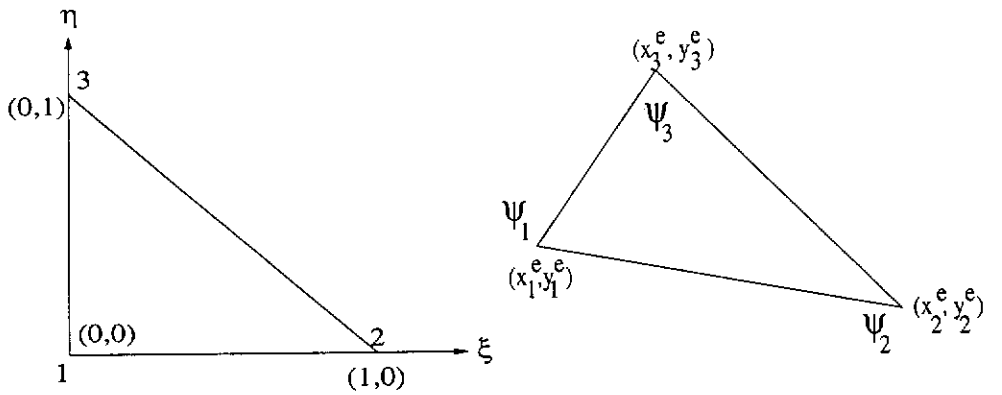

Figure 7.2: (a) Parent element for the linear isoparametric triangle. (b) A real element.

be determined at the vertices of each tessellation that is, at each circumcentre of the Delaunay triangles, a simple means of determining these components is by using linear isoparametric triangles. Using isoparametric elements the shape functions for each real element can be easily found. The parent element and a real element are shown in Fig. 7.2. On the parent element, the stream function can be interpolated using

$$\psi = \sum_{k=1}^{3} \psi_k \phi_k(\xi, \eta)$$

where the shape functions are given by $\phi_1(\xi,\eta) = 1 - \xi - \eta$, $\phi_2(\xi,\eta) = \xi$ and $\phi_3(\xi,\eta) = \eta$, and ξ and η are related to the physical plane through

$$\xi = \frac{\gamma(x - x_1^e) - \alpha(y - y_1^e)}{d}$$

and

$$\eta = \frac{\beta(y - y_1^e) - \delta(x - x_1^e)}{d}$$

with $\alpha = x_3^e - x_1^e$, $\beta = x_2^e - x_1^e$, $\gamma = y_3^e - y_1^e$ and $\delta = y_2^e - y_1^e$, and $d = \gamma\beta - \alpha\delta$ represents twice the area of the real element. Using the isoparametric element, we observe that

$$\begin{aligned} u_x = \frac{\partial \psi}{\partial y} &= \frac{\partial \psi}{\partial \xi}\frac{\partial \xi}{\partial y} + \frac{\partial \psi}{\partial \eta}\frac{\partial \eta}{\partial y} \\ &= -\frac{\alpha}{d}(\psi_2 - \psi_1) + \frac{\beta}{d}(\psi_3 - \psi_1) \end{aligned}$$

and

$$u_y = -\frac{\partial \psi}{\partial x} = -\frac{\gamma}{d}(\psi_2 - \psi_1) + \frac{\delta}{d}(\psi_3 - \psi_1).$$

Along l_{ij} we use

$$u_x \approx \frac{u_x|_{ij;1} + u_x|_{ij;2}}{2} = \bar{u}_{x_{ij}}$$

and

$$\frac{\partial u_y}{\partial s} \approx \frac{u_y|_{ij;2} - u_y|_{ij;1}}{|l_{ij}|} = \bar{u}_{y_{ij}}$$

to estimate u_x and $\frac{\partial u_y}{\partial s}$. Here $u_x|_{ij;1}$ and $u_x|_{ij;2}$ denote the value of u_x at $\boldsymbol{x}_{ij;1}$ and $\boldsymbol{x}_{ij;2}$ shown in Fig. (5.1). Likewise, $u_y|_{ij;1}$ and $u_y|_{ij;2}$ denote the value of u_y at $\boldsymbol{x}_{ij;1}$ and $\boldsymbol{x}_{ij;2}$. Thus, at each time step, the magnitude of the rate-of-deformation tensor at each interior node ($\dot{\gamma}_i^k$) is estimated from

$$\dot{\gamma}_i^k \approx \left[\left(\zeta_i^k\right)^2 - \frac{4|l_{ij}|}{|d_i|}\sum_{j\in I_i} \bar{u}_{x_{ij}}^k \bar{u}_{y_{ij}}^k\right]^{1/2}. \tag{7.1.28}$$

Since closed expressions for u_x and u_y along the no-slip surfaces are easily found, exact integration on these surfaces is used to determine $\int_{l_{ij}} u_x \frac{\partial u_y}{\partial s} ds$ when estimating $\dot{\gamma}$ at boundary nodes.

Once $\dot{\gamma}_i^k$ is found, the apparent viscosity over each tessellation can be determined through

$$h_i^k = \begin{cases} k_1\left(\dot{\gamma}_i^k\right)^{\alpha-1} & \text{for} \quad \dot{\gamma}_i^k > \dot{\gamma}_c, \\ k_1\left(\dot{\gamma}_c\right)^{\alpha-1} & \text{for} \quad \dot{\gamma}_i^k \leq \dot{\gamma}_c. \end{cases} \tag{7.1.29}$$

The methods used to estimate the Dirichlet conditions for both the stream and vorticity functions at each time step along the no-slip conditions are those used in the second model. Thus, the estimates given in equations (5.2.1), (5.2.3), (5.2.4), (5.2.5) and (5.2.6) are used here to estimate the behaviour of the stream and vorticity functions at the no-slip surfaces. Equations (7.1.19), (7.1.24) and (7.1.29) represent a non-linearly coupled system; however, this system can be linearised by solving the three equations in sequence. The iterative scheme used to decouple these equations will now be given.

7.2 Solving the Governing Equations in Sequence

The non-linear system given by equations (7.1.19), (7.1.24) and (7.1.29) is decoupled into a system of three linear equations. An iterative scheme is used to accomplish this where the outer (non-linear) iteration is denoted by k, thus, the three equations are solved only once per time step. At the inner level, each of the linear equations (i.e., equations (7.1.19) and (7.1.24)) is solved (approximately) using the CGS method given by Sonneveld [83]. Incomplete LU factorisation of the coefficient matrices is used to precondition the matrices, and n denotes the n^{th} iterate at the inner level. Due to the lack of information for the Dirichlet boundary conditions for the stream function, the discretised Poisson equation and estimates $\bar{K}_2$ and $\bar{K}_3^q$ are solved repeatedly until self-consistent solutions are obtained. The numerical stability of the solver for equations (7.1.19) and (7.1.24) is ensured if the coefficient matrices $I+cD^k$ and A are M-matrices. At first sight, A is an M-matrix and D^k is an L-matrix (i.e., $d_{ii}^k > 0$ and $d_{ij}^k \leq 0$ $(i \neq j)$). Using the property $B(x) \geq B(|x|)$, we can show that a sufficient condition for D^k to be diagonally dominant and, therefore, represent a non-singular M-matrix is that $\bar{u}_{ij}^k > S\bar{h}_{ij}^k$ for $j \in I_i$. However, we cannot determine if this condition holds in the entire flow domain. During the solution process, we can determine if $I+cD^k$ is an M-matrix from the diagonal entries of the lower and upper triangular matrices generated when performing the incomplete LU decomposition of the matrix. $I+cD^k$ is a non-singular M-matrix if all of the diagonal entries of L and U are positive (see Barnett [8]). For all problems considered in Chapter 8, $I+cD^k$ is a non-singular M-matrix, thus, ensuring the numerical stability of the CGS scheme. At the end of each time step (i.e., each outer iteration), $\left(\tilde{\Psi}^k, \tilde{Z}^k, H^k\right)$ denote the scalar fields for the stream, vorticity and viscosity functions, respectively, and the scalar fields

after a given number of time steps are compared to establish convergence. We use r to denote the sequence of solution fields, found at fixed time lengths, used to obtain steady-state solutions. The iterative scheme used to obtain steady-state (i.e., converged) solutions will now be outlined.

1. Choose tolerances ϵ_0, ϵ_1, ϵ_2, ϵ_3 and ϵ_4; smoothing parameters δ_1, δ_2 and $\delta_3 \in [0,1)$; and parameters α, k_1, S, $\bar{U}$ and $\dot{\gamma}_c$. Use a suitable initial guess for Z^k, $\bar{K}_2^{j,k}$, $\bar{K}_3^{j,k}$ and the viscosity function H^k. Put $j,k,r=0$. Choose the size of time step Δt_k and the time increment (ti) over which comparisons of the solution fields are made.

2. Solve (7.1.24) i.e.,

$$A\Psi^{j+1,k+1} + B^{j+1,k+1} = Z^k$$

iteratively using the CGS (with preconditioning) until

$$\|\Psi^{j+1,n} - \Psi^{j+1,n-1}\|_\infty < \epsilon_0.$$

$\Psi^{j+1,n}$ denotes the estimate for $\Psi^{j+1,k+1}$ after n iterations of the CGS method.

3. Update $\bar{K}_2^{j+1,k+1}$ and $\bar{K}_3^{j+1,k+1}$ using (5.2.3) and (5.2.1) and the smoothing parameter δ_1 i.e.,

$$\left.\begin{aligned} \bar{K}_2^{j+1,k+1} &:= (1-\delta_1)\bar{K}_2^{j+1,k+1} + \delta_1 \bar{K}_2^{j,k+1} \\ \bar{K}_3^{j+1,k+1} &:= (1-\delta_1)\bar{K}_3^{j+1,k+1} + \delta_1 \bar{K}_3^{j,k+1}. \end{aligned}\right\}$$

4. Put $j = j+1$ and repeat steps $2-3$ until the following convergence criterion is met

$$\max\left\{|\bar{K}_2^{j+1,k+1} - \bar{K}_2^{j,k+1}|, \|\bar{K}_3^{j+1,k+1} - \bar{K}_3^{j,k+1}\|_\infty\right\} < \epsilon_1.$$

5. Put $\Psi^{k+1} = \Psi^{j+1,k+1}$, $\bar{K}_2^{k+1} = \bar{K}_2^{j+1,k+1}$ and $\bar{K}_3^{k+1} = \bar{K}_3^{j+1,k+1}$, and use Ψ^{k+1}, $\bar{K}_2^{k+1}$ and $\bar{K}_3^{k+1}$ to define the nodal values of the stream function at time step $k+1$ $\left(\tilde{\Psi}^{k+1}\right)$.

6. Approximate vorticity at the no-slip surfaces, Z_b^{k+1}, using (5.2.4), (5.2.5) and (5.2.6). Smooth these values using the parameter δ_2, i.e.,

$$Z_b^{k+1} := (1-\delta_2)Z_b^{k+1} + \delta_2 Z_b^{k+1}.$$

7. Solve (7.1.19) i.e.,

$$\left(I + cD^{k+1}\right) Z^{k+1} + E^{k+1} = \left(I + [c-1]D^{k+1}\right) Z^k$$

iteratively using the CGS (with preconditioning) until

$$\|Z^{k+1,n} - Z^{k+1,n-1}\| < \epsilon_0.$$

$Z^{k+1,n}$ denotes the estimate for Z^{k+1} after n iterations of the CGS method. Smooth Z^{k+1} using δ_2, i.e.,

$$Z^{k+1} := (1-\delta_2)Z^{k+1} + \delta_2 Z^{k+1}.$$

Use Z_b^{k+1} and Z^{k+1} to define the vorticity field at the current time step $(\tilde{Z}^{k+1})$.

8. Determine the magnitude of the rate-of-deformation tensor at each node $(\dot{\gamma}_i^{k+1})$ using equation (7.1.28), ie.,

$$\dot{\gamma}_i^{k+1} \approx \left[\left(\tilde{\zeta}_i^{k+1}\right)^2 - \frac{4|l_{ij}|}{|d_i|}\sum_{j\in I_i} \bar{u}_{x_{ij}}^{k+1}\bar{u}_{y_{ij}}^{k+1}\right]^{1/2}.$$

where $\tilde{Z}^{k+1} = [\tilde{\zeta}_i^{k+1}]$.

9. Using the bi-viscosity model given in (7.1.29), i.e.,

$$h_i^{k+1} = \begin{cases} k_1 \left(\dot{\gamma}_i^{k+1}\right)^{\alpha-1} & \text{for} \quad \dot{\gamma}_i^{k+1} > \dot{\gamma}_c, \\ k_1 \left(\dot{\gamma}_c\right)^{\alpha-1} & \text{for} \quad \dot{\gamma}_i^{k+1} \leq \dot{\gamma}_c, \end{cases}$$

estimate the current viscosity function in the flow field (H^{k+1}). Smooth this function using δ_3

$$H^{k+1} := (1 - \delta_3)H^{k+1} + \delta_3 H^k.$$

10. Put $k = k + 1, j = 0$ and repeat steps $2 - 9$ until $k + 1 \bmod ti/\Delta t_k = 0$. Put $\tilde{\Psi}^{k+1} = \tilde{\Psi}^{r+1}$, $\tilde{Z}^{k+1} = \tilde{Z}^{r+1}$, $H^{k+1} = H^{r+1}$ and $r = r + 1$. Check for steady-state fields over the time length ti. Steady-state is reached if

$$\|\tilde{\Psi}^{r+1} - \tilde{\Psi}^r\|_\infty < \epsilon_2, \quad \|\tilde{Z}^{r+1} - \tilde{Z}^r\|_\infty < \epsilon_3 \quad \text{and} \quad \frac{\|H^{r+1} - H^r\|_\infty}{\|H^{r+1}\|_\infty} < \epsilon_4. \tag{7.2.1}$$

Here $\|\cdot\|_\infty$ represents the maximum norm. Comparing the algorithm given above with the algorithm given in Section 5.3, we observe that in the current model, accurate solutions at the intermediate steps are not obtained but rather the long-term solution is looked for instead. To study the behaviour of the non-Newtonian fluid in the flow domain, we apply the above algorithm when $\bar{\epsilon} = 0.7$, $0.2 \leq S \leq 5.0$, $-2.0 \leq \bar{U} \leq -10.0$, $0.2 \leq \alpha \leq 0.8$ and $10^{-3} \leq \dot{\gamma} \leq 1.0$. The convergence criteria given in step 10 becomes increasingly more difficult to satisfy as either S or $|\bar{U}|$ become large or when α is made small. The rate of convergence of the iterative scheme is at best linear and is affected by the initial guess and also by the length of the time step, Δt_k, used. The choice of initial guess depends on the parameters $(S, \alpha, \bar{U})$ to be solved for. If the flow pattern is wanted for large S or $|\bar{U}|$, we use the steady-state (i.e., converged) solution to a problem with smaller S or $|\bar{U}|$ as the initial guess. A similar process is used when obtaining steady-state solutions for small α,

i.e., the steady-state solution for a higher α is used as the inital guess. We also note that the use of the smoothing parameters, together with obtaining self-consistent solutions for the stream function at the interior and the no-slip boundaries, are essential for the stability of the iterative scheme. Some success can be made in speeding up the solution process if large time steps are used initially; however, this technique does not work for all ranges of the parameters used to study the flow pattern. To obtain converged solutions for high values for S, $|\bar{U}|$ or low values for α, a suitable initial guess is applied and time steps of no larger than 10^{-3} are used. As small time steps are used in our solution process, we discretise the time component using the Crank-Nicholson scheme. Thus, we put $c = 1/2$ in equation (7.1.19). Steady-state solutions for the stream function, vorticity function and viscosity function were established when the error in each of these scalar fields, over a (non-dimensional) time length of 0.1, is sufficiently small. Therefore, errors are computed between scalar fields over this time length. Using this approach, there are at least 100 time steps between each comparison step and up to 30, 000 time steps have been needed to obtain converged solutions. The dimensionless torque exerted on the rotor (T_p) by the pseudoplastic fluid can be estimated. Given

$$T_p = \int_0^{2\pi} h(\dot{\gamma})\, e_{r\theta}|_{\partial\Omega_1}\, d\theta, \tag{7.2.2}$$

where, in polar coordinates

$$e_{r\theta} = \frac{1}{r}\frac{\partial v_r}{\partial \theta} + \frac{\partial v_\theta}{\partial r} - \frac{v_\theta}{r}$$

and

$$\dot{\gamma} = \left[2\left(\frac{\partial v_r}{\partial r}\right)^2 + \frac{2}{r^2}\left(\frac{\partial v_\theta}{\partial \theta} + v_r\right)^2 + \left(\frac{1}{r}\frac{\partial v_r}{\partial \theta} - \frac{v_\theta}{r} + \frac{\partial v_\theta}{\partial r}\right)^2\right]^{1/2}$$

where $\mathbf{v} = [v_r, v_\theta, 0]$, then using the continuity equation $tr\,(\dot{\gamma}_{ij}) = \nabla \cdot \mathbf{v} = 0$ and recalling $e_{r\theta}|_{\partial\Omega_1} = (\zeta - 2v_\theta/r)|_{\partial\Omega_1}$, equation (7.2.2) simplifies to

$$T_p = \int_0^{2\pi} \left|\zeta|_{\partial\Omega_1} - \frac{2\bar{U}}{c}\right|^{\alpha-1} \left(\zeta|_{\partial\Omega_1} - \frac{2\bar{U}}{c}\right) d\theta. \tag{7.2.3}$$

T_p given above is scaled by k_1 so that (7.2.3) reduces to equation (5.3.3) when $\alpha = 1$. The trapezoidal rule is used to estimate T_p from the vorticity data along the rotor.

Chapter 8

Results for Model Three

Chapter 6 gives the dimensions of the two-dimensional model shown in Fig. 2.1 and defines the meshes used to approximate the steady-state flow fields for Newtonian fluids. Here, the construction of the flow domain is the same as that done in the second model and Mesh C, given in Fig. 6.8, is used to estimate the steady-state flow fields of pseudoplastic fluids within the domain Ω. In applying the algorithm given in Section 7.2, we set $\epsilon_0 = 10^{-6}$, $\epsilon_1 = 10^{-4}$, $\epsilon_2 = 5 \times 10^{-4}$, $\epsilon_3 = 5 \times 10^{-2}$ and $\epsilon_4 = 5 \times 10^{-2}$. Also, we put $\delta_1 = 0.85$, $\delta_2 = 0.95$ and $\delta_3 = 0.95$; however, for problems that involve large S or $|\bar{U}|$, or small α, δ_2 has been made as large as 0.99 to obtain convergence.

To study the flow around the slotted sleeve, we fix the eccentricity ratio and the fluid consistency coefficient at 0.7 and 0.2, respectively, and study the effect that S, α, $\bar{U}$ and $\dot{\gamma}_c$ have on the flow field when the bounding cylinders rotate in opposite senses. We use the parameter set $\{S, \alpha, \bar{U}, \dot{\gamma}_c\}$ to define a given problem and use MATLAB [57] to generate the contour plots of the stream function. In each contour plot, the streamlines are given in increments of 0.2 and are superimposed onto the apparent viscosity function, $h(\dot{\gamma})$, represented using a colour plot. The colours shown in the plots presented indicate the relative values of $h(\dot{\gamma})$ for a given problem. The colour map "hsv" defined in [57] is used here and the colour key used to scale the values of $h(\dot{\gamma})$ is given in Fig 8.1.

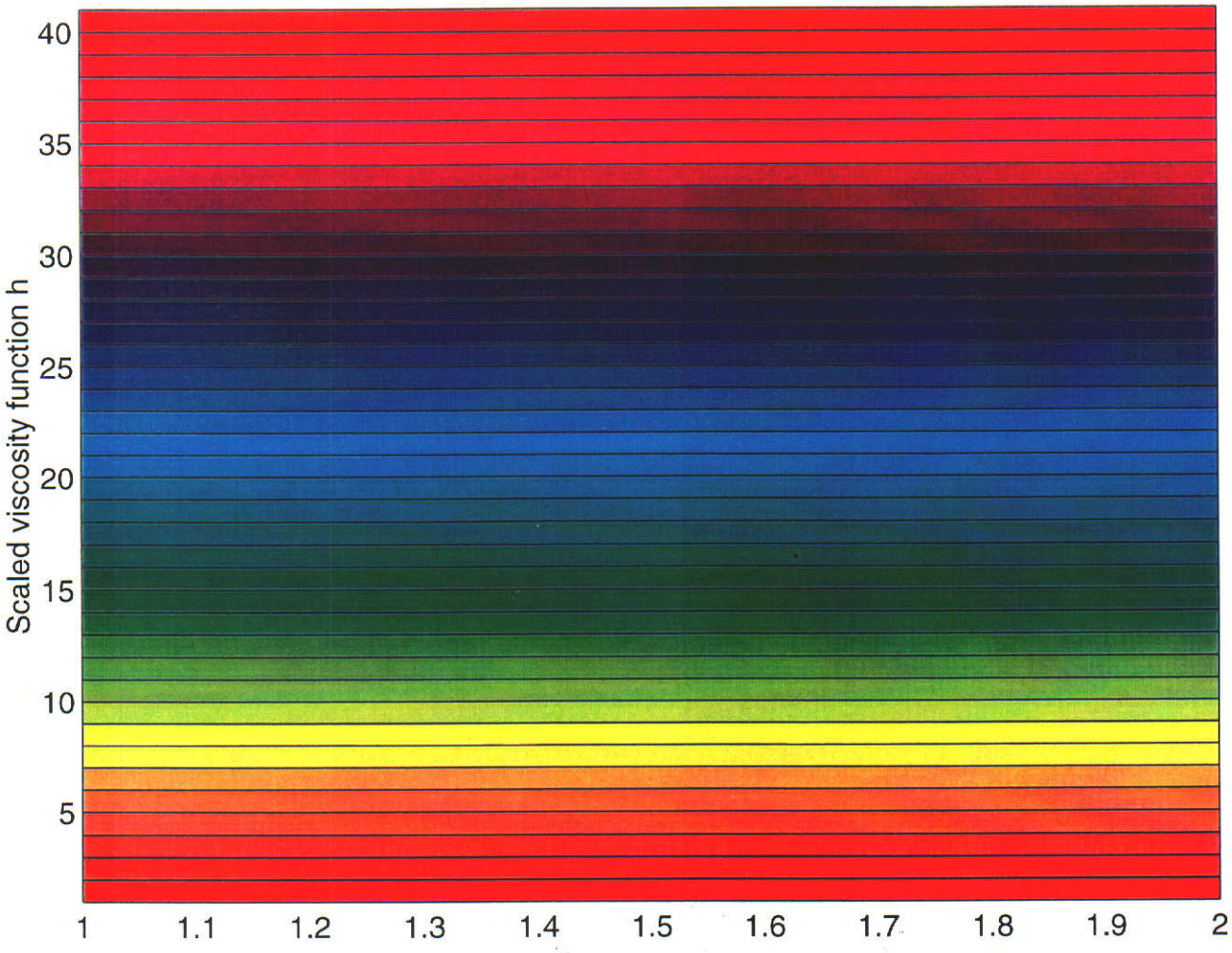

Figure 8.1: Colour key.

S	(x_c, y_c)	ψ_c	ζ_c	h_c	T_p
0.2	$(2.38, -0.32)$	1.38	0.66	0.250	128.55
1.0	$(2.38, -0.32)$	1.17	0.81	0.243	150.70
5.0	$(2.48, 0.00)$	1.71	2.08	0.220	153.08

Table 8.1: Values of ψ, ζ and $h(\dot{\gamma})$ at (x_c, y_c) and torque along the rotor when S is varied.

8.1 The Effect of Diffusivity on the Flow Pattern

To study the effect of the parameter S on the developed flow field, problems $\{0.2, 0.8, -5.0, 10^{-3}\}$, $\{1.0, 0.8, -5.0, 10^{-3}\}$ and $\{5.0, 0.8, -5.0, 10^{-3}\}$ are solved. The flow fields for the extreme values of S are given in Figs. 8.2 and 8.3, and the location of the eddy centre and the nodal values of the stream function, vorticity function and apparent viscosity there, together with the torque exerted along the rotor, are given in Table 8.1. Using the colour key given in Fig. 8.1, regions of high shear rate (i.e., low apparent viscosity) within the annulus and along the surface of the bowl (i.e., within the boundary layers) are observed. From Fig. 8.2, the shear rate reduces quickly away from the slotted sleeve and along an arc following the streamlines that form the lower portion of the counter-rotating eddy present within the flow domain. Furthermore, a region of low shear rate is located along the dividing streamline present within the flow domain. As S is increased, Fig. 8.3 shows a gradual decrease in the shear rate away from the annulus, and the eddy moves in the direction of rotation of the bowl producing a more symmetric flow field and an increase in the fluid flowing through the contraction (i.e., the region where the sleeve is closest to the bowl). The change in the distribution of the apparent viscosity upon

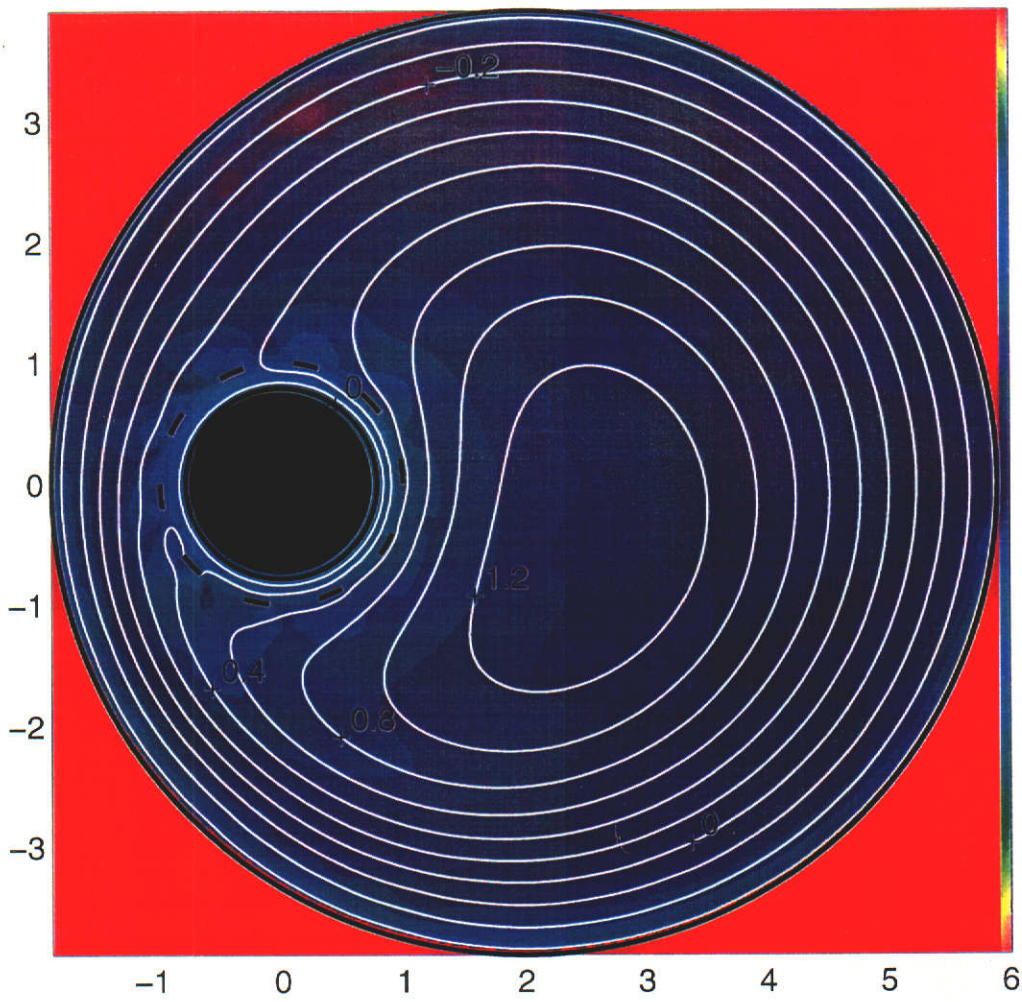

Figure 8.2: Contour plot of the flow field for $S = 0.2$, $\alpha = 0.8$ and $\bar{U} = -5.0$.

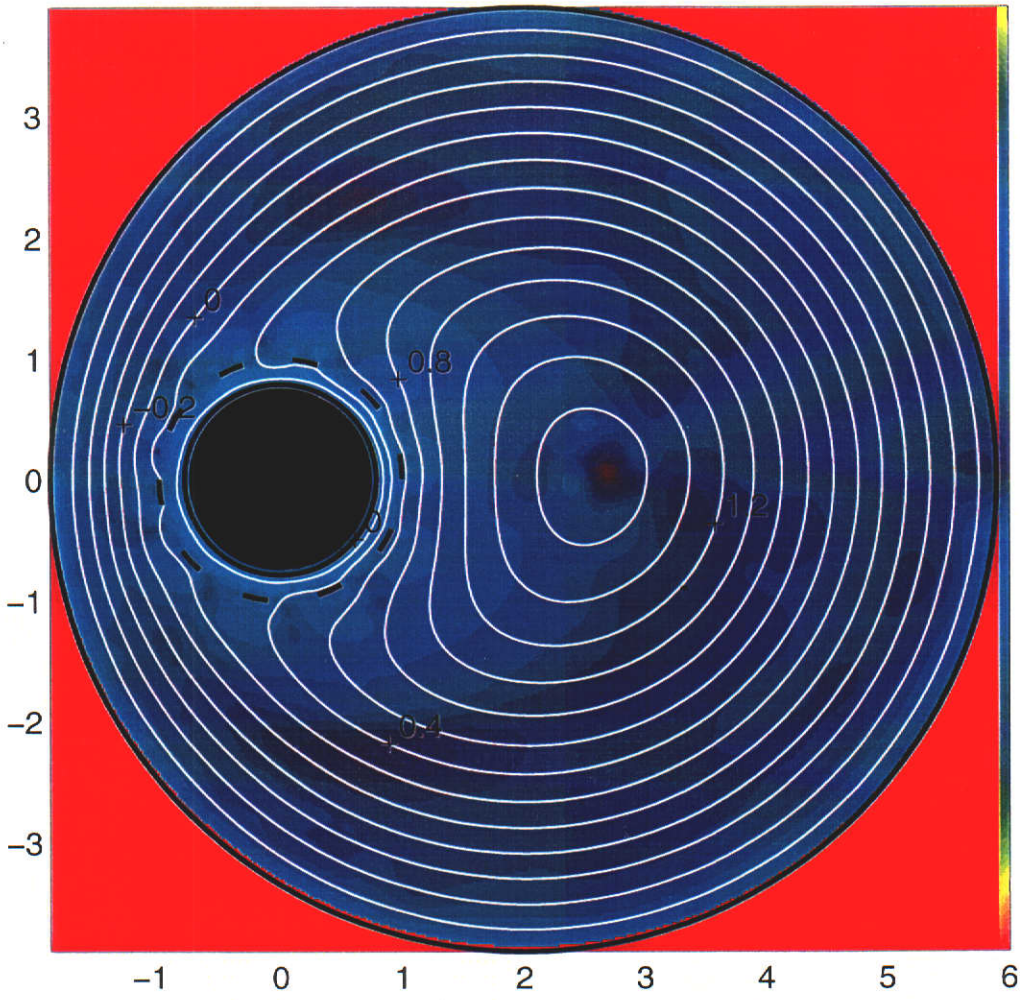

Figure 8.3: Contour plot of the flow field for $S = 5.0$, $\alpha = 0.8$ and $\bar{U} = -5.0$.

increasing S can be explained in two ways. From equation (2.1.13), S can be regarded as the diffusivity for both ζ and $h(\dot{\gamma})$; thus, as S increases, the rate of diffusion of these functions is increased. The immediate relationship between ζ and $h(\dot{\gamma})$ is also seen in (7.1.7). Consequently, in Fig. 8.2 the convection of viscosity (and also vorticity) away from the no-slip surfaces is dominant; whereas, in Fig. 8.3 the diffusion of viscosity (and vorticity) away from the slotted sleeve and bowl is dominant. The second explanation interprets the dimensionless parameter, S, as the ratio of shear forces to inertial forces. An increase in S corresponds to an increase in shear forces within the flow domain (since $\bar{U}$ is fixed). The increase in shear forces is seen in Table 8.1 through the increase in the vorticity and the decrease in the apparent viscosity at the eddy centre. Also, the increase in torque around the rotor with increasing diffusivity, S, indicates an increase (in magnitude) of vorticity generated at this no-slip surface.

8.2 The Effect of the Power Law Index on the Flow Pattern

We now study the effect of varying the power law index, α, by solving the problems $\{0.2, 0.8, -2.0, 10^{-3}\}$, $\{0.2, 0.5, -2.0, 10^{-3}\}$, $\{0.2, 0.35, -2.0, 10^{-3}\}$ and $\{0.2, 0.2, -2.0, 10^{-3}\}$. The contour plots for the extreme values of α are given in Figs. 8.4 and 8.5. Nodal values of the three scalar fields at the eddy centre, together with the torque along the rotor, are presented in Table 8.2. We expect, from the shear-thinning behaviour of a fluid in one-dimensional motion, that as the power law index is reduced, the apparent viscosity of the fluid decreases in regions of high shear and increases in regions of low shear. Thus, for our model, we observe from Table 8.2 that as the non-Newtonian behaviour of the fluid is increased, the torque along the rotor decreases, indicating a decrease in the shear stress within the annulus. Similarly, the increase in apparent

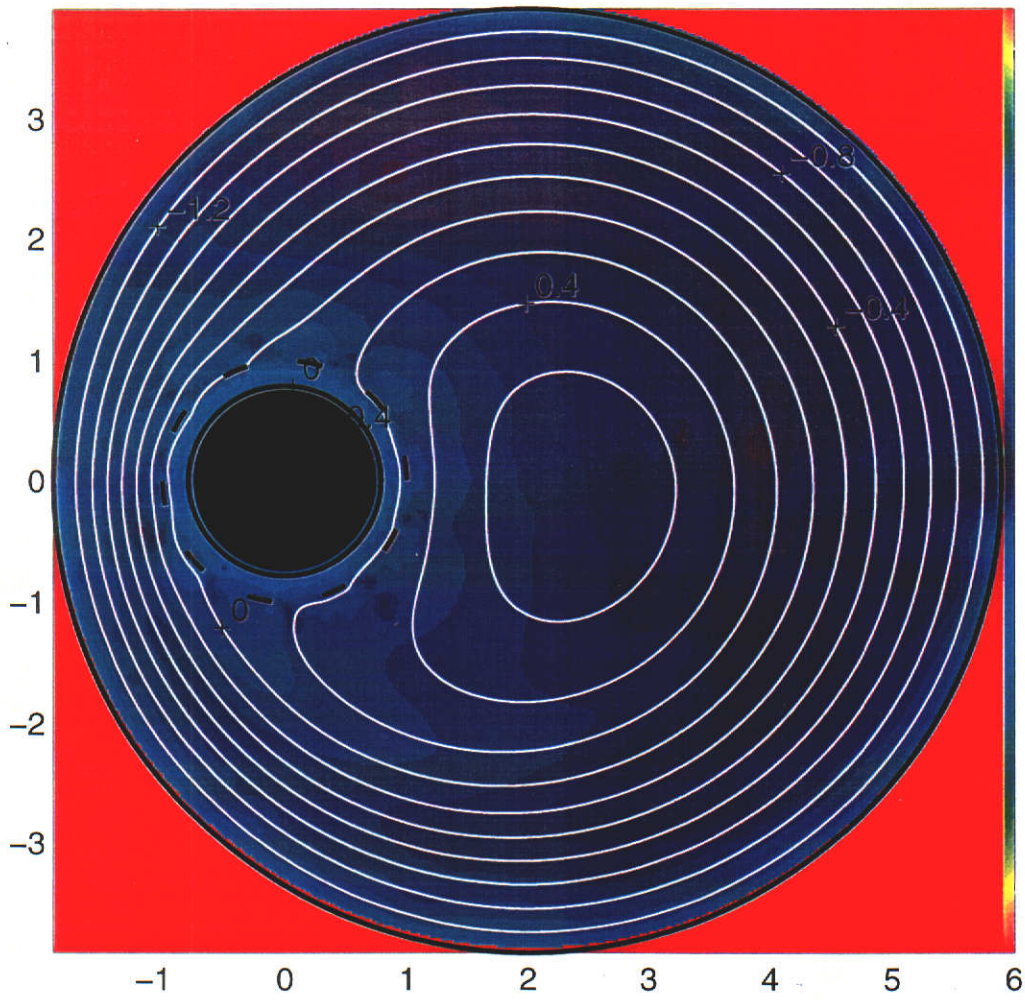

Figure 8.4: Contour plot of the flow field for $\alpha = 0.8$, $S = 0.2$ and $\bar{U} = -2.0$.

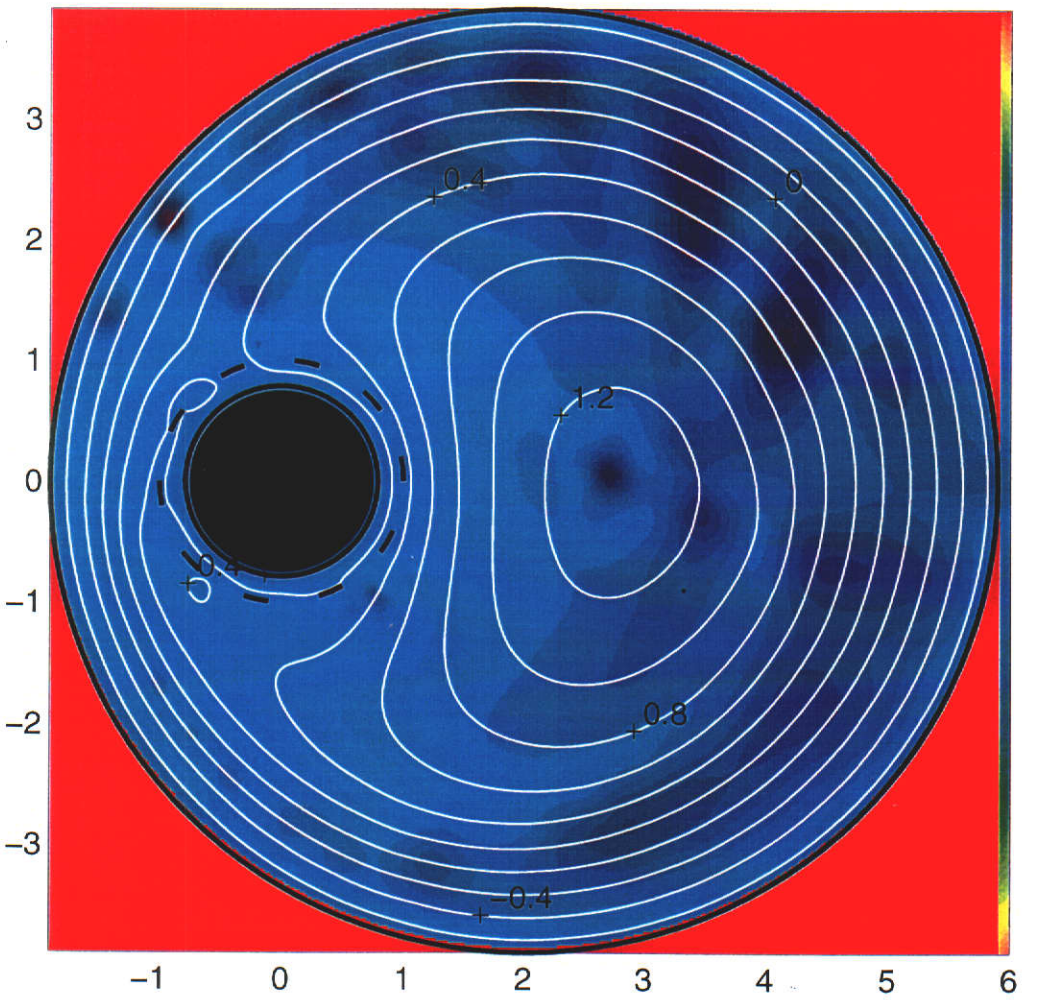

Figure 8.5: Contour plot of the flow field for $\alpha = 0.2$, $S = 0.2$ and $\bar{U} = -2.0$.

α	(x_c, y_c)	ψ_c	ζ_c	h_c	T_p
0.8	(2.47, 0.00)	0.73	0.60	0.285	78.90
0.5	(2.69, 0.06)	1.11	0.60	0.345	25.94
0.35	(2.81, 0.10)	1.12	0.66	0.460	15.91
0.20	(2.89, 0.16)	1.31	1.21	0.507	9.80

Table 8.2: Values of ψ, ζ and $h(\dot{\gamma})$ at (x_c, y_c) and torque along the rotor when α is varied.

viscosity at the eddy centre as the fluid departs from a Newtonian behaviour indicates a region of low shear. Table 8.2 shows that the nodal value of the stream and vorticity functions at the eddy centre increase as the fluid becomes more non-Newtonian. Furthermore, from Figs. 8.4 and 8.5, the change in apparent viscosity is easily seen. As α decreases, there is less variation in the apparent viscosity around the sleeve; while, the shear rate remains low along the dividing streamline. From the contour lines shown in Figs. 8.4 and 8.5, bidirectional flow occurs within the annular region and by observing the number of streamlines within the contraction and the amount of bunching present, we note that upon reducing α, less fluid flows through the contraction with less speed and the streamlines become more circular.

8.3 The Effect of the Rotor Speed on the Flow Pattern

Another parameter that is expected to influence the behaviour of the fluid within the flow domain is the relative rotational speed of the rotor, $\bar{U}$. To study the numerical simulation of the flow fields for various $\bar{U}$, we solve problems $\{0.2, 0.5, -2.0, 10^{-3}\}$, $\{0.2, 0.5, -5.0, 10^{-3}\}$ and $\{0.2, 0.5, -10.0, 10^{-3}\}$. Figs. 8.6 and 8.7 give the steady-state flow fields when $\bar{U} = -2.0$ and $\bar{U} = -10.0$, respectively, and Table 8.3 gives the location of the eddy centre, the nodal

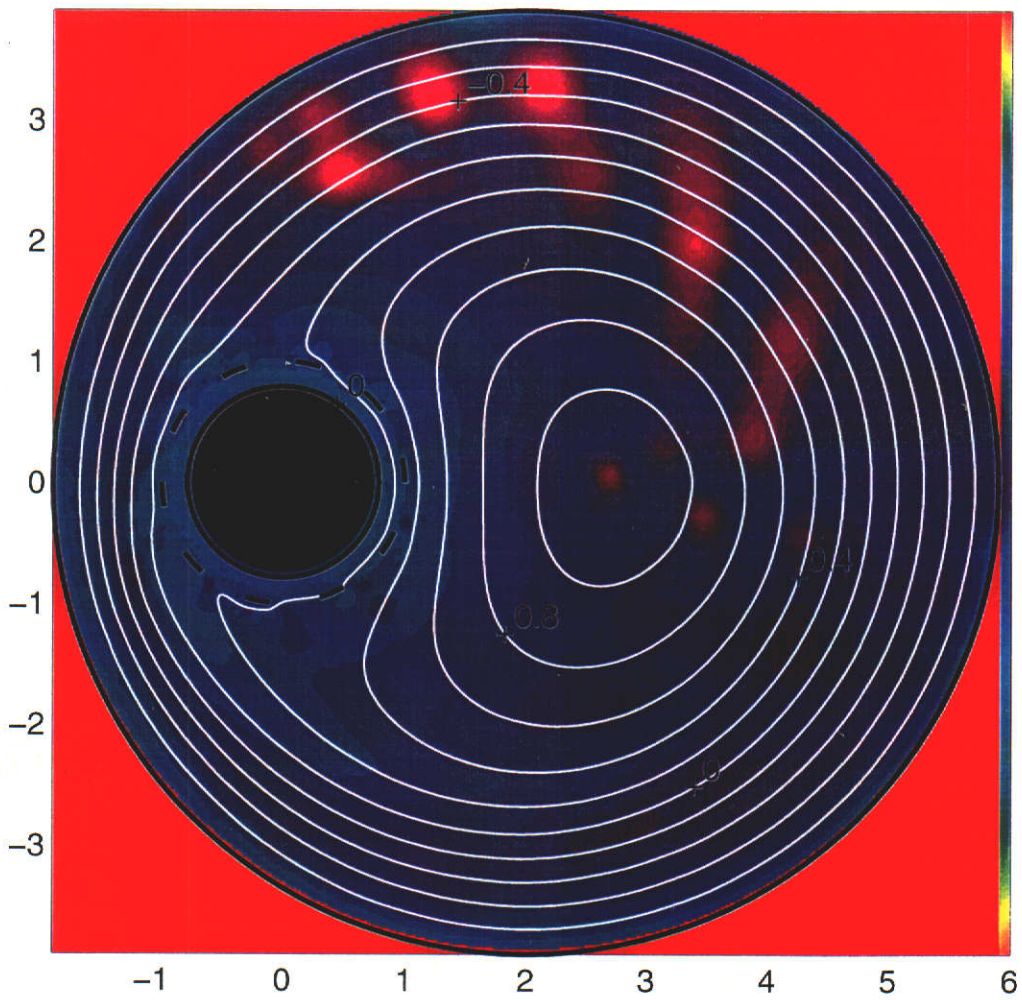

Figure 8.6: Contour plot of the flow field for $\bar{U} = -2.0$, $\alpha = 0.5$ and $S = 0.2$.

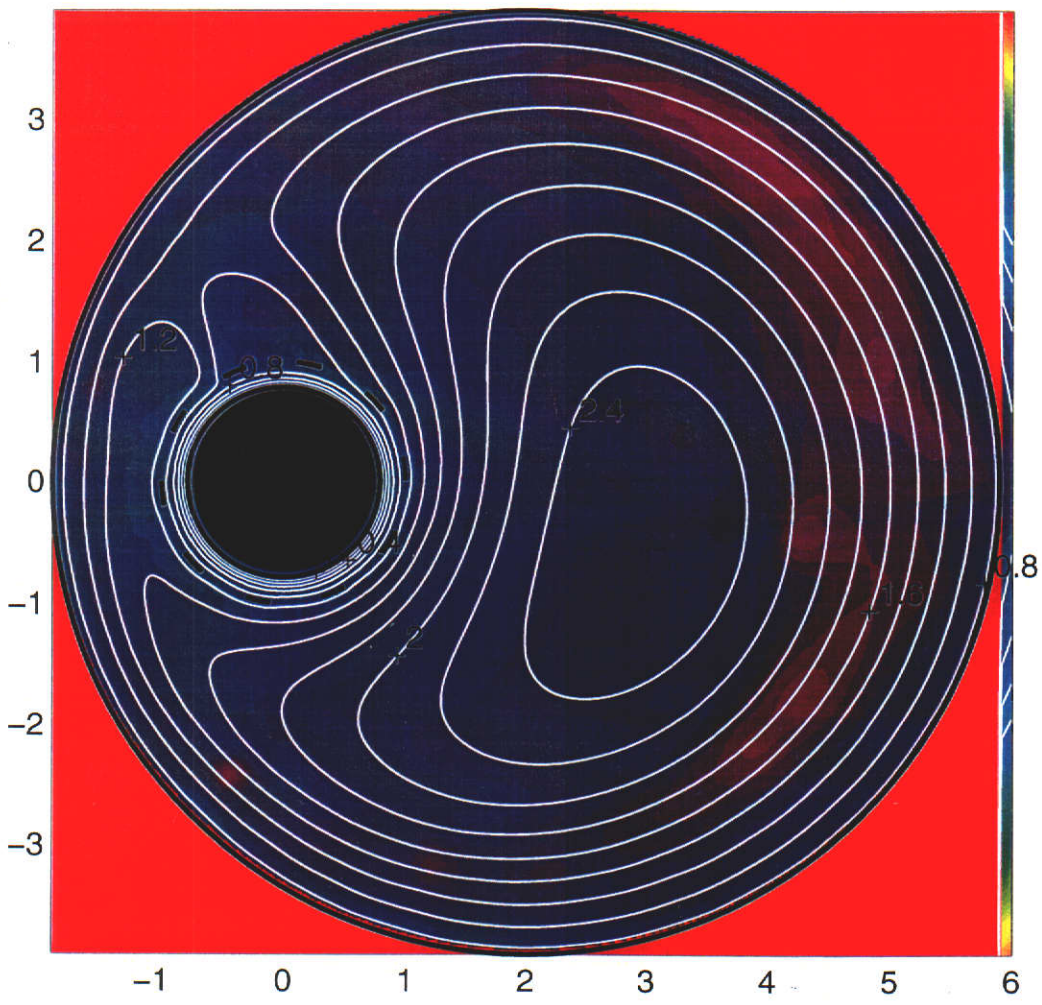

Figure 8.7: Contour plot of the flow field for $\bar{U} = -10.0$ $\alpha = 0.5$ and $S = 0.2$.

values of the scalar fields there and the torque exerted on the rotor. From this table, we observe that increasing the speed of the rotor both increases the vorticity at the eddy centre and the torque exerted on the rotor.

$\bar{U}$	(x_c, y_c)	ψ_c	ζ_c	h_c	T_p
-2.0	$(2.69, 0.06)$	1.11	0.60	0.345	25.94
-5.0	$(2.81, -0.21)$	1.69	0.71	0.357	38.45
-10.0	$(3.04, -0.62)$	2.58	0.73	0.354	53.07

Table 8.3: Values of ψ, ζ and $h(\dot{\gamma})$ at (x_c, y_c) and torque along the rotor when $\bar{U}$ is varied.

We see from Fig. 8.7 that as $|\bar{U}|$ is increased, it appears that only the velocity gradients within the annulus are affected, and increasing the rotor speed does not reduce the regions of low shear present within the main flow field-quite the opposite is observed. In addition, as the rotor speed is increased, there is less fluid flowing both through the contraction and through the slotted sleeve, causing the eddy to move in the direction of the rotation of the rotor. This eddy movement, with increasing rotational speed, has also been observed for Newtonian fluids (see Fig. 6.14). Fig. 8.7 indicates that when the rotor speed is sufficiently large, there exists a region of low shear rate at the entrance to the contraction where a pair of counter-rotating eddies exist; thus, restricting the flow through this region. Comparing Fig. 6.14 with Fig. 8.7, we see that the moderate-Reynolds-number flow can withstand a larger rotor speed, than that used in Fig. 8.7, before a severe restriction in the flow through the contraction is encountered.

8.4 The Effect of the Critical Shear Rate on the Flow Pattern

Until now, a critical shear rate of 10^{-3} has been used when implementing the bi-viscosity model given in equation (7.1.29). This model is used to prevent the possibility of $h(\dot{\gamma})$ from becoming unbounded during the numerical simulation. The need to use this type of technique becomes important as either the rotor speed is increased or as the fluid becomes more non-Newtonian. This can be observed from Table 8.4 which gives (for a given parameter set) the minimum shear rate measured and the approximate maximum value of $h(\dot{\gamma})$ when the bi-viscosity model is used ($\tilde{h}$) and when it is not used ($\hat{h}$). The effect of altering the critical shear rate on the flow field can be seen from Figs. 8.9 and 8.10 which represent the steady-state flow fields for $\{0.2, 0.8, -5.0, 10^{-1}\}$ and $\{0.2, 0.8, -5.0, 1.0\}$. As the critical shear rate is increased, the bi-viscosity model affects more of the fluid by artificially increasing the shear rate of the fluid and therefore resulting in a more uniform distribution in the apparent viscosity. The effect of changing $\dot{\gamma}_c$ can also be seen in Fig. 8.8. This figure displays the value of $h(\dot{\gamma})$ at each node corresponding to the flow fields given in Figs. 8.9 and 8.10. Clearly, as $\dot{\gamma}_c$ is increased, a greater proportion of nodes are fixed at the imposed maximum value of $h(\dot{\gamma})$.

Parameters	$\min(\dot{\gamma})$	$\tilde{h}$	$\hat{h}$
$\{0.2, 0.5, -2.0, 10^{-3}\}$	4.6×10^{-3}	1	1
$\{0.2, 0.5, -5.0, 10^{-3}\}$	9.0×10^{-4}	1	7
$\{0.2, 0.5, -10.0, 10^{-3}\}$	1.4×10^{-4}	2	17
$\{0.2, 0.35, -2.0, 10^{-3}\}$	2.6×10^{-4}	2	43
$\{0.2, 0.2, -2.0, 10^{-3}\}$	7.7×10^{-4}	3	62

Table 8.4: The effect of using the bi-viscosity model.

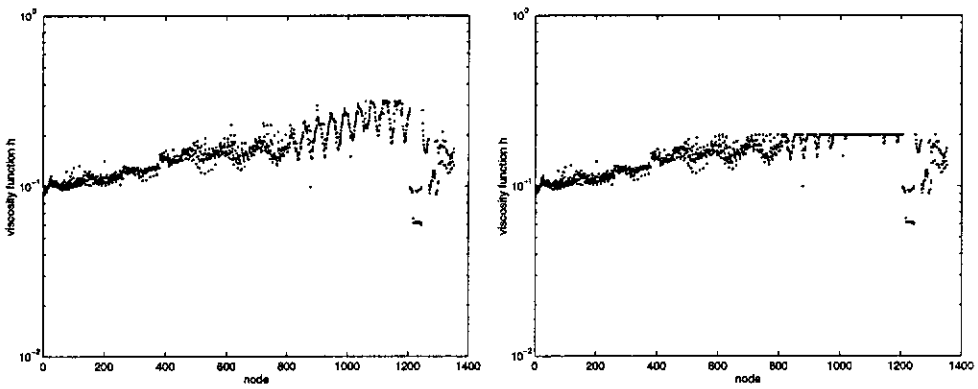

(a) $\dot{\gamma}_c = 10^{-1}$. (b) $\dot{\gamma}_c = 1.0$.

Figure 8.8: Effect of $\dot{\gamma}_c$ on $h(\dot{\gamma})$.

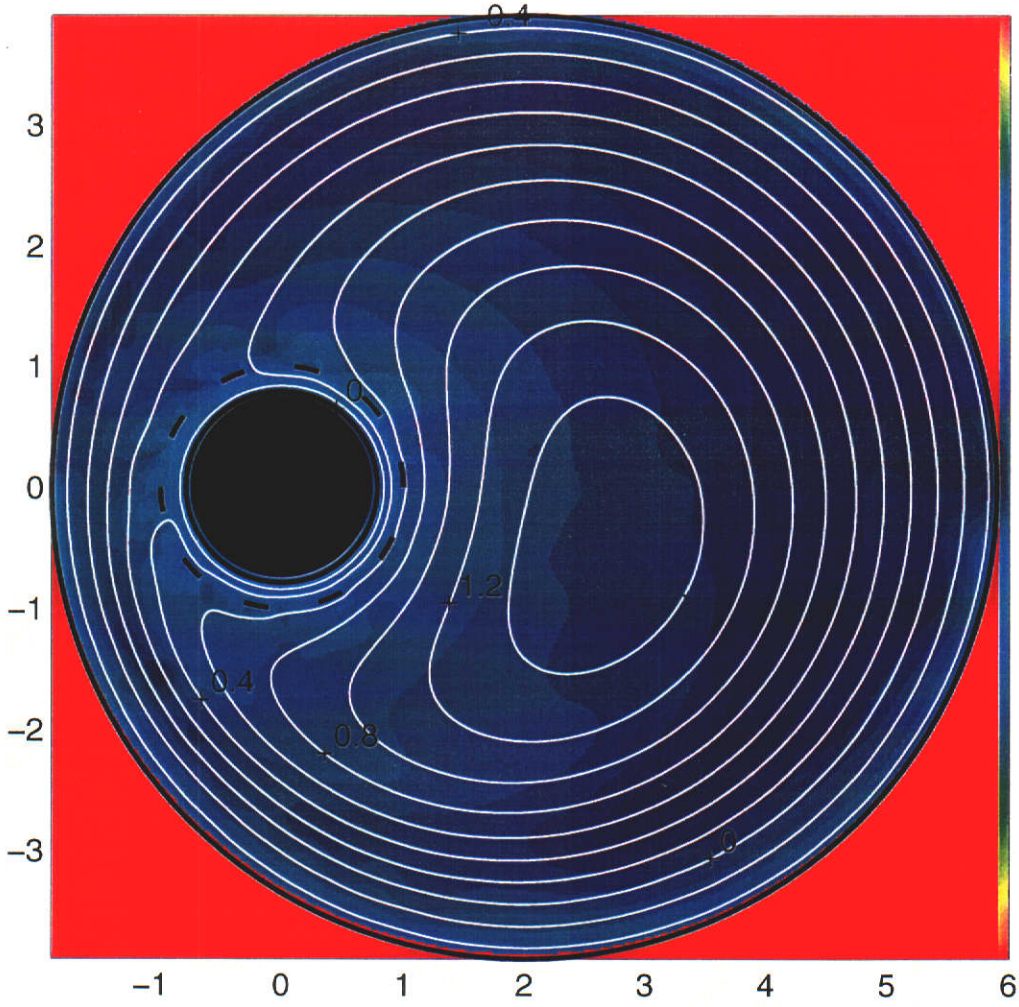

Figure 8.9: Contour plot of a flow field when $\dot{\gamma}_c = 10^{-1}$.

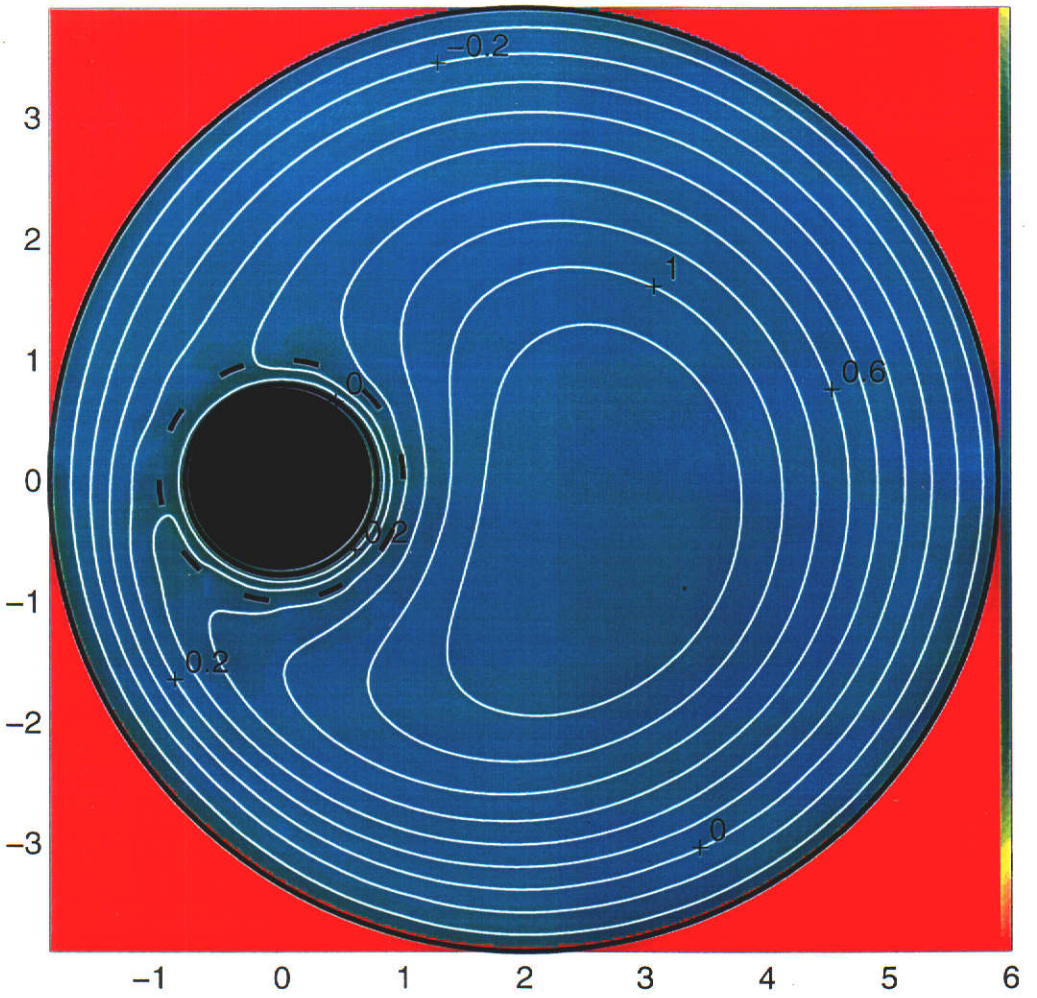

Figure 8.10: Contour plot of a flow field when $\dot{\gamma}_c = 1.0$.

8.5 Summary

Flow patterns have been developed when a pseudoplastic fluid is contained between eccentric counter-rotating cylinders with a slotted sleeve placed around the inner cylinder. For the large-eccentricity flows given here, a large eddy, rotating counter-clockwise, is present within the domain. In addition, for the majority of the problems solved, the results indicate a region of low shear rate approximately along the dividing streamline present within the flow field. The dimensionless parameter S can be regarded as either the diffusivity of both the vorticity and the apparent viscosity or as the ratio of shear forces to inertial forces. When S is small, the convection of $h(\dot{\gamma})$ into the main flow domain is observed (see Fig. 8.3), but for large S, the diffusivity is dominant and the flow pattern becomes more symmetric, with an increase in flow through the contraction, and the eddy is seen to move in the direction of the rotation of the bowl.

The flow patterns of non-Newtonian fluids of varying strength have also been studied. As the non-Newtonian behaviour of the fluid is increased (i.e., reducing α), less variation in the apparent viscosity within the entire flow domain is observed. Furthermore, the streamlines become more circular with a decrease in the amount of fluid flowing through the contraction.

The rotor speed is seen to have a significant effect on the flow through the sleeve. Increasing the rotor speed reduces the amount of fluid flowing both through the sleeve and through the contraction; causing the eddy to move in the direction of the rotation of the rotor. Also, by increasing the rotor speed, a pair of counter-rotating eddies, located at the entrance to the contraction, appear to exist. The rotor speed needed to severely restrict the flow through the contraction is lower for pseudoplastic fluids than for Newtonian fluids. The use of the bi-viscosity model is seen to become more important as either

the rotor speed or the non-Newtonian behaviour is increased. By varying the critical shear rate, the apparent viscosity function can be influenced to reduce its variation within the flow field.

Chapter 9

Conclusions and Directions for Future Research

The research undertaken in this dissertation examines the behaviour of the fluid flow around a slotted sleeve placed concentrically around the interior cylinder of two eccentric rotating cylinders. The geometry represents a two-dimensional model of the viscometer designed by Overend et al [68] and used by the Curtin University Slurry Research Group to measure the viscosity of mineral-based slurries that have a tendency to settle. There are many factors that affect the performance of this viscometer, for example, the presence of large masses of particles and the formation of sediment. These two important factors have been addressed by studying the amount of flow through the slotted sleeve and by locating the regions of low shear rate for a single-phase fluid. Three two-dimensional models are used to acomplish this. From the results presented here, the mixing of the slurry is expected to be enhanced by moving the rotor and slotted sleeve close to the rotating bowl and using low to moderate rotational speeds of the rotor and bowl. In addition, when the bounding cylinders rotate in the same direction, two counter-rotating eddies are present within the flow field. Their presence inhibits the flow through the slotted sleeve. When the cylinders rotate in opposite directions, the counter-rotating eddy present within the domain promotes the flow through the sleeve.

As expected, increasing the rotor speed restricts the flow through the sleeve and through the narrow region between the sleeve and the bowl. The rotor speed needed to severely restrict the flow through this region is less for a pseudoplastic fluid than for a Newtonian fluid (of moderate to large Reynolds number).

From the distribution of the apparent viscosity within the flow field, for moderate to high values of the power law index, a region of low shear is located near the dividing streamline present within the flow field. Thus, from the two-dimensional study undertaken, we would expect to see the particles of the corresponding slurries in the three-dimensional flow agglomerate in approximately the same region. Consequently, the mixture filling the annulus used to determine the apparent viscosity, as the shear rate is varied, will not be an accurate sample of the composition of the slurry being tested. Of course, these masses can be broken down by increasing the shear forces within the flow domain, that is, by increasing the rotor speed but this will have a detrimental effect on the flow through the sleeve, leading to the formation of sediment and, therefore, reducing the accuracy of the measurements taken. Furthermore, the mixing of the slurry can also be impeded by the presence of eddies within the main flow domain. The location of these eddies, and, therefore, the regions of entry into the annulus, is affected by the eccentricity, rotor speed and diffusivity of the apparent viscosity within the domain.

The work presented here is certainly an improvement over the initial work of Hird and Siew [42] in that the current work takes into account the large-slot construction of the sleeve and the, approximate, non-Newtonian behaviour of slurries. However, the results presented here are obtained by imposing the assumptions that the flow of slurries within the viscometer bears a close relationship to the two-dimensional flow of a single-phase fluid between non-coaxial rotating cylinders where a slotted sleeve is placed around the inner cylinder.

Consequently, only a limited amount of information can be extracted from the results presented. The ultimate goal would be the three-dimensional flow of heterogeneous mixtures within the viscometer shown in Fig. 1.1. This would involve taking into account the orientation of the bowl, the profiled surface of the rotor and the thickness of the sleeve. In addition, suitable governing equations, used to model the transport properties and the particle-to-particle interaction of the different phases of the mixture, must be defined. An immediate improvement on the models presented here would be to study the flow fields generated using viscoplastic fluids. This approach, although still two-dimensional, will show the plug regions, if any, within the flow domain. A three dimensional CFD approach would also give an insite into the function of the viscometer. Furthermore, although the stability of Newtonian and non-Newtonian flows between concentric and eccentric rotating cylinders has been studied, no work, as yet, has been done to study the effect that the slotted sleeve has on those parameters that signal the transition from laminar to secondary flow and beyond to bifurcation.

Bibliography

[1] M. Abramowitz and I.A. Stegun (eds.), *Handbook of mathematical functions* (Dover, New York, 1970).

[2] Y. Achdou and O. Pironneau, "A fast solver for Navier-Stokes equations in the laminar regime using mortar finite element and boundary element methods", *SIAM Journal of Numerical Analysis* **32** (4) (1995) 985–1016.

[3] I. Ashino and K. Yoshida, "Slow motion between eccentric rotating cylinders", *Bulletin of the Japan Society of Mechanical Engineers* **18** (117) (1975) 280–285.

[4] A.J. Baker, "Finite element solution algorithm for viscous incompressible fluid dynamics", *International Journal for Numerical Methods in Engineering* **6** (1973) 89–101.

[5] B.Y. Ballal and R.S. Rivlin, "Flow of a Newtonian fluid between eccentric rotating cylinders:inertial effects", *Archive for Rational Mechanics and Analysis* **62** (1977) 237–294.

[6] R.E. Bank, J.F. Bürgler, W. Fichtner and R.K. Smith, "Some upwind techniques for finite element approximations of convection-diffusion equations", *Numerische Mathematik* **58** (1990) 185–202.

[7] H.A. Barnes, "A review of the slip (wall depletion) of polymer solutions, emulsions and particle suspensions in viscometers: its cause, character,

and cure", *Journal of non-Newtonian Fluid Mechanics* **56** (1995) 221–251.

[8] S. Barnett, *Matrices:Methods and Applications* (Clarendon Press, Oxford, England, 1990).

[9] G.K. Batchelor, "On steady laminar flow with closed streamlines at large Reynolds number", *Journal of Fluid Mechanics* **1** (1956) 177–190.

[10] G.K. Batchelor, *An introduction to fluid dynamics.* (Cambridge University Press, London, 1967).

[11] M. Bentwich and C. Elata, "Eddy formation in an eccentric annular domain", *The Physics of Fluids* **8** (12) (1965) 2204–2210.

[12] M. Bercovier and M. Engelman, "A finite-element method for incompressible non-Newtonian flow.", *Journal of Computational Physics* **36** (1980) 313–326.

[13] R.B. Bird, W.E. Stewart and E.N. Lightfoot, *Transport phenomena.* (Wiley, New York, 1960).

[14] S.H. Bittleston and O. Hassager, "Flow of viscoplastic fluids in a rotating concentric annulus", *Journal of non-Newtonian Fluid Mechanics* **42** (1992) 19–36.

[15] A. Brandt and I. Yavneh, "Inadequacy of first-order upwind difference schemes for some recirculating flows", *Journal of Computational Physics* **93** (1991) 128–143.

[16] A.N. Brooks and T.J.R. Hughes, "Streamline upwind/Petrov-Galerkin formulations for convection dominated flows with particular emphasis on the incompressible Navier-Stokes equations", *Computer Methods in Applied Mechanics and Engineering* **32** (1982) 199–259.

[17] E.M. Buturla, P.E. Cottrell, B.M. Grossman and K.A. Salsburg, "Finite-element analysis of semiconductor devices: the FIELDAY program", *IBM Journal of Research and Development* **25** (4) (1981) 218–231.

[18] A. Campion-Renson and M.J. Crochet, "On the stream function-vorticity finite element solutions of Navier-Stokes equations", *International Journal for Numerical Methods in Engineering* **12** (1978) 1809–1818.

[19] C. Canuto and V. Van Kemenade, "Bubble-stabilized spectral methods for the incompressible Navier-Stokes equations", *Computer Methods in Applied Mechanics and Engineering* **135** (1996) 35–61.

[20] H.D. Chandler and R.L. Jones, "Flow kinetics in concentrated suspensions of silica-iron(III) oxide-water", *Philosophical Magazine A* **59** (3) (1989) 645–660.

[21] S.C. Chang, "The method of space-time conservation element and solution element-a new approach for solving the Navier-Stokes and Euler equations", *Journal of Computational Physics* **119** (1995) 295–324.

[22] B.W. Char, K.O. Geddes, G.H. Gonnet, M.B. Monagan and S.M. Watt, *Maple reference manual*, 5th ed. (Watcom, Canada, 1988).

[23] D.P. Chen and Z. Zhao, "A weighted penalty finite element method for the analysis of power-law fluid flow problems.", *Applied Mathematics and Mechanics* **11** (4) (1990) 297–300.

[24] P.D. Chipman and P.W. Duck, "On the high-Reynolds-number flow between non-coaxial rotating cylinders", *Quarterly Journal of Mechanics and Applied Mathematics* **46** (2) (1993) 163–191.

[25] J.A. Cole, "Taylor-vortex instability and annulus-length effects.", *Journal of Fluid Mechanics* **75** (1) (1976) 1–15.

[26] G. Comini, M. Manzan and C. Nonino, "Finite element solution of the streamfunction-vorticity equations for the incompressible two-dimensional flows", *International Journal for Numerical Methods in Fluids* **19** (1994) 513–525.

[27] R.V. Craster, "Yield surfaces for Herschel-Bulkley flows in complex geometries.", *IMA Journal of Applied Mathematics.* **56** (1996) 253–276.

[28] M.J. Crochet, A.R. Davies and K. Walters (eds.), *Numerical simulation of non-Newtonian flow* (Elsevier, Amsterdam, 1984).

[29] G. Dhatt, K. Bonaventure and C. Bourque, "A ψ-ζ finite element formulation for the Navier-Stokes equations", *International Journal for Numerical Methods in Engineering* **17** (1981) 199–212.

[30] I.K. Dien and H.G. Elrod, "A generalized steady-state Reynolds equation for non-Newtonian fluids, with application to journal bearings.", *Journal of Lubrication Technology Trans. ASME* **105** (1983) 385–390.

[31] R.C. DiPrima and J.T. Stuart, "Flow between eccentric rotating cylinders.", *Journal of Lubrication Technology Trans. ASME* **67** (1) (1972) 266–274.

[32] R.W. Flumerfelt, M.W. Pierick, S.L. Cooper and R.B. Bird, "Generalized plane Couette flow of a non-Newtonian fluid.", *Industrial and Engineering Chemistry Fundamentals.* **8** (2) (1969) 354–357.

[33] U. Ghia, K.N. Ghia and C.T. Shin, "High-Re solutions for incompressible flow using the Navier-Stokes equations and a multigrid method", *Journal of Computational Physics* **48** (1982) 387–411.

[34] R. Glowinski and O. Pironneau, "Numerical methods for the first biharmonic equation and for the two-dimensional Stokes problem", *SIAM Review* **21** (2) (1979) 167–212.

[35] P.M. Gresho, "Some current cfd issues relevant to the incompressible Navier-Stokes equations", *Computer Methods in Applied Mechanics and Engineering* **87** (1991) 201–252.

[36] P.M. Gresho and R.L. Lee, "Don't suppress the wiggles-they're telling you something!", *Computers and Fluids* **9** (1981) 223–253.

[37] M.D. Gunzburger and J.S. Peterson, "Finite-element methods for the streamfunction-vorticity equations:boundary-condition treatments and multiply connected domains.", *SIAM Journal of Scientific and Statistical Computing* **9** (4) (1988) 650–668.

[38] M.M. Gupta and R.P. Manohar, "Boundary approximations and accuracy in viscous flow computations", *Journal of Computational Physics* **31** (1979) 265–288.

[39] R.W. Hanks and K.M. Larsen, "The flow of power-law non-Newtonian fluids in concentric annuli.", *Industrial and Engineering Chemistry Fundamentals.* **18** (1) (1979) 33–35.

[40] P. Henriksen and O. Hassager, "Corner flow of power law fluids", *Journal of Rheology* **33** (6) (1989) 865–879.

[41] L.D. Hird, "Viscous flow between rotating cylinders", M. Sc. Thesis, School of Mathematics and Statistics, Curtin University of Technology, 1993.

[42] L.D. Hird and P.F. Siew, "Small Reynolds number flow between eccentric rotating cylinders with a permeable sleeve", *Journal of the Australian Mathematical Society Series B* **38** (2) (1996) 255–273.

[43] L.D. Hird and P.F. Siew, "An analytical solution to the large Reynolds number flow between eccentric rotating cylinders with a permeable sleeve", Technical Report 12/97, School of Mathematics and Statistics, Curtin University of Technology, 1997.

[44] L.D. Hird, P.F. Siew and S. Wang, "A numerical solution to the flow between eccentric rotating cylinders with a slotted sleeve", Journal of the Australian Mathematical Society Series B, submitted for publication, 1997.

[45] M. Hriberšek and L. Škerget, "Iterative methods in solving Navier-Stokes equations by the boundary element method", *International Journal for Numerical Methods in Engineering* **39** (1996) 115–139.

[46] R.R. Huilgol and M.P. Panizza, "On the determination of the plug flow region in Bingham fluids through the application of variational inequalities", *Journal of non-Newtonian Fluid Mechanics* **58** (1995) 207–217.

[47] M. Ikegawa, "A new finite element technique for the analysis of steady viscous flow problems", *International Journal for Numerical Methods in Engineering* **14** (1979) 103–113.

[48] C. Ilicali and S.T. Engez, "Laminar flow of power law fluid foods in concentric annuli.", *Journal of Food Engineering* **30** (1996) 255–262.

[49] M.W. Johnson, Jr and S. Mangkoesoebroto, "Analysis of lubrication theory for the power law fluid.", *Journal of Tribology Trans. ASME* **115** (1993) 71–77.

[50] M.M. Kamal, "Separation in the flow between eccentric rotating cylinders.", *Journal of Basic Engineering Trans. ASME* **88** (1966) 717–724.

[51] E.S. Kulinski and S. Ostrach, "Journal-bearing velocity profiles for small-eccentricity and moderate modified Reynolds numbers.", *Journal of Applied Mechanics Trans. ASME* **34** (1) (1967) 16–22.

[52] S.J. Liao and J.M. Zhu, "A short note on high-order streamfunction-vorticity formulations of 2d steady state Navier-Stokes equations", *International Journal for Numerical Methods in Fluids* **22** (1996) 1–9.

[53] S.H. Lin and C.C. Hsu, "Generalized Couette flow of a non-Newtonian fluid in annuli.", *Industrial and Engineering Chemistry Fundamentals.* **19** (1980) 421–424.

[54] C. Logos and Q.D. Nguyen, "Effect of particle size on the flow properties of a South Australian coal-water slurry", *Powder Technology* **88** (1996) 55–58.

[55] R.H. MacNeal, "An asymmetrical finite difference network", *Quarterly Journal of Applied Mathematics* **11** (3) (1953) 295–310.

[56] R. Malik and U.V. Shenoy, "Generalized annular Couette flow of a power-law fluid.", *Industrial and Engineering Chemistry Research.* **30** (1991) 1950–1954.

[57] The MathWorks Inc., *MATLAB:high-performance numeric computation and visualization software*, 1995.

[58] B.J. McCartin, "Discretization of the semiconducter device equations", in *New Problems and New Solutions for Device and Process Modelling* (ed. J.J.H. Miller), (Boole, Dublin, 1985).

[59] J.A. Meijerink and H.A. van der Vorst, "An iterative solution method for linear systems of which the coefficient matrix is a symmetric M-matrix", *Mathematics of Computation* **31** (137) (1977) 148–162.

[60] J.J.H. Miller and S. Wang, "An exponentially fitted finite volume method for the numerical solution to 2d unsteady incompressible flow problems", *Journal of Computational Physics* **115** (1) (1994) 56–64.

[61] J.J.H. Miller and S. Wang, "A new non-conforming Petrov-Galerkin finite-element method with triangular elements for a singularly perturbed advection-diffusion problem", *IMA Journal of Numerical Analysis* **14** (1994) 257–276.

[62] N. Miyazaki, "Some finite element formulations for flow analysis of power law fluid.", in *Computational Mechanics '86 : theory and applications : Proceedings of the International Conference on Computational Mechanics*, (Tokyo, 1986), 121–126.

[63] H.K. Moffatt, "Viscous and resistive eddies near a sharp corner", *Journal of Fluid Mechanics* **18** (1964) 1–18.

[64] S. Mukhopadhyay and B.C. Basu, "Second-order accurate no-slip conditions for solving problems of incompressible viscous flows", *Journal of Computational Physics* **111** (1994) 53–61.

[65] J.D. Murray, *Asymptotic Analysis* (Springer-Verlag, New York, 1984).

[66] C.M. Myllerup and B.J. Hamrock, "Perturbation approach to hydrodynamic lubrication theory.", *Journal of Tribology Trans. ASME* **116** (1994) 110–118.

[67] A. Okabe, B. Boots and K. Sugihara, *Spatial tessellations: concepts and applications of Voronoi diagrams* (Wiley, England, 1992).

[68] I.J. Overend, R.R. Horsley, R.L. Jones and R.K. Vinycomb, "A new method for the measurement of rheological properties of settling slurries", in *IXth International Congress of Rheology.*, (Mexico, 1984), 583–590.

[69] J.P. Pascal, "Unsteady rotating shear flow of power law fluids", *Mathematical and Computer Modelling* **18** (9) (1993) 31–53.

[70] P. Perrochet, "A streamline-upwind-full-Galerkin method for space-time convection dominated transport problems", *International Journal for Numerical Methods in Engineering* **36** (1993) 4165–4183.

[71] N. Phan-Thien, A.L. Graham, S.A. Altobelli, J.R. Abbott and L.A. Mondy, "Hydrodynamic particle migration in a concentrated suspension undergoing flow between rotating eccentric cylinders.", *Industrial Engineering and Chemical Research* **34** (1995) 3187–3194.

[72] W.H. Press, S.A. Teukolsky, W.T. Vetterling and B.P. Flannery, *Numerical recipes in FORTRAN*, 2nd ed. (Cambridge University Press, England, 1992).

[73] B.V. Ratish Kumar and K.B. Naidu, "A streamline upwinding streamfunction-vorticity finite element analysis of Navier-Stokes equations", *Applied Numerical Mathematics* **13** (1993) 335–344.

[74] H.A. Rodriguez-Prada, F.F. Pironti and A.E. Sáez, "Fundamental solutions of the streamfunction-vorticity formulation of the Navier-Stokes equations", *International Journal for Numerical Methods in Fluids* **10** (1990) 1–12.

[75] N.S. Roh, D.H. Shin, D.C. Kim and J.D. Kim, "Rheological behaviour of coal-water mixtures", *Fuel* **74** (9) (1995) 1313–1318.

[76] L. Rosenhead (ed.), *Laminar boundary layers* (Dover, New York, 1963).

[77] Z.S. Safar, "Journal bearings operating with non-Newtonian lubricant films.", *Wear* **53** (1979) 95–100.

[78] A. San Andres and A.Z. Szeri, "Flow between eccentric rotating cylinders.", *Journal of Applied Mechanics* **51** (1984) 869–878.

[79] A.E. Scheidegger, *The physics of flow through porous media* (Oxford Univeristy Press, London, 1963).

[80] L.A. Segel, "Application of conformal mapping to viscous flow between moving circular cylinders.", *Quarterly of Applied Mathematics* **18** (4) (1961) 335–353.

[81] P.F. Siew and L.D. Hird, "Symbolic computation and viscous flows between eccentric cylinders", in *The sixth Asian congress of fluid mechanics.*, (Singapore, 1995), 460–463.

[82] J.C. Simo and F. Armero, "Unconditional stability and long-term behavior of transient algorithms for the incompressible Navier-Stokes and Euler equations", *Computer Methods in Applied Mechanics and Engineering* **111** (1994) 111–154.

[83] P. Sonneveld, "CGS, a fast lanczos-type solver for nonsymmetric linear systems", *SIAM Journal of Scientific and Statistical Computing* **10** (1) (1989) 36–52.

[84] D.R. Sood and H.G. Elrod, "Numerical solution of the incompressible Navier-Stokes equations in doubly-connected regions.", *AIAA Journal* **12** (5) (1974) 636–641.

[85] P. Szabo and O. Hassager, "Flow of viscoplastic fluids in eccentric annular geometries", *Journal of non-Newtonian Fluid Mechanics* **45** (1992) 149–169.

[86] R.I. Tanner and X. Huang, "Stress singularities in non-Newtonian stick-slip and edge flows", *Journal of non-Newtonian Fluid Mechanics* **50** (1993) 135–160.

[87] R.I. Tanner and J.F. Milthorpe, "Numerical simulation of the flow of fluids with yield stresses.", in *Third International Conference on Numerical Methods in Laminar and Turbulent Flow.*, (Seattle, 1983), 680–690.

[88] C. Taylor and P. Hood, "A numerical solution for the Navier-Stokes equations using the finite element technique", *Computers and Fluids* **1** (1973) 73–100.

[89] C. Tiu and S. Bhattacharyya, "Developing and fully developed velocity profiles for inelastic power law fluids in an annulus.", *AIChE, Journal.* **20** (6) (1974) 1140–1144.

[90] R.S. Varga, "M-matrix theory and recent results in numerical linear algebra", in *Sparse matrix computations* (eds. J.R. Bunch and D.J. Rose), (Academic Press, New York, 1976).

[91] P.L. Versteegen and D.F. Jankowski, "Experiments on the stability of viscous flow between eccentric rotating cylinders", *The Physics of Fluids* **12** (6) (1969) 1138–1143.

[92] G.H. Wannier, "A contribution to the hydrodynamics of lubrication.", *Quarterly of Applied Mathematics* **8** (1950) 1–32.

[93] G.N. Watson, *A treatise on the theory of Bessel functions* (Cambridge University Press, London, 1944).

[94] W.L. Wilkinson, *Non-Newtonian fluids.* (Pergamon Press, London, 1960).

[95] W.W. Wood, "The asymptotic expansions at large Reynolds numbers for steady motion between non-coaxial rotating cylinders", *Journal of Fluid Mechanics* **13** (2) (1957) 159–175.

[96] Y. Yamada and K. Nakabayashi, "On the flow between eccentric rotating cylinders when the outer cylinder rotates.", *Bulletin of the Japan Society of Mechanical Engineers* **11** (45) (1968) 455–462.

[97] L. Yang and G.A. Chukwu, "A simplified Couette flow solution of non-Newtonian power-law fluids in eccentric annuli.", *The Canadian Journal of Chemical Engineering* **73** (1995) 241–247.

Appendix A

Using the WKB Method to generate Asymptotic Expansions for $\xi_m(\rho; Re)$

The exponential character of the solutions to the Bessel equation given in equation (3.4.6) can be found by using the WKB method (see Murray [65]). Equation (3.4.6) can be written in the form

$$\Theta''(\rho; Re) + \left(-\frac{imRe(A_o\rho^2 + B_o)}{\rho^2} + \frac{1 - 4m^2}{4\rho^2} \right) \Theta(\rho; Re) = 0 \qquad \text{(A.0.1)}$$

through the substitution $\xi_m(\rho; Re) = \dfrac{\Theta(\rho; Re)}{\rho^{1/2}}$, and following the WKB method, we put

$$\Theta(\rho; Re) \sim exp\left\{ \sum_{n=0}^{\infty} g_n(Re) s_n(\rho) \right\}, \qquad Re \to \infty, \qquad \text{(A.0.2)}$$

where, from the form of equation (A.0.1), $g_n(Re)$ is the sequence $\{Re^{(1-n)/2}\}$. Substituting equation (A.0.2) into (A.0.1) and balancing terms, we find

$$\begin{aligned}
O(Re) &: \left(s_0'(\rho)\right)^2 \sim \frac{im\,(A_o\rho^2 + B_o)}{\rho^2}, \\
O(\sqrt{Re}) &: s_0''(\rho) + 2s_0'(\rho)s_1'(\rho) \sim 0, \\
O(1) &: s_1''(\rho) + \left(s_1'(\rho)\right)^2 + 2s_0'(\rho)s_2'(\rho) \sim \frac{4m^2 - 1}{4\rho^2}, \\
O(1/\sqrt{Re}) &: s_2''(\rho) + 2\left(s_1'(\rho)s_2'(\rho) + s_0'(\rho)s_3'(\rho)\right) \sim 0, \\
O(Re^{-1}) &: s_3''(\rho) + \left(s_2'(\rho)\right)^2 + 2\left(s_1'(\rho)s_3'(\rho) + s_0'(\rho)s_4'(\rho)\right) \sim 0,
\end{aligned} \qquad \text{(A.0.3)}$$

and so on. Before we solve the above equations for $s_n(\rho)$, we note from equation (3.3.5) that the slip velocity dictates the sign and relative magnitudes of both A_o and B_o. Consequently, different expansions will exist depending on these factors.

If both A_o and B_o are positive, then let $N(\rho) = A_o\rho^2 + B_o$ (where $N(\rho)$ is positive within the outer regime) and we find from equation (A.0.3)

$$\begin{aligned} s_0(\rho) &= \pm\sqrt{im}\sigma(\rho), \quad \text{where} \qquad (A.0.4)\\ \sigma(\rho) &= \int^{\rho} \frac{\sqrt{N(s)}}{s} ds = \sqrt{N(\rho)} + \sqrt{B_o}\ln\left(\frac{\sqrt{N(\rho)} - \sqrt{B_o}}{\sqrt{A_o}\rho}\right), \end{aligned}$$

$$s_1(\rho) = -1/4\ln\left(N(\rho)\right) + 1/2\ln\rho, \qquad (A.0.5)$$

$$s_2(\rho) = \pm\frac{3\sqrt{B_o}A_o\rho^2 - 2B_o^{3/2} - 12m^2(N(\rho))^{3/2}\text{arctanh}\left(\sqrt{N(\rho)}/\sqrt{B_o}\right)}{24\sqrt{imB_o}(N(\rho))^{3/2}},$$

and (A.0.6)

$$s_3(\rho) = -\frac{(4m^2-1)A_o^2\rho^4 + (1+2m^2)4A_oB_o\rho^2 + 4m^2B_o^2}{16im(N(\rho))^3}, \qquad (A.0.7)$$

and so on. As we shall see, Defining $N(\rho)$ to be positive within the outer regime allows a clear interpretation of the exponential nature of the expansions developed.

If A_o is positive, B_o is negative and $\frac{1}{\rho}\left|\frac{B_o}{A_o}\right|^{1/2} < 1$ (i.e., $|A_o|\rho^2 - |B_o| > 0$ within the outer regime), then we define $N(\rho) = |A_o|\rho^2 - |B_o|$ and observe

$$\begin{aligned} s_0(\rho) &= \pm\sqrt{im}\sigma(\rho), \quad \text{where} \qquad (A.0.8)\\ \sigma(\rho) &= \sqrt{N(\rho)} + i\sqrt{|B_o|}\log\left(\frac{\sqrt{|B_o|} + i\sqrt{N(\rho)}}{\sqrt{|A_o|}\rho}\right), \end{aligned}$$

$$s_1(\rho) = -1/4\ln\left(N(\rho)\right) + 1/2\ln\rho, \qquad (A.0.9)$$

$$s_2(\rho) = \pm\frac{2|B_o|^{3/2} - 3\sqrt{|B_o|}|A_o|\rho^2 - 12m^2(N(\rho))^{3/2}\arctan\left(\sqrt{N(\rho)}/\sqrt{|B_o|}\right)}{24\sqrt{im|B_o|}(N(\rho))^{3/2}},$$

and (A.0.10)

$$s_3(\rho) = \frac{(4m^2-1)|A_o|^2\rho^4 + (1+2m^2)4|A_o||B_o|\rho^2 + 4m^2B_o^2}{16im(N(\rho))^3}, \quad \text{(A.0.11)}$$

and so on; however, if $\frac{1}{\rho}\left|\frac{B_o}{A_o}\right|^{1/2} > 1$ (i.e., $|A_o|\rho^2 - |B_o| < 0$) then we put $N(\rho) = |B_o| - |A_o|\rho^2$ and define

$$s_0(\rho) = \pm\sqrt{-im}\sigma(\rho) \quad \text{where} \quad \text{(A.0.12)}$$

$$\sigma(\rho) = \sqrt{N(\rho)} - \sqrt{|B_o|}\ln\left(\frac{\sqrt{|B_o|}+\sqrt{N(\rho)}}{\sqrt{|A_o|}\rho}\right),$$

$$s_1(\rho) = -1/4\ln(N(\rho)) + 1/2\ln\rho, \quad \text{(A.0.13)}$$

$$s_2(\rho) = \pm\frac{2|B_o|^{3/2} + 3\sqrt{|B_o|}|A_o|\rho^2 + 12m^2(N(\rho))^{3/2}\text{arctanh}\left(\sqrt{N(\rho)}/\sqrt{|B_o|}\right)}{24\sqrt{-im|B_o|}(N(\rho))^{3/2}},$$

and (A.0.14)

$$s_3(\rho) = \frac{(1-4m^2)|A_o|^2\rho^4 + (1+2m^2)4|A_o||B_o|\rho^2 - 4m^2B_o^2}{16im(N(\rho))^3}, \quad \text{(A.0.15)}$$

and so on.

For a given slip velocity, the only remaining occurence is the case when A_o is negative, B_o is positive and $\frac{1}{\rho}\left|\frac{B_o}{A_o}\right|^{1/2} > 1$. Here we put $N(\rho) = |B_o| - |A_o|\rho^2$ and use

$$s_0(\rho) = \pm\sqrt{im}\sigma(\rho) \quad \text{where} \quad \text{(A.0.16)}$$

$$\sigma(\rho) = \sqrt{N(\rho)} - \sqrt{|B_o|}\ln\left(\frac{\sqrt{|B_o|}+\sqrt{N(\rho)}}{\sqrt{|A_o|}\rho}\right),$$

$$s_1(\rho) = -1/4\ln(N(\rho)) + 1/2\ln\rho, \quad \text{(A.0.17)}$$

$$s_2(\rho) = \pm\frac{3\sqrt{|B_o|}|A_o|\rho^2 + 2|B_o|^{3/2} + 12m^2(N(\rho))^{3/2}\text{arctanh}\left(\sqrt{N(\rho)}/\sqrt{|B_o|}\right)}{24\sqrt{im|B_o|}(N(\rho))^{3/2}},$$

and (A.0.18)

$$s_3(\rho) = \frac{(4m^2-1)|A_o|^2\rho^4 - (1+2m^2)4|A_o||B_o|\rho^2 + 4m^2B_o^2}{16im(N(\rho))^3}, \quad \text{(A.0.19)}$$

and so on to obtain the asymptotic expansions. If we now define functions $S_i(\rho)$, $i = 0, 1, 2, \ldots$, so that

$$s_0(\rho) = \pm S_o(\rho), \quad s_1(\rho) = S_1(\rho), \quad s_2(\rho) = \pm S_2(\rho),$$

and so on, then depending on the value of g_0, the asymptotic WKB approximation to ξ_m for large Reynolds number is given by

$$\begin{aligned}\xi_m(\rho; Re) \sim & \frac{\mathcal{A}_1(Re)}{(N(\rho))^{1/4}} \exp\left\{P\sqrt{mRe/2}\sigma(\rho) + \frac{S_2(\rho)}{\sqrt{Re}} + \frac{S_3(\rho)}{Re} + \frac{S_4(\rho)}{Re^{3/2}} + \ldots\right\} + \\ & \frac{\mathcal{A}_2(Re)}{(N(\rho))^{1/4}} \exp\left\{-P\sqrt{mRe/2}\sigma(\rho) - \frac{S_2(\rho)}{\sqrt{Re}} + \frac{S_3(\rho)}{Re} - \frac{S_4(\rho)}{Re^{3/2}} + \ldots\right\},\end{aligned} \tag{A.0.20}$$

where we take $\sqrt{i} = (1+i)/\sqrt{2}$ and $\sqrt{-i} = (1-i)/\sqrt{2}$ and define P accordingly. Equation (A.0.20) can be written as

$$\begin{aligned}\xi_m(\rho; Re) \sim & \frac{\mathcal{A}_1(Re) e^{P\sqrt{mRe/2}\sigma(\rho)}}{(N(\rho))^{1/4}} \left[1 + \frac{\tau_1(\rho)}{\sqrt{Re}} + \frac{\tau_2(\rho)}{Re} + \frac{\tau_3(\rho)}{Re^{3/2}} + \ldots\right] \\ & + \frac{\mathcal{A}_2(Re) e^{-P\sqrt{mRe/2}\sigma(\rho)}}{(N(\rho))^{1/4}} \left[1 - \frac{\tau_1(\rho)}{\sqrt{Re}} + \frac{\tau_2(\rho)}{Re} - \frac{\tau_3(\rho)}{Re^{3/2}} + \ldots\right],\end{aligned} \tag{A.0.21}$$

where

$$\tau_1(\rho) = S_2(\rho), \tag{A.0.22}$$

$$\tau_2(\rho) = S_3(\rho) + S_2^2(\rho)/2, \tag{A.0.23}$$

$$\tau_3(\rho) = S_4(\rho) + S_2(\rho)S_3(\rho) + 2S_2^3(\rho)/6, \tag{A.0.24}$$

and so on.

As pointed out earlier, the form of the expansions obtained here depend on the sign of A_o and B_o as well as the magnitude of $\frac{1}{\rho}\left|\frac{B_o}{A_o}\right|^{1/2}$. The relationship between the relative magnitudes and the slip velocity is seen through the following bounds,

$$\frac{1}{\rho}\left|\frac{B_o}{A_o}\right|^{1/2} > 1 \quad \text{when } g_0 > \frac{\beta^2+1}{2\beta}, \text{ for } 1 \le \rho \le \beta, \tag{A.0.25}$$

$$\text{and} \quad \frac{1}{\rho}\left|\frac{B_o}{A_o}\right|^{1/2} < 1 \quad \text{when } 0 < g_0 < \frac{2\beta}{\beta^2+1}, \text{ for } 1 \leq \rho \leq \beta. \text{(A.0.26)}$$

Furthermore, bounds can be given for the various combinations of the signs of A_o and B_o, viz

$$A_o > 0, B_o > 0 \quad \text{when} \quad \frac{1}{\beta} < g_0 < \beta, \tag{A.0.27}$$

$$A_o > 0, B_o < 0 \quad \text{when} \quad g_0 < \frac{1}{\beta}, \tag{A.0.28}$$

$$\text{and} \qquad A_o < 0, B_o > 0 \quad \text{when} \quad g_0 > \beta. \tag{A.0.29}$$

From these bounds we deduce that the slip velocity, g_0, must be positive. That is, the tangential velocities of the membrane and the outer cylinder must be in the same direction, and, therefore, the unperturbed azimuthal velocity will not vanish within the outer regime. If an expansion for $\xi_m(\rho)$ can be found for a given value of the slip velocity, and noting the close relationship between the unperturbed azimuthal velocity and $\sigma(\rho)$ (or $N(\rho)$), $\sigma(\rho)$ represents a monotonic increasing function and since $N(\rho)$ does not vanish, the expansion is analytic within the outer regime.

In the ensuing analysis, the complex coefficients $\mathcal{A}_1(Re)$ and $\mathcal{A}_2(Re)$ need not be known but can be determined by comparing the dominant behaviour of $\xi_m(\rho)$ with the leading behaviour of $J_{\mu_m}(\lambda_m\rho)$ and $H^{(1)}_{\mu_m}(\lambda_m\rho)$ obtained through tables (see Abramowitz and Stegun [1]). The first term in (A.0.21) corresponds to the asymptotic expansion for $J_{\mu_m}(\lambda_m\rho)$; while, the second term corresponds to the asymptotic expansion for $H^{(1)}_{\mu_m}(\lambda_m\rho)$. Furthermore, we note from (A.0.21) that both Bessel functions possess a rapidly oscillating component producing waves of wave length $O(\sqrt{2/mRe})$ as ρ increases; however, the amplitude of $J_{\mu_m}(\lambda_m\rho)$ decays exponentially away from the bowl and the amplitude of $H^{(1)}_{\mu_m}(\lambda_m\rho)$ decays exponentially away from the membrane. Therefore, within the outer regime, the first order vorticity function comprises of two components that are significant close to the bounding surfaces but decay

exponentially away from these boundaries.